

Scuola di Scienze

Dipartimento di Fisica e Astronomia


Corso di Laurea magistrale in Astrofisica e Cosmologia

**A Dynamical and Spectrophotometric Study of
Russian Molniya/Meridian Satellite
Constellation**

Tesi di laurea

Presentata da:
Filippo Matassoni

Relatore:
Chiar.mo Prof. Alberto Buzzoni



Co-relatori:

Dott. Alain Figer

Dott. Silvia Galletti

Dott. Jose' Guichard

Sessione II

Anno accademico 2016-2017

May the force be with you

ABSTRACT

In questo lavoro di tesi abbiamo svolto un'analisi delle caratteristiche spettrofotometriche e dinamiche della costellazione di satelliti Molniya e Meridian. Molniya e Meridian sono satelliti per le telecomunicazioni militari russi. Il nostro lavoro rientra nel contesto della space debris science, e in particolare nello studio degli space debris (o detriti spaziali) nell'ottica di creare una base di partenza per la soluzione del problema della sindrome di Kessel. Ci siamo basati su immagini fotometriche e spettrali acquisite durante dieci notti d'osservazione con il telescopio Cassini dell'Osservatorio astronomico di Bologna nella parte finale del 2016, su immagini fotometriche acquisite dal professor Alberto Buzzoni tra il 2014 e il 2016 e su immagini acquisite da Alain Figer. In questo lavoro ci siamo focalizzati su quattro argomenti diversi.

- Lo studio delle instabilità rotazionali che questi satelliti sviluppano una volta fuori controllo e la loro evoluzione temporale. Abbiamo analizzato con un periodogramma le curve di luce dei satelliti, e dove possibile abbiamo estratto il periodo rotazionale. In seguito abbiamo cercato in osservazioni precedenti i periodi rotazionali dei satelliti di cui abbiamo trovato un periodo con le osservazioni di fine 2016. Per cinque satelliti abbiamo così ottenuto il periodo rotazionale riferito a due tempi diversi. Abbiamo quindi costruito un modello fenomenologico per riprodurre i rallentamenti osservati del periodo rotazionale. Il modello risultante è un modello esponenziale con tempo caratteristico 28.44 anni.
- Lo studio delle instabilità gravitazionali alle quali sono sottoposti i satelliti con orbita di tipo Molniya. Le perturbazioni tendono a portare il satellite vicino alla zona di frenamento atmosferico causandone il rientro in atmosfera. Il ruolo fondamentale nel condizionare l'evoluzione dell'altezza del perigeo è giocato dalla longitudine del nodo ascendente, mentre l'argomento del perigeo rimane costante per via dell'inclinazione dell'orbita tipo Molniya. Leggere variazioni di inclinazione sono sufficienti a innescare l'evoluzione dell'argomento del perigeo, condizionando perciò l'intera storia orbitale.
- La relazione che lega la magnitudine apparente e l'angolo di fase. Abbiamo costruito quattro modelli differenti per spiegare il trend decrescente della magnitudine al crescere dell'angolo di fase. I quattro modelli sono: un modello Lunar ROLO, un modello sferico lambertiano, un modello lunare e un modello lambertiano planare. Il modello di best fit è quello lambertiano sferico in tutti i filtri fotometrici. Il modello ci ha permesso di fissare un limite inferiore all'albedo, $a_{min} = 0.09$ nel filtro B, $a_{min} = 0.28$ nel filtro I, $a_{min} = 0.15$ nel filtro R e $a_{min} = 0.10$ nel filtro V. Questi valori sono stati calcolati considerando l'area riflettente del satellite uguale all' RCS.
- Lo studio delle proprietà spettrali e degli indici di colore dei Molniya debris. Abbiamo costruito i grafici colore-colore per questi satelliti e abbiamo studiato cercato evoluzioni di colore dovute all'età o all'angolo di fase. Non sono state trovate dipendenze dei colori dall'età né dall'angolo di fase. I grafici colore-colore ci hanno tuttavia permesso di comprendere come le capacità riflettive dei satelliti tipo Molniya variano con la

lunghezza d'onda, in particolare sono elevate in banda I e calano via via passando dalla banda R, alla V fino alla B. Questo ha in parte confermato i valori di albedo trovati con i modelli di magnitudine contro angolo di fase. Abbiamo inoltre tentato un confronto fra i colori dei satelliti e i colori dei materiali di cui sono costruiti. I satelliti hanno colori più rossi rispetto ai materiali, i materiali che più si avvicinano ai colori dei Molniya sono il Mylar e i pannelli solari. Con gli spettri abbiamo calcolato la funzione di riflettanza dei Molniya al fine di compararla con le misure di laboratorio dei materiali di cui questi satelliti sono composti e per cercare eventuali trend con l'età. Gli spettri analizzati non presentano le somiglianze attese con le funzioni di riflettanza dell'alluminio nei pannelli solari, ma si dispongono in una zona intermedia fra questi due. Questo suggerisce che i colori osservati siano la somma di queste due componenti. Come per gli indici di colore non è stato nemmeno trovato alcun trend con l'età.

ABSTRACT

In this thesis work we carried out an analysis of the spectrophotometric and dynamical characteristics of Molniya and Meridian satellites constellation. Molniya and Meridian satellites are Russian payloads for military communications. Our work falls within the context of space debris Science, and in particular in the study of space debris in order to create a starting base for the resolution of the Kessler syndrome problem. We based on photometric and spectroscopic images taken during ten nights of observation with the Cassini telescope at the Bologna Astronomical Observatory in the final part of 2016, photometric images taken by professor Alberto Buzzoni in 2014, 2015 and 2016, and images made by Alain Figer. In this work we have focused on four main topics.

- The study of rotational instabilities that these satellites develop after they went out of control and their temporal evolution. We analyzed the satellite light curves with a periodogram, and where possible we extracted the tumbling period. Later we searched in previous observations the tumbling periods of the satellites of which we have found a period with the observations of 2016. For five satellites we have thus obtained a rotational period referred to two different times. We build then a phenomenological model to reproduce the observed spindown rate of the tumbling period. The model is an exponential with characteristic time of 28.44 years.
- The study of gravitational instabilities to which Molniya orbit satellites are subjected and their consequences on their orbital life. Perturbations tend to bring the satellite near the atmospheric drag zone causing the re-entry into atmosphere. The fundamental role is played by the longitude of the ascending node in conditioning the evolution of the height of the perigee, while the argument of the perigee remains constant due to the inclination of Molniya type orbits. Small variation of inclination are sufficient to trigger the argument of the perigee evolution, thus conditioning the entire orbital history.

- The relation that ties the apparent magnitude and the phase angle. We developed four possible models to explain the observed decreasing trend of magnitude with increasing phase angle. The four models were a Lunar ROLO model, a spherical lambertian model, a Lunar model, and a planar lambertian model. The best-fit model was the spherical lambertian model in all the photometric filters analyzed. The models allowed us to put a lower limit on the albedo value for Molniya debris, $a_{min} = 0.09$ for filter B, $a_{min} = 0.28$ for filter I, $a_{min} = 0.15$ for filter R, and $a_{min} = 0.10$ for filter V. This values were calculated considering the reflecting area of the satellite equal to the RCS.
- The study of spectral properties and color indexes of Molniya debris. We built color-color diagrams for these satellites and we searched for color evolution with age and phase angle. Color dependencies on age or phase angle have not been found. Color-color diagrams, however, have made it possible to understand how the reflective capacities of Molniya-type satellites vary with the wavelength, in particular they are high in band I and fall off by passing from band R to V to B. This has in part confirmed the albedo values obtained with magnitude vs. phase angle models. We also tried to compare the colors of the satellites and the colors of the materials of which they are constructed. The satellites have redder colors than the materials, the materials closest to Molniya's colors are the Mylar and the solar panels. With the spectra we calculated the Molniya reflective function in order to compare it with the laboratory measurements of the materials of which these satellites are composed and to look for any trend with the age. The spectra analyzed do not exhibit the similarities expected with the reflection functions of aluminum or solar panels, but they are located in an intermediate zone between these two. This suggests that the observed colors are the sum of these two components. As with color indexes, no trend has been found with age.

Contents

1	Introduction	1
1.1	Satellite general characteristics and history	1
1.1.1	Orbital categories	3
1.1.2	Geostationary orbit	4
1.2	Molniya orbit	5
1.3	Space debris	6
1.4	Molniya and Meridian satellite	8
1.5	Optical tracking and imaging of space debris	9
2	Data acquisition and reduction	11
2.1	Instrumentation	11
2.1.1	Cassini telescope	11
2.1.2	BFOSC	12
2.2	Observational techniques	14
2.3	Image pre-reduction	15
2.4	Photometryc data reduction	16
2.4.1	Extraction of the Light Curves	16
2.4.2	Magnitude calibration	17
2.5	Spectroscopic reduction	19
2.5.1	Extraction of the 1D spectra	21
2.5.2	Wavelength calibration	21
2.5.3	Flux calibration	24
2.6	Figer images	26
2.7	Periodogram analysis	29
2.8	Phase angle calculation	30
3	Periodogram analysis	33
3.1	Introduction	33
3.2	Molniya 1-88	33
3.3	Molniya 1-63	41
3.4	Molniya 3-3	45
3.5	Meridian 1	49
3.6	Molniya 2-10	53
3.7	Molniya 3-42	56
3.8	Molniya 1-53	59
3.9	Molniya 1-69	63
3.10	Molniya 3-8	67
3.11	Molniya 2-9	69

3.12	Molniya 1-S	71
3.13	Molniya 3-27	78
3.14	Molniya 2-17	81
3.15	Molniya 1-87	85
3.16	Molniya 2-13	87
3.17	Molniya 1-62	88
3.18	Molniya 1-32	94
3.19	Molniya 3-40	95
3.20	Molniya 3-50	96
3.21	Molniya 3-13	98
3.22	Molniya 1-56	98
3.23	Molniya 3-24	98
3.24	Molniya 3-51	99
3.25	Molniya 1-90	101
3.26	Molniya 1-80	105
3.27	Molniya 1-86	107
3.28	Meridian 2	108
3.29	Meridian 4	108
3.30	The special cases of Molniya 1-86 and Molniya 1-44	110
4	Molniya and Meridian constellation general properties	113
4.1	Phase angle - Magnitude relation	113
4.2	Photometric and Spectral analysis of Molniya and Meridian constellation	124
4.2.1	Color indexes analysis	124
4.2.2	Spectral analysis	129
4.3	Tumbling period slowdown model	135
4.3.1	The case of Molniya 3-08	142
4.4	The fallen	143
5	Conclusions	151
A	Observations	155
A.1	Night 2016/08/01-02	155
A.2	Night 2016/08/02-03	174
A.3	Night 2016/09/26-27	182
A.4	Night 2016/09/27-28	196
A.5	Night 2016/11/26-27	211
A.6	Night 2016/12/22-23	235
A.7	Night 2016/12/23-24	258
B	Codes	265
B.1	Cubic spline c++ code	265
B.2	Phase angle c++ calculation code	268
B.3	Periodogram supermongo macro	270
B.4	Phase angle magnitude model supermongo macro	273
B.5	Tumbling period slowdown model supermongo macro	275
B.6	Spectral analysis macro	279

List of Figures

1.1	Orbital elements of Kepler	2
1.2	Generalized elliptical orbit	3
1.3	The two main perturbaton effects on a geostationary orbit from dynamical models, N-S (top) and E-W (bottom). Colombo and Gkolias (2017)	4
1.4	Molniya orbit.	5
1.5	Molniya orbit ground track.	6
1.6	Representation of the position of all satellites orbiting around the earth	7
1.7	Molniya spacecraft.	8
1.8	Meridian spacecraft.	9
2.1	The Loiano telescope site	11
2.2	Schematic representation of the BFOSC	12
2.3	Different grisms spectral range and resolution. Grism #4 has a "free spectral range" smaller than the value shown in the table. In fact the table shows the first order spectral coverage but the range free from second order overlap ends at 700 nm. Grisms #10 , #11, and #12 are cross-dispersers to be used mainly with echelle grism #9 and are mounted on the filters wheel. They are optimized according to the working band: grism #10 has a peak efficiency in the blue, grism #11 in the visible and grism #12 in the red. Also the number of orders on the detector varies with the cross-disperser: grism #10 gives 13 orders, grism #11 gives 9 orders and grism #12 gives 6 orders.	14
2.4	Airmass correction constant vs. Wavelength	18
2.5	Loiano CCD cardinal points position.	19
2.6	Example of photometric zero points obtained by comparing observed and tabulated magnitudes of two standard fields (PG0231-051 and PG1047-003)	20
2.7	Example of an observed (left) standard filed in R filter and its image (right) as reported on Landolt (1992).	20
2.8	Example of aperture extraction of standard standard star spectra and a debris spectra, as you can see the debris spectra is more noisy and partially hidden by backround stras spectra crossing the slit during the exposition	22
2.9	Example of trace fitting and extracted specra of a standard star.	23
2.10	Example of manual (top) and automatic (bottom) identification of emission lines	24

2.11	Example of the operation of the STANDARD task	25
2.12	Example of the operation of the SENSFUNC task	26
2.13	Example of image taken by Figer, exposition time = 4 s. Here is not plotted the full image but only a central portion to make the details more visible. The full image is about twice the size of this one.	27
2.14	Example of image obtained by adding ten Figer's images, in rai- bow colors. Here the sky is prominent and the brightness gradient due to light pollution is evident.	28
2.15	Example of image obtained by adding ten Figer's images and sub- tracting their median ten times, in rainbow colors. The cleaning process has dramatically improved the image by making it clear the satellite track, however, the traces of the stars remain.	28
2.16	In the left panel is represented the situation described by equation 2.5, in the right panel we find the application of the cosine rule to the calculation of the phase angle.	31
3.1	Filter R periodogram analysis of Molniya 1-88, December obser- vations.	34
3.2	Filter V periodogram analysis of Molniya 1-88, December obser- vations.	36
3.3	Filter I periodogram analysis of Molniya 1-88, December obser- vations.	36
3.4	Filter B periodogram analysis of Molniya 1-88, December obser- vations.	37
3.5	Here is plotted a zoom of the periodogram analysis of R-band images of Molniya1-88, near the two main peak at $P = 3.583$ and $P = 10.75$, the error on the period is determined by the width of the peak curve.	37
3.6	Filter R periodogram analysis of Molniya 1-88, November obser- vations.	38
3.7	Filter V periodogram analysis of Molniya 1-88, November obser- vations.	38
3.8	Filter I periodogram analysis of Molniya 1-88, November obser- vations.	39
3.9	Filter B periodogram analysis of Molniya 1-88, November obser- vations.	39
3.10	Filter R periodogram analysis of Molniya 1-88, September obser- vations.	40
3.11	Zoom of filter R periodogram analysis of Molniya 1-88, September observations, in the regions of the two main peak at $P = 3.565$ s and $P = 7.13$ s.	40
3.12	Filter R periodogram analysis of Molniya 1-63, December obser- vations.	42
3.13	Filter V periodogram analysis of Molniya 1-63, December obser- vations.	42
3.14	Filter I periodogram analysis of Molniya 1-63, December obser- vations.	43
3.15	Filter B periodogram analysis of Molniya 1-63, December obser- vations.	43

3.16	Zoom of periodogram analysis of Molniya 1-63 in filter R (top left), V (bottom left), I (top right) and B (bottom right).	44
3.17	Fit of the LC of Molniya 1-63 with $P = 4.079$ s and $P = 2.0395$ s.	44
3.18	Filter R periodogram analysis of Molniya 3-3.	46
3.19	Filter V periodogram analysis of Molniya 3-3.	47
3.20	Filter I periodogram analysis of Molniya 3-3.	47
3.21	Filter B periodogram analysis of Molniya 3-3.	48
3.22	Zoom of periodogram analysis of Molniya 3-3 in filter R (top left), V (bottom left), I (top right) and B (bottom right).	48
3.23	Filter R periodogram analysis of Meridian 1.	50
3.24	Filter V periodogram analysis of Meridian 1.	50
3.25	Filter I periodogram analysis of Meridian 1.	51
3.26	Filter B periodogram analysis of Meridian 1.	51
3.27	Zoom of periodogram analysis in filter R (top left), I (top right), V (bottom left), B (bottom right).	52
3.28	Filter R periodogram analysis check made using onl the first tree R filter exposures	52
3.29	Filter R periodogram analysis of Molniya 2-10.	54
3.30	Filter V periodogram analysis of Molniya 2-10.	54
3.31	Filter I periodogram analysis of Molniya 2-10.	55
3.32	Filter B periodogram analysis of Molniya 2-10.	55
3.33	Filter R periodogram analysis of Molniya 3-42.	57
3.34	Filter V periodogram analysis of Molniya 3-42.	57
3.35	Filter I periodogram analysis of Molniya 3-42.	58
3.36	Filter B periodogram analysis of Molniya 3-42.	58
3.37	Zoom of periodogram analysis in filter R (top left), I (top right), V (bottom left), B (bottom right).	59
3.38	Filter R periodogram analysis of Molniya 1-53.	60
3.39	Filter V periodogram analysis of Molniya 1-53.	61
3.40	Filter I periodogram analysis of Molniya 1-53.	61
3.41	Filter B periodogram analysis of Molniya 1-53.	62
3.42	Zoom of periodogram analysis of Molniya 1-53 in filter R (top left), V (bottom left), I (top right) and B (bottom right), night 02-03.	62
3.43	Molniya 1-53 filter R LC fit with $P = 13$ s and $P = 13.4$ s.	63
3.44	Filter R periodogram analysis of Molniya 1-69.	64
3.45	Filter V periodogram analysis of Molniya 1-69.	65
3.46	Filter I periodogram analysis of Molniya 1-69.	65
3.47	Filter B periodogram analysis of Molniya 1-69.	66
3.48	Filter R (left) and V (right) periodogram analysis of Molniya 1-69.	66
3.49	Filter I (left) and B (right) periodogram analysis of Molniya 1-69.	67
3.50	Filter R (left) and B (right) periodogram analysis of Molniya 3-8.	68
3.51	Filter R periodogram analysis of Molniya 2-9.	69
3.52	Filter V periodogram analysis of Molniya 2-9.	70
3.53	Filter I periodogram analysis of Molniya 2-9.	70
3.54	Filter B periodogram analysis of Molniya 2-9.	71
3.55	Filter R periodogram analysis of Molniya 1-S, night 01-02.	73
3.56	Filter V periodogram analysis of Molniya 1-S, night 01-02.	74
3.57	Filter I periodogram analysis of Molniya 1-S, night 01-02.	74
3.58	Filter B periodogram analysis of Molniya 1-S, night 01-02.	75

3.59	Filter R periodogram analysis of Molniya 1-S, night 02-03.	75
3.60	Filter V periodogram analysis of Molniya 1-S, night 02-03.	76
3.61	Filter I periodogram analysis of Molniya 1-S, night 02-03.	76
3.62	Filter B periodogram analysis of Molniya 1-S, night 02-03.	77
3.63	Zoom of periodogram analysis of Molniya 1-S in filter R (top left), V (bottom left), I (top right) and B (bottom right), night 01-02.	77
3.64	Zoom of periodogram analysis of Molniya 1-S in filter R (top left), V (bottom left), I (top right) and B (bottom right), night 02-03.	78
3.65	Filter R periodogram analysis of Molniya 3-27.	79
3.66	Filter V periodogram analysis of Molniya 3-27.	79
3.67	Filter I periodogram analysis of Molniya 3-27.	80
3.68	Filter B periodogram analysis of Molniya 3-27.	80
3.69	Filter R (left) and V (right) periodogram analysis of Molniya 2-17, night 27-28.	82
3.70	Filter I (left) and B (right) periodogram analysis of Molniya 2-17, night 27-28.	82
3.71	Fit of filter R light curve with $P = 54.55$ s.	83
3.72	Filter R (left) and V (right) periodogram analysis of Molniya 2-17, night 26-27.	83
3.73	Filter I (left) and B (right) periodogram analysis of Molniya 2-17, night 26-27.	84
3.74	Filter R combined analysis of Molniya 2-17	84
3.75	Zoom of filter R combined analysis of Molniya 2-17	84
3.76	Filter R combined analysis of Molniya 2-17	85
3.77	Magnitude vs time of Molniya 1-87 in filter R (top left), V (bot- tom left), I (top right) and B (bottom right), December 22 ob- servations.	86
3.78	Filter R periodogram analysis of Molniya 2-13.	87
3.79	Filter I periodogram analysis of Molniya 2-13.	88
3.80	Filter R periodogram analysis of Molniya 1-62.	89
3.81	Filter V periodogram analysis of Molniya 1-62.	90
3.82	Filter I periodogram analysis of Molniya 1-62.	90
3.83	Filter B periodogram analysis of Molniya 1-62.	91
3.84	Filter R (top left), V (bottom left), I (top right), B (bottom right) fit of Molniya 1-62 light curves with period $P = 78.14$ s.	91
3.85	Fit of Molniya 1-62 filter R light curves with period $P = 78.14$ s.	92
3.86	Fit of Molniya 1-62 filter V light curves with period $P = 78.14$ s.	92
3.87	Fit of Molniya 1-62 filter I light curves with period $P = 78.14$ s.	93
3.88	Fit of Molniya 1-62 filter B light curves with period $P = 78.14$ s.	93
3.89	Molniya 1-32 magnitude vs time in I, night 2016/08/02-03. There's evidence of a long rotational period.	94
3.90	Molniya 1-32 magnitude vs time in filter R (top left), V (bottom left), I (top right) and B (bottom right), night 2016/09/26-27. There's a evidence of a long rotational period.	95
3.91	Molniya 3-40 magnitude vs time in filter R (top left), V (bottom left), I (top right) and B (bottom right), night 2016/09/26-27. There's a clear presence of a long rotational period.	96
3.92	Molniya 3-50 magnitude vs time in filter R (top left), V (bottom left), I (top right) and B (bottom right), night 2016/09/26-27. There's a clear presence of a long rotational period.	97

3.93	Molniya 3-51 periodogram analysis in filter R (left) and V (right)	100
3.94	Molniya 3-51 periodogram analysis in filter I (left) and B (right)	100
3.95	Filter R periodogram analysis of Molniya 1-90.	103
3.96	Filter V periodogram analysis of Molniya 1-90.	103
3.97	Filter I periodogram analysis of Molniya 1-90.	104
3.98	Filter B periodogram analysis of Molniya 1-90.	104
3.99	Filter R fit of Molniya 1-90 light curves with period $P = 95.5$ s 96.1 s.	105
3.100	Filter R (top left), V (bottom left), I (top right) and B (bottom right) magnitude vs time plot for Molniya 1-90.	106
3.101	Molniya 1-86 magnitude vs time in filter R (top left), V (bottom left), I (top right) and B (bottom right), night 2016/09/26-27. There's a clear presence of a long rotational period.	107
3.102	Meridian 2 magnitude vs time in filter R (top left), V (bottom left), I (top right) and B (bottom right).	109
3.103	Meridian 4 magnitude vs time in filter R (top left), V (bottom left), I (top right) and B (bottom right).	109
3.104	Molniya 1-44 (top) and Molniya 1-86 (bottom) periodogram anal- ysis of Figer images, the magnitude in the y axis of the top left plot is not a true magnitude is calculated as the logarithm of the counts multiplied by the number of pixels on which the light curve was mediated.	111
4.1	Phase angle vs Magnitude plots for observed satellite of Molniya costellation. The magnitude is the integrated magnitude of each light curve, a magnitude calibration and distance correction have been applied. The colors are referred to the filters, blue for filter B, red R, green V and magenta I.	114
4.2	Linear regression for Phase angle - magnitude plot.	116
4.3	Linear regression for Phase angle - magnitude plot after the cut- ting process, every filter has the point that hasn't been eliminated by the cutting process colored by the filters colour and other two colors that represent the points rejected respectively in the first and in the second implementation of the cutting process.	116
4.4	Modeling for Phase angle - magnitude relation in Filter R.	119
4.5	Modeling for Phase angle - magnitude relation in Filter V.	120
4.6	Modeling for Phase angle - magnitude relation in Filter I.	120
4.7	Modeling for Phase angle - magnitude relation in Filter B.	121
4.8	Models for Phase angle - magnitude plot after the cutting process in filter R, every point that hasn't been eliminated by the cutting process is colored in red, in green and blue are plotted the points rejected respectively in the first and in the second implementation of the cutting process.	122
4.9	Models for Phase angle - magnitude plot after the cutting process in filter V, every point that hasn't been eliminated by the cutting process is colored in green, in blue and red are plotted the points rejected respectively in the first and in the second implementation of the cutting process.	123

4.10	Models for Phase angle - magnitude plot after the cutting process in filter I, every point that hasn't been eliminated by the cutting process is colored in magenta, in green and red are plotted the points rejected respectively in the first and in the second implementation of the cutting process.	123
4.11	Models for Phase angle - magnitude plot after the cutting process in filter B, every point that hasn't been eliminated by the cutting process is colored in blue, in green and red are plotted the points rejected respectively in the first and in the second implementation of the cutting process.	124
4.12	Color-color diagrams for Molniya and Meridian satellite constellation. The different colors are referred to the launch year, blue for satellites that has been launched between 1970 and 1980, magenta between 1980 and 1990, green between 1990 and 2000 and red for satellites that has been launched after 2000.	125
4.13	Color vs launch year.	126
4.14	Color vs phase angle.	127
4.15	B-R versus R-I diagram for Molniya and Meridian satellites and laboratory data.	129
4.16	Example of approved spectrum	131
4.17	Example of rejected for I photometry spectrum	131
4.18	Exaple of rejected spectrum	132
4.19	Laboratory measurements treated as telescopic observations, and normalized in the wavelength region 7500 to 8000 Angstroms, taken from Seitzer et al. (2012).	133
4.20	Meridian spectra after division by solar spectrum and normalized at 7000 Å. In parenthesis there's the launch year.	134
4.21	Molniya approved spectra after division by solar spectrum and normalized at 7000 Å. In parenthesis there's the launch year.	134
4.22	Molniya I photometry rejected spectra after division by solar spectrum and normalized at 7000 Å. In parenthesis there's the launch year.	135
4.23	Exponential model of the time vs period relation for Molniya 1-49	137
4.24	Exponential model of the time vs period relation for Molniya 2-09	138
4.25	Exponential model of the time vs period relation for Molniya 3-42	138
4.26	Exponential model of the time vs period relation for Molniya 1-88	139
4.27	Exponential model of the time vs period relation for Molniya 3-08	139
4.28	P vs dP/dt diagram for the period slowdown model.	140
4.29	Final plot of the period slowdown model for Molniya debris.	141
4.30	Final logarithmic plot of the period slowdown model for Molniya debris.	142
4.31	Velocity of changing of parameter r_π of the "Molniya" type orbit depending on Ω and ω_0 , image from Kolyuka et al. (2009)	145
4.32	Orbital parameter evolution for Molniya 1-44	147
4.33	Orbital parameter evolution for Molniya 1-93	148
4.34	Orbital parameter evolution for Molniya 3-51	149
A.1	Photometric zero points 2016/08/01-02, magnitudes from Landolt (1992)	158
A.2	Molniya 1-S filter V light curves	159

A.3	Molniya 1-S filter V light curves	159
A.4	Molniya 1-S filter V light curves	159
A.5	Molniya 1-S filter V light curves	160
A.6	Molniya 1-S filter R light curves	160
A.7	Molniya 1-S filter R light curves	160
A.8	Molniya 1-S filter R light curves	161
A.9	Molniya 1-S filter R light curves	161
A.10	Molniya 1-S filter R light curves	161
A.11	Molniya 1-S filter I light curves	162
A.12	Molniya 1-S filter I light curves	162
A.13	Molniya 1-S filter I light curves	162
A.14	Molniya 1-S filter I light curves	163
A.15	Molniya 1-S filter B light curves	163
A.16	Molniya 1-S filter B light curves	163
A.17	Molniya 1-S filter B light curves	164
A.18	Molniya 1-S filter B light curves	164
A.19	Molniya 1-80 filter V light curves	164
A.20	Molniya 1-80 filter V light curves	165
A.21	Molniya 1-80 filter V light curves	165
A.22	Molniya 1-80 filter R light curves	165
A.23	Molniya 1-80 filter R light curves	166
A.24	Molniya 1-80 filter R light curves	166
A.25	Molniya 1-80 filter I light curves	166
A.26	Molniya 1-80 filter I light curves	167
A.27	Molniya 1-80 filter I light curves	167
A.28	Molniya 1-80 filter B light curves	167
A.29	Molniya 1-80 filter B light curves	168
A.30	Molniya 3-51 filter V light curves	168
A.31	Molniya 3-51 filter V light curves	168
A.32	Molniya 3-51 filter R light curves	169
A.33	Molniya 3-51 filter R light curves	169
A.34	Molniya 3-51 filter I light curves	169
A.35	Molniya 3-51 filter I light curves	170
A.36	Molniya 3-51 filter B light curves	170
A.37	Molniya 3-51 filter B light curves	170
A.38	Molniya 3-51 Spectra	171
A.39	Molniya 1-S Spectra	172
A.40	Molniya 1-80 Spectra	172
A.41	Molniya 1-32 Spectra	173
A.42	Photometric zero points 2016/08/02-03, magnitudes from Landolt (1992)	175
A.43	Molniya 1-S filter V light curves	176
A.44	Molniya 1-S filter V light curves	176
A.45	Molniya 1-S filter V light curves	176
A.46	Molniya 1-S filter R light curves	177
A.47	Molniya 1-S filter R light curves	177
A.48	Molniya 1-S filter R light curves	177
A.49	Molniya 1-S filter R light curves	178
A.50	Molniya 1-S filter I light curves	178
A.51	Molniya 1-S filter I light curves	178

A.52 Molniya 1-S filter B light curves	179
A.53 Molniya 1-S filter B light curves	179
A.54 Molniya 1-32 filter V light curves	179
A.55 Molniya 1-32 filter I light curves	180
A.56 Molniya 1-75 Spectra	180
A.57 Molniya 2-17 Spectra	181
A.58 Photometric zero points 2016/09/26-27, magnitudes from Landolt (1992)	184
A.59 Molniya 1-32 filter R light curves	185
A.60 Molniya 1-32 filter R light curves	185
A.61 Molniya 1-32 filter I light curves	185
A.62 Molniya 1-32 filter V light curves	186
A.63 Molniya 1-32 filter B light curves	186
A.64 Molniya 1-32 filter B light curves	186
A.65 Molniya 3-40 filter R light curves	187
A.66 Molniya 3-40 filter I light curves	187
A.67 Molniya 3-40 filter V light curves	187
A.68 Molniya 3-40 filter B light curves	188
A.69 Molniya 3-50 filter R light curves	188
A.70 Molniya 3-50 filter I light curves	188
A.71 Molniya 3-50 filter V light curves	189
A.72 Molniya 3-50 filter V light curves	189
A.73 Molniya 3-50 filter B light curves	189
A.74 Molniya 2-17 filter R light curves	190
A.75 Molniya 2-17 filter I light curves	190
A.76 Molniya 2-17 filter V light curves	190
A.77 Molniya 2-17 filter B light curves	191
A.78 Molniya 1-62 filter R light curves	191
A.79 Molniya 1-62 filter R light curves	191
A.80 Molniya 1-62 filter I light curves	192
A.81 Molniya 1-62 filter V light curves	192
A.82 Molniya 1-62 filter B light curves	192
A.83 Molniya 1-32 Spectra	193
A.84 Molniya 1-62 Spectra	194
A.85 Molniya 3-40 Spectra	195
A.86 Photometric zero points 2016/09/27-28, magnitudes from Landolt (1992)	198
A.87 Molniya 1-56 light curves	199
A.88 Molniya 2-17 light curves	199
A.89 Molniya 2-17 light curves	200
A.90 Molniya 2-9 light curves	200
A.91 Molniya 3-50 light curves	201
A.92 Molniya 3-50 light curves	201
A.93 Molniya 1-87 light curves	202
A.94 Molniya 1-87 light curves	202
A.95 Molniya 3-27 light curves	203
A.96 Molniya 3-27 light curves	203
A.97 Molniya 3-24 light curves	204
A.98 Molniya 1-88 light curves	204
A.99 Molniya 1-56 Spectra	205

A.100	Molniya 2-17 Spectra	206
A.101	Molniya 2-9 Spectra	207
A.102	Molniya 3-50 Spectra	208
A.103	Molniya 1-80 Spectra	209
A.104	Molniya 3-27 Spectra	210
A.105	Photometric zero points 2016/11/26-27, magnitudes from Landolt (1992)	214
A.106	Molniya 1-90 filter R light curves	215
A.107	Molniya 1-90 filter I light curves	215
A.108	Molniya 1-90 filter V light curves	216
A.109	Molniya 1-90 filter B light curves	216
A.110	Molniya 1-88 filter R light curves	216
A.111	Molniya 1-88 filter R light curves	217
A.112	Molniya 1-88 filter I light curves	217
A.113	Molniya 1-88 filter V light curves	217
A.114	Molniya 1-88 filter B light curves	218
A.115	Molniya 2-13 light curves	218
A.116	Molniya 2-13 filter R light curves	219
A.117	Molniya 1-86 filter R light curves	219
A.118	Molniya 1-86 filter I light curves	219
A.119	Molniya 1-86 filter V light curves	220
A.120	Molniya 1-86 filter B light curves	220
A.121	Molniya 2-10 filter R light curves	220
A.122	Molniya 2-10 filter R light curves	221
A.123	Molniya 2-10 filter I light curves	221
A.124	Molniya 2-10 filter V light curves	221
A.125	Molniya 2-10 filter B light curves	222
A.126	Meridian 1 filter R light curves	222
A.127	Meridian 1 filter R light curves	223
A.128	Meridian 1 filter I light curves	223
A.129	Meridian 1 filter V light curves	224
A.130	Meridian 1 filter B light curves	224
A.131	Molniya 3-42 filter R light curves	225
A.132	Molniya 3-42 filter R light curves	225
A.133	Molniya 3-42 filter R light curves	225
A.134	Molniya 3-42 filter I light curves	226
A.135	Molniya 3-42 filter I light curves	226
A.136	Molniya 3-42 filter V light curves	226
A.137	Molniya 3-42 filter V light curves	227
A.138	Molniya 3-42 filter B light curves	227
A.139	Molniya 3-42 filter B light curves	227
A.140	Molniya 1-69 filter R light curves	228
A.141	Molniya 1-69 filter I light curves	228
A.142	Molniya 1-69 filter V light curves	228
A.143	Molniya 1-69 filter B light curves	229
A.144	Molniya 2-13 Spectra	230
A.145	Meridian 1 Spectra	231
A.146	Molniya 3-42 Spectra	232
A.147	Molniya 1-69 Spectra	233
A.148	Molniya 2-10 Spectra	234

A.14	Photometric zero points 2016/12/22-23-24, magnitudes from Landolt (1992)	238
A.150	Molniya 1-87 filter R light curves	239
A.151	Molniya 1-87 filter R light curves	239
A.152	Molniya 1-87 filter I light curves	240
A.153	Molniya 1-87 filter V light curves	240
A.154	Molniya 1-87 filter B light curves	240
A.155	Molniya 3-13 light curves	241
A.156	Molniya 1-88 filter B light curves	241
A.157	Molniya 1-88 filter I light curves	241
A.158	Molniya 1-88 filter R light curves	242
A.159	Molniya 1-88 filter V light curves	242
A.160	Meridian 2 filter R light curves	243
A.161	Meridian 2 filter R light curves	243
A.162	Meridian 2 filter I light curves	243
A.163	Meridian 2 filter V light curves	244
A.164	Meridian 2 filter B light curves	244
A.165	Molniya 3-3 filter R light curves	244
A.166	Molniya 3-3 filter R light curves	245
A.167	Molniya 3-3 filter R light curves	245
A.168	Molniya 3-3 filter I light curves	245
A.169	Molniya 3-3 filter V light curves	246
A.170	Molniya 3-3 filter B light curves	246
A.171	Molniya 1-53 filter R light curves	246
A.172	Molniya 1-53 filter R light curves	247
A.173	Molniya 1-53 filter I light curves	247
A.174	Molniya 1-53 filter V light curves	247
A.175	Molniya 1-53 filter B light curves	248
A.176	Meridian 4 filter R light curves	248
A.177	Meridian 4 filter I light curves	248
A.178	Meridian 4 filter V light curves	249
A.179	Meridian 4 filter B light curves	249
A.180	Molniya 1-87 Spectra	249
A.181	Molniya 1-87 Spectra	250
A.182	Molniya 3-13 Spectra	251
A.183	Molniya 1-88 Spectra	252
A.184	Meridian 2 Spectra	253
A.185	Molniya 1-53 Spectra	254
A.186	Molniya 3-3 Spectra	255
A.187	Molniya 3-3 Spectra	256
A.188	Meridian 4 Spectra	256
A.189	Meridian 4 Spectra	257
A.190	Molniya 1-63 filter R light curves	259
A.191	Molniya 1-63 light curves	259
A.192	Molniya 1-90 filter R light curves	260
A.193	Molniya 1-90 filter R light curves	260
A.194	Molniya 1-90 filter I light curves	261
A.195	Molniya 1-90 filter V light curves	261
A.196	Molniya 1-90 filter B light curves	261
A.197	Molniya 3-8 light curves	262

A.198Molniya 1-71 Spectra	262
A.199Molniya 1-90 Spectra	263
A.200Molniya 1-63 Spectra	263
A.201Molniya 1-63 Spectra	264

List of Tables

2.1	Example of the tabulated values for standard stars magnitudes and color indexes from Landolt (1992)	17
3.1	Molniya 1-88 data	35
3.2	Molniya 1-63 data	41
3.3	Molniya 1-63 periods found with periodogram analysis	41
3.4	Molniya 3-3 data	45
3.5	Molniya 3-3 periods found with periodogram analysis	45
3.6	Meridian 1 data	49
3.7	Meridian 1 periods found with periodogram analysis	50
3.8	Molniya 2-10 periods found with periodogram analysis	53
3.9	Molniya 2-10 data	53
3.10	Molniya 3-42 periods found with periodogram analysis	56
3.11	Molniya 3-42 data	56
3.12	Molniya 1-53 data	59
3.13	Molniya 1-53 periods found with periodogram analysis	60
3.14	Molniya 1-69 data	63
3.15	Molniya 3-8 data	67
3.16	Molniya 2-9 data	69
3.17	Molniya 1-S periods found with periodogram analysis	71
3.18	Molniya 1-S data	72
3.19	Molniya 1-S data	73
3.20	Molniya 3-27 periods found with periodogram analysis	78
3.21	Molniya 3-27 data	79
3.22	Molniya 2-17 data	81
3.23	Molniya 1-87 data	86
3.24	Molniya 2-13 data	87
3.25	Molniya 1-62 data	89
3.26	Molniya 1-32 data	94
3.27	Molniya 3-40 data	95
3.28	Molniya 3-50 data	97
3.29	Molniya 3-13 data	98
3.30	Molniya 1-56 data	98
3.31	Molniya 3-13 data	98
3.32	Molniya 3-51 data	99
3.33	Molniya 1-90 periods found with periodogram analysis	101
3.34	Molniya 1-90 data	102
3.35	Molniya 1-80 data	106
3.36	Molniya 1-86 data	107

3.37	Meridian 2 data	108
3.38	Meridian 4 data	108
3.39	Orbital characteristics of Molniya 1-44 and Molniya 1-86 orbits	110
4.1	Phase functions employed for the physical models to describe the phase angle - magnitude relation.	118
4.2	Least square <i>Aeff</i> , albedo and RMS values	118
4.3	Least square <i>Aeff</i> , albedo and RMS values for every model and filter after the cutting process.	122
4.4	Molniya and Meridian spectra photometry check	130
4.5	Molniya tumbling periods	136
4.6	Molniya characteristic time of decay	140
A.1	Logbook 2016/08/01-02	155
A.2	Logbook 2016/08/01-02	156
A.3	Logbook 2016/08/01-02	157
A.4	Standard stars magnitudes and color indexes from Landolt (1992)	158
A.5	Logbook 2016/08/02-03	174
A.6	Standard stars magnitudes and color indexes from Landolt (1992)	175
A.7	Logbook 2016/09/26-27	182
A.8	Logbook 2016/09/26-27	183
A.9	Standard stars magnitudes and color indexes from Landolt (1992)	184
A.10	Logbook 2016/09/27-28	196
A.11	Logbook 2016/09/27-28	197
A.12	Standard stars magnitudes and color indexes from Landolt (1992)	198
A.13	Logbook 2016/11/26-27	211
A.14	Logbook 2016/11/26-27	212
A.15	Logbook 2016/11/26-27	213
A.16	Standard stars magnitudes and color indexes from Landolt (1992)	214
A.17	Logbook 2016/12/22-23	235
A.18	Logbook 2016/12/22-23	236
A.19	Logbook 2016/12/22-23	237
A.20	Standard stars magnitudes and color indexes from Landolt (1992)	238
A.21	Logbook 2016/12/23-24	258

Chapter 1

Introduction

1.1 Satellite general characteristics and history

A satellite is an artificial object which has been intentionally placed into orbit. The story of human space exploration begins in 1957 with the launch by the Soviet Union of Sputnik 1. Since then, about 6600 satellites from more than 40 countries have been launched. Satellites are used for many purposes. Common types include military and civilian Earth observation satellites, communications satellites, navigation satellites, weather satellites, and space telescopes. Space stations and human spacecraft in orbit are also satellites. Every satellite has been launched using a launch vehicle or rocket that throws the satellite into orbit. Rockets often do not fall into the atmosphere after launch but remain in orbit, helping to populate the sky. Satellite orbits are generally at altitudes in the range of 180 to several thousand kilometres. Their altitude, shape, and orientation of orbital trajectories are strongly dependent on the mission they are to perform. The orbits in their most general form may be circular or elliptical. The laws ruling the operation of orbits have gone down in history as the three laws of Kepler applicable for both satellites and planets:

- The orbit of a planet (satellite) is an ellipse with the Sun (Earth) at one of the two foci.
- A line segment joining a planet (satellite) and the Sun (Earth) sweeps out equal areas during equal intervals of time.
- The square of the orbital period of a planet (satellite) is proportional to the cube of the semi-major axis of its orbit.

In order to completely define the location of a satellite in its excursion around the Earth it is necessary to define six Keplerian orbital elements, as follows:

- Ω = longitude of the ascending node, is the angle measured in plane of equator between the direction of the vernal equinox and the direction of ascending node, which is the intersection of the orbit with the equator.
- i = inclination of the plane, angle between plane of equator and plane of orbit measured at the ascending node ($0^\circ \leq i \leq 180^\circ$). The inclination

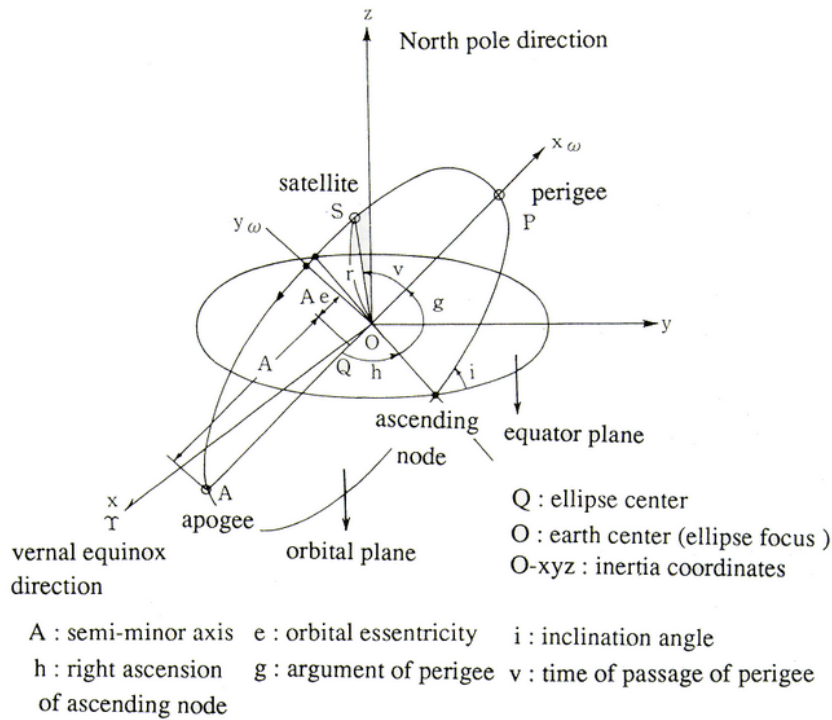


Figure 1.1: Orbital elements of Kepler

also indicates the direction of the satellite around the Earth, eastword if $0^\circ \leq i \leq 90^\circ$, westword if $90^\circ \leq i \leq 180^\circ$.

- ω_0 = argument of the perigee, angle from the ascending node to the perigee in the orbital plane ($0^\circ \leq \omega_0 \leq 360^\circ$).
- e = eccentricity, determines the shape of the orbit, defined as $e = c/a$ where c is the distance from the foci and a is the semi-major axis, if $e = 0$ the orbit is circular if $e = 1$ the orbit is a parabola, if $0 < e < 1$ is an ellipse.
- a = semi-major axis
- ν = true anomaly, aple measured at the focus between the perigee direction and the satellite position, for example $\nu = 180^\circ$ with the satellite at the apogee.

The first three elements are frequently defined as orbit orientation elements while the latter three are referred as orbit dimensional elements. All the orbit orientation elements are represented in Figure 1.2. The generalized form of the conic section orbit is given in polar form with focus at the origin by:

$$r = \frac{p}{1 + e \cos \nu} \quad (1.1)$$

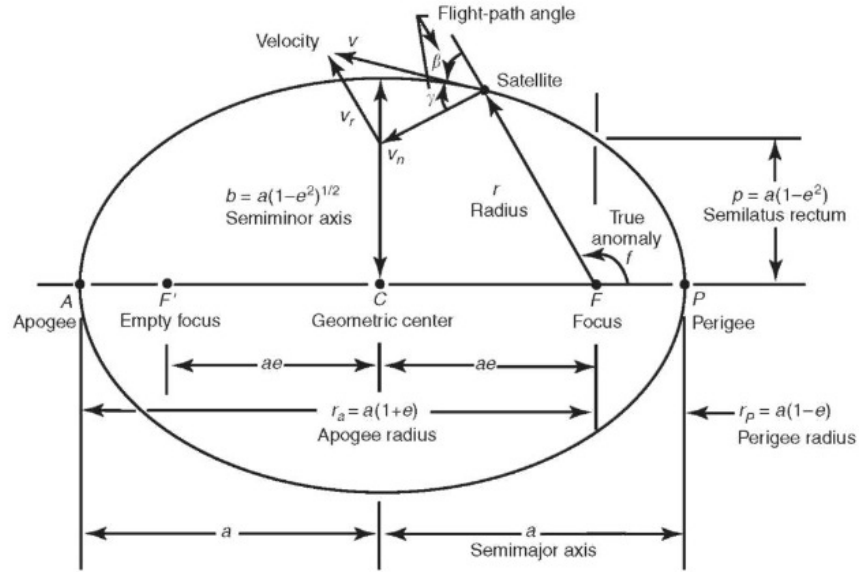


Figure 1.2: Generalized elliptical orbit

where P is the semi latus rectum of the conic, expressible as $P = a(1 - e^2)$. The orbit shape depends on P and e . Additional relations for an ellipse include: $r_p = a(1 - e)$ perigee radius, $r_a = a(1 + e)$ apogee radius, $B = a(1 - e^2)^{1/2}$ semi-minor axis and $e = (1 - (\frac{b}{a})^2)^{1/2}$ eccentricity.

1.1.1 Orbital categories

The most common classification of satellite orbits is divided i 4 categories:

- Low Earth orbit (LEO): Geocentric orbits ranging in altitude from 180 km - 2000 km
- Medium Earth orbit (MEO): Geocentric orbits ranging in altitude from 2000 km - 35786 km. Also known as an intermediate circular orbit.
- Geosynchronous Orbit (GEO): Geocentric circular orbit with an altitude of 35786 kilometres. The period of the orbit equals one sidereal day, coinciding with the rotation period of Earth. The speed is approximately 3000 metres per second. This category includes the geostationary satellites.
- High Earth orbit (HEO): Geocentric orbits above the altitude of geosynchronous orbit 35786 km.

Of the many existing types of orbits and their many possible catalogs, we will focus on two important orbits for this work. The geostationary orbit and the Molniya orbit. Of all satellites observed for this work, only one is geostationary, but geostationary orbit is important to better understand the Molniya orbit.

1.1.2 Geostationary orbit

The geostationary orbit has special properties which makes it highly suitable for communications applications. In fact, it has been demonstrated that a satellite placed in a circular orbit in the plane of the equator and located at an altitude of 35786 km having an orbital period of 24 hours would appear to be stationary when viewed from earth. Such a circular orbit is described by the following equations:

$$v = \left(\frac{GM}{r}\right)^{\frac{1}{2}} \quad \omega = \frac{(GM)^{\frac{1}{2}}}{r^{\frac{3}{2}}} \quad T = \frac{2\pi r^{\frac{3}{2}}}{(GM)^{\frac{1}{2}}} \quad (1.2)$$

Where v is the satellite velocity, ω is the angular velocity and T is the period. It is now easy to calculate that an orbit described by the features shown above is found to have $v = 3$ km/s, $\omega = 73 \cdot 10^{-6}$ rad and $T = 86146$ s or 23.934 hours. Therefore the period of the geostationary satellite isn't 24 hours but 23 hours 56 minutes and 4 seconds, the exact duration of a sidereal day, that is, the time that Earth takes to make a full turn on itself. A satellite with these characteristic will therefore remain in the sky in the same position throughout his life at least in theory. In reality a satellite in geostationary orbit is never really in the ideal orbit described above. There are forces which cause perturbations to this ideal orbit. This forces include solar and lunar gravity, solar pressure, and varying gravitational forces on the equatorial plane because of the triaxiality of earth (Colombo and Gkolias (2017)). The solar/lunar gravity causes a N-S movement, which affects the inclination of the orbit. In one year the inclination (if the effect is not corrected) can increase between 0.75° and 0.95° . The long term cyclic periodicity of the variation is 17 years, and if not corrected can change the inclination up to about 14° in 27 years. A satellite subject to forces which cause the orbit to incline with regard to the equator will no longer be seen from the ground as a fixed point. If the period remains 24 hours the satellite will oscillate above and below the equator. To correct for this orbital perturbation, regular orbital stationkeeping manoeuvres are necessary, amounting to a ΔV of approximately 50 m/s per year. A second effect to be taken into account is the longitude drift, caused by the asymmetry of the Earth. There are two stable (at 75.3° E and 252° E) and two unstable (at 165.3° E and 14.7° W) equilibrium points. Any geostationary object placed between the equilibrium points would (without any action) be slowly accelerated towards

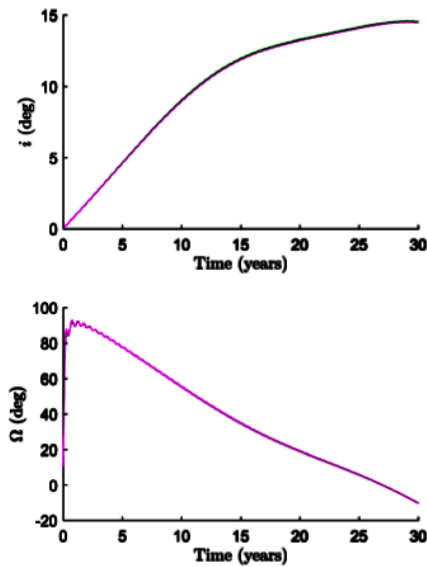


Figure 1.3: The two main perturbation effects on a geostationary orbit from dynamical models, N-S (top) and E-W (bottom). Colombo and Gkolias (2017)

the stable equilibrium position, causing a periodic longitude variation. The correction of this effect requires station-keeping maneuvers with a maximal ΔV of about 2 m/s per year, depending on the desired longitude. Solar wind and radiation pressure also exert small forces on satellites; over time, these cause them to slowly drift away from their prescribed orbits, in particular this perturbation manifests itself as an increase of eccentricity with an attendant increase in E-W longitudinal motion. In the absence of servicing missions from the Earth or a renewable propulsion method, the consumption of thruster propellant for station keeping places a limitation on the lifetime of the satellite. The fuel requirements for N-S station keeping are the more stringent, N-S station keeping consumes a factor ten more than E-W station keeping.

1.2 Molniya orbit

Molniya orbit is of particular interest to this work since the observed satellites belong to this category of objects. In fact this work is based on the observation of the Molniya communications satellites, a constellation of satellites used by the Soviet Union for its military communications launched between 1965 (first launch) and the beginning of the 2000s. Molniya orbit is built to provide the most satisfying coverage on the Russian territory. The orbit is characterized by a very high inclination ($i = 63.4^\circ$) and has the apogee in the northern hemisphere. The orbital period is 12 hours. A typical Molniya orbit is shown in Figure 1.4. From Kepler second law, the satellite spends a considerable amount of time near its apogee. The apogee is at 39500 km altitude while perigee is at 1000 km altitude. The eccentricity is about 0.72. These characteristics guarantee that the satellite spends ten hours out of twelve in the northern part of its orbit, providing thus coverage during these ten hours (F. Kolyuka et al. (2017)). However one only satellite isn't able to provide a satisfying coverage, but three are needed, with the same apogee longitudes, and with the passage to the apogee spaced of eight hours.

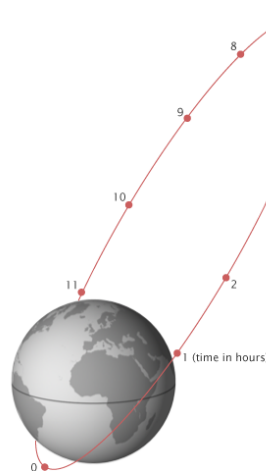


Figure 1.4: Molniya orbit.

Neither the height of the apogee nor the inclination are random, you had surely noted that the height of the apogee is very close to the height of the geostationary satellites, this has been made to maximize the time spent in the higher part of the orbit and to make the satellite appear to remain quasi-stationary in this part of the orbit (see Figure 1.5). The inclination neither is random, in fact the inclination value of 63.4° was chosen to cancel the precession of the argument of perigee due to the oblateness of the Earth. Likewise what happens to geostationary satellites, high inclination satellite are exposed to two orbital perturbations, that are different with respect to those of the geostationary orbits. In particular the oblateness of the Earth perturbs the argument of perigee

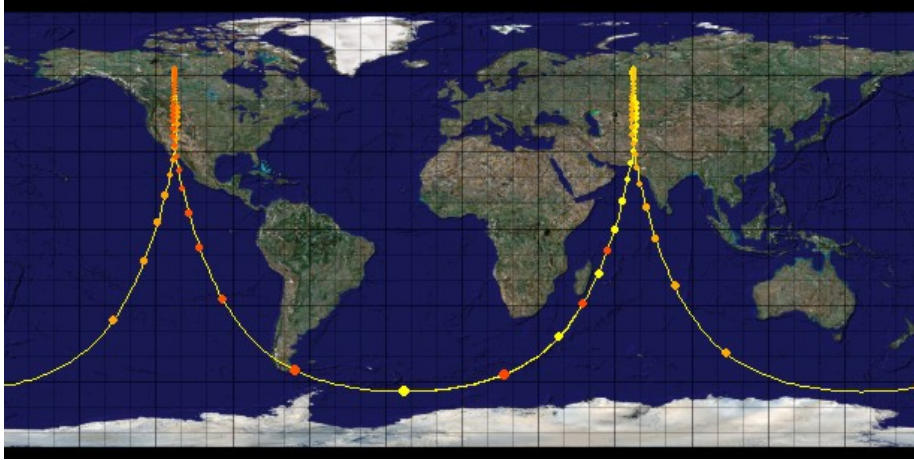


Figure 1.5: Molniya orbit ground track.

(F. Kolyuka et al. (2017)), so that even if the apogee started near the north pole, it would gradually move unless constantly corrected with station-keeping thruster burns. The equation that describes this phenomenon is the following:

$$\frac{d\omega}{dt} = K \left[\left(\frac{5}{2} \right) \cos^2 i - 2 \right] \quad (1.3)$$

it's easy at this point to prove that the term is canceled for $i = 63.4^\circ$. So the Molniya orbit inclination was chosen to avoid this type of perturbation (F. Kolyuka et al. (2017)). This inclination value however does not cancel the other perturbation term on the right ascension of the ascending node ($d\Omega/dt = 3K \sin i$), that must be gradually corrected with time. Of course, other perturbations are present as that for radiation pressure or atmospheric drag. The second in particular does not occur if the satellite maintain the pre-determined orbit, in fact, the perigee of this orbit is fixed at 1000 km outside the atmospheric drag zone, but close enough to make a small orbital shift bring the satellite in contact with this area. Once out of control (i.e. once the fuel is over) it may happen that this kind of satellites come into contact with the drag zone and start falling to the ground. As we will see this phenomenon has already happened for three of the studied satellites.

1.3 Space debris

In the context of artificial satellites we focused on space debris, and in particular on Molniya debris. The term Space debris means the totality of defunct human-made objects in earth orbit, such as old satellites, spent rocket stages, and fragments from disintegration, erosion and collisions. Since the launch of Sputnik in 1957, over 26,000 man-made objects have been catalogued, many of which have since reentered the atmosphere. It is calculated that 17852 (2016, July 5)¹ space debris are currently orbiting around the Earth and only 1,419 of these are still operational. This with regard to the debris trackable from the ground. There are however a myriad of orbiting objects that are too small to be

¹<https://orbitaldebris.jsc.nasa.gov/quarterly-news/pdfs/odqnv20i3.pdf>

tracked. According to models there are at least 29000 debris of sizes larger than 10 cm, 670000 larger than 1 cm and more than 170 million larger than 1 mm.² The presence in orbit of an increasing number of debris is creating an increasingly challenging collision problem. Each collision creates a very high number of small and medium sized debris increasing the likelihood of other collisions and creating a chain reaction. This problem is known as Kessler syndrome and was proposed for the first time by Donald J. Kessel in 1978. The Kessler syndrome is a scenario where the density of objects especially in low earth orbit (LEO) became high enough that collisions between objects become probable. The collisions starts increasing the probability of other collisions, and a cascade process triggers (Kessler (1991)). The consequences of this process may be very unpleasant making the LEO orbital area unavailable for several years, perhaps even centuries. The uselessness of satellites due to the impossibility of keeping them in orbit because of the high probability of collisions could paralyze our communicative systems forcing us to give up many of the technological innovations that characterized the 21st century and the last century. It is already clear that the presence of many wandering objects in orbit is a danger to operative satellites and especially for space stations where people live and a collision could endanger the lives of occupants. As of December 2016, five satellite collisions have resulted in generating space waste, clear signal that the chain process is slowly beginning.

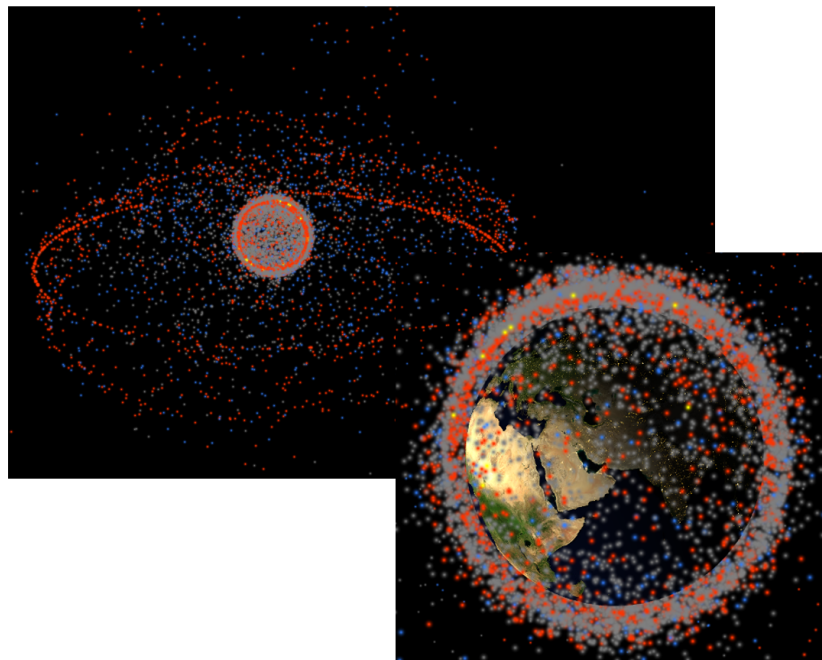


Figure 1.6: Representation of the position of all satellites orbiting around the earth

²http://www.esa.int/Our_Activities/Space_Engineering_Technology/Clean_Space/How_many_space_debris_objects_are_currently_in_orbit

1.4 Molniya and Meridian satellite

Molniya satellites are Russian payloads for military communications service. The satellite (a representation of which is visible in the Figure 1.7) consists of a hermetically sealed, pressurized main section with 2.5 cubic meters internal volume. This keeps the electronic components at a stable temperature during the day-night cycle. The spacecraft is provided with an orientation system that points the solar panels at the sun and the antenna at the earth during communications session, a gyroscopic stabilizer is present to improve pointing accuracy. An optical sensor is used for antenna pointing. The Alfa on-board retransmitter operated on the 10 m band in both simplex and duplex modes. Main propulsion was provided with AK-20 nitric acid and UDMH propellants. Total impulse delivered by the three-chamber motor is 8,000 kg-sec, with a specific impulse of 290 seconds. The spacecraft had a span of 8 m across its solar panels and an initial mass on-orbit of 1650 kg. The first two launches, on 2 January and 6 June 1964, were unsuccessful. The first successful launch only came on 14 October 1965. The main characteristics are the following:

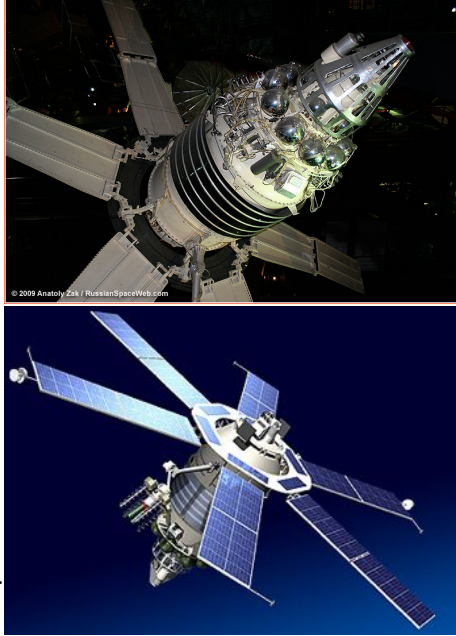


Figure 1.7: Molniya spacecraft.

- Length: 4.40 m.
- Maximum Diameter: 1.40 m.
- Span: 8.20 m (solar panels).
- Initial mass: 1,650 kg.
- RCS Impulse: 78 kgf-sec.
- Main Engine: KDU-414.
- Main Engine Thrust: 1.960 kN.
- Main Engine Propellants: Nitric Acid/UDMH.
- Main Engine Isp: 290 sec.
- Electrical System: Solar panels.
- Electric System: 1.30 average kW.
- Associated Launch Vehicle: Molniya 8K78, Molniya 8K78M, Proton 8K82K / 11S86.

- Launch site: Plesetsk cosmodrome

Meridian satellite are the technological evolution of Molniya satellite. In other words the Meridian program was create by russian government to replace the Molniya program. Meridian satellite are identical to Molniya for purpose and orbit, the only difference between the two satellite are the shape, the weight and of course the technology on board. Meridian in fact are larger heaviest and equipped with more advanced technology than Molniya. Meridian satellites weigh 2000 kg, an artistic representation of this satellite is shown in Figure 1.8. The first launch was in 2006-12-24, there are currently seven of these satelllites in orbit.

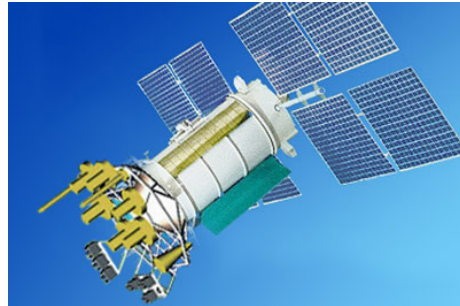


Figure 1.8: Meridian spacecraft.

1.5 Optical tracking and imaging of space debris

Given the growing number of space debris orbiting around Earth and given the growing threat that these debris are becoming for operative satellites and for the exploitation of satellite technology for the most varied purposes (already listed in the previous sections), ground observation of satellites is becoming a very important aspect of space science in recent years. In this context the technique of optical tracking has been born in recent years, alongside the classic use of the radio band for this type of service. At the same time a new photometric characterization technique has being developed with the aim of developing a knowledge of photometric properties that will allow in future the recognition and catalogation of unknown objects like old rockets or various stages left in orbit by old launches. The optical observation of space debris has some advantages with respect to the ground-based radars observation. The main advantages are three: higher resolution (an optical telescope has 10^5 more resolution than a radio telescope with the same diameter), higher efficiency with increasing distance and less operating costs (Veis (1963)). The biggest disadvantage is of course that optical tracking can only be done at night and only if the satellite is illuminated by the Sun.

We can summarize the goals of optical space debris observation as follow:

- maintaining the dynamical data base on space object orbits
- estimation of real population of artificial objects in orbit
- determining of possible origin of the discovered objects
- verification of the space debris distribution and evolution models
- estimation of the level of danger caused by space debris objects for operational spacecrafts at present and in the future
- control of implementation of measures directed on decreasing the space debris population

Our work fits in this context, in particular we have devoted ourselves not only to the spectrophotometric characterization of the constellation of Russian satellites Molniya, but also to the study the free rotational motion of this satellites and the gravitational instabilities to which they are subject. It is known that out-of-control satellites tend to develop a rotational motion. The study of the tumbling motion and the study of gravitational instability, can be relevant to study how long the exploitation of these satellites can be extend after they have finished the fuel. All with a view to maximizing the exploitation of these satellites, in order to put a brake on the overpopulation of the orbits around the Earth. The study of the tumbling motion provides also an additional opportunity to study Earth magnetic field.

For our purposes we used two types of images, photometry and spectroscopy. The first is definitely the most important in fact it allows to characterize the colors of the satellites and therefore the reflection properties of the various materials they are composed of (Cowardin et al. (2010)), properties linked to aging, and magnitude variations due to the observation phase angle (Jin et al. (2011)). The phase angle-magnitude relation can be used also for the recognition of unknown objects since it can provide informations on the shape of the observed object (Hejduk et al. (2012)). Photometry also allow to study the rotational properties of this satellites, thanks to the light curves they draw in the sky (Bennett et al. (2006)), and consequently to investigate the time evolution of the tumbling periods. Light curves can also provide useful informations for the recognition of unknown objects (O. Fulco et al. (2012)). Spectroscopy instead provides a more valuable information, thus allowing us to refine our knowledge of the reflective properties of these objects (Seitzer et al. (2012)). For this reason it also conceals pitfalls, being much more difficult and expensive to obtain, both in terms of exposure time and precision required in the observation. In fact, spectroscopy requires, as we will explain further on, an a posteriori check (provided by photometry) to verify its reliability.

Chapter 2

Data acquisition and reduction

Our work is mainly based on the analysis of 480 photometry images and 54 spectra of Molniya space debris. The images were taken during ten nights with the Cassini 152 cm telescope of the Bologna Astronomical Observatory located in Via Orzale 16, 40050 Loiano Bologna, Italy.

2.1 Instrumentation

2.1.1 Cassini telescope



Figure 2.1: The Loiano telescope site

The 152 cm telescope, inaugurated in September 1976, is dedicated to Gian Domenico Cassini. It is located on Mount Orzale, 500 m from the old 60 cm reflector. The telescope was designed by the French firm REOSC. The telescope G.D. Cassini is a Ritchey-Chretien type instrument with equatorial frame, and it has a very peculiar structure : there is no tube, and the optics are supported by an iron framework. There are counterweights balancing the telescope, in order to minimize the stress which could compromise pointing and tracking accuracy. The optical system is formed by a main mirror with a diameter of 152 cm, with a central hole, and by a secondary mirror with a diameter of about 60 cm. The secondary mirror is located in front of the main mirror and reflects the light through the hole, into the observing instruments. The Ritchey – Chrétien optical system has a wide (70-arcminute) corrected field. The telescope Characteristics are presented below:

- Optical configuration : Ritchey-Chrétien
- Mount Type : English

- Total weight : 9000 Kg
- Main concave mirror : total diameter 152.4 cm, useful diameter 150.0 cm, focal ratio F/3
- Secondary mirror : total diameter 58.0 cm, useful diameter 55.5 cm
- Mirror distance : 308.7 cm
- Cassegrain Focus : equivalent focal length 1200 cm , equivalent focal ratio F/8 , scale 17"/mm , useful corrected field 70'

The telescope is equipped with the BFOSC (Bologna Faint Object Spectrograph & Camera) a device designed to capture both images and spectra with a simple change of configuration.

2.1.2 BFOSC

The main features of this device are:

- Collimator-Camera system that reduces the telescope's focus.
- Presence of a parallel beam area.
- Easily interchangeable slits, gratings and filters.
- High efficiency.

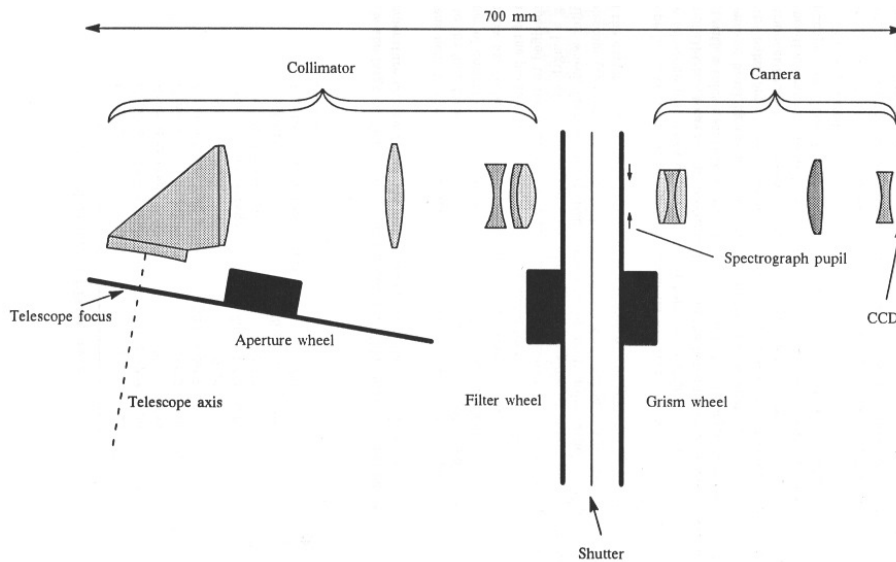


Figure 2.2: Schematic representation of the BFOSC

The instrument consists of a rigid support hosting the collimator, the camera and the detector. Mounted on it are the shutter and three moving wheels that carry slits, filters and grism respectively. The last optical element of the

BFOSC is the camera that is in contact with the cryostat window. The detector used is a CCD EEV LN/1300-EB/1 1300x1340 pixels, coating AR Visar, back illuminated. The detector RON is $3.06 e^-/\text{pix}$ and the gain is $2.22 e^-/\text{ADU}$. The wheels on which slits, filters and grism are mounted have eight positions each. Filters and grism intervene on the parallel beam, namely between collimator and camera, while the slit wheel is placed on the focal plane of the telescope. Among the filters and the grism a wheel is mounted which acts as a shutter for the CCD. The optical axis of the instrument is 110° tilted in respect to the optical axis of the telescope, in order to limit the dimensions of the instrument. A schematic representation of the BFOSC is presented in Figure 2.2.

The main characteristics of the instrument are as follows:

- Focal length of collimator: 252.1 mm
- Linear collimator field: 52.9 x 52.9 mm
- Beam Diameter: 31.5 mm
- Camera focal length: 146.3 mm
- Linear camera field: 30.7 x 30.7 mm
- Reduction ratio: 0.58
- Spectral coverage: 330,1100 nm
- Maximum spectral resolution: 4200
- Projected dimension with the CCD EEV D129915: 0.58 arcsec/pixel
- Field dimension with the CCD EEV D129915: 13' x 12.6'

In order to guarantee a good transmission in the UV (Cut-off at 350 nm) optics have been built using FK54 and UBK7 glasses and have been coated with a single layer of MgF_2 , centered to 500nm, to improve anti-reflection characteristics. Reflection losses have a value of about 1.5 % in the central wavelength that increase to 2.5 % at the extremes. As mentioned above the instrument has three moving wheels, every wheel has 8 available positions, which is reduced to 7 because one of this positions is intentionally left empty to allow direct imaging. BFOSC is equipped with five slits (1.5", 2", 2.5", 5", 12") normally oriented in E-W direction, nine filters (U, B, V, R, I Johnson-Kron-Cousin and G, R, Z, I, Thuan-Gunn) and eleven grisms (#3, #4, #5, #6, #7, #8, #9 Ech, #10 C.D., #11 C.D., #12 C.D., #13). Different grisms spectral range and resolution are shown in Figure 2.3.

The BFOSC shutter has been made using a wheel with two apertures allowing the light to reach the detector, placed in the parallel beam area, that moves turning 90° each time. The speed of the wheel is electronically controlled in such a way to keep the shutter speed rotation constant during the closing or opening phase. Acceleration and deceleration phases are timed to happen out of the CCD field of view. For this reason there aren't illumination effects due to shutter movement. Exposure times have a 0.1 sec resolution. The camera is focused using the Hartmann masks mounted on the filters wheel. Since the camera focus change with temperature, a compensation table has been prepared. The camera focus procedure is known and under control of the technical

personnel. Spectral wavelength calibration is obtained through exposures of an Fe hollow-cathod lamp filled with He-AR.

Grism #	L blaze (nm)	L grism (nm)	Dispersion (nm/mm)	D L (nm)	LL EEV (nm)	LL Thom. (nm)	L/pix EEV (nm/pix)
3	390	430	17	0.55	330 ÷ 642	330 ÷ 580	0.27
4	480	580	22	0.83	380 ÷ 470	394 ÷ 786*	0.40*
5	650	700	22	0.75	480 ÷ 980	520 ÷ 905	0.40
6	390	400	11	0.39	330 ÷ 535	330 ÷ 495	0.17
7	530	525	11	0.41	420 ÷ 600	430 ÷ 625	0.10
8	650	700	8.8	0.30	610 ÷ 818	620 ÷ 785	0.10
9 Ech	17 orders		2.6	0.12	350 ÷ 1020	335 ÷ 940	
10 C. D.	380	390	46	1.7		330 ÷ 640	
11 C.D.	520	500	34	1.3		400 ÷ 700	
12 C.D.	730	700	91	3.7		530 ÷ 1020	
13	510	525	3.6	0.12		495 ÷ 560	

Figure 2.3: Different gratings spectral range and resolution. Grism #4 has a "free spectral range" smaller than the value shown in the table. In fact the table shows the first order spectral coverage but the range free from second order overlap ends at 700 nm. Grisms #10, #11, and #12 are cross-dispersers to be used mainly with echelle grism #9 and are mounted on the filters wheel. They are optimized according to the working band: grism #10 has a peak efficiency in the blue, grism #11 in the visible and grism #12 in the red. Also the number of orders on the detector varies with the cross-disperser: grism #10 gives 13 orders, grism #11 gives 9 orders and grism #12 gives 6 orders.

2.2 Observational techniques

The main difficulty encountered in observing space debris is that the debris moves in relation to the fixed stars. Therefore the first step the observer has to do is calculate the ephemeris (α & δ) of the satellite. This could be done using some useful programs like Heavensat. Heavensat is a program for visual observing of artificial satellites, which basically shows satellites on the local horizon of observer in relation to bright stars in a given moment of time, and it's able to calculate ephemeris. For this work two different types of images have been chosen, photometry and spectroscopy. Photometry (B,V Johnson and R,I Cousins) consists in pointing the telescope in a given position, where you know the satellite will pass at a certain time, keeping the telescope in sidereal tracking in order to maintain background stars still. Then the observer has to wait for the satellite enter the CCD field, using the fast read function of the CCD Camera. When the satellite enters the field the exposure starts and the satellite swipes on the CCD. The result image is a stripe on the CCD that can be translated in a Light Curve (Time-Magnitude). The shape of the LC is determined by the velocity and distance of the satellite, the phase angle, the reflection characteristics of the satellite (shape, spinning, reflectivity). Sometimes the satellite moves so fast that it crosses the entire field during the exposition. In this case the observer has two possibilities: reduce the exposure time or track the satellite to reduce its apparent velocity on the CCD.

The main problem of these types of images are the background stars that modify the LC and complicate the extraction of the LC and the sky subtraction, especially in crowded fields. Things are a bit more complicated when the observer is forced to track the satellite, because in this case background stars also will swipe on the CCD, increasing the chance of the LC being crossed by stars.

The second observational technique is spectroscopy. The main difficulty in this case is to maintain the satellite in the slit. This is a very difficult task for many reasons. First the observer needs very accurate ephemeris, to calculate the angular velocity. Practically the observer needs to provide a three columns file (Julian Day, α velocity, δ velocity, both expressed in arcseconds per hour) to the pointing system of the telescope. Unfortunately Heavensat is able to provide precise ephemeris with a step time of only about one minute, which is not enough to guarantee the precision needed. If the step time is reduced Heavensat approximations make coordinates less accurate. In order to avoid this problem a cubic spline has been used to fit the ephemeris provided by Heavensat with a step time of one minute, and to calculate ephemeris with a step time of 10 seconds. This ruse has allowed us to maintain the satellite in the slit for one minute, or two in the luckiest cases. Probably the equatorial mount of the Cassini telescope is responsible for complicating this types of observations. The balancing system of the telescope with the counterweights does not allow a very accurate tracking.

The maintenance of the satellite in the slit is extremely important for two reasons, the first is obvious, if the satellite goes out of the slit some of the radiation is lost, causing the resultant spectra to be noisier, the second is more risky. When the satellite goes out of the slit, because of the differential refraction of terrestrial atmosphere, the blue part of satellite's light (or the red) escape first if the satellite goes out shifting north (south), and this causes a deformation of the spectra, compromising its scientific effectiveness. However the effectiveness of the spectra can be checked by plotting the B,V,R,I magnitudes obtained from photometry images on the spectra and checking if they match.

2.3 Image pre-reduction

The image pre-reduction operations have been made using IRAF (Image Reduction and Analysis Facility,) a general purpose software system for the reduction and analysis of astronomical data. We start to follow the IRAF standard pre-reduction operations in a way which can be summarised as follows:

- calculation of the Masterbias
- subtraction of the Masterbias from each image (scientific and flat field)
- averaging flat field images
- normalisation of the average flat field image dividing it by its mean value
- division of each scientific image by the normalized flat field

The purpose of the pre-reduction operations is to remove all possible instrumental effects from the scientific image. To do that biases and flat fields are required. Bias are images obtained with the shutter close and null exposure time, so that

they represent the Read Out Noise (RON) of the CCD Camera. Biases have to be combined using the IRAF task ZEROCOMBINE that averages many (usually ten) biases in order to obtain a Masterbias file, this file should be subtracted from each image. The subtraction of the Masterbias has been done with the IRAF task CCDPROC.

Flat field images are obtained by exposing the CCD camera to a uniform light source, in our case the illuminated dome, and are used to eliminate efficiency irregularities of single pixels. Unlike biases, which are valid for any image, flat fields should be taken for each Filter and Grism that has been used during the night. Flat field also have to be combined with another IRAF task called FLATCOMBINE that averages the flat field images. Once the average flat field has been obtained it should be normalised. The normalization is different between photometry and spectroscopy, in the first case the normalization is made by dividing the average flat field by its mean value (obtained with the IRAF task IMSTAT). This operation is done with CCDPROC. As regards the spectra, things are a bit more complicated because the normalization should be done line by line (or column by column). This is due to the fact that lighting along the y axis is not homogeneous. It depends on the spectrum of the lamp we are using to illuminate the dome and the efficiency of the grism. Therefore, we can not compare lines with different y values. We must then, for each y fixed, divide the FF by the mean value of the counts to that y. This could be done using the IRAF task RESPONSE. Once the normalized flat field is calculated, every spectra should be divided by it using CCDPROC. Here the pre-reduction operations end.

2.4 Photometryc data reduction

2.4.1 Extraction of the Light Curves

Once the pre-reduction operations have been made, we proceed in our analysis using ESO-MIDAS (another software for image processing and data reduction). As previously stated in the Observational techniques section our photometry images consist in swipes of the satellite on the CCD, therefore the first step to obtain the light curve of the satellite is to rotate the image in order to make the swipe move along one axis, this could easily be done with the MIDAS command EXTRA/ROTATE. There is then the extraction of the light curve, which is made by the averaging of the pixels. Let us suppose that the swipe is positioned along the y-axis, with the MIDAS command GET/CUR we produce a cursor, and with the cursor we position left and right of the LC, midas gives us the position in pixel. Now we have to average the pixel value between the two positions we chose, this is made running the AVERAGE/COLUMN (or AVERAGE/ROW if the LC is along the x-axis) MIDAS command, the correct syntax of the command is the following: “ave/col Light Curve = Rotated Image @pixelvalue 1,@pixelvalue 2”. Then we have to obtain an estimation of the sky value, for the most of our images the sky has been taken in the same way of the LC, being careful to avoid too many background stars falling into the pixel range we chose. In some cases however the observing field was so crowded that this method wasn't satisfactory so we decided to estimate the sky as a constant averaging ten values of the sky taken in different points of the image (this points

should obviously be clear of stars). Once we have the sky value (as a function of y-axis or as a constant) the sky should be subtracted from the LC to obtain the final LC file. The subtraction is made using the COMP/IMA command of MIDAS, the correct syntax for this command is: “comp/ima Normalized Light Curve = Light Curve - Sky”. Before starting with the magnitude calibration the LC files that are in bdf format should be printed on an ascii file. This can be carried out using two simple commands: “ass/print file LightCurve.dat” which tells MIDAS to write in the file LightCurve.dat and “print/ima NormalizedLightCurve [<:>] h 1” that prints the light curve in a two columns file (position,signal).

2.4.2 Magnitude calibration

The magnitude calibration needs observations of a standard field in every filter, to calculate the Zero Point. We chose standard fields from Landolt (1992), an example of a standard field is shown in Figure 2.7. The standard field images have to be processed as the other images with bias and flat field correction, then the instrumental magnitude of stars in the field must be calculated, this could be done with the midas command MAGNITUDE/CIRCLE (“mag/circle ? ? r_1, r_2, r_3 ”) which allows the user to draw three concentric circles, the signal is taken in the inner circle while the sky is taken in the external ring, midas manages the subtraction itself, and calculates the instrumental magnitude as $-2.5 \cdot \log(Counts)$. Once the instrumental magnitude is known, it has to be compared with the tabulated values to calculate the conversion constant, an example of tabulated values is reported in Table 2.1.

Object	V	B-V	V-R	V-I
PG0231051	16.105	-0.329	-0.162	-0.534
PG0231+051 A	12.772	0.71	0.405	0.799
PG0231+051 B	14.735	1.448	0.954	1.951
PG0231+051 C	13.702	0.671	0.399	0.783
PG0231+051 D	14.027	1.088	0.675	1.256
PG0231+051 E	13.804	0.667	0.39	0.757
PG1047+003	13.474	-0.29	-0.132	-0.295
PG1047+003 A	13.512	0.688	0.422	0.84
PG1047+003 B	14.751	0.679	0.391	0.764
PG1047+003 C	12.453	0.607	0.378	0.737

Table 2.1: Example of the tabulated values for standard stars magnitudes and color indexes from Landolt (1992)

This process has to take the extinction due to atmosphere and the exposition time of the image into account. To calculate the zero points the following formula has been used:

$$ZP_{filter} = Mag_{tab} - (Mag_{instr} + 2.5 \cdot \log(t_{exp}) - cost(filter) \cdot Airmass) \quad (2.1)$$

The Zero Point must be calculated for every filter, since the atmosphere extinction depends on the wavelength the value of the constant for the Airmass

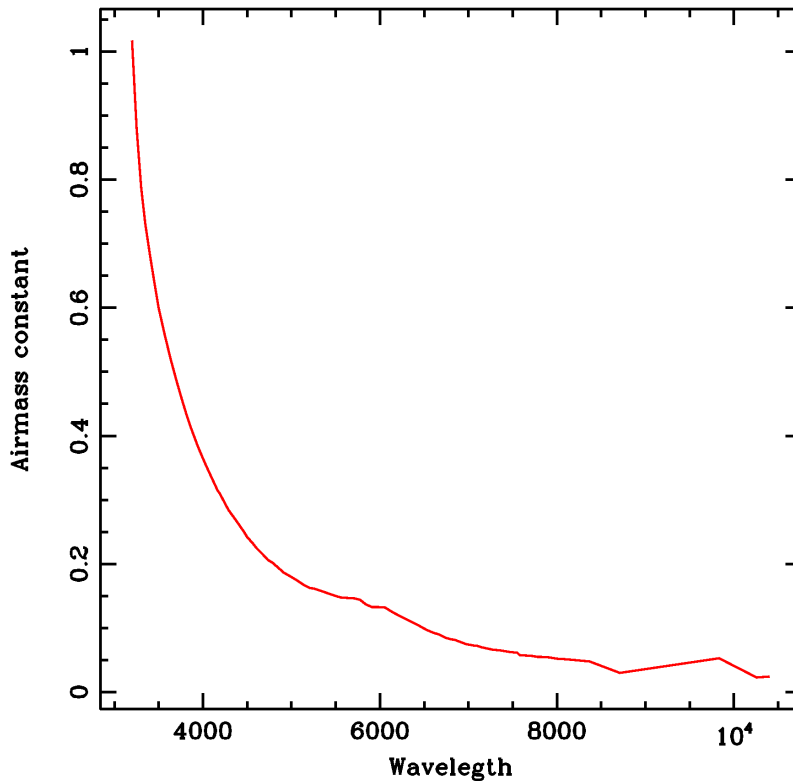


Figure 2.4: Airmass correction constant vs. Wavelength

correction depends on the filter. The dependence of the constant for the airmass correction with wavelength is plotted in Figure 2.4. We chose 0.2 for filter B, 0.1 for filter V, 0.08 for filter R and 0.06 for filter I.

So the previous equation must be applied to every filter and every star of the field we are considering. For each star and filter we obtain a Zero Point, these ZP must be averaged to obtain the final Zero Points of the night, an example of the result of this operation is plotted in Figure 2.6. The calculation of the ZP is influenced by the possible presence of clouds at the time of exposure, this presence could falsify the results. To avoid this problem is a good practice to take many exposures of different standard fields and compare the single result obtained for every single exposure. If one of these exposures presents a ZP sufficiently different from the other could be possible that some clouds affect the results, and so data from this exposure must be rejected.

Once the ZP are known, the magnitude calibration of the LC begins. The magnitude calibration uses the same equation adopted for the evaluation of the ZP but in a different arrangement:

$$\begin{aligned}
 Mag_{true} = & Mag_{instr} + 2.5 \cdot \log(t_{exp}) - cost(f) \cdot Airm + ZP_{filter} + 2.5 \cdot \log(n_{pix}) \\
 & - 5 \cdot \log(d/30000)
 \end{aligned}
 \tag{2.2}$$

where t_{exp} is the exposition time for every pixel (calculated as the exposition time of the image divided by the pixel length of the LC: $t_{exp} = t_{exp,tot}/n_{pixel,tot}$), and $\log(n_{pixel})$ is a constant that originates from the fact that an average on the pixels has been made to extract the LC. Therefore to obtain the total magnitude we have to multiply the counts by the number of pixel on wich the average has been made.

The last term of the equation is the distance correction. This term arises from the fact that the apparent magnitude of the satellite depends on the distance of the satellite, therefore to compare different expositions the magnitude should be corrected to bring the satellites back to the same distance. We choose a reference distance of 30000 km. In this way the satellite magnitudes are expressed as if all the satellites had been observed at thirty thousand kilometers. The error on the magnitude calibration is represented by the σ of the calibration plot, reported for each night in Appendix A. This error however is not truly representative of the error on each

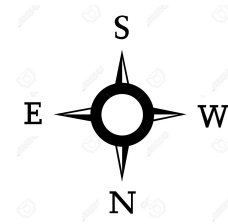


Figure 2.5: Loiano CCD cardinal points position.

exposition of the satellites, especially for the integrated magnitudes. In fact the strummental integrated magnitude is calculated with the midas command `mag/rect ? ? x,y,z,t` where x and y are the sides of the rectangle, z is the number of pixel that separate the zone where the signal is taken and the zone where the sky is taken, and t is the sky zone width. So what we have done is draw three rectangles, one containing the CL, one that separates the signal zone from and the sky zone, and one where the sky is taken. For this reasons the magnitude calibration error is not fully representative of the true error on the integrated magnitude. Often happens, especially in very crowded fields, that many stars falls into the signal or the sky zone, introducing errors that can not be quantitatively evaluated. This aspect is more under control in the calibration of the individual pixels of the light curves, where it is easier to see if a star is in the selection of the sky or the signal, since its feature can be seeing in the final trace of the light curve. The last step of the Light Curve extraction is to convert the x-axis from pixels to time, a very easy task once exposition time and gps time at the start of the exposition is known. The only complication is to decide the direction of the time axis, to do this the sign of α and δ velocity of the satellite at the time of the exposure must be known, to decide if the satellite was going north or south. Once the two velocity are known we look at the image on the ccd, and reminding that the Loiano CCd has the cardinal points organized as shown in Figure 2.5, we decide the time axis direction.

2.5 Spectroscopic reduction

Sepectroscopic reduction is made in three main steps:

- Extraction of the 1D spectra from the 2D images
- Wavelength calibration
- Flux calibration

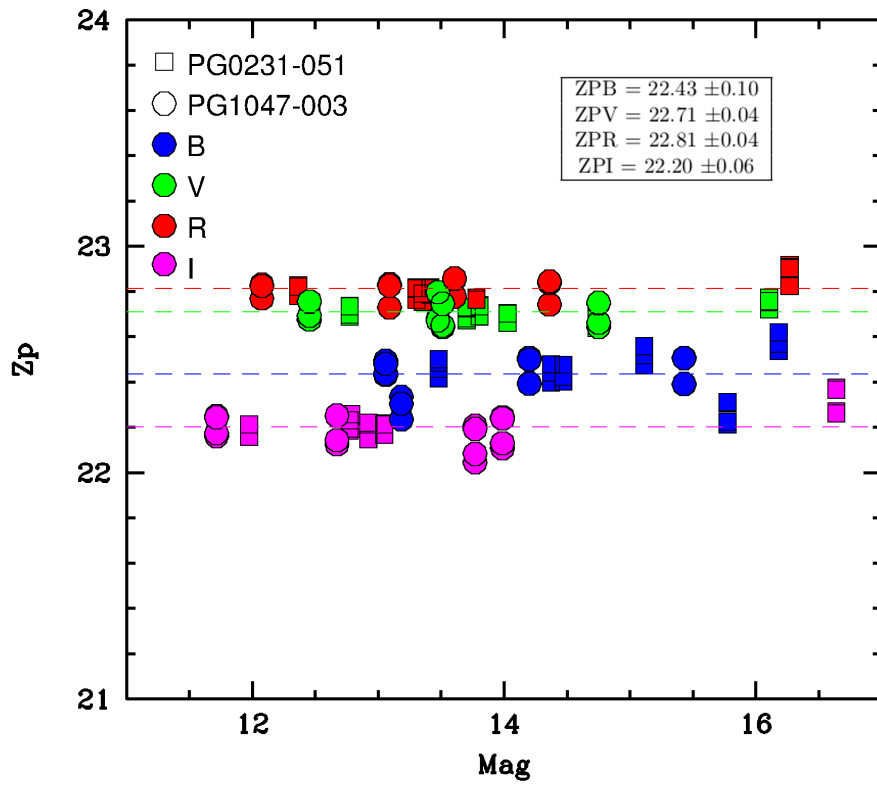


Figure 2.6: Example of photometric zero points obtained by comparing observed and tabulated magnitudes of two standard fields (PG0231-051 and PG1047-003)

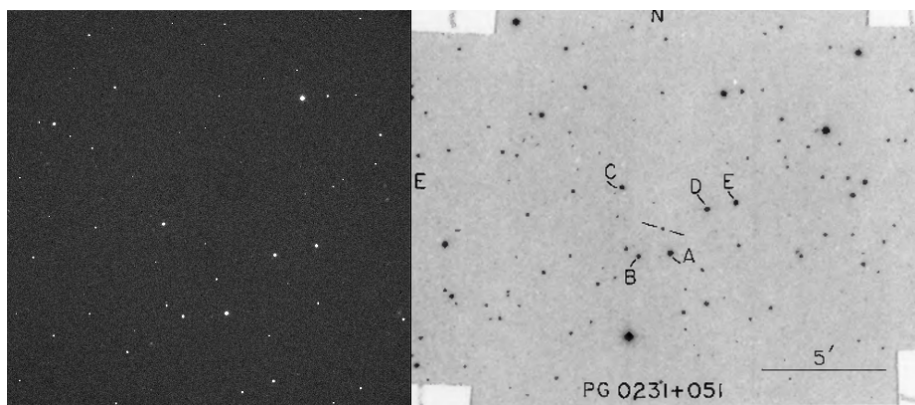


Figure 2.7: Example of an observed (left) standard field in R filter and its image (right) as reported on Landolt (1992).

2.5.1 Extraction of the 1D spectra

The extraction of the 1D spectra has been made using the IRAF Task APALL. The task provides functions for defining, modifying, tracing, and extracting apertures from two dimensional spectra. When running APALL the user has to do some standard operations. First the user has to edit the extraction aperture. Editing the aperture is a simple step if the user is reducing stars spectra but could become harder for debris spectra. The difficulty arises from the fact that during the exposure many stars cross the slit (because the exposure is made with the tracking on in order to keep the satellite in the slit) which means that the satellite spectra would probably be hidden under many stars spectra. However the satellite spectra will surely not be easily recognizable. To avoid this problem we decided to make a direct image of the satellite before or after the spectrum acquisition to memorise the position of the satellite on the CCD. Another factor that helps is the fact that the satellite spectra will be thinner (if the tracking is good) than stars spectra because the stars entering the slit will move in both x and y direction so that the resultant spectra will be spread on x axis. APALL allows the user to edit aperture dimension too.

Once the aperture is selected the user has to select the region where the background will be extracted and fitted. Generally background is taken near the aperture, but for debris spectra this is again not always possible because of the background stars. For this reason background has been taken in the available empty regions of the 2D image. An example of aperture extraction and background fitting is shown in Figure 2.8, in which are plotted the extraction of a standard star spectra and a noisy and partially hidden debris spectra. After the background fitting and subtraction APALL will generate the trace allowing the user to interact with the fit of the trace, deleting points and changing order and function of fitting. After this operation the 1D spectra is ready for the wavelength calibration. An example of trace fitting and resultant spectra is plotted in Figure 2.9.

2.5.2 Wavelength calibration

The wavelength calibration is obtained by comparing the observed spectrum of a lamp (in our case HeAr) with its tabulated values. Practically emission lines have to be identified to reconstruct a pixel-lambda function which will be applied to scientific spectra. This process could be made using three IRAF tasks: IDENTIFY, REIDENTIFY and DISPCOR. First of all the lamp's spectrum should be extracted with APALL properly editing the task parameter. When the lamp's spectrum is ready we proceed with the identification of the emission line. The idea is now to manually identify a few lines in the spectrum. This gives IRAF a initial idea of the calibration function. Then the user has to tell IRAF which sort of lamp produced the comparison spectrum (providing a file on which are printed the wavelength values of the emission lines of the lamp) and ask it to proceed automatically to identify all the other lines. The user has to check and perhaps modify these additional identifications and finally tell IRAF to proceed with the fitting of the wavelength solution using all validated comparison lines. After we spent much time determining the wavelength solution of the first calibration image all other lamps could be identified using REIDENTIFY. The task uses the solution found with IDENTIFY to identify

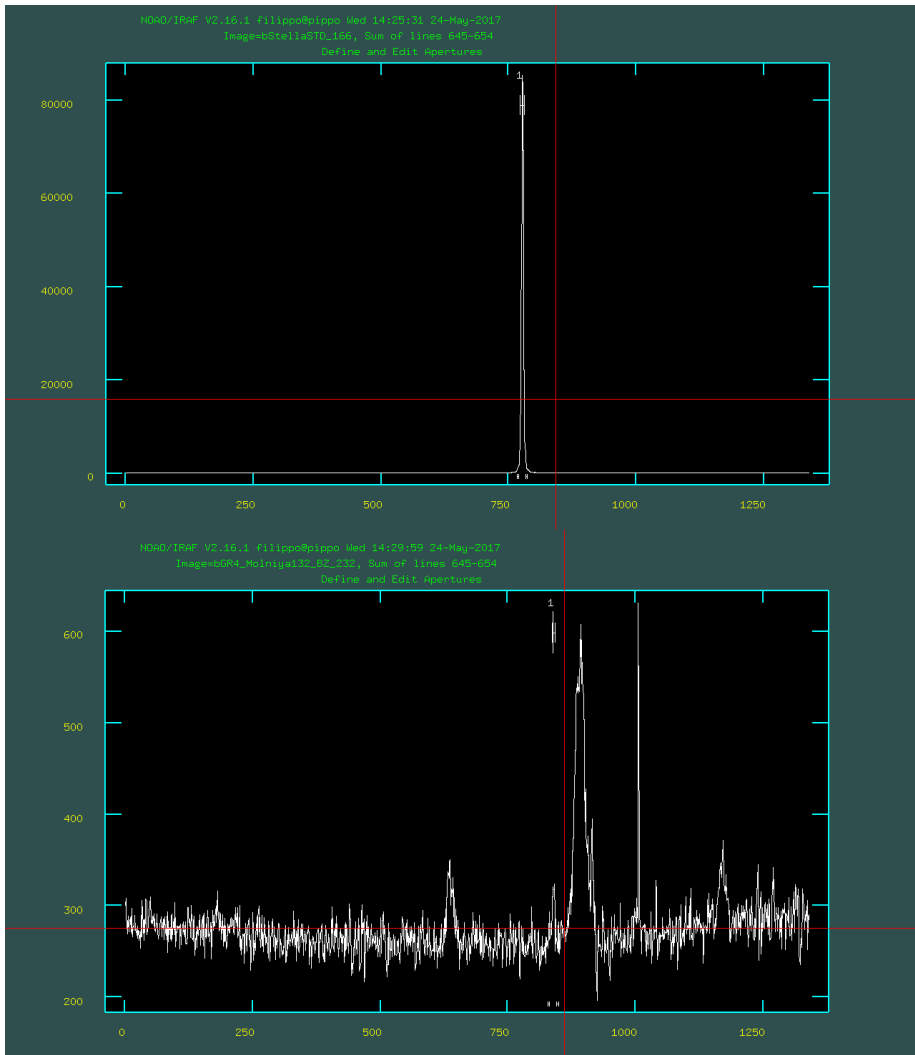


Figure 2.8: Example of aperture extraction of standard standard star spectra and a debris spectra, as you can see the debris spectra is more noisy and partially hidden by background stras spectra crossing the slit during the exposition

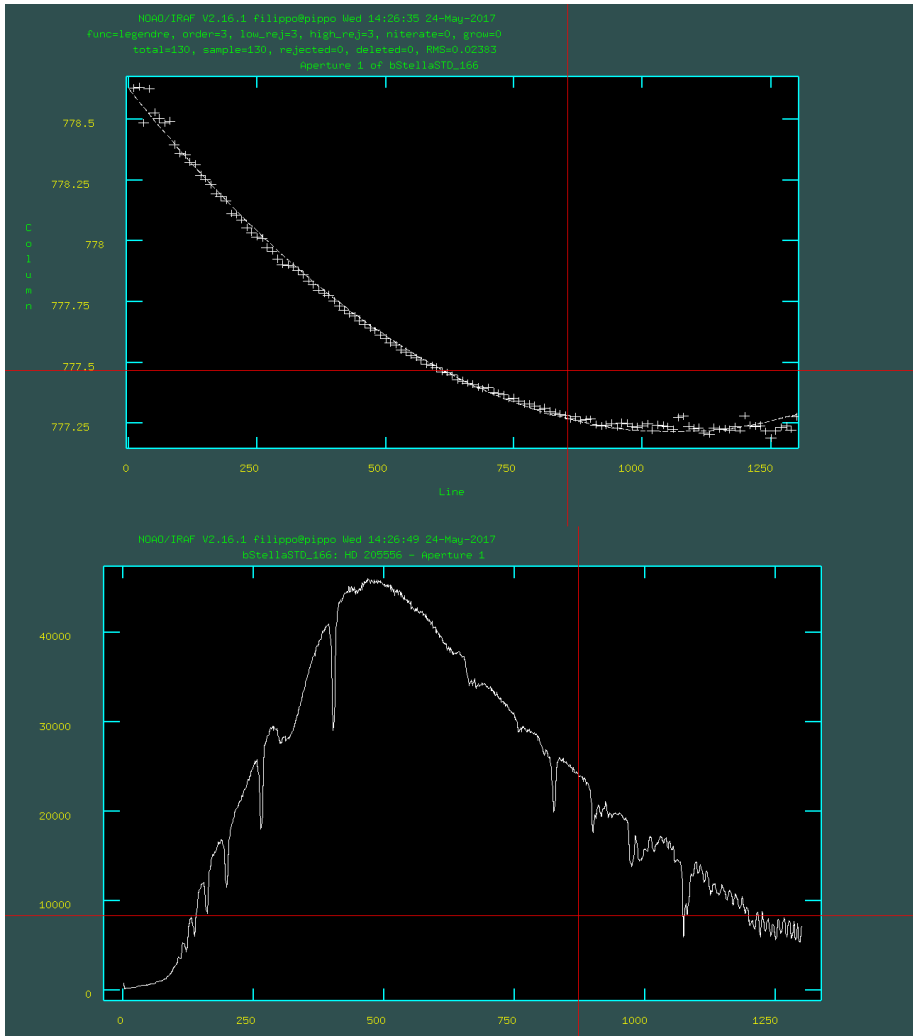


Figure 2.9: Example of trace fitting and extracted spectra of a standard star.

the solution for other lamps but allows for simple shifts in the spectrum that are due to spectrograph differential flexures when observing in different directions and/or small changes on the focal plane geometry induced by changes in the environment temperature. Finally the wavelength solution has to be applied to a specific science spectrum. To tell IRAF which wavelength solution to use, the image header should be edited writing the following instruction: `"hedit Spectrum1D refspec1 lamp1D add+ ver-"` which writes in the header of `Spectrum1D` that its reference spectrum for wavelength calibration is `lamp1D`. Finally the solution is applied with DISPCOR.

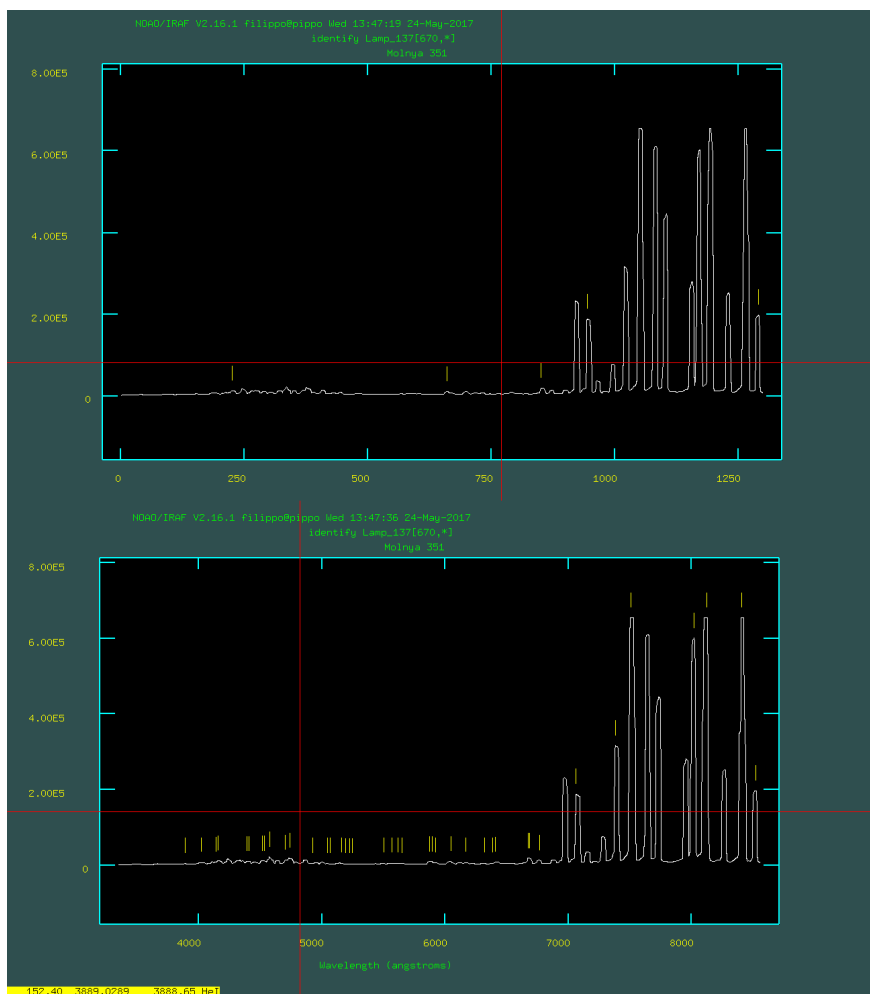


Figure 2.10: Example of manual (top) and automatic (bottom) identification of emission lines

2.5.3 Flux calibration

An accurate flux calibration of spectra is a difficult task as even tiny cirrus clouds can spoil the result. First of all observations of standards stars are

needed, we chose stars from Gutierrez-Moreno et al. (1988). The standard star spectra should be extracted and calibrated following the procedure seen so far. Then the user has to check or edit the observatory parameters, this could be done with the task OBSERVATORY or by inserting a file `obsbd.dat` in the directory `iraf/noao/lib`. The file should contain observatory latitude, longitude, altitude and timezone. Once we are sure that the observatory is well set we can begin the flux calibration.

The aim is to calibrate the CCD chip response, also considering the atmospheric extinction. The result is a spectrum as observed from outside the atmosphere with an ideal uniformly sensitive detector-telescope-spectrograph. In short, the user has to:

- Take the energy distribution of the observed standard star
- Correct this energy distribution for wavelength-dependent atmospheric extinction
- Compare it to the energy distribution of the observed spectrum
- Derive from such a comparison the function that gives the response of the system for every wavelength

This process is made using the IRAF task STANDARD, which determines calibration pass-bands and writes them (together with data on extinction and airmass) to a file called `std`. STANDARD needs in input extinction and flux calibration files (a three column file with λ , flux, width of the bandpass), an example of this procedure is plotted in Figure 2.11.

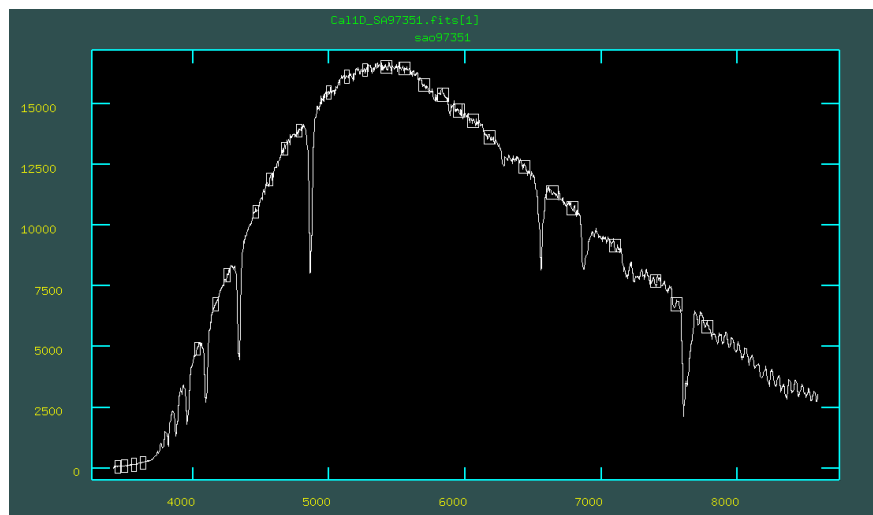


Figure 2.11: Example of the operation of the STANDARD task

After running STANDARD once for each exposure of a standard star, the different solutions must be combined to find a proper wavelength dependence of instrumental sensitivity and atmosphere transparency. This is done with the

SENSFUNC task. The user may use a single standard star and adopt an extinction function, or may combine observations of several standard stars observed at different airmasses to solve simultaneously for the sensitivity function and atmospheric extinction. We have chosen the first option. If the task is run interactively a graphic window will open with the plot of sensitivity function and residuals of the current fit, and the user will be able to delete some of the points if necessary. User can also type `:g sre1` to plot 2 more graphs: extinction function and flux-calibrated spectrum (of the standard star). An example of this 4 graphs is plotted in Figure 2.12.

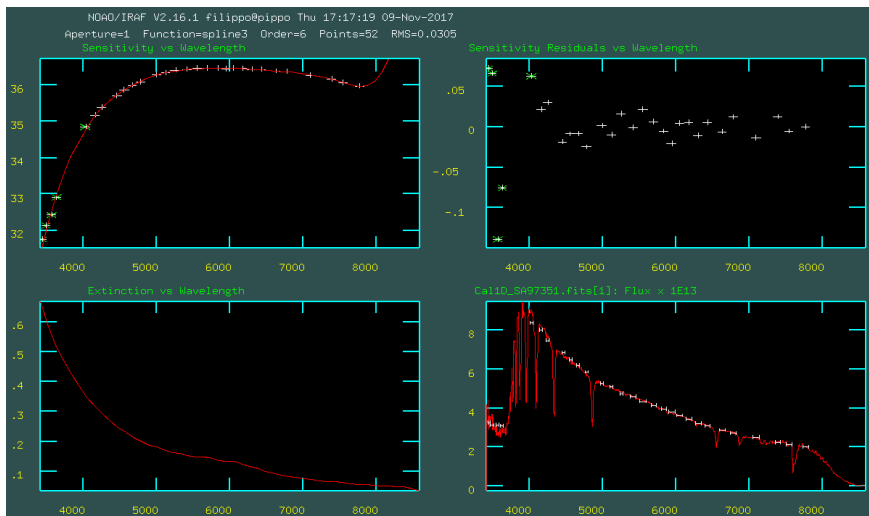


Figure 2.12: Example of the operation of the SENSFUNC task

The user is therefore able to check the accuracy of the sensitivity function. The last step of the flux calibration is to apply the function to all the scientific spectra. This is done with the task CALIBRATE, which takes the atmospheric extinction and exposition time into account and applies the calibration function. Here ends the calibration of spectra.

2.6 Figer images

In some cases we weren't able to observe some objects due to their high apparent angular velocity in the sky, that didn't allowed us to observe them with the Cassini Telescope that has a upper limit of the angular velocity tracking function of about 100000 arcseconds per hour. This are the cases of Molniya 1-44 and Molniya 1-86 that in 2016 had already begun their phase of return to atmosphere, and had very peculiar high velocity orbits. In particular Molniya 1-44 (decayed in October 23, 2017) had a orbital period of about two hours (a sixth of normal). In this case we asked to Alain Figer, a French amateur astronomer and one of the most prominent figures in European amateur astronomy, to give us some of his observations. Figer uses amateur instrumentation which are not equipped with the classic optical astronomical filters and therefore can not be

calibrated in magnitude, but are excellent to study the tumbling period of the satellites. In fact Figer instrumentation is provided of a wide field of view, that allows very long time expositions and observation of high apparent angular velocity objects. An example of Figer's images is plotted in Figure 2.13. For every satellite requested Figer provided many series of images like the one plotted in Figure 2.13, taken with exposition time = 4 or = 5 s, spaced temporally by one second from each other. To analyze this type of images we could not follow the classic approach (there are no Bias or Flat Fields), the main problem was that adding several images the sky became very high. Moreover the images were not taken with a sidereal tracking consequently adding many images the result was that not only the satellite left a swipe but also the stars, contributing even more to increase the sky background. We choose to add the images in groups of ten (Figure 2.14). To calculate the sky we used a median applied to the ten images that were added, and then to obtain the final image we subtract from the sum image the median multiplied by ten. An example of the results of this operation is presented in Figure 2.15. This type of process which allows to clean up images from the sky background while leaving traces of the stars visible, has been applied to all Figer's images. After the cleaning process the extraction of the light curves was made in the same way as that of images made with the Cassini telescope with the difference that the LC were not calibrated in magnitude. The fact that the expositions in sequence are spaced temporally by a second is evident in Figure 2.15 where traces left by the satellite or stars are not continuous but seem to be dashed due to the second between any pose in which the camera shutter closes.



Figure 2.13: Example of image taken by Figer, exposition time = 4 s. Here is not plotted the full image but only a central portion to make the details more visible. The full image is about twice the size of this one.

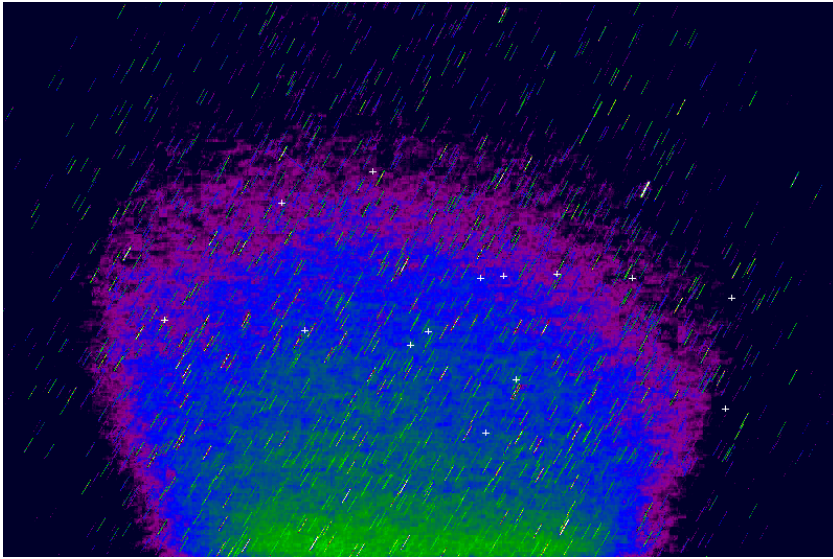


Figure 2.14: Example of image obtained by adding ten Figer's images, in rainbow colors. Here the sky is prominent and the brightness gradient due to light pollution is evident.

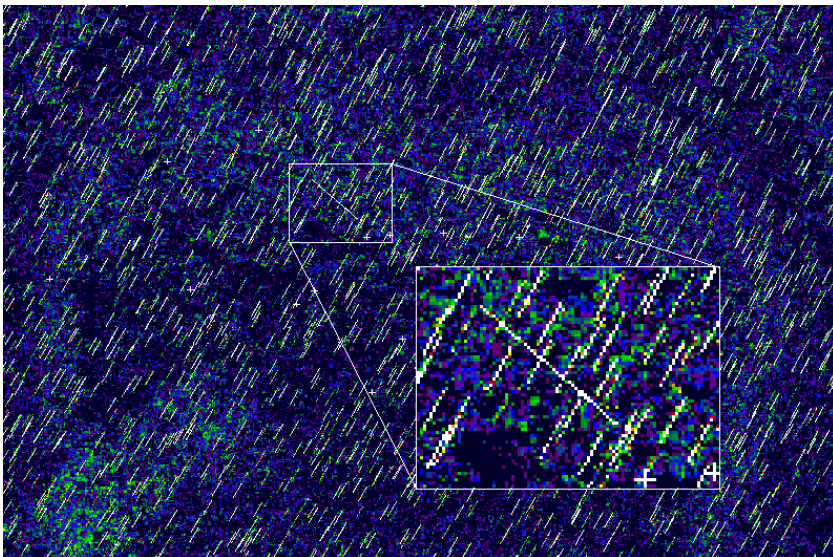


Figure 2.15: Example of image obtained by adding ten Figer's images and subtracting their median ten times, in rainbow colors. The cleaning process has dramatically improved the image by making it clear the satellite track, however, the traces of the stars remain.

2.7 Periodogram analysis

Once the light curves are extracted and calibrated we proceed with the periodogram analysis to find the tumbling period of each satellite. In signal processing, a periodogram is an estimate of the spectral density of a signal. The spectral density (or power spectrum) describes the distribution of power into frequency components composing that signal. According to Fourier analysis any physical signal can be decomposed into a number of discrete frequencies, or a spectrum of frequencies over a continuous range. In order to look for periodic signals, there are several mathematical tools. A periodogram is one of them. For data obtained at uniformly spaced intervals, standard methods are available like Fast Fourier Transform, and their results are reliable. A periodogram is similar to the Fourier Transform, but is optimized for unevenly time-sampled data, and for different shapes in periodic signals. The periodogram calculates the significance of different frequencies in time-series data to identify any intrinsic periodic signals. In other words periodogram is an statistical method that allows to discover the presence of any periodicity on the basis of a time sampling of a certain quantity (in our case magnitude). Generally the statistical significance of each frequency is computed based upon a series of algebraic operations that depend on the particular algorithm used and periodic signal shape assumed. We have developed a simple code, that can be summarized as follow. The code reads the data files of the Ligth Curves and write time and magnitudes values in two vectors (t, mag) . Then a period (p) is supposed, and the code calculate the phase of each point of the two vectors. First the time is divided by the period, $Phase_1 = t/p$, then the integer part is calculated $Phase_2 = int(Phase_1)$, and then the integer part is subtracted $Phase = Phase_1 - Phase_2$. Practically with this operations a integer number of periods is subtracted from all the points of the time vector in order to obtain the phase. Then the phase vector is sorted (keeping each magnitude matched with its time value), in this way all the light curves data are phased. This is done for all the possible period values (according to the availability of light curves and the exposition times), in a do loop. Now the goodness or badness of each value supposed for the period must be checked. To do this a new variable N is introduced, defined as follows:

$$N = \sqrt{\frac{\sum_{i=1}^n (mag(i) - mag(i-1))^2}{n}} \quad (2.3)$$

The variable N can be interpreted as an estimate of the Light Curve noiness, if the period is good then the points of the light curves are phased correctly, therefore the average value of $mag(i) - mag(i-1)$ becomes little and so N also should be little. If the period isn't good points are not well phased, and so on average the difference of magnitudes and accordingly the value of N grow. Finally the N value is compared with the maximum magnitude difference, to calculate a new variable S/N defined as:

$$S/N = \frac{mag_{max} - mag_{min}}{N} \quad (2.4)$$

S/N is a kind of signal-to-noise ratio, the higher is the value of S/N the better is (theoretically speaking) the period. The periodogram then finds a period, in general, when a peak is found in the signal to noise ratio, the error over this

period is given by the full width at half maximum of the peak. Periodogram analysis must be used every time with a certain amount of caution, because its reliability is not always guaranteed (Baluev (2008)). There are many complications that affect the periodogram results. First of all the fact that our exposition aren't uniformly time spaced and are sometime very noisy. Moreover the light curves sampling isn't often satisfactory and the exposition times are sometime shorter than the rotational period of the satellite. A poor sampling cause one of the most common problem, the aliasing phenomenon. Aliasing is that phenomenon that occurs in a periodogram analysis when the sampling of the signal being analyzed is too poor, this causes the periodogram analysis to find not one single peak in the signal-to-noise ratio but an entire spectrum of peaks that makes difficult and sometimes impossible to decide which one of that many peaks is the correct one. Another fact that could compromise the periodogram reliability is that sometimes observations are made at different phase angle. The phase angle affect the magnitude of the satellite, therefore confronting observation at different phase angle causes the value of N to grow. To avoid this complication is good practice to confront exposure taken at similar phase angle. Normally if the exposures aren't temporally distant the value of phase angle doesn't change much, because many exposure are taken while the satellite is passing near the apogee. If the satellite is passing near the apogee it's velocity is little, therefore the phase angle remains approximately constant. Sometimes though the exposure is taken in the ascending or descending phase of the orbit. In this case the value of the phase angle change even with small temporal differences. In this cases a phase angle correction should be applied, but this type of correction is not taken for granted. There are in literature many examples of possible phase correction for the magnitude, that depend on the shape of the observed object and its characteristics. Many examples of phase correction curves could be found in Li et al. (2015a). We didn't employ a phase angle correction, because of the complexity of the problem related to the peculiar shape of Molniya satellite, so we make attention to avoid the confront of too temporally distant Light Curves. Is lastly good practice, once the periodogram has found a peak in the signal-to-noise ratio, to check if the fit of the phased light curves with that value of the rotational period is good. The fit is not a classical fit, but is done with a smoothing function. Anyhow the eyes are more trustworthy of any statistical estimate, so the search for periodicity also goes through the ability of the observer. The goodness or the badness of the periods values found by the periodogram must be checked.

2.8 Phase angle calculation

In Chapter 4 section 4.1 we discuss the relation between the magnitude of the satellite and the phase angle at the time of observation. The phase angle should of course be calculated for every exposition. The phase angle is defined as the angle between the light incident onto an observed object and the light reflected from the object. In other words phase angle is the angle Sun-object-observer. The phase angle determines the object portion illuminated by the Sun and therefore its apparent magnitude. The relation between the apparent magnitude and the phase angle depends on the shape and the characteristic of the observed object. The calculation of the phase angle employ the fundamental identity of

spherical trigonometry, the cosine rule 2.5. The cosine rule establishes that in a spherical triangle the angular size of a side is related to the other sides following the next equation.

$$\cos(a) = \cos(b) \cdot \cos(c) + \sin(b) \cdot \sin(c) \cdot \cos(A) \quad (2.5)$$

A graphic representation of the situation described by equation 2.5 is plotted in Figure 2.16. Equation 2.5 can be applied to calculate the phase angle of

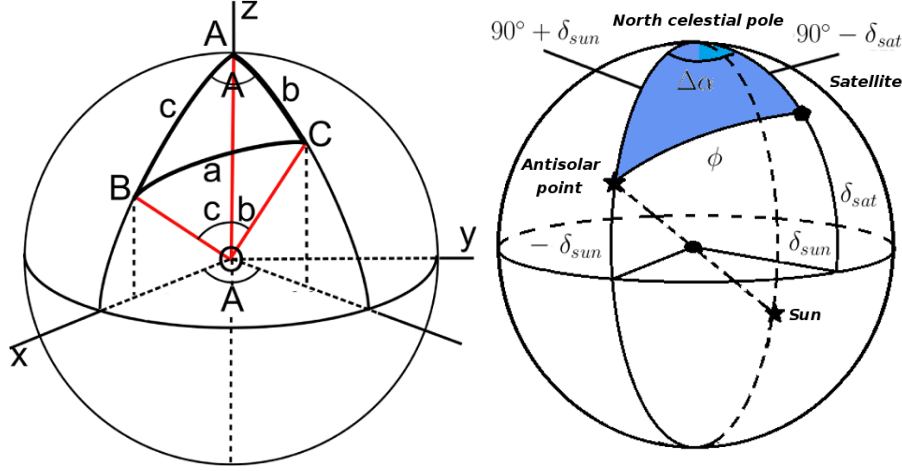


Figure 2.16: In the left panel is represented the situation described by equation 2.5, in the right panel we find the application of the cosine rule to the calculation of the phase angle.

an observation replacing it's terms properly. Being the satellite coordinates α_{sat} , δ_{sat} and the Sun coordiantes α_{sun} , δ_{sun} , the previous equation becomes as follows:

$$\begin{aligned} \cos(\phi) = & \cos(90^\circ - \delta_{sat}) \cdot \cos(90^\circ + \delta_{sun}) \\ & + \sin(90^\circ - \delta_{sat}) \cdot \sin(90^\circ + \delta_{sun}) \cdot \cos(180^\circ + \Delta\alpha) \end{aligned} \quad (2.6)$$

Where $\Delta\alpha$ is the difference between Sun and satellite right ascension. As you can see the term a of equation 2.5 is the phase angle, the term b is expresses as $90^\circ - \delta_{sat}$ and the term c is expressed as $90^\circ + \delta_{sun}$. The sign in the two terms is inverted, this is due to the fact that the c side of the spherical triangle connects the north pole and the antisolar point, that has coordinates $180^\circ + \alpha_{sun}$, $-\delta_{sun}$, for this reason the sun declination appears with positive sign. Angle A is the difference between antisolar point and satellite right ascension and so is expressed as $180^\circ + \Delta\alpha$. Finally equation 2.6 can be written with some simple trigonometric operation as follows:

$$\cos(\phi) = \sin(-\delta_{sun}) \cdot \sin(\delta_{sat}) - \cos(\delta_{sun}) \cdot \cos(\delta_{sat}) \cdot \cos(\Delta\alpha) \quad (2.7)$$

This equation has been applied for every exposition, using the celestial coordinates of the setellite at the time of observation and the Sun celestial coordinates, the celestial coordinates were provided by Heavensat.

Chapter 3

Periodogram analysis

3.1 Introduction

The periodogram analysis has been applied to the photometric images to calculate if and how fast the satellites are tumbling. During the years has been noted that artificial satellites that have finished their life cycle (in other words satellites that are no longer able to operate because they has finished the fuel) tend to start tumbling. The tumbling period varies from satellite to stellite and can change with time thanks to the Earth's magnetic field. The study of this phenomenon can provide useful information on the Earth's magnetic field and on the development of dynamical instability by out-of-control satellites. For this reason we worked on the most complete possible characterization of the Molniya rotational periods.

We start now a long list of results obtained with the application of the periodogram analysis to each satellite observed during the night of observation made with the Cassini Telescope in the final part of 2016. We apologize with the reader for the length of this chapter and its repetition, but this was the clearest and most comprehensive way to present this type of results and to provide a characterization of Molniya debris tumbilg periods as complete as possible.

3.2 Molniya 1-88

With the periodogram analysis of December data we discover that Molniya 1-88 is rotating with a period $P = 3.583 \pm 0.002$ s, the periodogram results are plotted in Figure 3.1, Figure 3.2, Figure 3.3 and Figure 3.4. As it can be seen, in all filters, there's a peak of the signal-to-noise ratio at $P = 3.583$ s , $P = 7.166$ s and $P = 10.75$ s, the fact that the second and the third peak are multiple integers of the first suggests that the period of rotation is the first ($P = 3.583$ s). Apparently, the peak with the greatest signal-to-noise ratio seems to be that at $P = 10.75$ s, this is due to the fact that the periodogram analysis fits the LC with every period between 0.01 s and 15 s with step 0.01 s, if we decrease the step we discover that the peak at $P = 3.583$ s has signal-to-noise ratio $S/N \sim 10$ similar to that at 10.75 s (Figure 3.5).

Once we discover that Molniya 1-88 were rotating at December 2016 with period $P = 3.583$ s we need to check if other observations confirm this result,

so we continue with the periodogram analysis of November and September LC. Here starts our first problem, as mentioned above the satellite in this two nights presents flashes in th LC, this could be connected with the value of the phase angle during the observations. While in the September image the flash are regular in the November images there's apparently no evidence of the presence of any regularity in the flashes (see Figure A.110, A.111, A.112, A.113, A.114 in Section A.5). It could be possible that some of the flashes are in reality background stars because the field of observation was crowded. Normally in this cases we cut the star signal, but in this case was very difficult to decide whether flashes were real or due to the presence of a star so we decided to not cut them. For this reason the periodogram don't clearly provide a period, and the fit with the previous value of the period aren't good (Figure 3.6, Figure 3.7, Figure 3.8, Figure 3.9). As you can see periodgram in V,I and B filter show clearly the presence of aliasing. Anyhow the most interesting thing is that the periodogram analysis of the September image provides a period $P = 3.565 \pm 0.1$ s (Figure 3.11), with a very good signal-to-noise ratio and a very good fit. The periodogram provides also another peak at $P = 7.13 \pm 0.1$ s exactly twice the first peak. The two different values for the period found in September and December make us think of a possible period evolution between September and December, that involved a slowdown of the period. The slowdown, if real, could be explained with the interaction with the earth magnetic field. This topic will be discussed in Chapter 4.

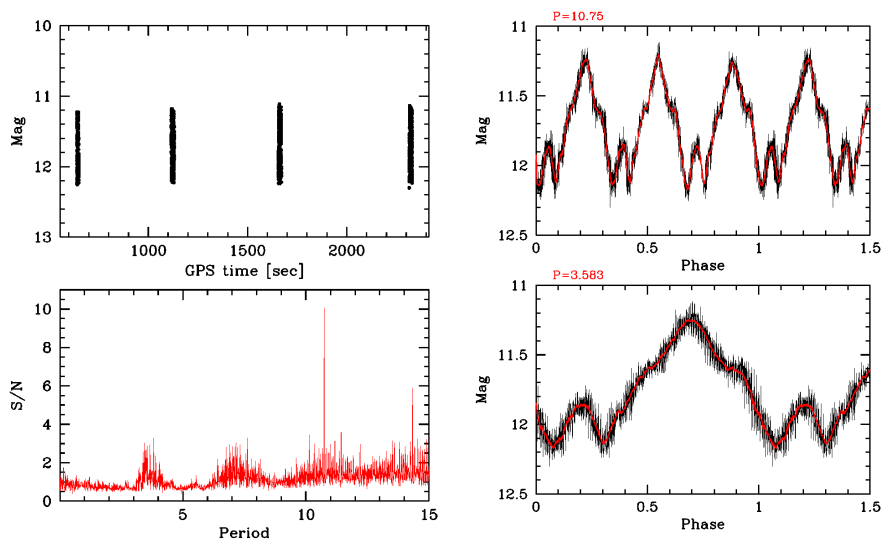


Figure 3.1: Filter R periodogram analysis of Molniya 1-88, December observations.

Day	UT(start)	Airm	Expt(s)	F	D(Km)	Mag	PA
2016-09-28	00:05:57	1.04	10	R	10401	11.060	59.82
2016-11-26	18:42:56	1.09	3	R	6248	11.327	66.09
2016-11-26	18:44:56	1.05	3	R	6577	11.235	62.15
2016-11-26	18:46:56	1.03	3	R	6939	11.889	58.79
2016-11-26	18:48:57	1.01	3	I	7326	10.191	55.96
2016-11-26	18:50:57	1.01	3	V	7731	11.404	53.58
2016-11-26	18:52:57	1	3	B	8149	12.550	51.59
2016-11-26	18:54:57	1.01	3	R	8574	11.460	49.94
2016-11-26	18:56:57	1.01	3	I	9004	10.513	48.56
2016-11-26	18:58:57	1.02	4	V	9435	11.952	47.42
2016-11-26	19:00:57	1.03	4	B	9867	12.775	46.47
2016-11-26	19:02:56	1.04	5	R	10296	11.532	45.69
2016-11-26	19:04:57	1.05	5	I	10723	10.914	45.06
2016-11-26	19:06:57	1.06	6	V	11145	12.200	44.54
2016-11-26	19:08:57	1.07	6	B	11563	13.200	44.12
2016-12-22	21:33:57	1.18	10	R	24885	11.696	35.98
2016-12-22	21:36:54	1.18	15	B	24956	13.370	35.81
2016-12-22	21:38:54	1.18	15	V	24999	12.356	35.71
2016-12-22	21:41:53	1.18	15	R	25056	11.681	35.57
2016-12-22	21:43:53	1.19	15	I	25089	11.008	35.48
2016-12-22	21:45:53	1.19	15	B	25118	13.346	35.41
2016-12-22	21:48:53	1.19	15	V	25154	12.313	35.3
2016-12-22	21:50:52	1.19	15	R	25173	11.691	35.24
2016-12-22	21:52:53	1.19	15	I	25189	11.000	35.18
2016-12-22	21:55:52	1.19	15	B	25205	13.328	35.11
2016-12-22	21:57:53	1.19	15	V	25211	12.358	35.08
2016-12-22	21:59:52	1.19	15	V	25213	12.157	35.05
2016-12-22	22:01:52	1.19	15	R	25211	11.668	35.02
2016-12-22	22:03:52	1.19	15	I	25206	10.998	35.01

Table 3.1: Molniya 1-88 data

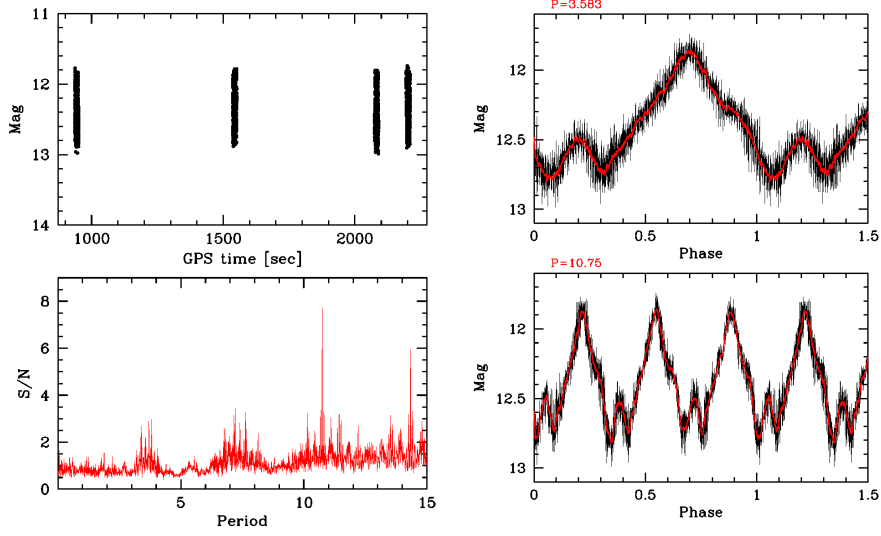


Figure 3.2: Filter V periodogram analysis of Molniya 1-88, December observations.

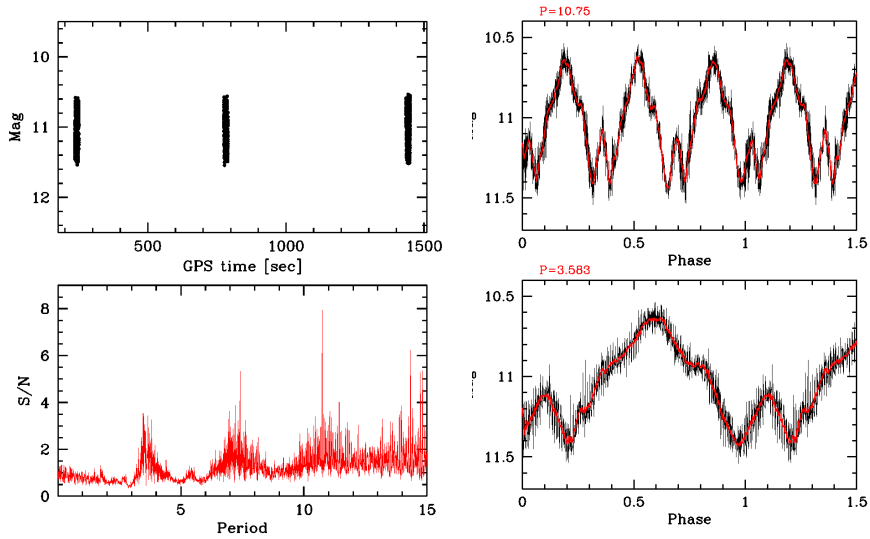


Figure 3.3: Filter I periodogram analysis of Molniya 1-88, December observations.

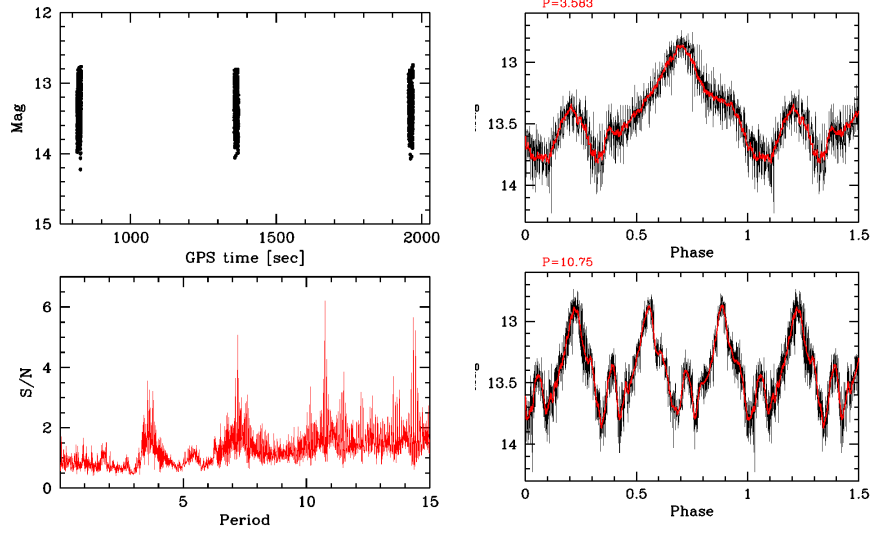


Figure 3.4: Filter B periodogram analysis of Molniya 1-88, December observations.

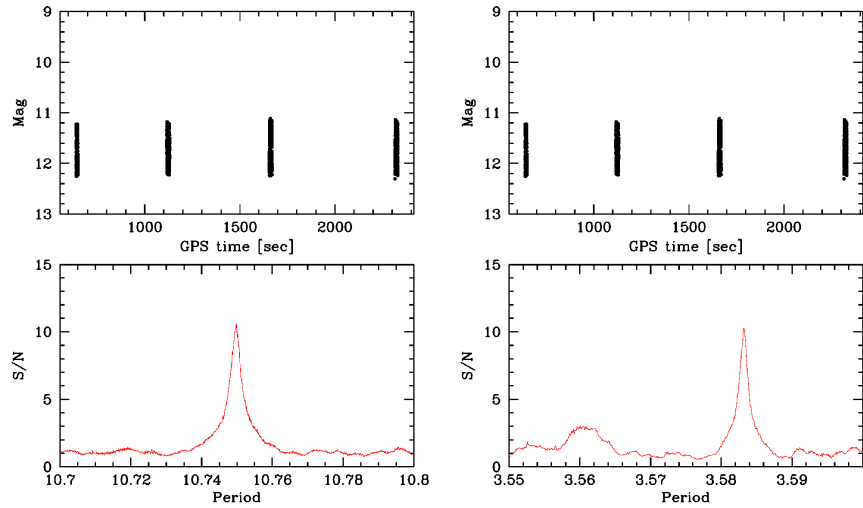


Figure 3.5: Here is plotted a zoom of the periodogram analysis of R-band images of Molniya1-88, near the two main peak at $P = 3.583$ and $P = 10.75$, the error on the period is determined by the width of the peak curve.

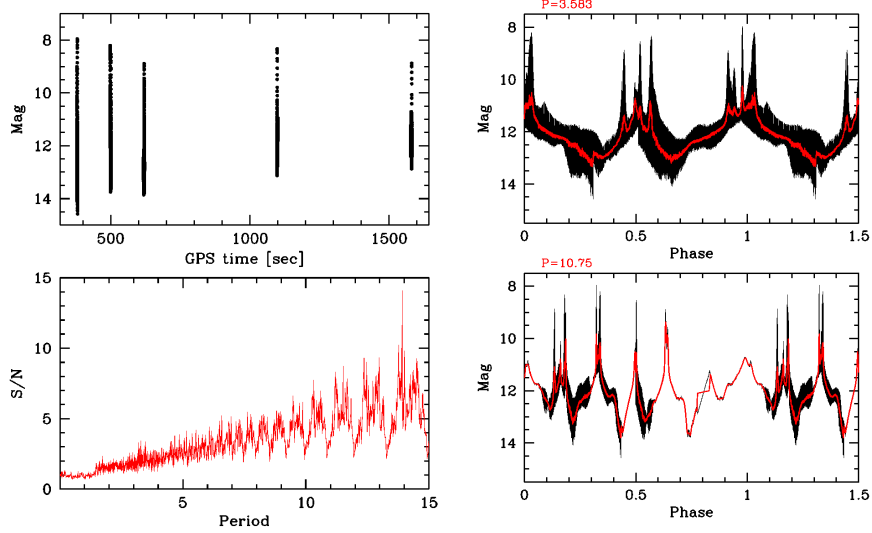


Figure 3.6: Filter R periodogram analysis of Molniya 1-88, November observations.

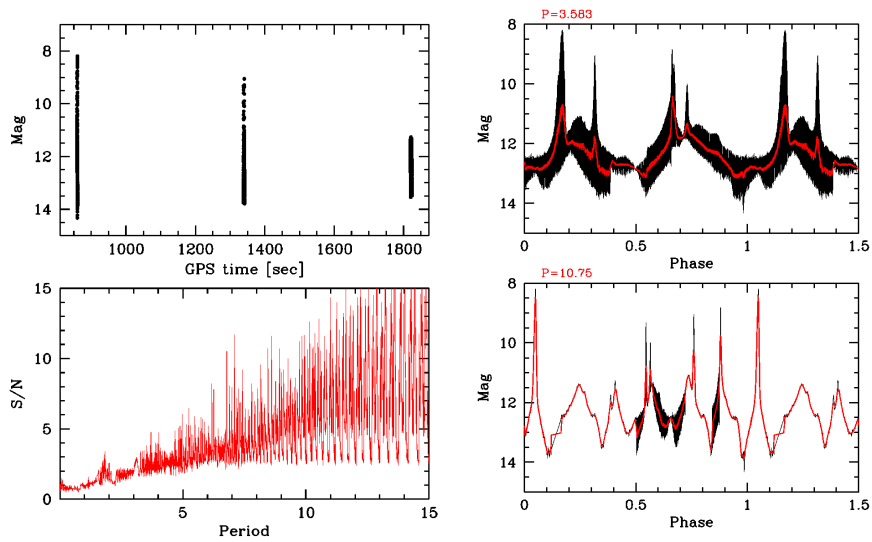


Figure 3.7: Filter V periodogram analysis of Molniya 1-88, November observations.

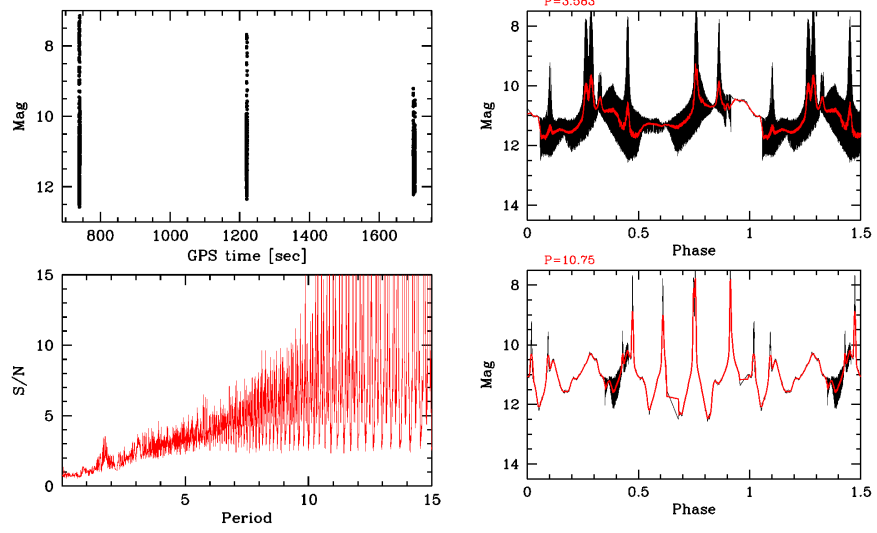


Figure 3.8: Filter I periodogram analysis of Molniya 1-88, November observations.

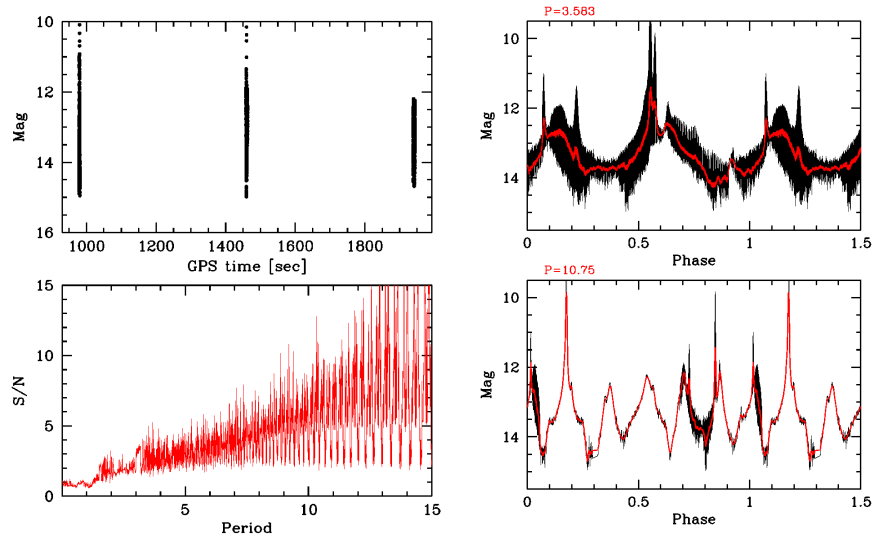


Figure 3.9: Filter B periodogram analysis of Molniya 1-88, November observations.

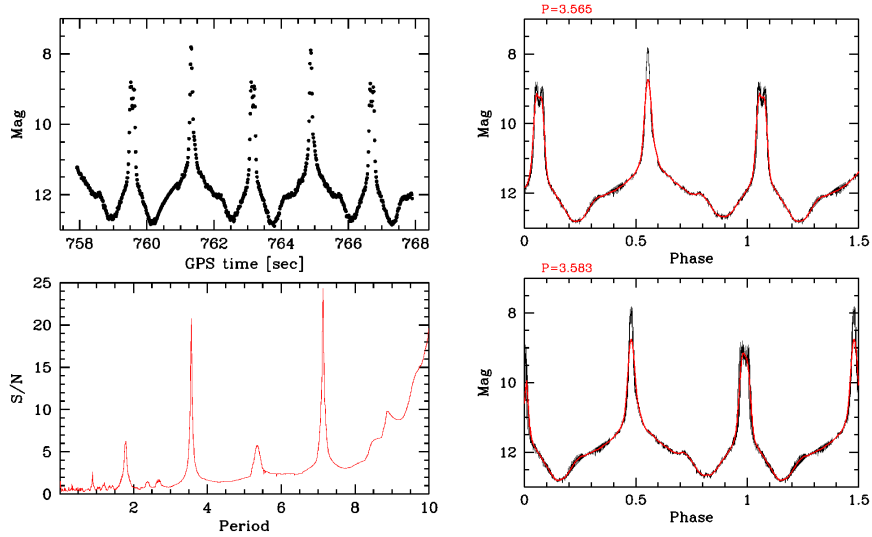


Figure 3.10: Filter R periodogram analysis of Molniya 1-88, September observations.

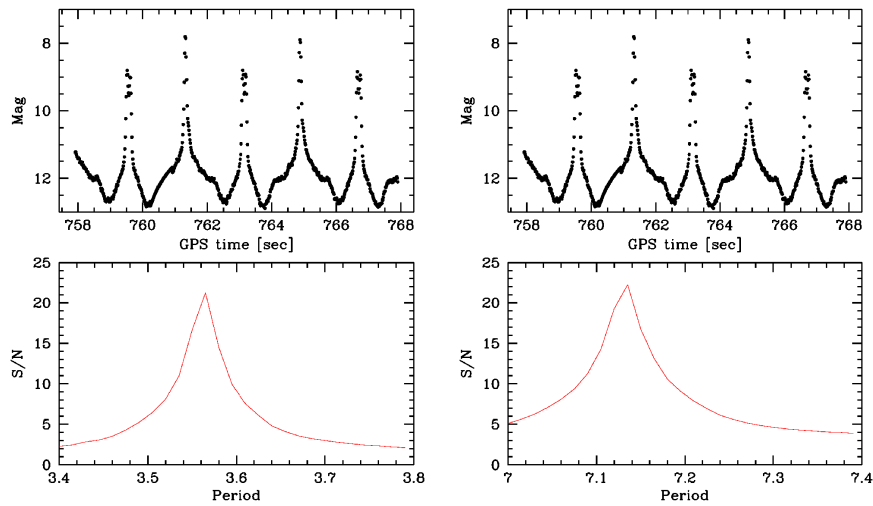


Figure 3.11: Zoom of filter R periodogram analysis of Molniya 1-88, September observations, in the regions of the two main peak at $P = 3.565$ s and $P = 7.13$ s.

3.3 Molniya 1-63

Day	UT(start)	Airm	Expt(s)	F	D(Km)	Mag	PA
2016-12-24	03:15:47	1.82	20	R	35966	10.916	41.34
2016-12-24	03:18:24	1.81	30	R	36178	10.773	41.23
2016-12-24	03:21:24	1.81	30	R	36385	10.721	41.06
2016-12-24	03:24:23	1.8	30	B	36587	11.949	40.9
2016-12-24	03:26:24	1.79	30	V	36718	11.161	40.8
2016-12-24	03:28:24	1.79	30	R	36848	10.724	40.7
2016-12-24	03:30:24	1.78	30	I	36848	9.924	40.61

Table 3.2: Molniya 1-63 data

With the periodogram analysis of December data we discover that Molniya 1-63 is rotating with a period $P = 4.10 \pm 0.13$ s, the periodogram results are plotted in Figure 3.12, Figure 3.13, Figure 3.14 and Figure 3.15. As can be seen the periodogram finds two main peaks near $P = 4$ s and $P = 8$ s, and two minor peaks at $P = 2$ s $P = 6$ s.

The precise value for each filter is plotted in Table 3.3, a zoom of the periodogram analysis (made tightening the sampling) is plotted in Figure 3.16. Again the fact that the second main peak is multiple of the first assure us that the rotational period is the smaller one. The minors peaks are due to the presence of two different type of flashes in the light curves, one of R magnitude ≈ 7.5 and the other of R magnitude ≈ 9.5 . This two peaks are due to the tubling of Molniya 1-63 and are emitted probably when the solar panels are in the right position to directly reflect the sunlight on the ground. The two flashes are emitted periodically separated by a 180 degrees rotation of the satellite, from which it's easy understand why the minor peak is positioned at the exact half of the period. In Figure 3.17 the fit with $P = 2.0395$ s is plotted, it's evident that the fit with this period value isn't good. The final value for the period has been obtained averaging on the four values found.

Filter	Period(s)	Error(s)
R	4.08	0.02
I	4.06	0.1
V	4.12	0.2
B	4.15	0.2

Table 3.3: Molniya 1-63 periods found with periodogram analysis

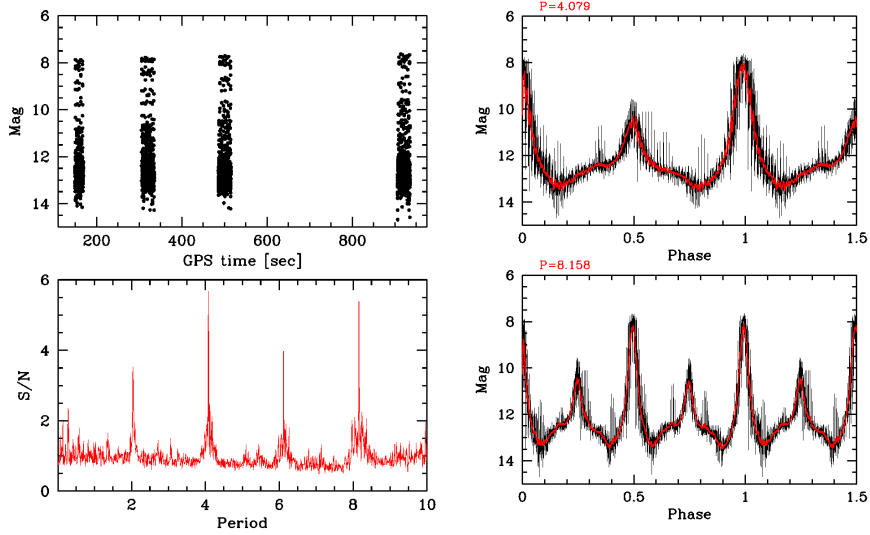


Figure 3.12: Filter R periodogram analysis of Molniya 1-63, December observations.

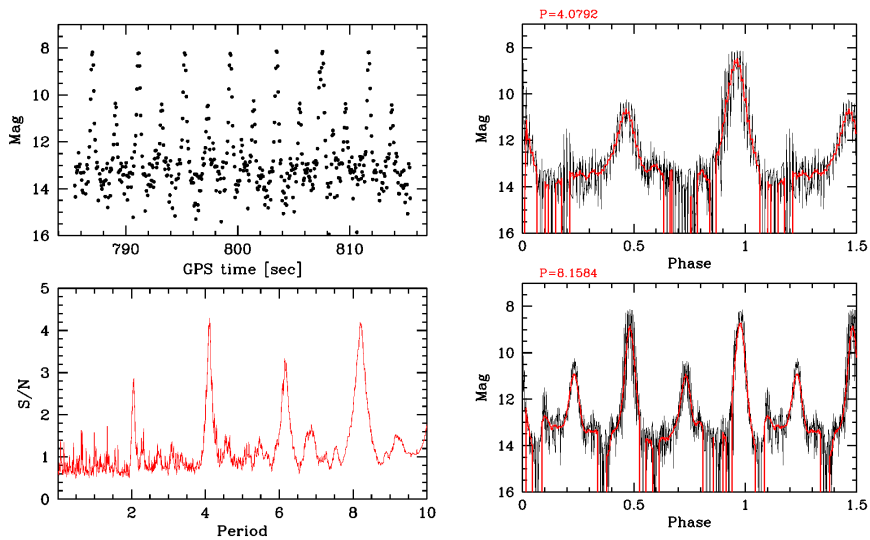


Figure 3.13: Filter V periodogram analysis of Molniya 1-63, December observations.

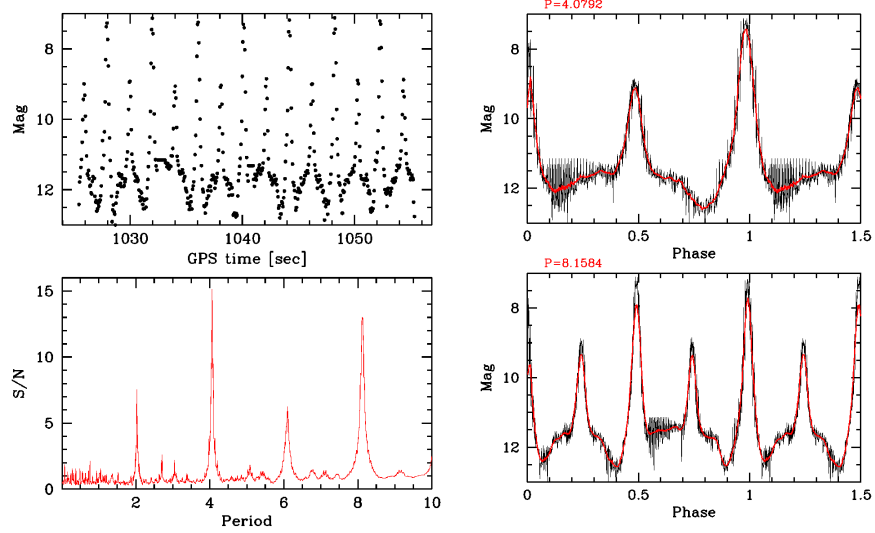


Figure 3.14: Filter I periodogram analysis of Molniya 1-63, December observations.

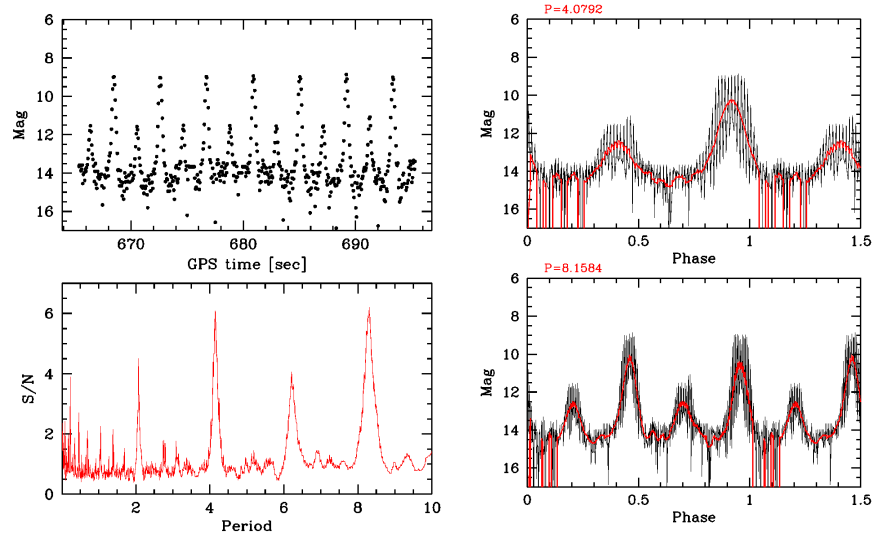


Figure 3.15: Filter B periodogram analysis of Molniya 1-63, December observations.

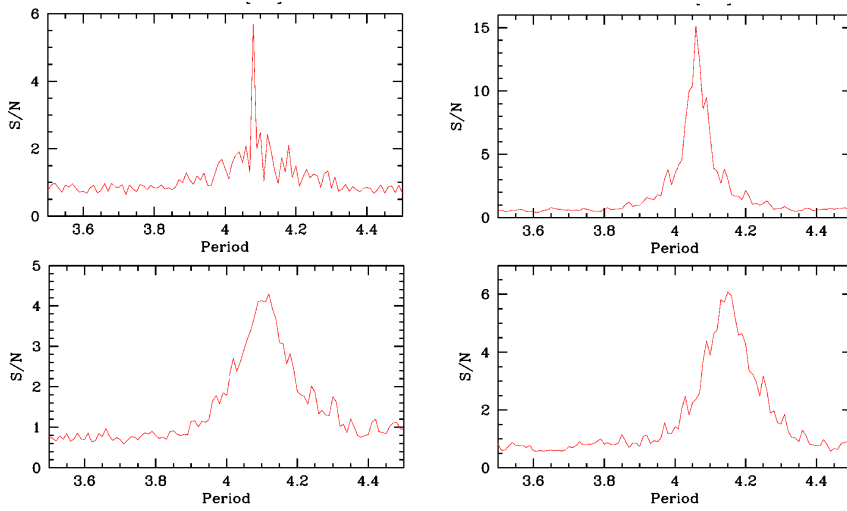


Figure 3.16: Zoom of periodogram analysis of Molniya 1-63 in filter R (top left), V (bottom left), I (top right) and B (bottom right).

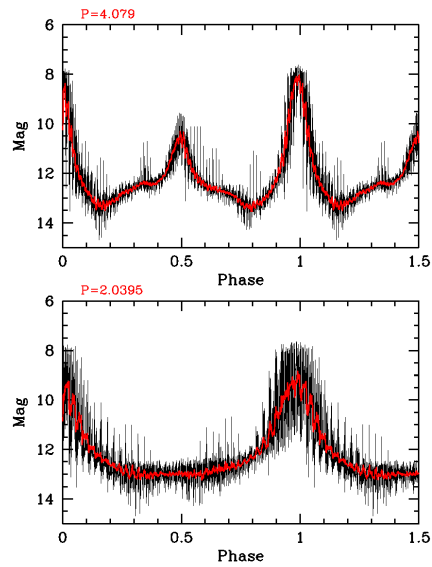


Figure 3.17: Fit of the LC of Molniya 1-63 with $P = 4.079$ s and $P = 2.0395$ s.

3.4 Molniya 3-3

Day	UT(start)	Airm	Expt(s)	F	D(Km)	Mag	PA
2016-12-31	01:26:58	1.57	10	R	25058	13.971	84.35
2016-12-31	01:34:54	1.53	15	R	26187	14.105	84.64
2016-12-31	01:38:53	1.51	15	R	26732	13.870	84.79
2016-12-31	01:41:54	1.5	20	R	27132	12.478	84.9
2016-12-31	01:44:51	1.49	30	R	27526	13.957	85.01
2016-12-31	01:48:51	1.48	30	B	28039	15.757	85.16
2016-12-31	01:51:51	1.47	30	V	28416	14.768	85.23
2016-12-31	01:54:51	1.46	30	R	28787	13.970	85.39
2016-12-31	01:56:51	1.45	30	I	29030	12.931	85.46
2016-12-31	01:58:51	1.45	30	B	29270	15.733	85.54
2016-12-31	02:00:51	1.44	30	V	29507	14.746	85.61
2016-12-31	02:02:50	1.43	30	R	29742	13.979	85.69
2016-12-31	02:04:52	1.43	30	I	29973	12.982	85.76
2016-12-31	02:06:51	1.42	30	B	30202	15.615	85.84
2016-12-31	02:08:52	1.42	30	V	30428	14.679	85.87
2016-12-31	02:10:52	1.42	30	R	30651	13.463	85.98
2016-12-31	02:12:51	1.41	30	I	30871	13.008	86.06

Table 3.4: Molniya 3-3 data

With the periodogram analysis of December data we discover that Molniya 3-3 is rotating with a period $P = 10.175 \pm 0.02$ s, the periodogram results are plotted in Figure 3.18, Figure 3.19, Figure 3.20 and Figure 3.21. The periodogram analysis finds two main peaks in filter R,V,I near $P = 10.2$ s and $P = 20.4$ s, while in filter B the peak near is found $P = 11.4$ s. The precise value of the period found in each filter and its error are plotted in Table 3.5. In Figure 3.22 a zoom of the periodogram analysis near the peaks in every filter is plotted. While the periods found in filter R,I,V are consistent, the period

Filter	Period(s)	Error(s)
R	10.173	0.01
I	10.177	0.025
V	10.175	0.025
B	11.143	0.05

Table 3.5: Molniya 3-3 periods found with periodogram analysis

found B is one second longer. This is due to the fact that filter B light curves had many negative value of the flux, that were replaced with a nominal value (0.01) to avoid the failure of the magnitude calibration. This ruse is efficient if the points with negative flux value are few but in this case where the points were many has caused the failure of the periodogram analysis. For this reason we decided to not consider filter B light curves. Averaging on the other filter we discover that Molniya 3-3 is rotating with period $P = 10.175 \pm 0.02$ s. Once

again the fact that the second peak is exactly the double of the first peak assure us that the correct period is the shorter, this can be checked also watching at the fit.

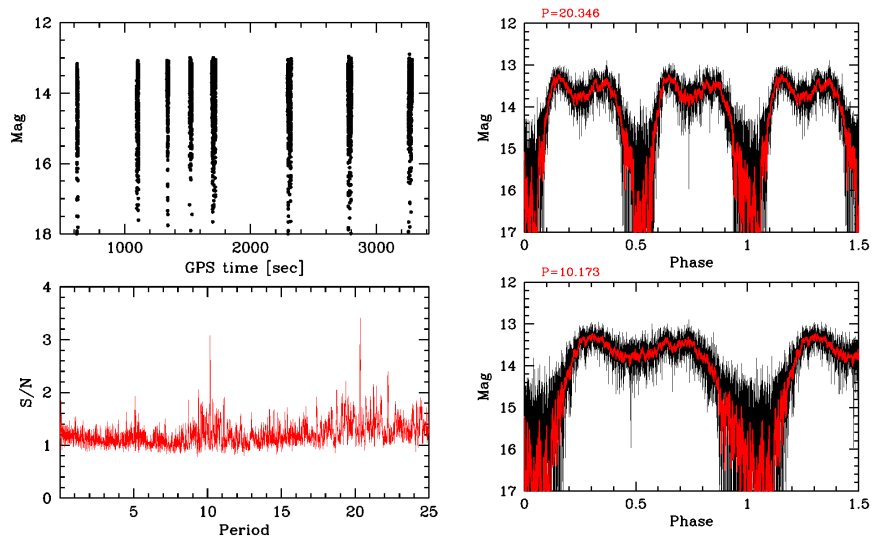


Figure 3.18: Filter R periodogram analysis of Molniya 3-3.

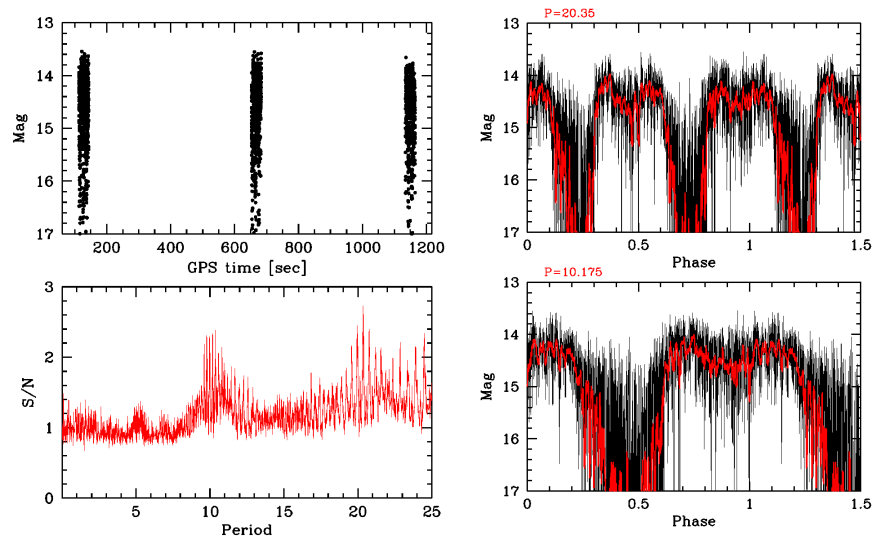


Figure 3.19: Filter V periodogram analysis of Molniya 3-3.

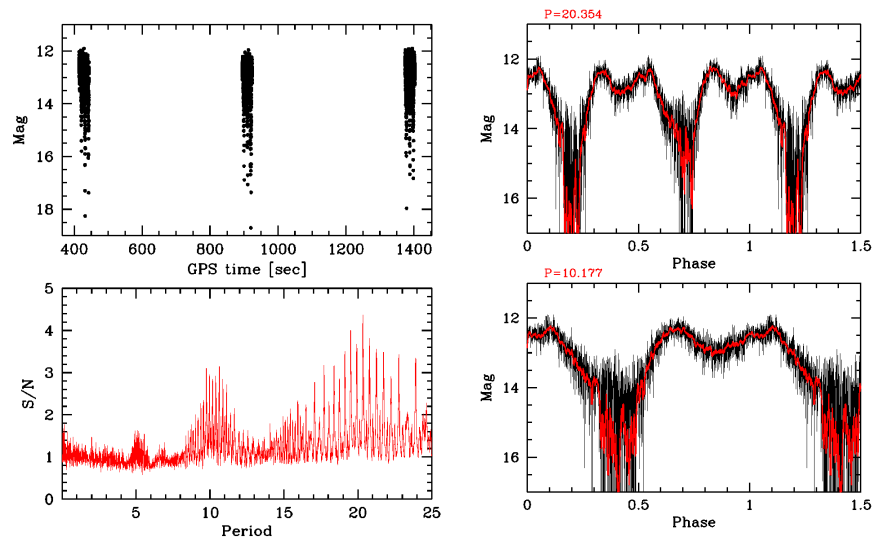


Figure 3.20: Filter I periodogram analysis of Molniya 3-3.

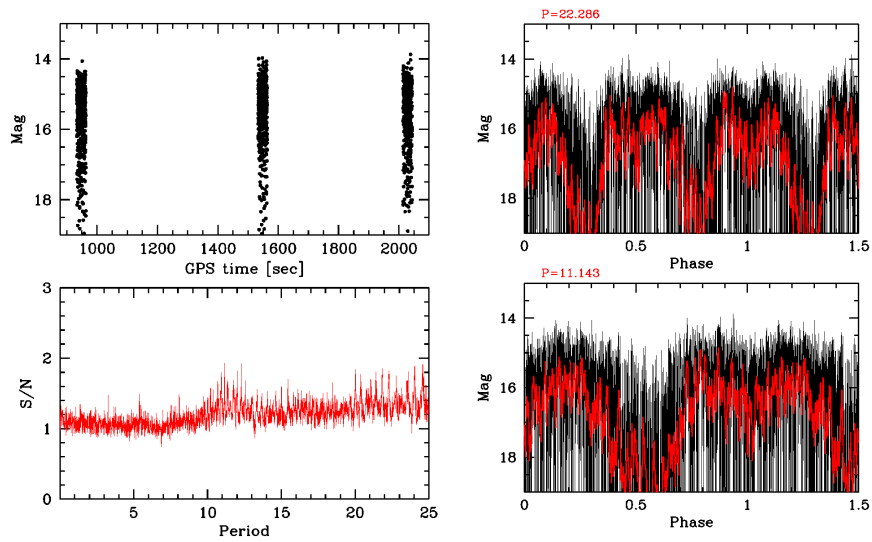


Figure 3.21: Filter B periodogram analysis of Molniya 3-3.

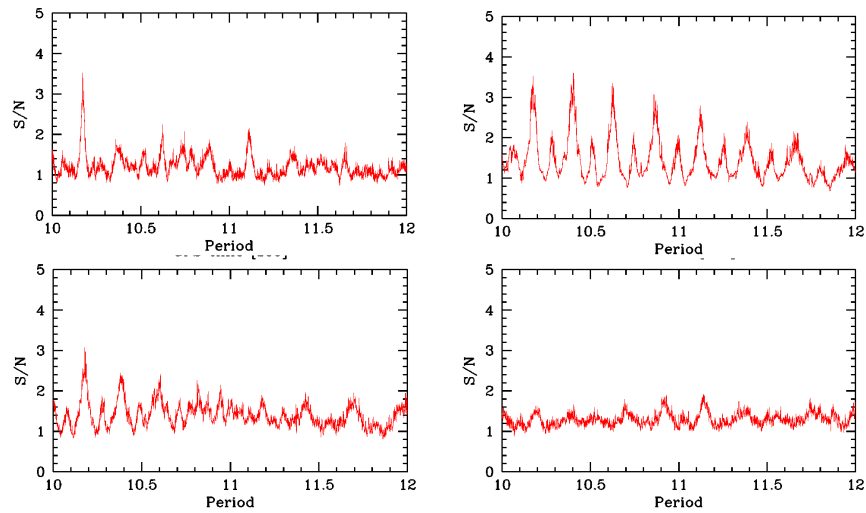


Figure 3.22: Zoom of periodogram analysis of Molniya 3-3 in filter R (top left), V (bottom left), I (top right) and B (bottom right)

3.5 Meridian 1

Day	UT(start)	Airm	Expt(s)	F	D(Km)	Mag	PA
2016-11-27	00:57:58	1.37	20	R	29983	10.771	70.3
2016-11-27	01:02:00	1.34	20	I	30362	10.104	70.37
2016-11-27	01:03:59	1.33	20	V	30548	11.461	70.44
2016-11-27	01:06:59	1.32	20	B	30822	12.411	70.51
2016-11-27	01:08:59	1.31	25	R	31002	10.789	70.56
2016-11-27	01:10:57	1.3	25	I	31180	10.106	70.62
2016-11-27	01:13:57	1.29	25	V	31443	11.448	70.69
2016-11-27	01:15:58	1.28	25	B	31616	12.516	70.75
2016-11-27	01:17:54	1.27	30	R	31786	10.794	70.8
2016-11-27	01:19:54	1.26	30	I	31955	10.133	70.86
2016-11-27	01:21:55	1.26	30	V	32121	11.362	70.92
2016-11-27	01:23:53	1.25	30	B	32285	12.481	70.98
2016-11-27	01:25:54	1.24	30	R	32446	10.780	71.03
2016-11-27	01:27:54	1.24	30	R	32606	10.839	71.09
2016-11-27	01:29:54	1.23	30	R	32764	10.849	71.15
2016-11-27	01:31:54	1.22	30	R	32919	10.868	71.21
2016-11-27	01:33:54	1.22	30	I	33073	10.188	71.27
2016-11-27	01:35:54	1.21	30	V	33224	11.578	71.34
2016-11-27	01:37:54	1.2	30	B	33373	12.549	71.4

Table 3.6: Meridian 1 data

With the periodogram analysis of the data we discover that Meridian 1 is rotating with a period $P = 30.18 \pm 0.2$ s, the periodogram results are plotted in Figure 3.23, Figure 3.24, Figure 3.25 and Figure 3.26. The periodogram finds two main peaks near $P = 30.18$ s and $P = 15.09$ s, in every filter. In the previous similar cases the correct period was the shorter, this is not true for Meridian 1. Watching the LC fit is clear that the correct period is that at $P = 30.18$ s. In Figure 3.27 is plotted the zoom of the periodograms (made again taightening the samples). As can be seen the peaks are all near $P = 30.18$ s but some little shift are present. Anyway the magnitude of the shift are smaller than the errors so we can say that the analysis in all filters confirm that Meridian 1 is rotating with period $P = 30.18$ s. The fact that the exposition times of the exposures are for the most part thirty seconds and the period has a value near thirty senconds made us think of a possible alias effect, so we check if the periodogram finds the peak near thirty seconds even using only the first the sencond and the third R filter exposure, which have exptime respectively 20, 25 and 30 s. The result of this check is plotted in figure 3.28, as you can see the peak is found also in this analysis even if the periodogram result is more noisy and the fit reamins also good, this assure us the effectivness of our results.

Filter	Period(s)	Error(s)
R	30.18	0.2
I	30.17	0.2
V	30.18	0.2
B	30.175	0.2

Table 3.7: Meridian 1 periods found with periodogram analysis

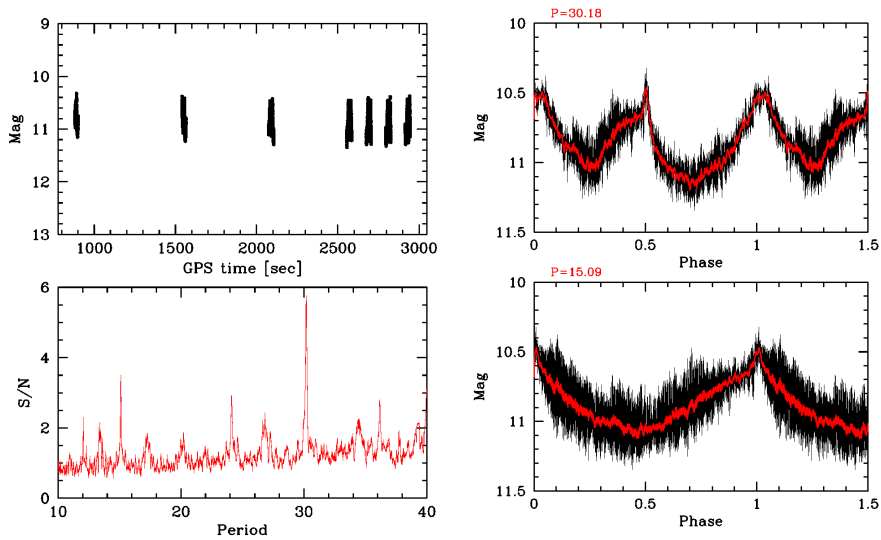


Figure 3.23: Filter R periodogram analysis of Meridian 1.

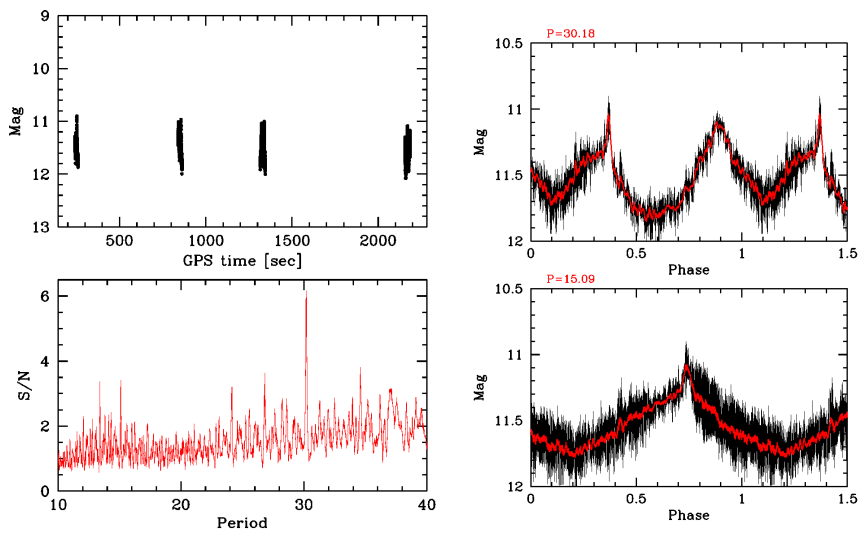


Figure 3.24: Filter V periodogram analysis of Meridian 1.

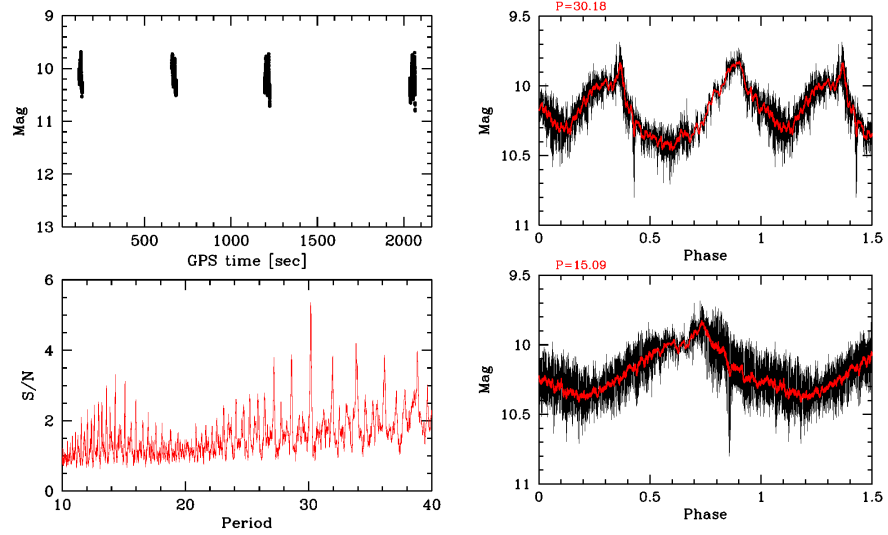


Figure 3.25: Filter I periodogram analysis of Meridian 1.

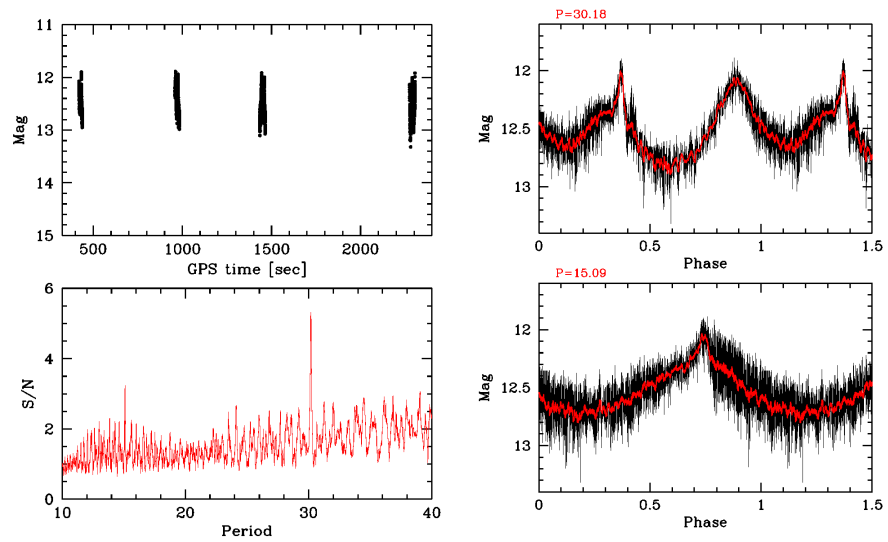


Figure 3.26: Filter B periodogram analysis of Meridian 1.

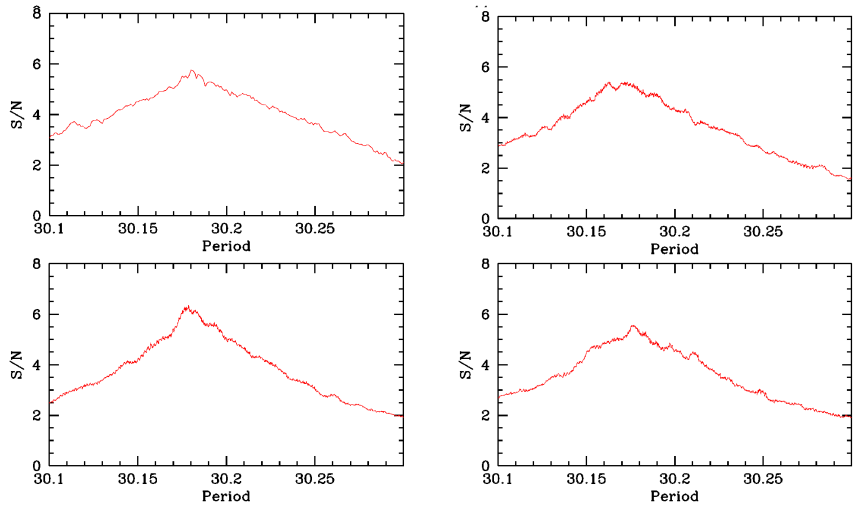


Figure 3.27: Zoom of periodogram analysis in filter R (top left), I (top right), V (bottom left), B (bottom right).

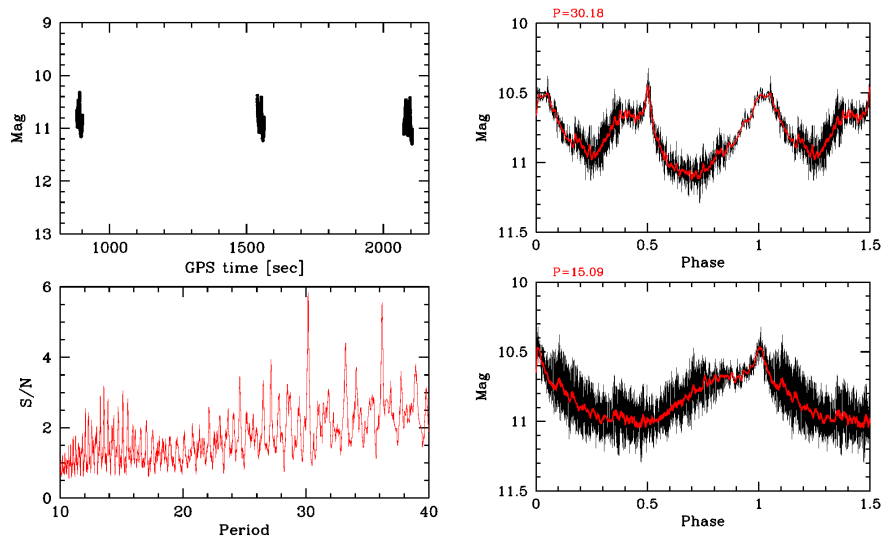


Figure 3.28: Filter R periodogram analysis check made using only the first tree R filter exposures

3.6 Molniya 2-10

With the periodogram analysis of the data we discover that Molniya 2-10 is rotating with a period $P = 41.255 \pm 0.15$ s, the periodogram results are plotted in Figure 3.29, Figure 3.30, Figure 3.31 and Figure 3.32. The periodogram analysis in all filter shows a peak of the signal-to-noise near $P = 41.2$ s, while in R filter the presece of the peak is clear in the other filters the peak is surrounded by others peaks. The noisness of the periodogram analysis in filter V,I and B is due to the high value of the period combined with the scarce samples of the light curves. Anyway the peck near $P = 41.2$ is found in all filters. In Table 3.8 the exact value of the period with the error for each filter is plotted. The final value of the period for Molniya 2-10 has been found averaging on these four values and is $P = 41.255 \pm 0.15$ s.

Filter	Period(s)	Error(s)
R	41.27	0.2
I	41.25	0.15
V	41.26	0.1
B	41.23	0.15

Table 3.8: Molniya 2-10 periods found with periodogram analysis

Day	UT(start)	Airm	Expt(s)	F	D(Km)	Mag	PA
2016-11-26	21:36:19	1.06	20	R	22918	12.225	47.89
2016-11-26	21:39:19	1.06	20	I	23390	11.800	47.61
2016-11-26	21:43:19	1.06	20	V	24006	13.474	47.27
2016-11-26	21:45:20	1.06	20	B	24308	13.987	47.12
2016-11-26	21:47:21	1.07	20	R	24606	12.570	46.97
2016-11-26	21:49:19	1.07	20	I	24900	12.275	46.83
2016-11-26	21:51:19	1.07	20	V	25191	12.989	46.7
2016-11-26	21:55:19	1.07	20	B	25761	14.761	46.47
2016-11-26	21:58:22	1.07	20	R	26179	13.026	46.3
2016-11-26	22:01:19	1.07	30	R	26589	13.022	46.16
2016-11-26	22:05:19	1.07	30	R	27123	12.759	45.98
2016-11-26	22:08:21	1.07	40	R	27515	12.918	45.86
2016-11-26	22:12:19	1.07	40	I	28025	11.618	45.71
2016-11-26	22:15:19	1.07	40	V	28399	13.589	45.61
2016-11-26	22:31:44	1.08	40	B	30380	14.763	45.2

Table 3.9: Molniya 2-10 data

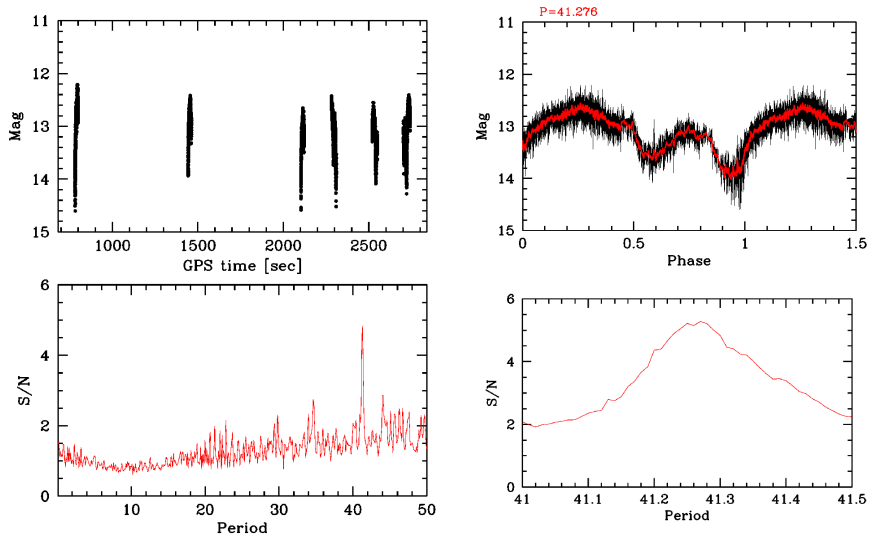


Figure 3.29: Filter R periodogram analysis of Molniya 2-10.

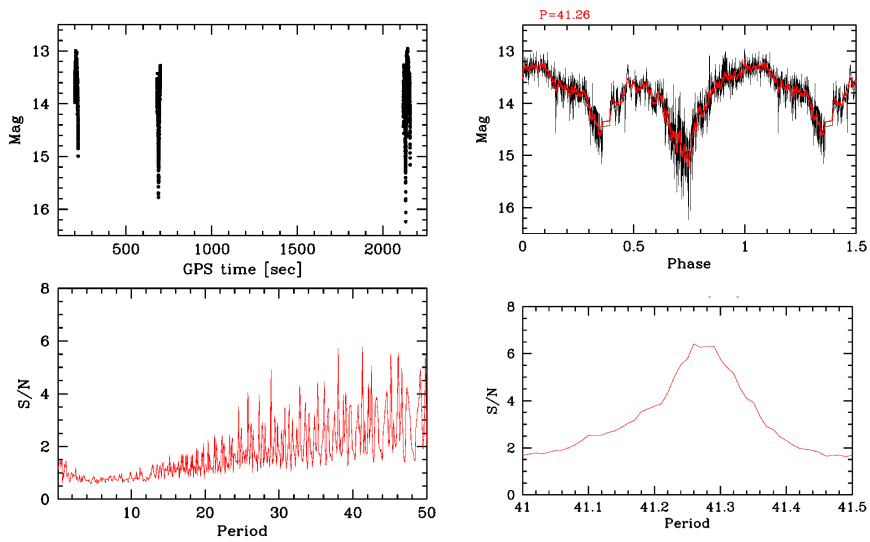


Figure 3.30: Filter V periodogram analysis of Molniya 2-10.

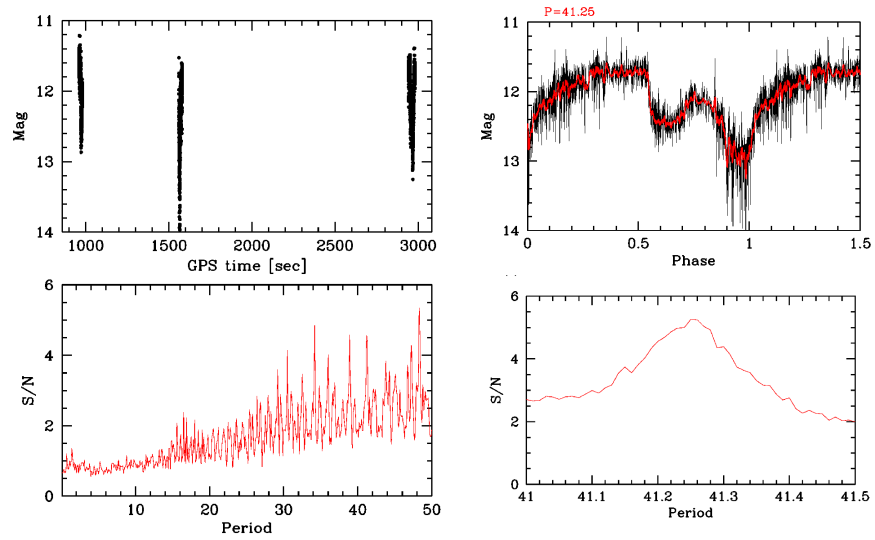


Figure 3.31: Filter I periodogram analysis of Molniya 2-10.

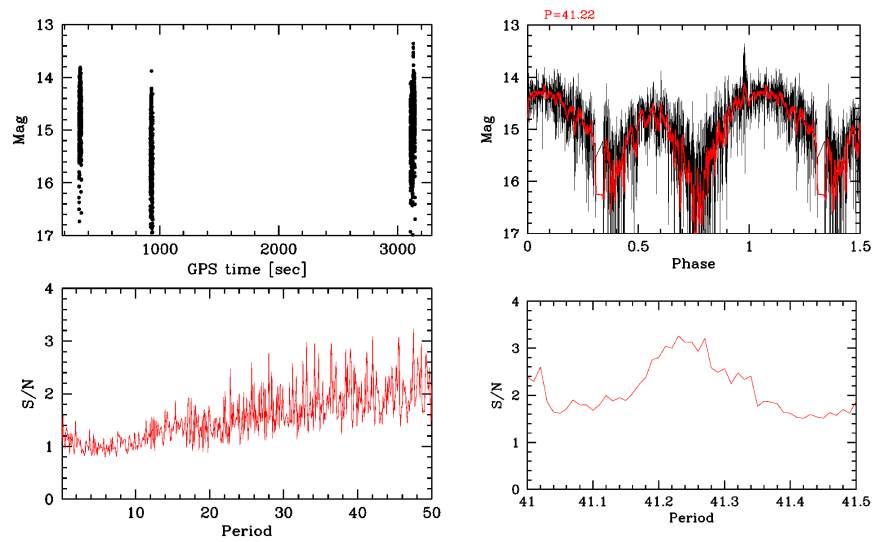


Figure 3.32: Filter B periodogram analysis of Molniya 2-10.

3.7 Molniya 3-42

With the periodogram analysis of the data we discover that Molniya 3-42 is rotating with a period $P = 4.807 \pm 0.002$ s, the periodogram results are plotted in Figure 3.33, Figure 3.34, Figure 3.35 and Figure 3.36. The peak in the signal-to-noise ratio is present in every filter with suprising precision, the exact position of the four peaks is shown in Table 3.10. We can conclude that the correct period is $P = 4.807 \pm 0.002$ s. In Figure 3.37 a zoom of the periodograms analysis near the peak is plotted.

Filter	Period(s)	Error(s)
R	4.807	0.002
I	4.807	0.002
V	4.807	0.002
B	4.806	0.004

Table 3.10: Molniya 3-42 periods found with periodogram analysis

Day	UT(start)	Airm	Expt(s)	F	D(Km)	Mag	PA
2016-11-27	02:06:58	1.28	3	R	10441	12.852	74.58
2016-11-27	02:08:58	1.25	3	R	10814	12.786	74.82
2016-11-27	02:11:58	1.22	3	R	11386	12.794	75.27
2016-11-27	02:13:59	1.2	3	I	11774	11.871	75.6
2016-11-27	02:15:58	1.19	3	V	12166	13.770	75.95
2016-11-27	02:17:59	1.18	4	B	12559	14.461	76.32
2016-11-27	02:19:58	1.17	5	R	12954	13.074	76.69
2016-11-27	02:21:59	1.17	5	I	13349	12.108	77.07
2016-11-27	02:23:59	1.16	5	V	13743	13.625	77.46
2016-11-27	02:25:59	1.16	5	B	14136	14.644	77.84
2016-11-27	02:27:59	1.16	7	R	14527	12.965	78.22
2016-11-27	02:29:58	1.16	7	I	14916	12.197	78.59
2016-11-27	02:31:58	1.16	8	V	15302	13.762	78.96
2016-11-27	02:33:58	1.16	8	B	15686	14.348	79.33
2016-11-27	02:35:58	1.16	10	R	16066	12.856	79.69
2016-11-27	02:37:58	1.16	10	I	16443	12.116	80.05
2016-11-27	02:39:58	1.16	10	V	16816	13.577	80.4
2016-11-27	02:43:59	1.17	10	B	17552	14.404	81.07
2016-11-27	02:46:05	1.17	10	R	17915	12.850	81.4
2016-11-27	02:50:05	1.17	10	I	18627	12.115	82.04
2016-11-27	02:52:03	1.18	12	V	18978	13.454	82.35
2016-11-27	02:54:03	1.18	12	B	19324	14.295	82.66
2016-11-27	02:56:03	1.18	14	R	19667	12.827	82.96

Table 3.11: Molniya 3-42 data

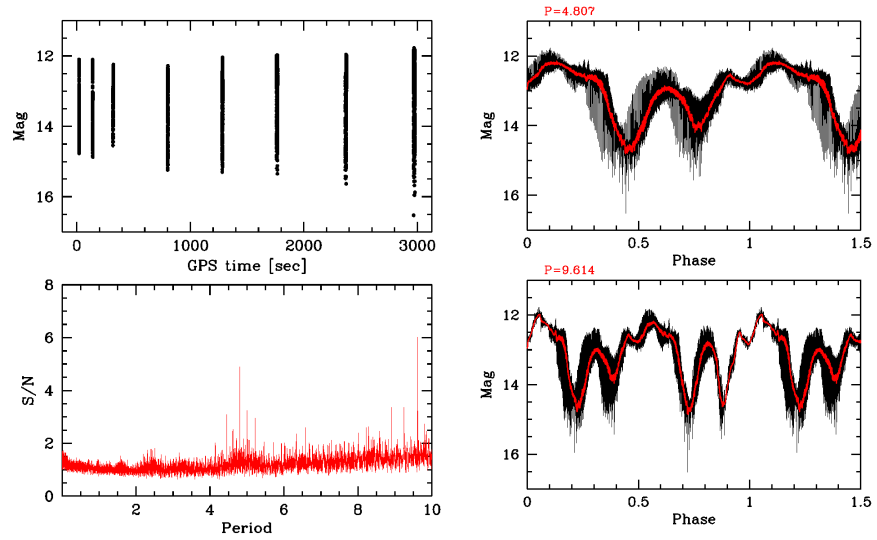


Figure 3.33: Filter R periodogram analysis of Molniya 3-42.

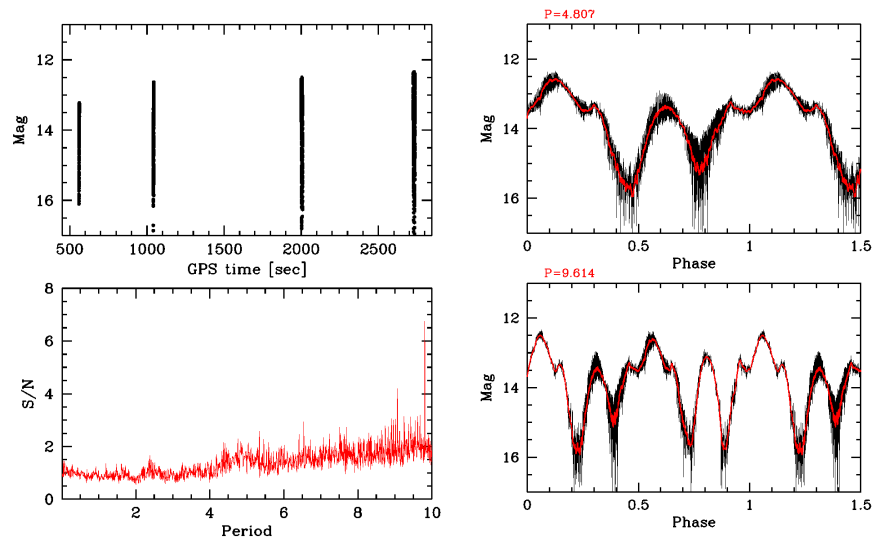


Figure 3.34: Filter V periodogram analysis of Molniya 3-42.

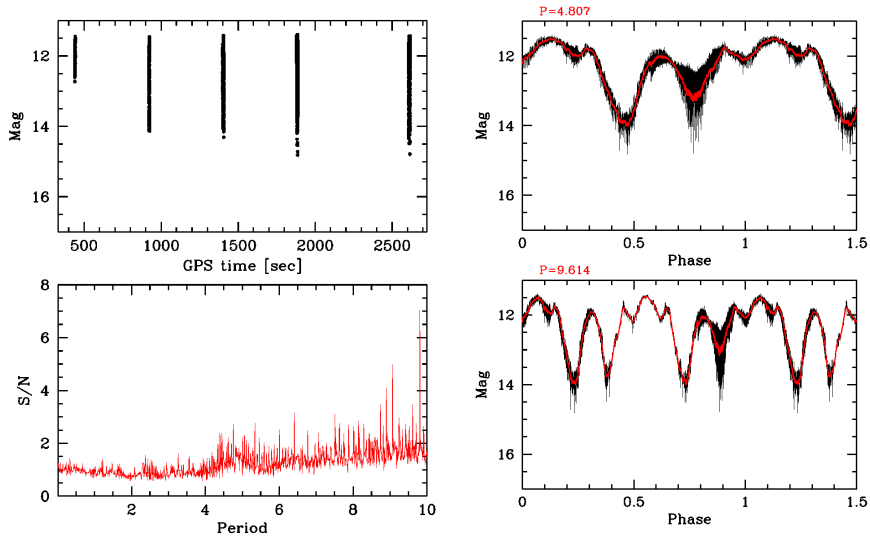


Figure 3.35: Filter I periodogram analysis of Molniya 3-42.

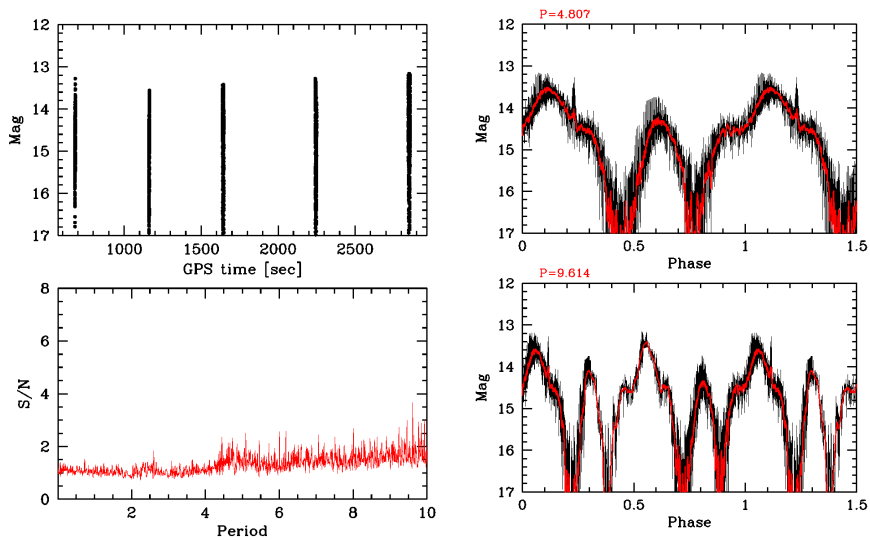


Figure 3.36: Filter B periodogram analysis of Molniya 3-42.

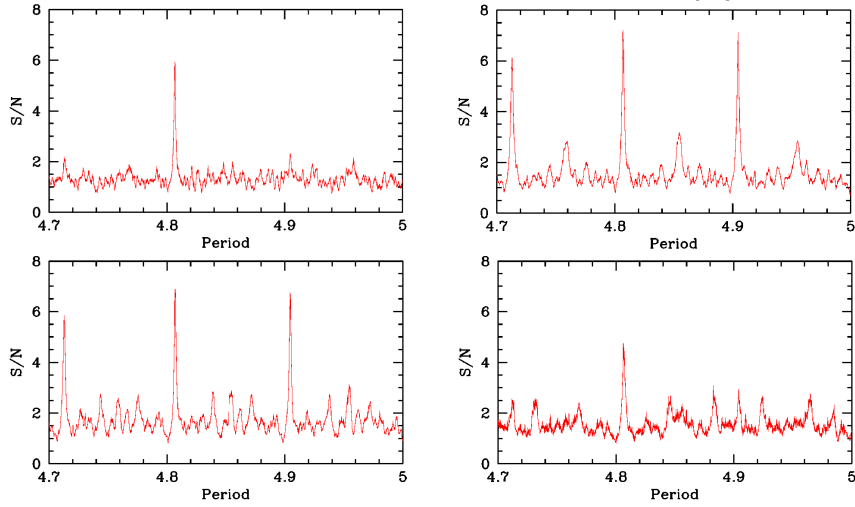


Figure 3.37: Zoom of periodogram analysis in filter R (top left), I (top right), V (bottom left), B (bottom right).

3.8 Molniya 1-53

Day	UT(start)	Airm	Expt(s)	F	D(Km)	Mag	PA
2016-12-23	02:48:57	1.35	10	R	29559	13.762	89.88
2016-12-23	02:50:57	1.35	20	R	29777	13.936	89.9
2016-12-23	02:52:54	1.34	30	R	29992	13.911	89.91
2016-12-23	02:55:53	1.34	30	R	30310	13.898	89.93
2016-12-23	02:57:54	1.33	30	B	30519	15.453	89.94
2016-12-23	02:59:54	1.33	30	V	30725	14.708	89.95
2016-12-23	03:01:54	1.32	30	R	30929	13.854	89.97
2016-12-23	03:03:54	1.32	30	I	31130	12.110	89.98
2016-12-23	03:05:54	1.32	30	B	31329	14.776	89.99
2016-12-23	03:07:54	1.31	30	V	31525	14.622	90.01
2016-12-23	03:09:54	1.31	30	R	31718	13.989	90.03
2016-12-23	03:11:54	1.3	30	I	31909	12.946	90.04

Table 3.12: Molniya 1-53 data

With the periodogram analysis of the data we discover that Molniya 1-53 is rotating with a period $P = 12.68 \pm 0.1$ s, the periodogram results are plotted in Figure 3.38, Figure 3.39, Figure 3.40 and Figure 3.41. The periodogram in R filter present two main peaks at $P = 12.68$ s and $P = 25.36$ s, while periodogram in filter I and V finds other peaks near the peaks found in R. This peaks have signal-to-noise ratio similar to that at $P = 12.68$ s, and are alias. The alias phenomenon is evident in filter I where there's alias at the first order near the peak at $P = 12.7$ and at the second order near $P = 25$ s. The filter B also finds a peak at $P = 12.68$ s but with a very low signal-to-noise ratio, probably because of the noisiness of the light curves and the problem with negative fluxes.

Anyway the fit is good in all filters with $P = 12.68$ s while the fits in filter R with other values of the period found with the filter I and V alias peaks aren't good (Figure 3.43). The exact position of the peaks in different filter is plotted in Table 3.13. In Figure 3.42 a zoom of the periodogram analysis is plotted. Once again filter R is the most reliable thanks to the greater sampling of the light curve, so we conclude that the satellite is rotating with period $P = 12.68 \pm 0.1$ s.

Filter	Period(s)	Error(s)
R	12.68	0.1
I	12.67	0.1
V	12.675	0.2
B	12.67	0.05

Table 3.13: Molniya 1-53 periods found with periodogram analysis

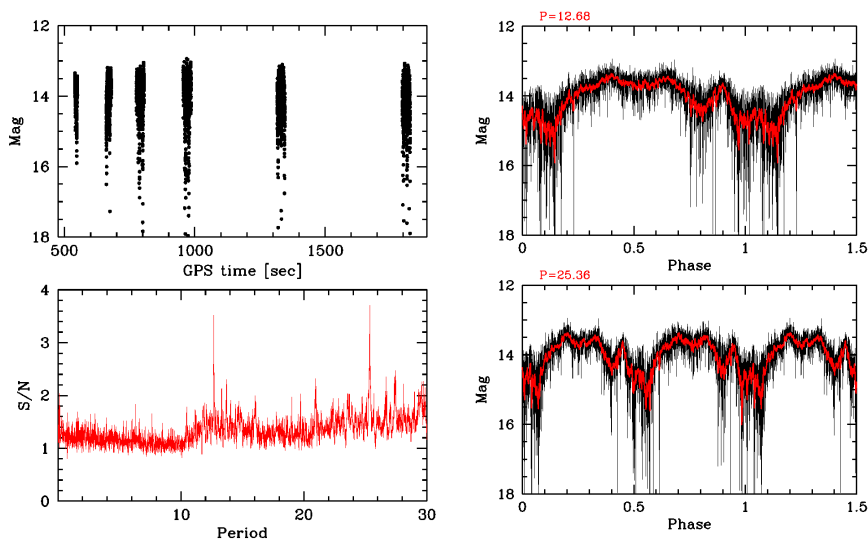


Figure 3.38: Filter R periodogram analysis of Molniya 1-53.

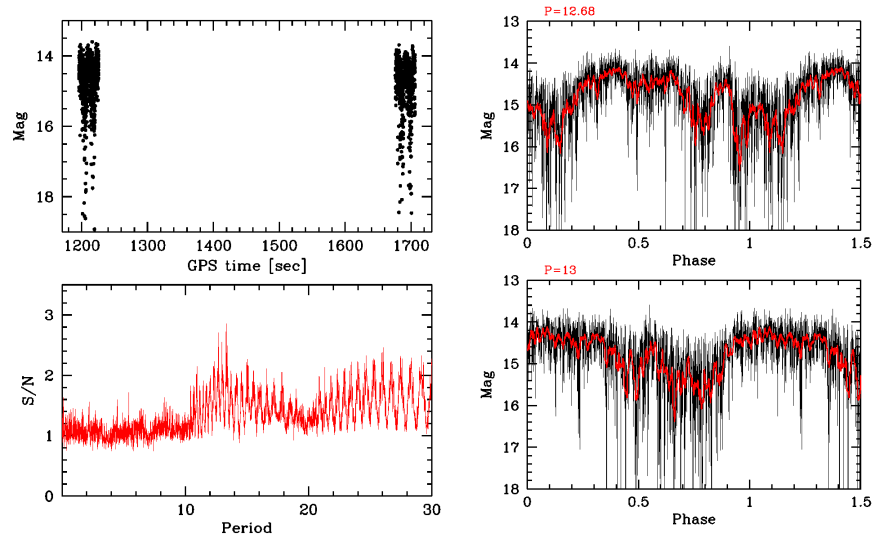


Figure 3.39: Filter V periodogram analysis of Molniya 1-53.

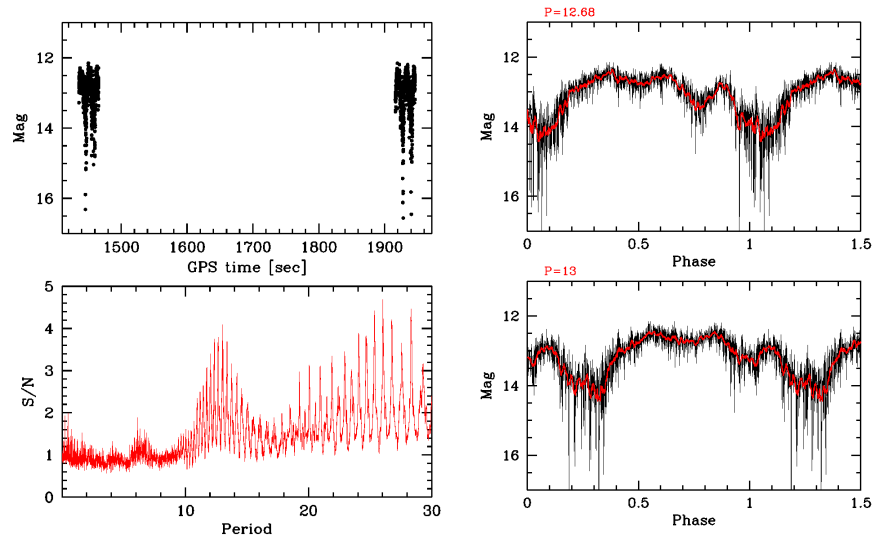


Figure 3.40: Filter I periodogram analysis of Molniya 1-53.

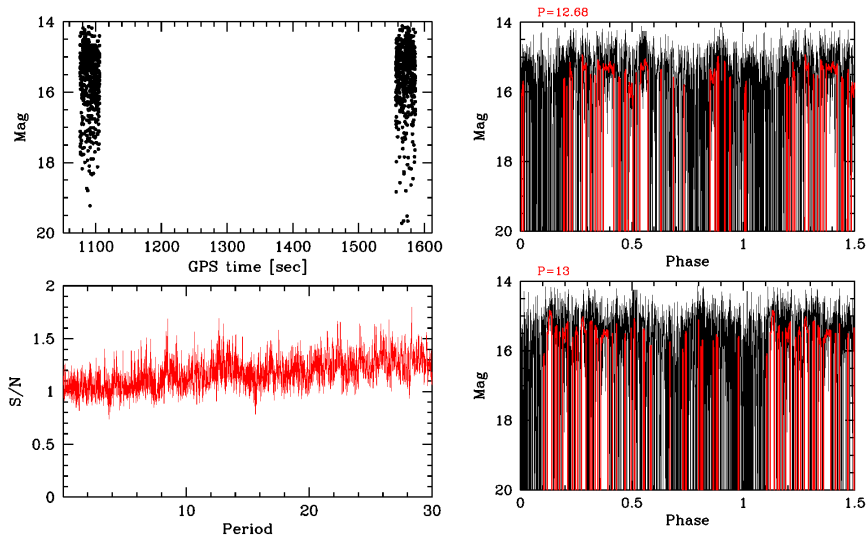


Figure 3.41: Filter B periodogram analysis of Molniya 1-53.

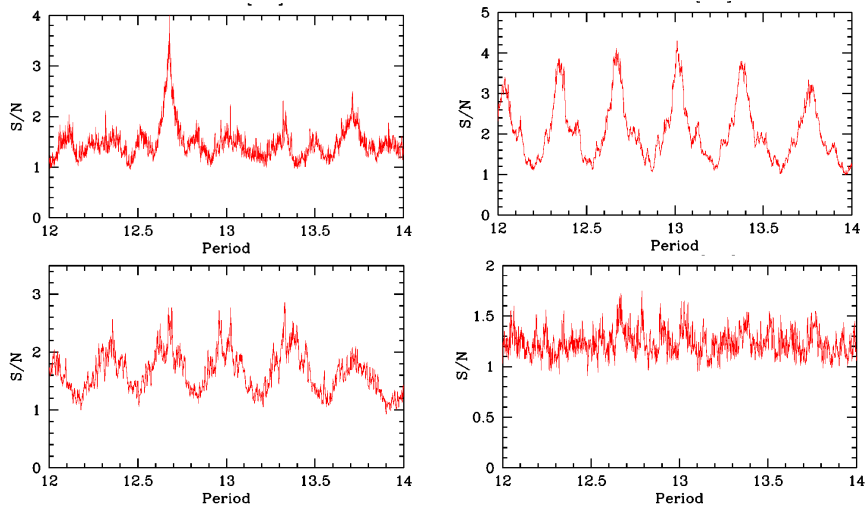


Figure 3.42: Zoom of periodogram analysis of Molniya 1-53 in filter R (top left), V (bottom left), I (top right) and B (bottom right), night 02-03.

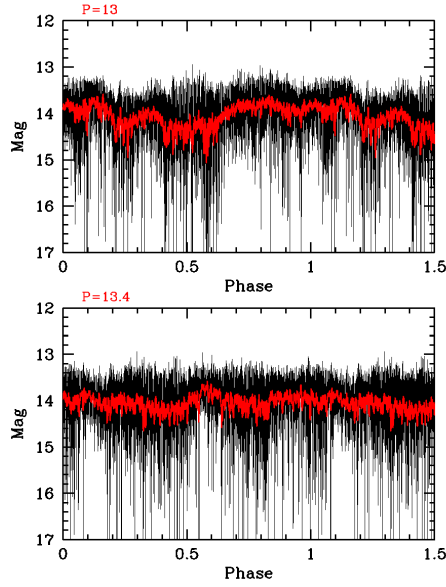


Figure 3.43: Molniya 1-53 filter R LC fit with $P = 13$ s and $P = 13.4$ s.

3.9 Molniya 1-69

Day	UT(start)	Airm	Expt(s)	F	D(Km)	Mag	PA
2016-11-27	03:36:58	1.15	20	R	33067	12.499	44.39
2016-11-27	03:39:59	1.15	20	I	33317	11.252	44.88
2016-11-27	03:42:59	1.15	20	V	33562	13.266	45.37
2016-11-27	03:45:49	1.15	30	B	33801	14.111	45.84
2016-11-27	03:48:39	1.15	40	R	34035	12.106	46.32
2016-11-27	03:51:39	1.15	40	I	34263	11.831	46.78
2016-11-27	03:54:37	1.15	40	V	34485	13.687	47.23
2016-11-27	03:57:42	1.15	40	B	34703	12.974	47.68

Table 3.14: Molniya 1-69 data

The analysis with periodogram of the Molniya 1-69 has revealed more complicated than expected. Indeed the R periodogram shows a clear peak at $P = 32.52 \pm 0.1$ s surrounded by other peaks with smaller signal-to-noise ratio that provides a good fit of the LC (Figure 3.44). The peak is found also by the periodogram in filter V, and the fit is also good (Figure 3.45). Filter I instead finds a clear peak at $P = 24.26 \pm 0.1$ s with a good fit, while the fit with the former value of the period is worst (Figure 3.46). Periodogram in filter B has no clear peaks and the fit isn't good with both the values found with other filters (Figure 3.47). Watching at the light curves (Figure A.140, A.141, A.142, A.143 in Section A.5) we deduced that the period has to be longer. As you can see the light curves show two different maxima, that assure that the period must be longer than 40 s, the periodogram in all filters except filter B show a peak

in the signal-to-noise ratio near $P = 65$ s (Figure 3.48, Figure 3.49), twice the value found in R and V filter analysis. These peaks seem to be an alias but the fit is good and especially shows the two different maxima. This makes us tend to believe that the correct period for Molniya-1-69 is $P = 65 \pm 0.5$ s. We try also a combined analysis with all the filter correcting the magnitudes with a constant to bring them all to the same level, to check if the period $P = 65$ s was correct, but the result was not satisfactory so we decided not to show it. The difficulty of periodogram analysis in providing the rotational period is due to the poor sampling of the Light Curve (we have only two exposures for every filter).

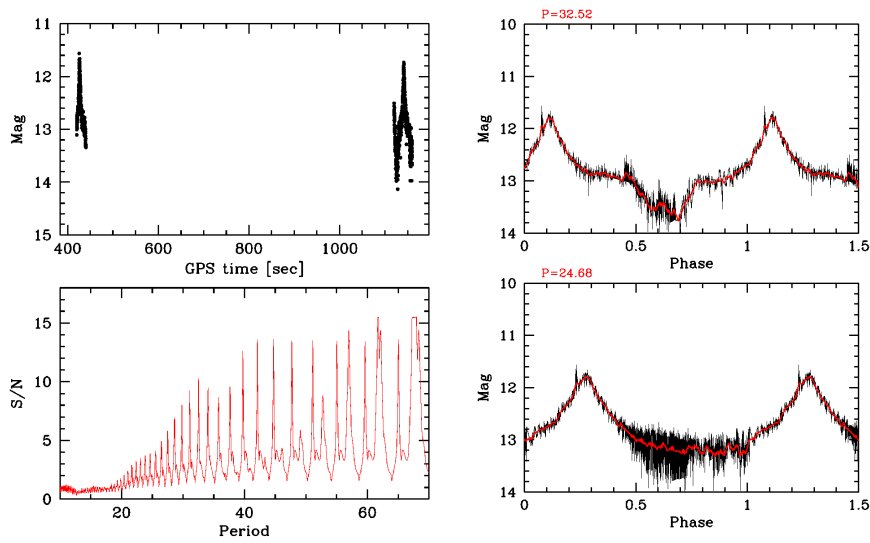


Figure 3.44: Filter R periodogram analysis of Molniya 1-69.

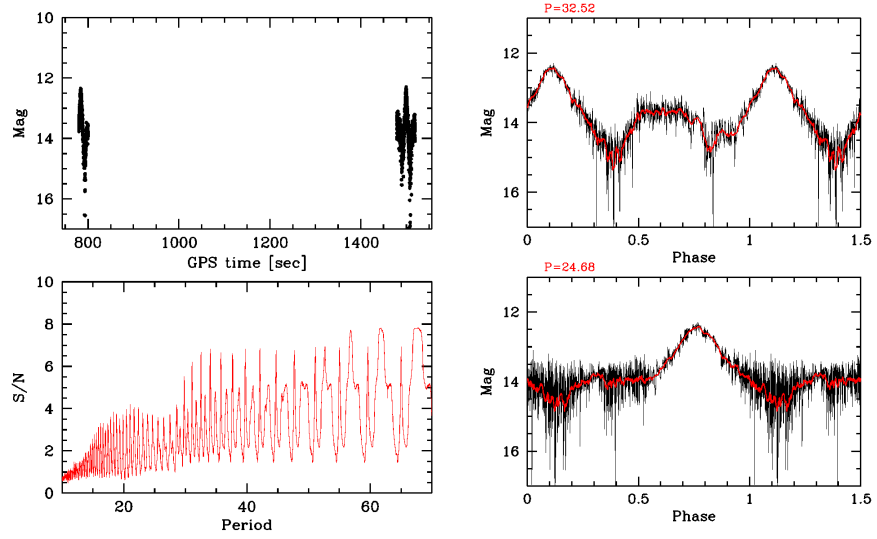


Figure 3.45: Filter V periodogram analysis of Molniya 1-69.

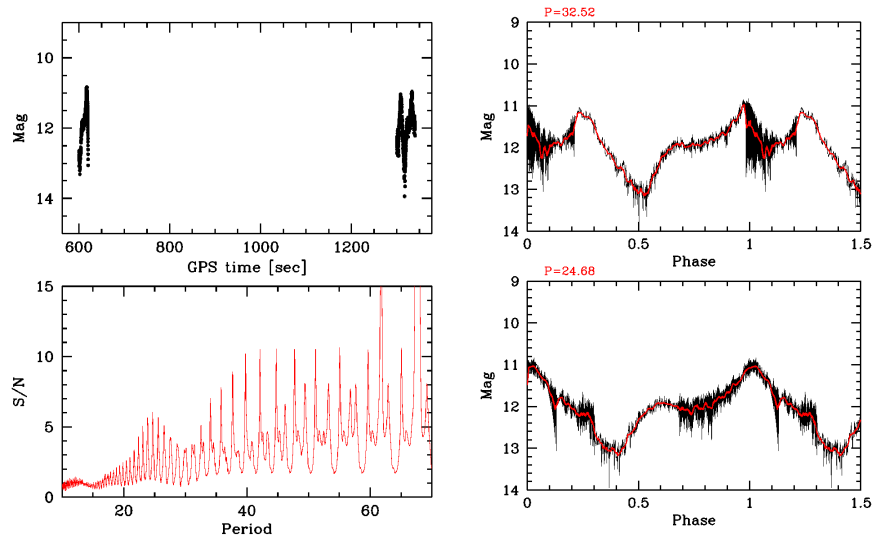


Figure 3.46: Filter I periodogram analysis of Molniya 1-69.

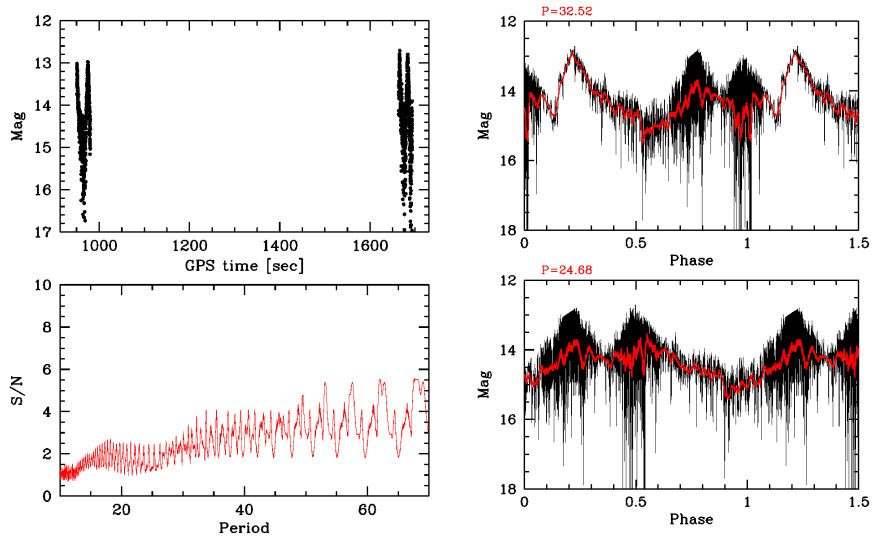


Figure 3.47: Filter B periodogram analysis of Molniya 1-69.

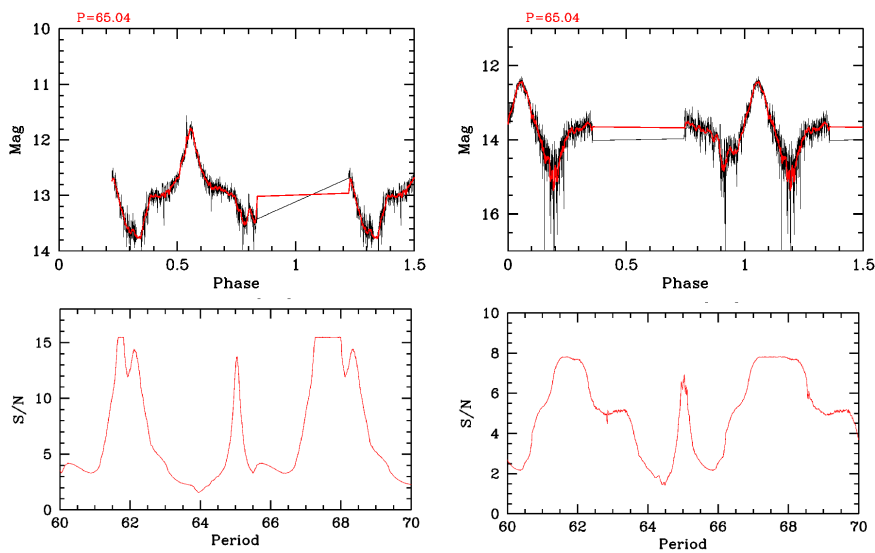


Figure 3.48: Filter R (left) and V (right) periodogram analysis of Molniya 1-69.

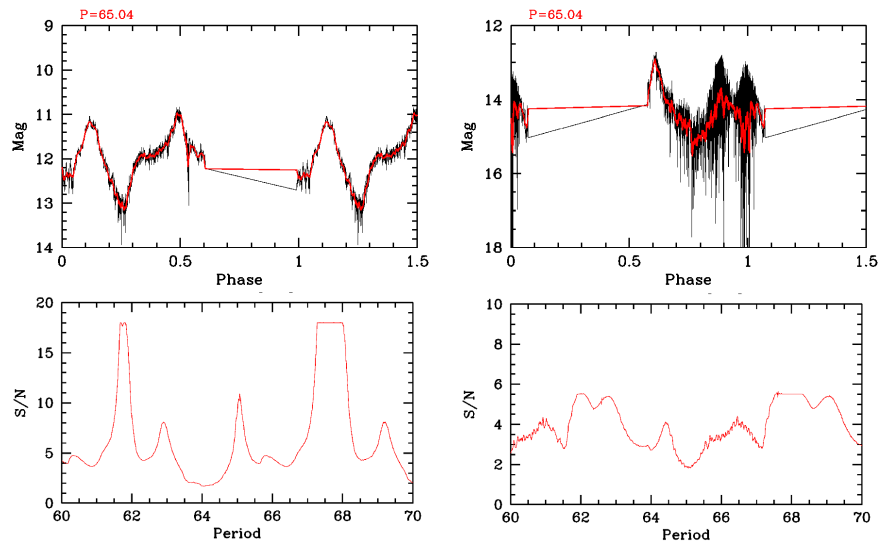


Figure 3.49: Filter I (left) and B (right) periodogram analysis of Molniya 1-69.

3.10 Molniya 3-8

Day	UT(start)	Airm	Expt(s)	F	D(Km)	Mag	PA
2016-12-23	06:31:54 PM	20	1.54	R	22938	12.483	17.55
2016-12-23	06:37:54 PM	20	1.58	B	22006	14.063	15.44

Table 3.15: Molniya 3-8 data

With the periodogram analysis of the data we discover that Molniya 3-8 is rotating with a period $P = 14.36 \pm 1$ s, the periodogram results are plotted in Figure 3.50. The error is 1 s in both filters, this is due to the fact that only two exposition of Molniya 3-8 were taken so there isn't sufficient statistics to get more precision.

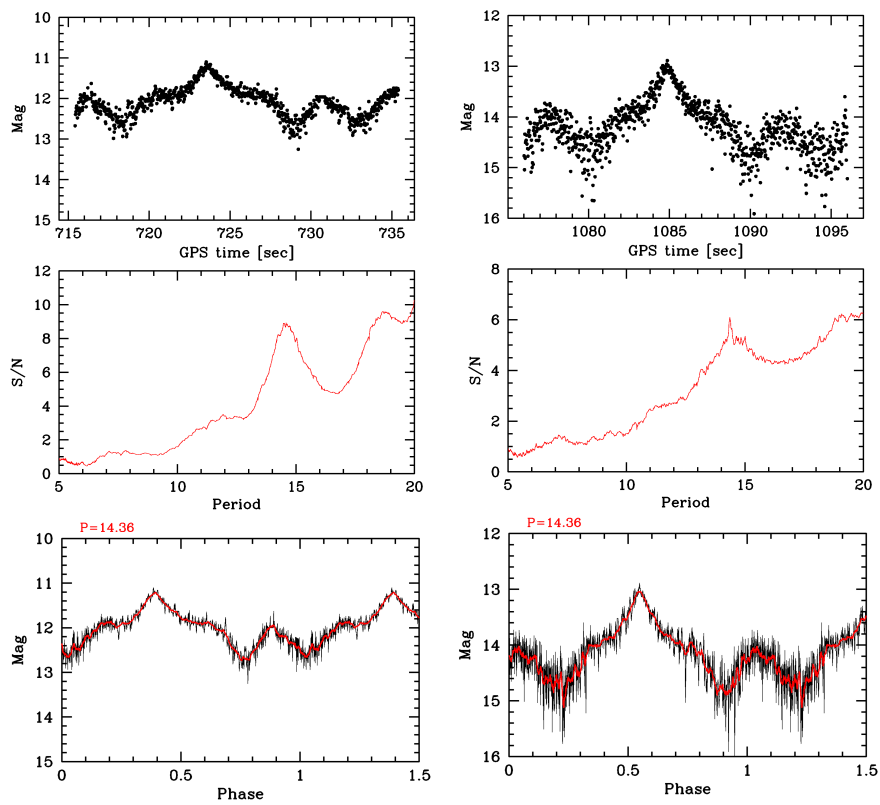


Figure 3.50: Filter R (left) and B (right) periodogram analysis of Molniya 3-8.

3.11 Molniya 2-9

Day	UT(start)	Airm	Expt(s)	F	D(Km)	Mag	PA
2016-09-27	22:12:45	1.55	20	R	27118	13.599	91.1
2016-09-27	22:14:44	1.54	20	I	27313	12.814	90.57
2016-09-27	22:17:44	1.52	20	V	27599	14.231	89.8
2016-09-27	22:20:45	1.51	20	B	27879	15.299	88.8

Table 3.16: Molniya 2-9 data

The periodogram analysis was very difficult because of the lack of statistics (we have only 4 exposition, one for each filter). The results are plotted in Figure 3.51, Figure 3.52, Figure 3.53 and Figure 3.54. The satellite is rotating with a period around 15 s, the error is high as you can see from the width of the peak. Periodogram in I finds a peak at $P = 14.7$ s while periodogram in R filter finds it at $P = 15$ s and $P = 15.2$ s. Periodogram in filter V and B doesn't provide any information because of, once again, the negative values of the flux in the light curves. We conclude that the period for Molniya 2-9 is $P = 15 \pm 1$ s.

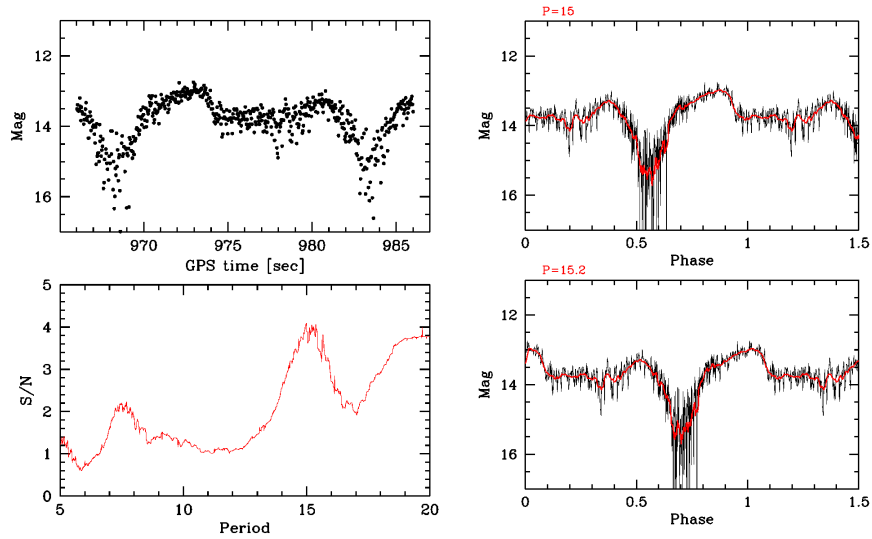


Figure 3.51: Filter R periodogram analysis of Molniya 2-9.

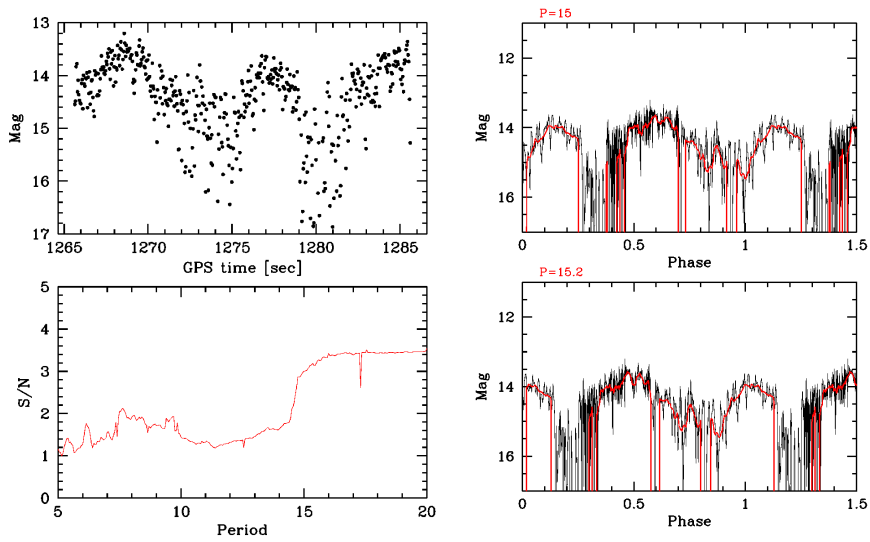


Figure 3.52: Filter V periodogram analysis of Molniya 2-9.

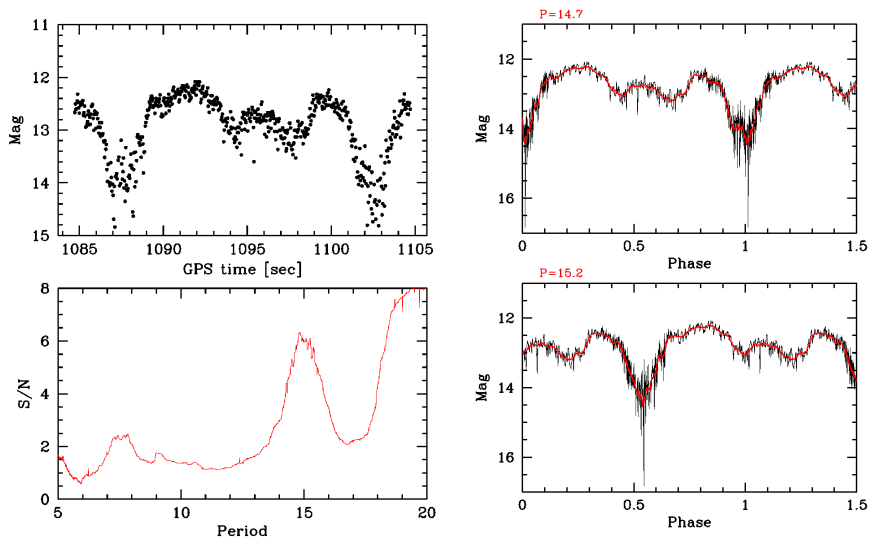


Figure 3.53: Filter I periodogram analysis of Molniya 2-9.

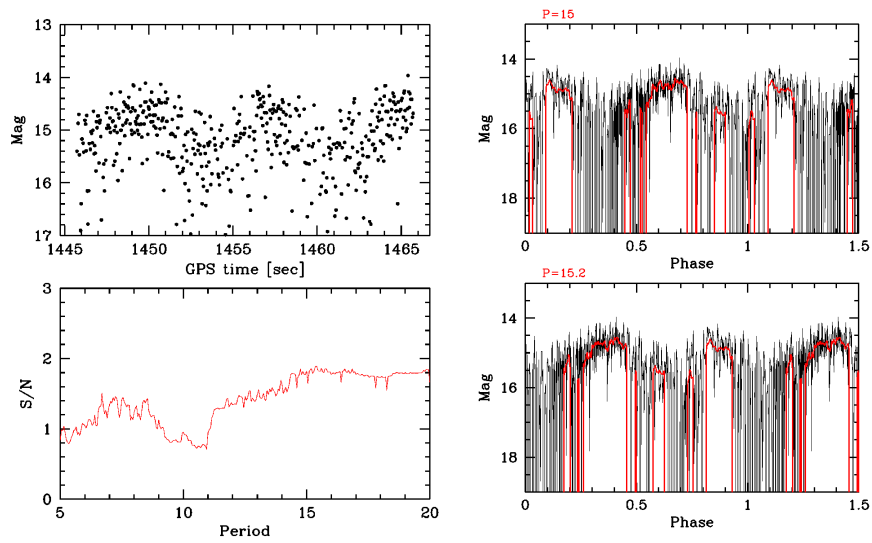


Figure 3.54: Filter B periodogram analysis of Molniya 2-9.

3.12 Molniya 1-S

With the periodogram analysis of the data we discover that Molniya 1-S is rotating with a period $P = 25.832 \pm 0.053$ s, the periodogram results are plotted in Figure 3.55, Figure 3.56, Figure 3.57, Figure 3.58, Figure 3.59, Figure 3.60, Figure 3.61 and Figure 3.62. In all filters a peak in the signal-to-noise ratio has been found near $P = 25.8$ s, the precise value for each filter is plotted in Table 3.19, a zoom of the periodogram analysis is plotted in Figure 3.63 and Figure 3.64. The final value of the period for Molniya 1-S has been found averaging on the eight values found. We notice that Molniya 1-S could have a second longer period, looking at the magnitude-time plot especially in the night between the second and the third August, to check this hypothesis longer exposures are needed.

Night	Filter	Period(s)	Error(s)
01-02/09/2016	R	25.826	0.05
01-02/09/2016	I	25.83	0.025
01-02/09/2016	V	25.823	0.05
01-02/09/2016	B	25.83	0.05
02-03/09/2016	R	25.845	0.05
02-03/09/2016	I	25.823	0.05
02-03/09/2016	V	25.845	0.05
02-03/09/2016	B	25.833	0.1

Table 3.17: Molniya 1-S periods found with periodogram analysis

Day	UT(start)	Airm	Expt(s)	F	D(Km)	Mag	PA
2016-08-01	19:48:40	2.323	25	V	38896	12.886	15.44
2016-08-01	19:52:17	2.318	30	V	38885	12.847	14.91
2016-08-01	19:53:22	2.317	30	R	38881	12.037	14.73
2016-08-01	19:54:28	2.304	30	I	38874	10.787	14.56
2016-08-01	19:56:44	2.298	30	B	38867	13.388	14.06
2016-08-01	23:30:22	1.786	15	V	38100	12.491	44.21
2016-08-01	23:31:13	1.786	15	R	38097	11.931	44.45
2016-08-01	23:32:05	1.786	15	I	38094	10.901	44.69
2016-08-01	23:32:56	1.786	15	B	38091	12.881	44.93
2016-08-01	23:34:23	1.784	25	V	38088	12.542	45.17
2016-08-01	23:35:24	1.781	25	R	38086	11.942	45.42
2016-08-01	23:36:25	1.781	25	I	38083	11.032	45.66
2016-08-01	23:37:26	1.779	25	B	38080	13.222	45.9
2016-08-01	23:38:39	1.776	40	V	38074	12.552	46.38
2016-08-01	23:39:55	1.776	40	R	38071	11.923	46.62
2016-08-01	23:41:10	1.776	40	I	38068	10.893	46.86
2016-08-01	23:42:26	1.772	40	B	38065	12.983	47.1
2016-08-01	23:44:22	1.771	40	V	38060	12.473	47.1
2016-08-01	23:45:37	1.768	40	R	38054	11.934	48.07
2016-08-01	23:46:53	1.768	40	I	38051	11.924	48.31
2016-08-01	23:48:09	1.763	40	B	38048	12.984	48.55
2016-08-01	23:49:53	1.763	40	V	38043	12.464	49.04
2016-08-01	23:51:10	1.762	40	R	38040	11.894	49.28
2016-08-01	23:52:26	1.762	40	I	38037	10.985	49.52
2016-08-01	23:53:41	1.757	40	B	38032	13.245	50.01
2016-08-01	23:55:06	1.757	40	V	38029	12.565	50.25
2016-08-01	23:56:23	1.755	40	R	38027	12.005	50.49
2016-08-01	23:57:38	1.755	40	I	38021	11.105	50.98
2016-08-01	23:58:54	1.754	40	B	38019	13.136	51.22
2016-08-02	00:01:16	1.747	240	R	38013	12.046	51.7
2016-08-02	00:23:30	1.723	40	V	37956	12.569	57.3
2016-08-02	00:24:46	1.723	40	R	37954	12.059	57.54
2016-08-02	00:26:01	1.723	40	I	37951	11.079	57.78
2016-08-02	00:27:17	1.723	40	B	37949	13.120	58.03
2016-08-02	00:29:28	1.717	40	V	37944	12.610	58.51
2016-08-02	00:30:44	1.717	40	R	37940	12.080	59
2016-08-02	00:32:01	1.717	40	I	37938	11.120	59.25
2016-08-02	00:33:17	1.717	40	B	37935	13.130	59.49
2016-08-02	00:39:04	1.708	40	V	37922	12.621	60.95
2016-08-02	00:40:20	1.708	40	R	37920	12.111	61.2
2016-08-02	00:41:36	1.708	40	I	37916	11.181	61.68
2016-08-02	00:42:50	1.708	40	B	37914	13.172	61.93
2016-08-02	00:45:48	1.702	40	V	37907	12.672	62.66
2016-08-02	00:47:04	1.702	40	R	37905	12.142	62.91
2016-08-02	00:48:21	1.702	40	I	37903	11.182	63.15
2016-08-02	00:49:36	1.702	40	B	37899	13.192	63.64

Table 3.18: Molniya 1-S data

Day	UT(start)	Airm	Expt(s)	F	D(Km)	Mag	PA
2016-08-03	00:02:51	1.752	40	V	38003	12.677	52.19
2016-08-03	00:04:07	1.752	40	R	38000	12.047	52.43
2016-08-03	00:05:22	1.752	40	I	37998	11.477	52.68
2016-08-03	00:14:47	1.732	40	V	37973	12.778	55.11
2016-08-03	00:16:04	1.731	40	R	37971	12.188	55.35
2016-08-03	00:17:20	1.731	40	I	37968	11.459	55.59
2016-08-03	00:18:36	1.73	40	B	37964	13.439	56.08
2016-08-03	00:22:53	1.724	40	V	37954	12.769	57.05
2016-08-03	00:24:10	1.723	40	R	37952	12.189	57.3
2016-08-03	00:25:27	1.722	40	I	37950	11.440	57.54
2016-08-03	00:26:43	1.722	40	B	37945	13.410	58.03
2016-08-03	00:29:34	1.717	40	V	37938	12.720	58.76
2016-08-03	00:30:51	1.717	40	R	37936	12.140	59
2016-08-03	00:32:07	1.716	40	I	37934	11.400	59.25
2016-08-03	00:33:24	1.716	40	B	37932	13.401	59.49
2016-08-03	00:36:42	1.711	50	V	37923	12.651	60.47
2016-08-03	00:38:09	1.71	50	R	37921	12.091	60.71
2016-08-03	00:39:37	1.709	50	I	37917	11.391	61.2
2016-08-03	00:41:03	1.709	50	B	37915	13.412	61.44
2016-08-03	00:43:02	1.708	50	V	37911	12.782	61.93
2016-08-03	00:44:29	1.707	50	R	37907	12.292	62.32
2016-08-03	00:45:55	1.706	50	I	37905	11.652	62.66
2016-08-03	00:47:22	1.706	50	B	37903	13.652	63.01
2016-08-03	00:50:47	1.699	300	R	37895	12.183	63.88
2016-08-03	00:56:23	1.696	300	R	37883	12.143	65.2
2016-08-03	01:04:48	1.691	240	V	37869	12.724	67.3

Table 3.19: Molniya 1-S data

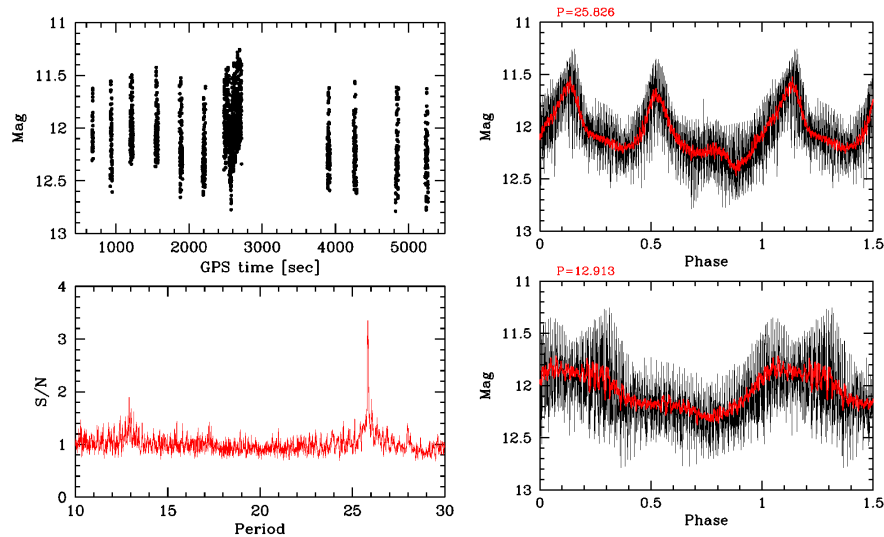


Figure 3.55: Filter R periodogram analysis of Molniya 1-S, night 01-02.

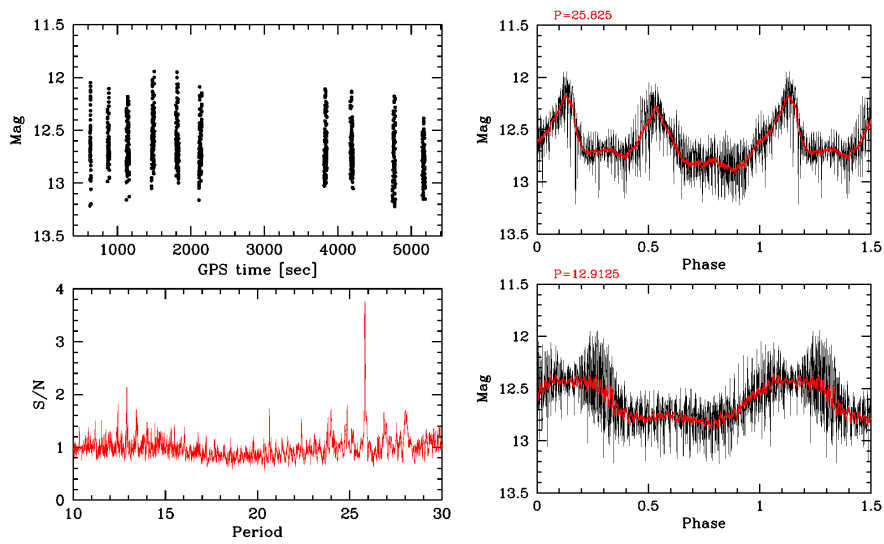


Figure 3.56: Filter V periodogram analysis of Molniya 1-S, night 01-02.

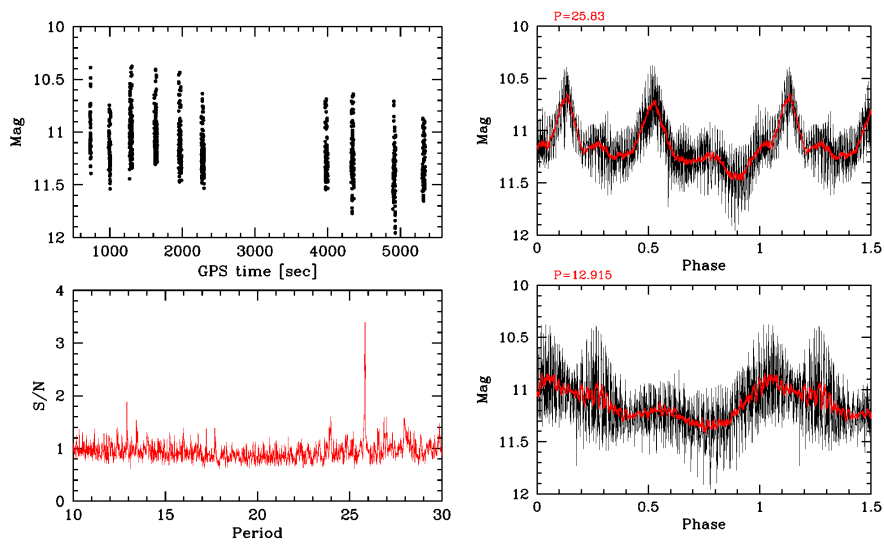


Figure 3.57: Filter I periodogram analysis of Molniya 1-S, night 01-02.

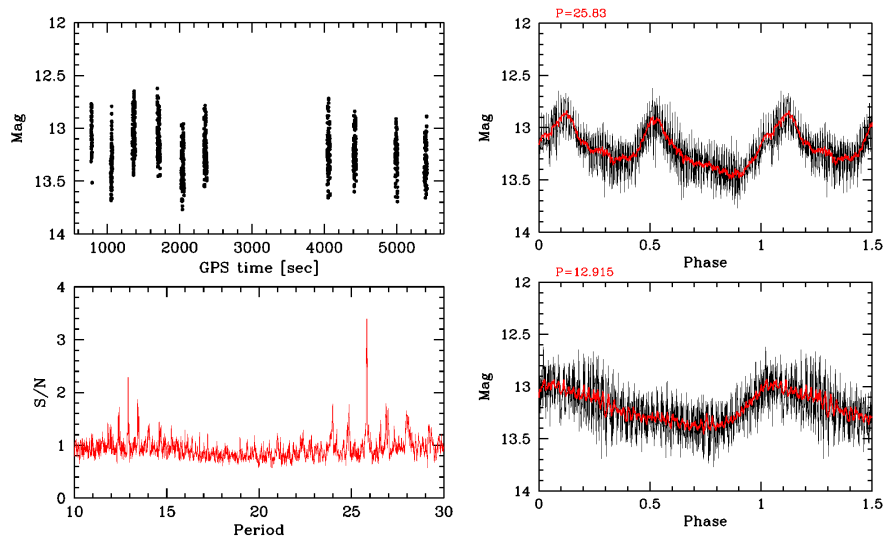


Figure 3.58: Filter B periodogram analysis of Molniya 1-S, night 01-02.

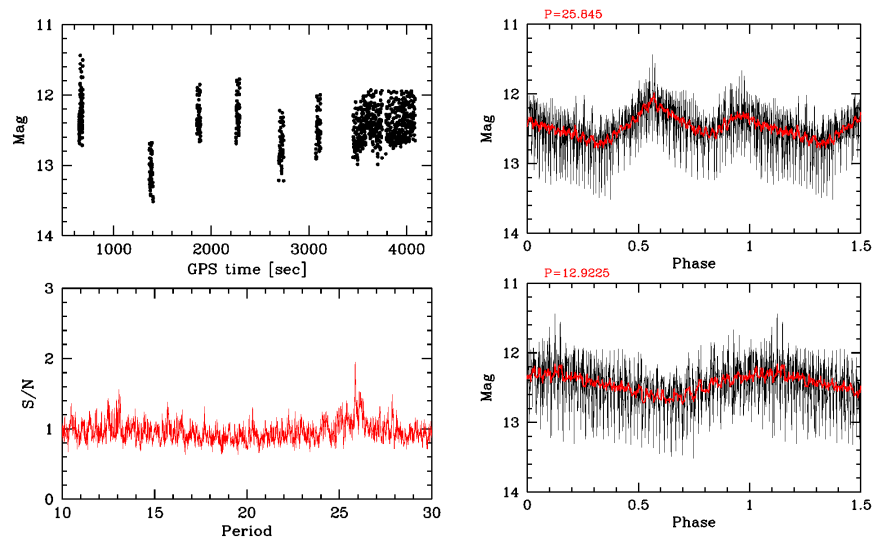


Figure 3.59: Filter R periodogram analysis of Molniya 1-S, night 02-03.

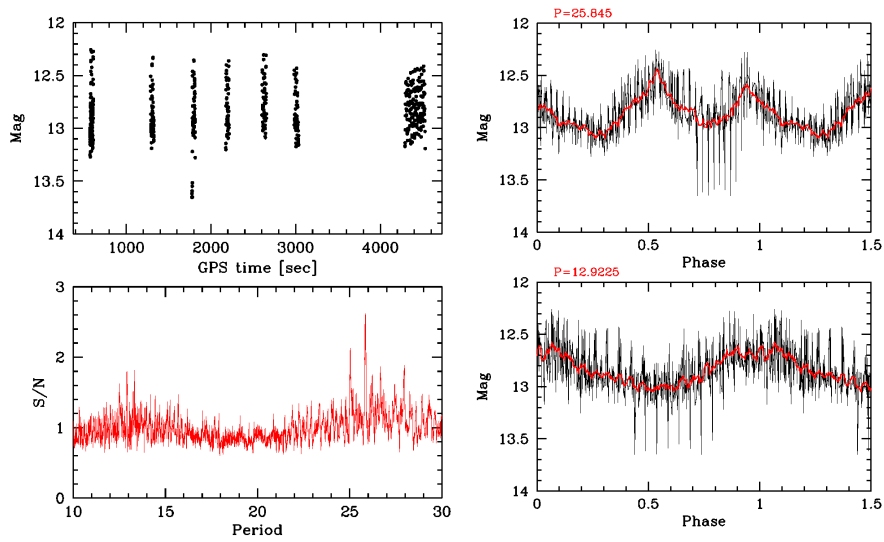


Figure 3.60: Filter V periodogram analysis of Molniya 1-S, night 02-03.

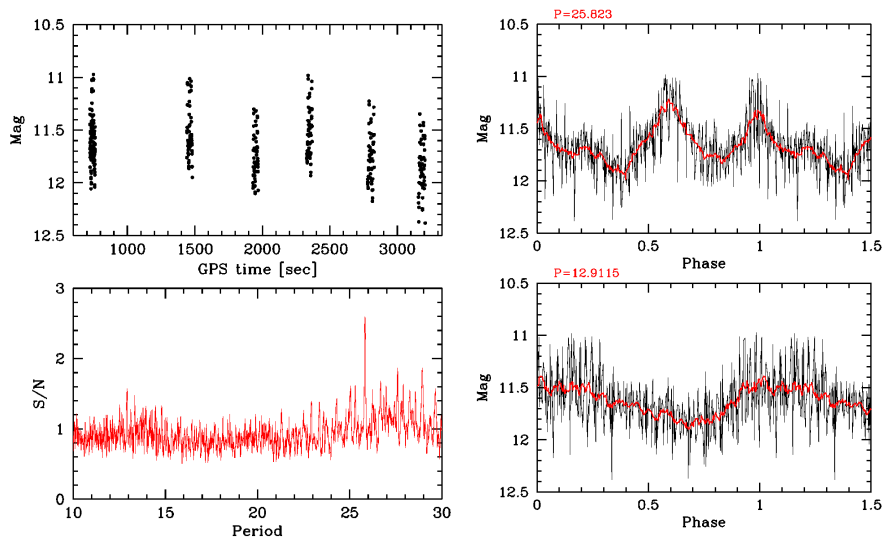


Figure 3.61: Filter I periodogram analysis of Molniya 1-S, night 02-03.

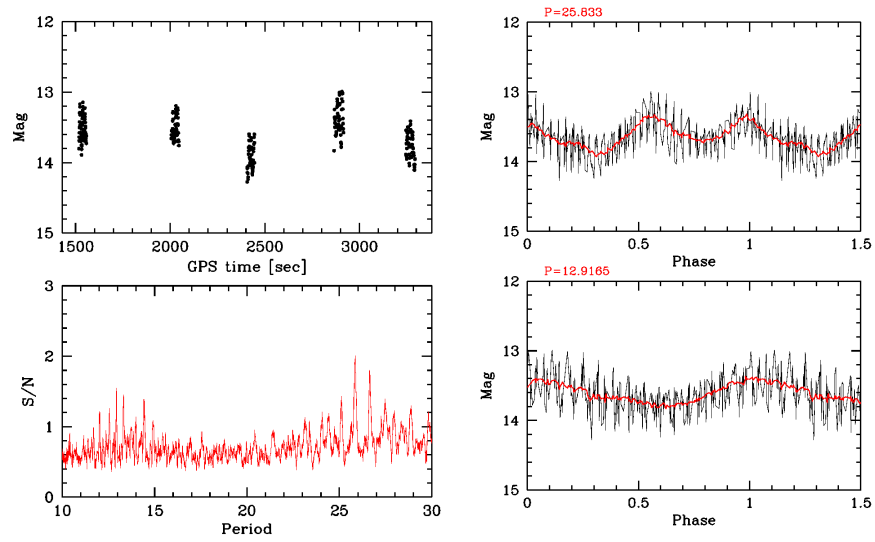


Figure 3.62: Filter B periodogram analysis of Molniya 1-S, night 02-03.

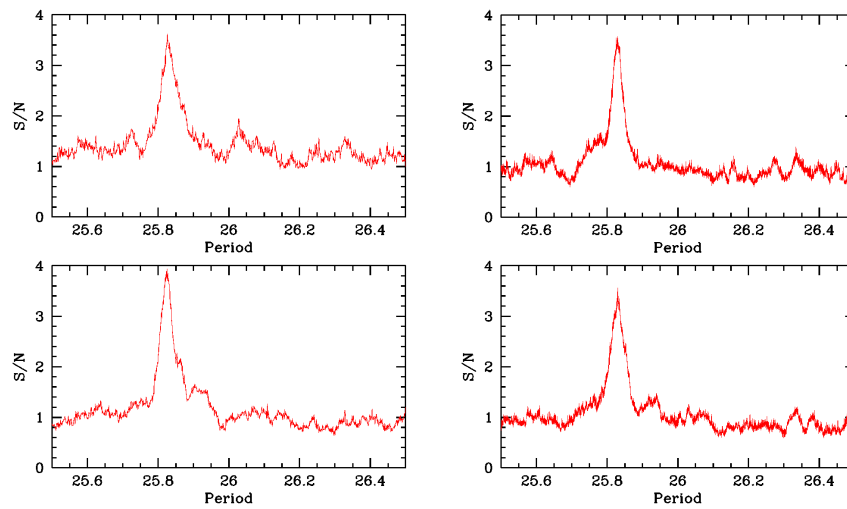


Figure 3.63: Zoom of periodogram analysis of Molniya 1-S in filter R (top left), V (bottom left), I (top right) and B (bottom right), night 01-02.

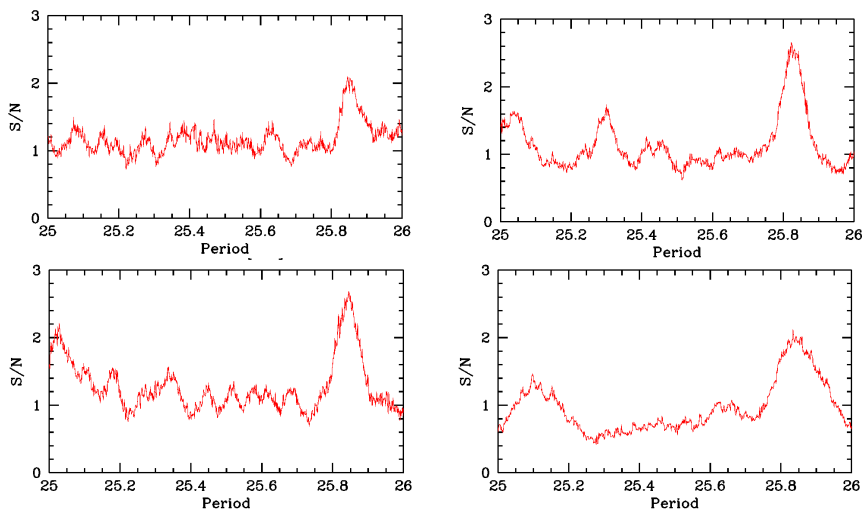


Figure 3.64: Zoom of periodogram analysis of Molniya 1-S in filter R (top left), V (bottom left), I (top right) and B (bottom right), night 02-03.

3.13 Molniya 3-27

The periodogram analysis for Molniya 3-27 was hard to do because of the scarce sampling, the results are plotted in Figure 3.65, Figure 3.66, Figure 3.67 and Figure 3.68. In all filters the periodograms find a peak near $P = 16.5$ s, the position of the peaks are variable and are plotted in Table 3.20, while in filter R where two exposition are available the periodogram finds another peak at $P = 32.9$ s. Looking at the fit of the light curve in R band, the period $P = 32.9$ appears to be the correct one, considering also that the periodogram analysis in filter R is the most reliable one because it is based on two exposures, while the other are based on only one exposition. We conclude that Molniya 3-27 is rotating with period $P = 32.9 \pm 0.03$ s.

Filter	Period(s)	Error(s)
R	16.45	0.015
R	32.9	0.03
I	16.4	0.5
V	17	1.0
B	16.15	0.5

Table 3.20: Molniya 3-27 periods found with periodogram analysis

Day	UT(start)	Airm	Expt(s)	F	D(Km)	Mag	PA
2016-09-28	00:46:59	1.46	20	R	31826	11.222	92.03
2016-09-28	00:49:58	1.46	30	I	31567	10.449	92.47
2016-09-28	00:52:55	1.46	30	V	31303	11.558	92.92
2016-09-28	00:55:56	1.46	30	B	31033	11.926	93.37
2016-09-28	00:58:56	1.47	40	R	30757	11.016	93.84

Table 3.21: Molniya 3-27 data

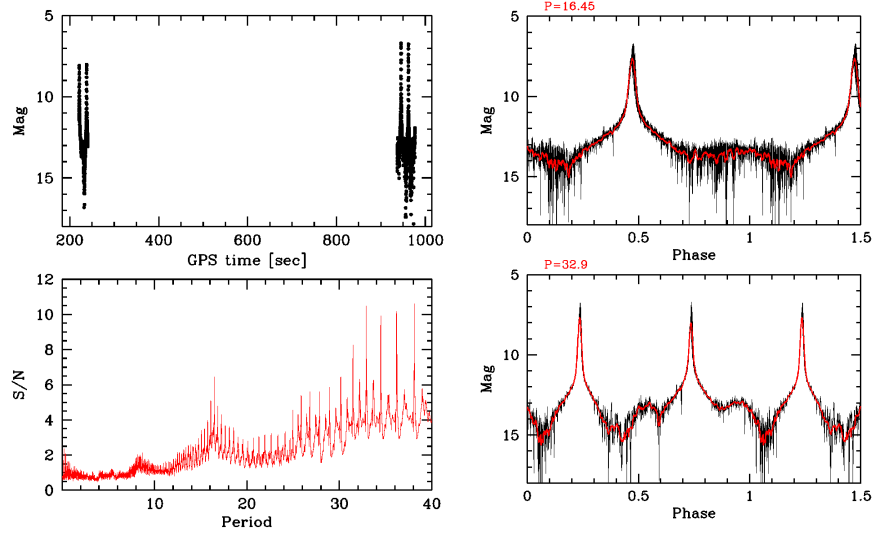


Figure 3.65: Filter R periodogram analysis of Molniya 3-27.

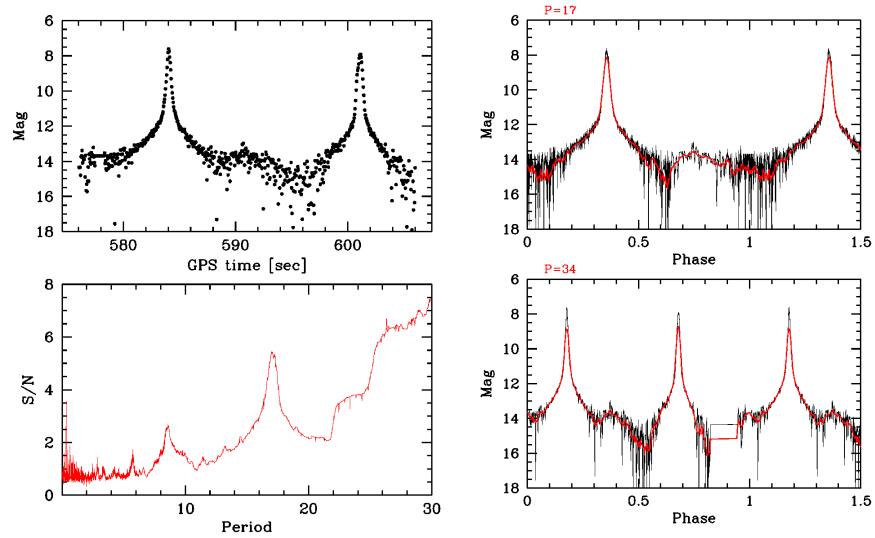


Figure 3.66: Filter V periodogram analysis of Molniya 3-27.

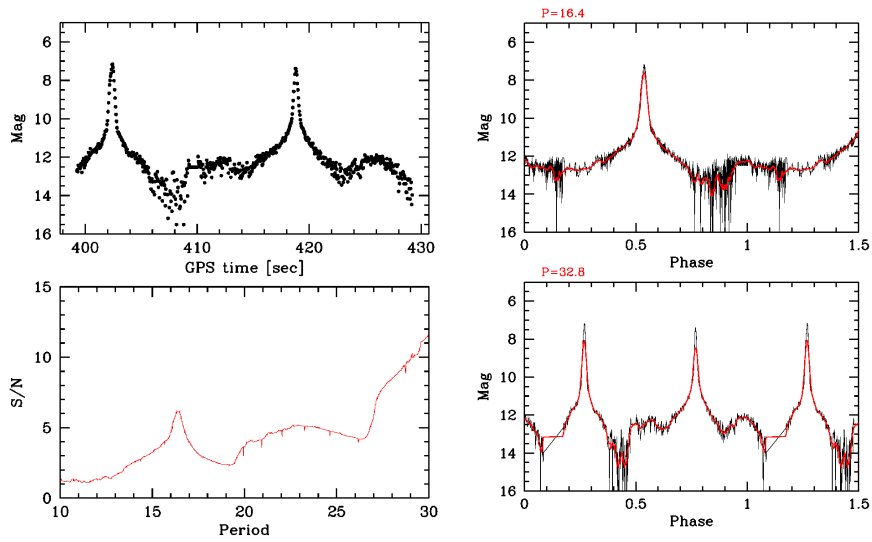


Figure 3.67: Filter I periodogram analysis of Molniya 3-27.

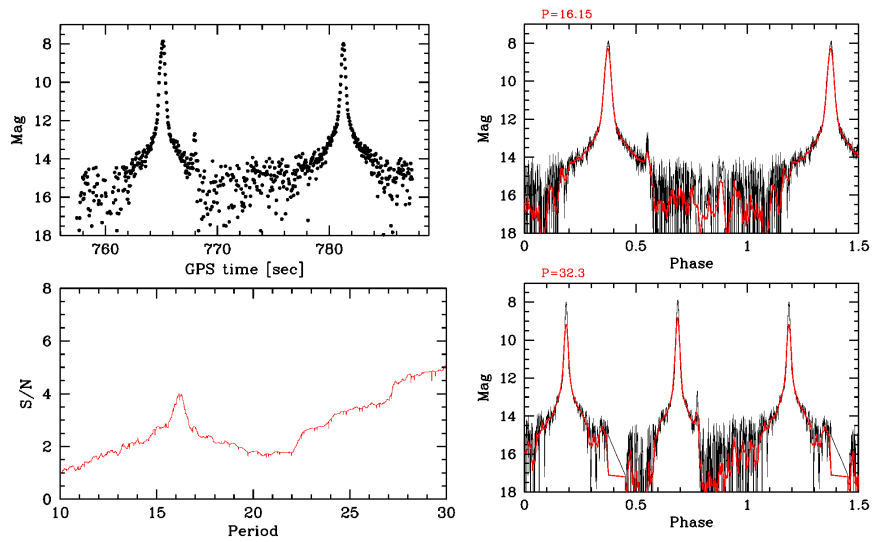


Figure 3.68: Filter B periodogram analysis of Molniya 3-27.

3.14 Molniya 2-17

Day	UT(start)	Airm	Expt(s)	F	D(Km)	Mag	PA
2016-09-27	00:40:54	1.16	8	R	15455	14.120	71.25
2016-09-27	00:42:53	1.18	8	I	15074	9.554	71.83
2016-09-27	00:45:54	1.2	8	V	14500	14.019	72.8
2016-09-27	00:47:53	1.21	8	B	14116	10.877	73.51
2016-09-27	00:49:53	1.23	8	R	13734	13.497	74.28
2016-09-27	00:51:53	1.26	7	I	12972	12.251	75.13
2016-09-27	00:53:54	1.28	7	V	12972	14.621	76.05
2016-09-27	00:57:54	1.36	7	B	12225	13.339	78.15
2016-09-27	18:57:05	1.05	30	R	39475	13.124	63.53
2016-09-27	18:59:59	1.05	30	I	39545	12.190	63.5
2016-09-27	19:02:59	1.05	30	V	39610	12.247	63.46
2016-09-27	19:05:59	1.05	30	B	39671	14.783	63.43
2016-09-27	19:08:49	1.05	70	R	39727	12.070	63.41
2016-09-27	19:12:49	1.05	70	R	39796	9.706	63.36
2016-09-27	19:17:44	1.05	80	R	39870	13.242	63.31

Table 3.22: Molniya 2-17 data

The periodogram analysis of Molniya 2-17 was one of the most difficult to do, because the satellite period is very long and few expositions were available. The exposition of September 26-27 night are too short in exposition time to give any information on the period, the periodogram isn't able to find any peak (Figure 3.72, Figure 3.73). With the exposition of the night between 27 and 28 the analysis improves a little. The results of the periodogram analysis are plotted in Figure 3.69, Figure 3.70, Figure 3.71. Only filter R analysis finds a peak at $P = 54.55 \pm 1$ s, while analysis with other filters isn't able to provide any information since it is made on one exposure only. To improve the precision on the period we try to combine the observations of the two nights in filter R, the result of this analysis are plotted in Figure 3.74, Figure 3.75 and Figure 3.76. As you can see this analysis finds many peaks near $P = 54.55$ s, precisely at $P = 54.36$, $P = 54.45$, $P = 54.54$, $P = 54.63$ and $P = 54.72$ s, all these peaks are separated by 0.09 s and are clearly due to an alias phenomenon. The peak with the highest signal-to-noise ratio is that at $P = 54.72$ s, but the peak nearest to that found with the former analysis is that at $P = 54.54$ s.

We conclude that Molniya 2-17 is rotating with period $P = 54.54 \pm 1$ s.

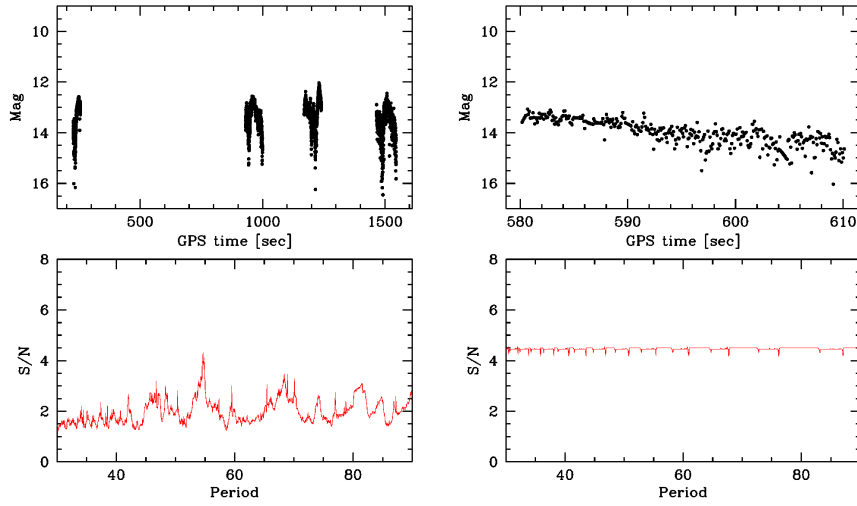


Figure 3.69: Filter R (left) and V (right) periodogram analysis of Molniya 2-17, night 27-28.

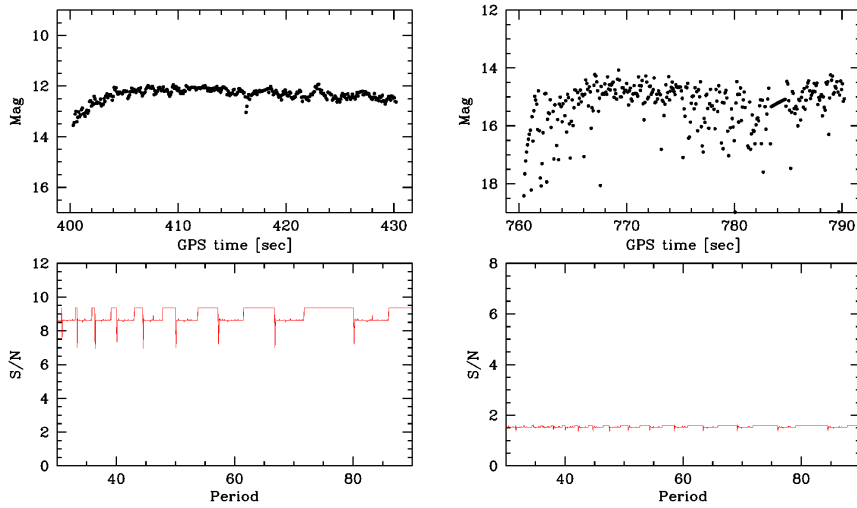


Figure 3.70: Filter I (left) and B (right) periodogram analysis of Molniya 2-17, night 27-28.

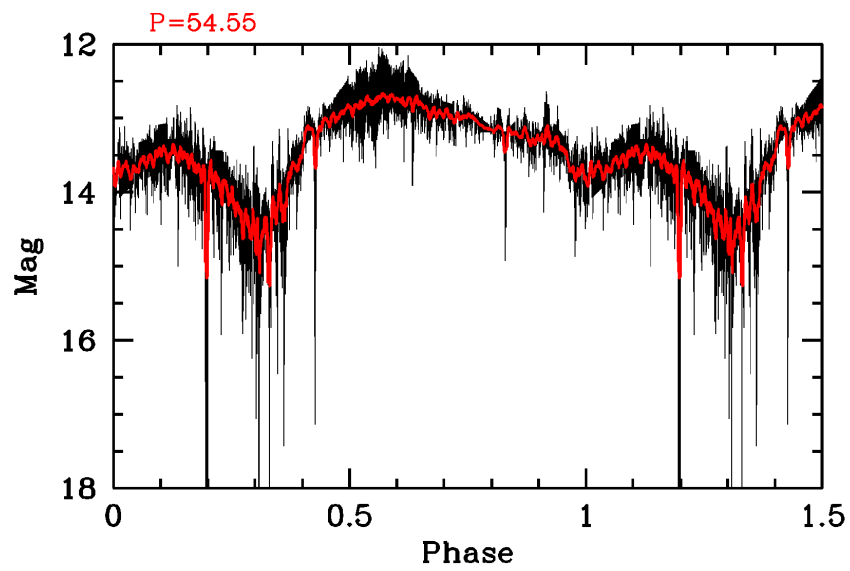


Figure 3.71: Fit of filter R light curve with $P = 54.55$ s.

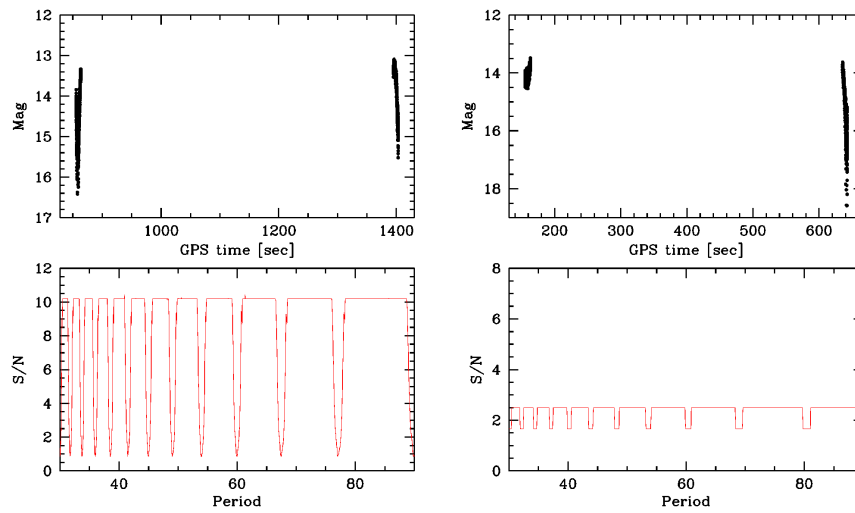


Figure 3.72: Filter R (left) and V (right) periodogram analysis of Molniya 2-17, night 26-27.

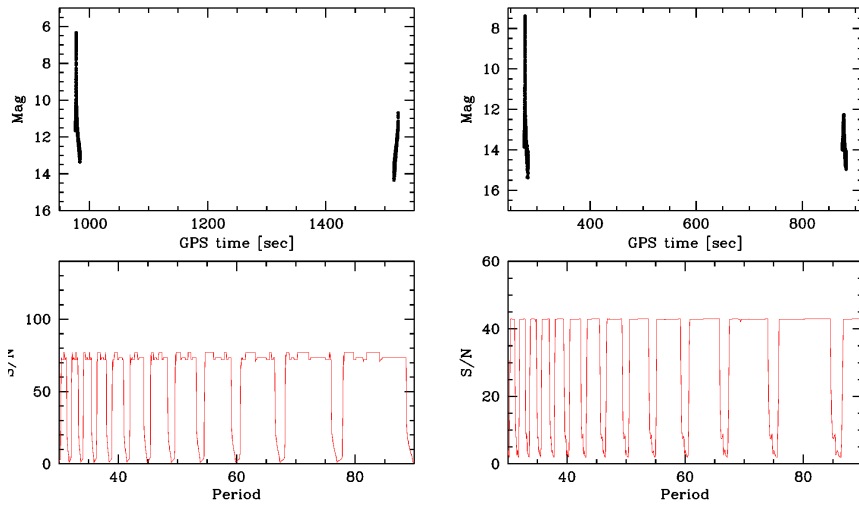


Figure 3.73: Filter I (left) and B (right) periodogram analysis of Molniya 2-17, night 26-27.

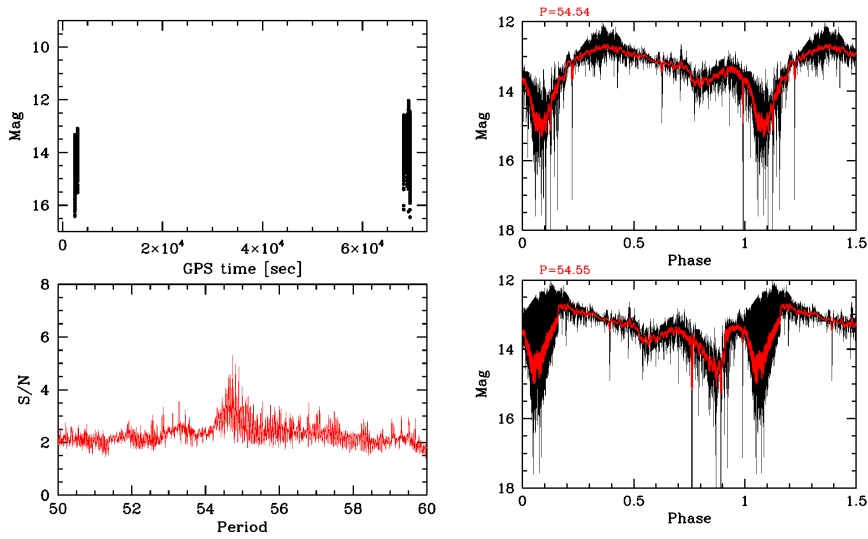


Figure 3.74: Filter R combined analysis of Molniya 2-17

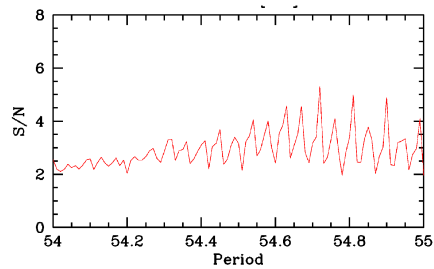


Figure 3.75: Zoom of filter R combined analysis of Molniya 2-17

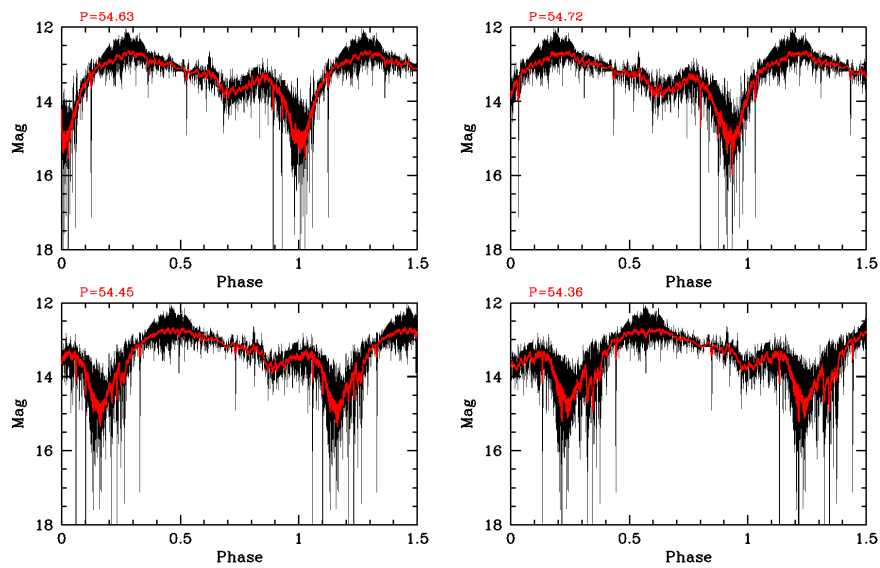


Figure 3.76: Filter R combined analysis of Molniya 2-17

3.15 Molniya 1-87

Molniya 1-87 periodogram analysis wasn't able to provide an estimate of the rotational period. Watching at the light curves (Figure A.150, A.151, A.152, A.153, A.154, Section A.6 and Figure A.93, A.94 in Section A.4) it's clear that the satellite is rotating with a very long period. Sadly our exposures have exposition time very short in both night, and so the sampling of the light curve is too poor to provide any information with periodogram analysis. The presence of a long period is clear also watching at the magnitude-time plot in Figure 3.77.

Day	UT(start)	Airm	Expt(s)	F	D(Km)	Mag	PA
2016-09-27	23:44:50	1.19	10	R	24588	12.559	71.93
2016-09-27	23:47:59	1.2	20	R	25049	12.892	72.7
2016-09-27	23:49:59	1.2	20	I	25351	11.676	73.2
2016-09-27	23:52:59	1.2	20	V	25796	13.508	73.94
2016-09-27	23:54:58	1.2	20	B	26089	15.453	74.41
2016-09-27	23:57:58	1.21	25	R	26520	12.548	75.11
2016-12-22	18:21:59	1.12	2	R	9874	13.013	84.07
2016-12-22	18:29:58	1.04	3	R	11541	12.814	75.47
2016-12-22	18:32:58	1.03	4	R	12182	12.257	72.94
2016-12-22	18:35:57	1.02	5	R	12823	13.476	70.7
2016-12-22	18:38:57	1.01	5	R	13462	13.030	68.71
2016-12-22	18:41:58	1.01	5	R	14096	12.940	66.92
2016-12-22	18:44:58	1.01	5	B	14723	13.146	65.31
2016-12-22	18:47:58	1.01	5	V	15344	13.356	63.85
2016-12-22	18:49:58	1.01	7	R	15752	13.609	62.96
2016-12-22	18:51:57	1.01	7	I	16157	11.694	62.11
2016-12-22	18:53:58	1.01	7	B	16558	15.961	61.31
2016-12-22	18:55:59	1.01	7	V	16954	13.529	60.57
2016-12-22	18:57:58	1.01	7	R	17346	14.040	59.52
2016-12-22	19:08:05	1.02	7	I	19240	11.215	56.82

Table 3.23: Molniya 1-87 data

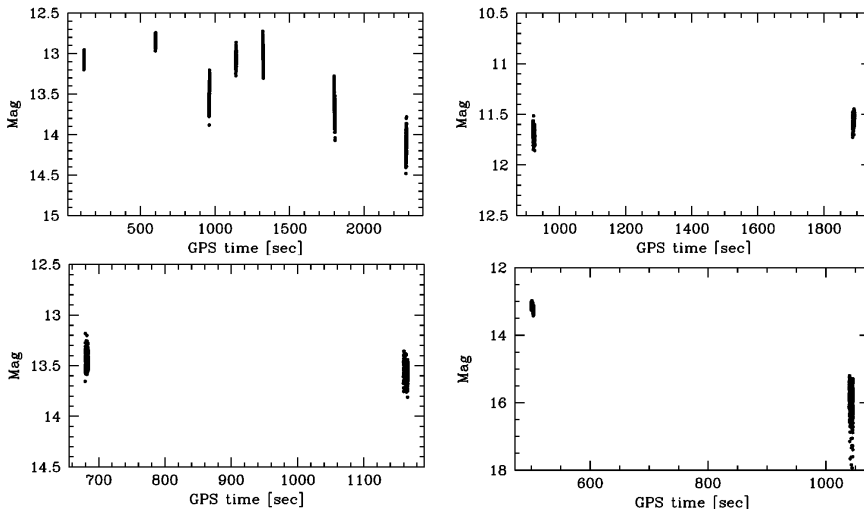


Figure 3.77: Magnitude vs time of Molniya 1-87 in filter R (top left), V (bottom left), I (top right) and B (bottom right), December 22 observations.

3.16 Molniya 2-13

The periodogram analysis of Molniya 2-13 was made only on filter R and I light curves, because in the other filter we had only one cuve, and it was very noisy (see Section A.5, Figures A.115, A.116). Filter R and I analysis results are plotted in Figure 3.78 and Figure 3.79. Filter R analysis shows two possible peaks near $P = 8$ s and $P = 10$ s, but the periodogram is very noisy and the fit with the two values isn't good, filter I analysis is even worse. In conclusion we weren't able to find a period for Molniya 2-13.

Day	UT(start)	Airm	Expt(s)	F	D(Km)	Mag	PA
2016-11-26	20:18:59	1.94	7	R	24890	13.525	99.65
2016-11-26	20:24:50	1.99	15	R	23984	13.396	99.76
2016-11-26	20:27:44	2.02	15	I	23519	12.239	99.82
2016-11-26	20:29:44	2.04	15	V	23206	12.228	99.86
2016-11-26	20:33:44	2.09	15	B	22568	13.618	99.96
2016-11-26	20:35:44	2.11	15	R	22243	12.980	100.01
2016-11-26	20:40:44	2.19	15	I	21418	12.822	100.16

Table 3.24: Molniya 2-13 data

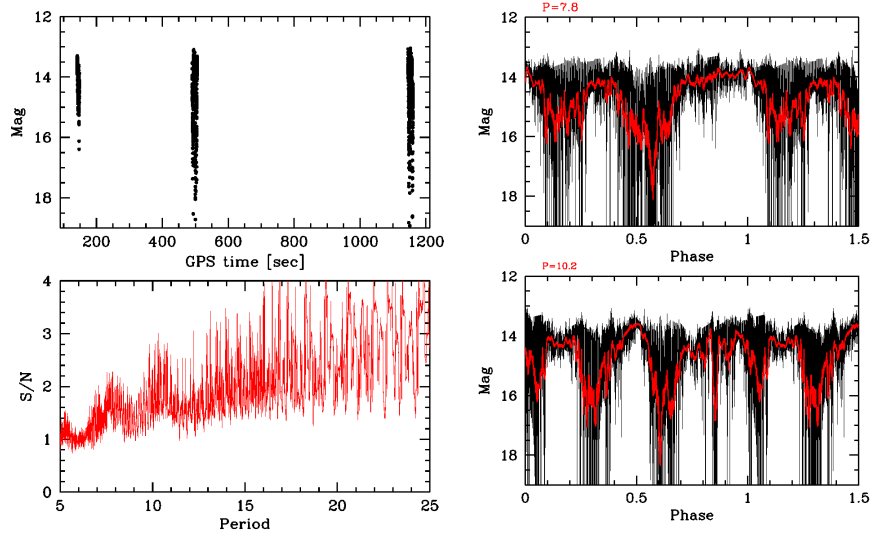


Figure 3.78: Filter R periodogram analysis of Molniya 2-13.

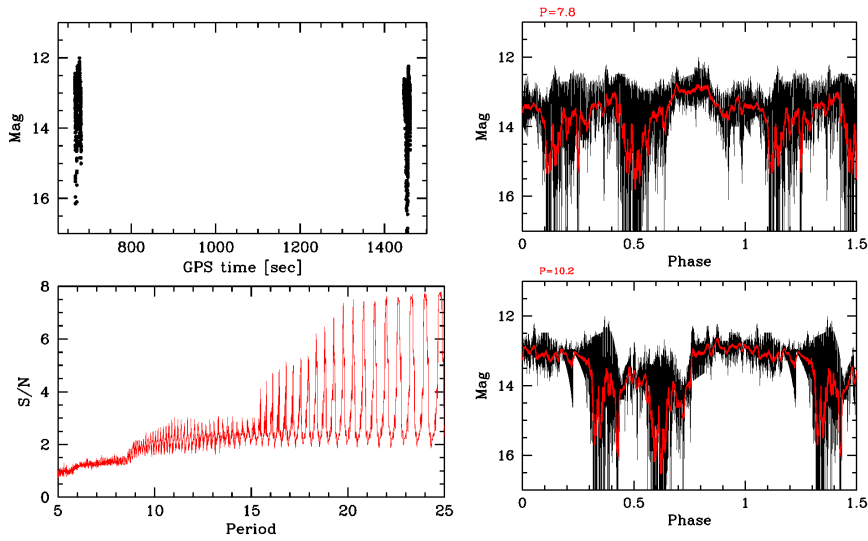


Figure 3.79: Filter I periodogram analysis of Molniya 2-13.

3.17 Molniya 1-62

The periodogram analysis of molniya 1-62 light curves has revealed very complex. Watching at the light cures (Section A.3, Figures A.78, A.79, A.80, A.81,A.82) it's clear that the satellite is rotating with period longer than ≈ 50 s. The results of periodogram analysis are plotted in figure 3.80, figure 3.81, figure 3.82 and figure 3.83. As you can se the signal-to-noise ratio is very noisy for all filters and preset some alias phenomena in filter I,V and B where less exposures were available. There is no clear presence of a main peak in any filter except perhaps filter R that shows a peak at $P = 78.14$, so we try to check if the fit with the many possible values for the period was good, and if there were some peaks appears in multiple periodograms. The results of this check are plotted in figure 3.84, figure 3.85, figure 3.86, figure 3.87 and figure 3.88. As you can see there are many values that provide a good fit in filter B,V and I but none of this provide a satisfactory fit in filter R, that being the filter with more exposures is the most reliable. The fit with the value found with R filter analysis isn't satisfactory in fitting other filters light curves. In conclusion we weren't able to find the true rotating period of Molniya 1-62.

Day	UT(start)	Airm	Expt(s)	F	D(Km)	Mag	PA
2016-09-27	01:10:59	1.09	10	R	40028	13.084	61.43
2016-09-27	01:13:58	1.09	20	R	40091	12.550	61.61
2016-09-27	01:18:58	1.09	30	V	40187	14.145	61.92
2016-09-27	01:22:59	1.09	30	B	40254	15.182	62.17
2016-09-27	01:26:29	1.09	60	R	40313	12.778	62.45
2016-09-27	01:29:28	1.09	60	R	40352	12.936	62.6
2016-09-27	01:33:28	1.1	60	R	40397	13.004	62.8
2016-09-27	01:37:28	1.1	60	I	40434	11.442	63.1
2016-09-27	01:40:29	1.1	60	V	40457	13.861	63.25
2016-09-27	01:43:28	1.1	60	B	40474	15.120	63.4
2016-09-27	01:46:29	1.1	60	R	40488	9.789	63.6
2016-09-27	01:49:28	1.1	60	I	40496	11.919	63.8
2016-09-27	01:52:28	1.1	60	V	40500	14.018	64
2016-09-27	01:56:28	1.1	60	B	40499	14.768	64.2

Table 3.25: Molniya 1-62 data

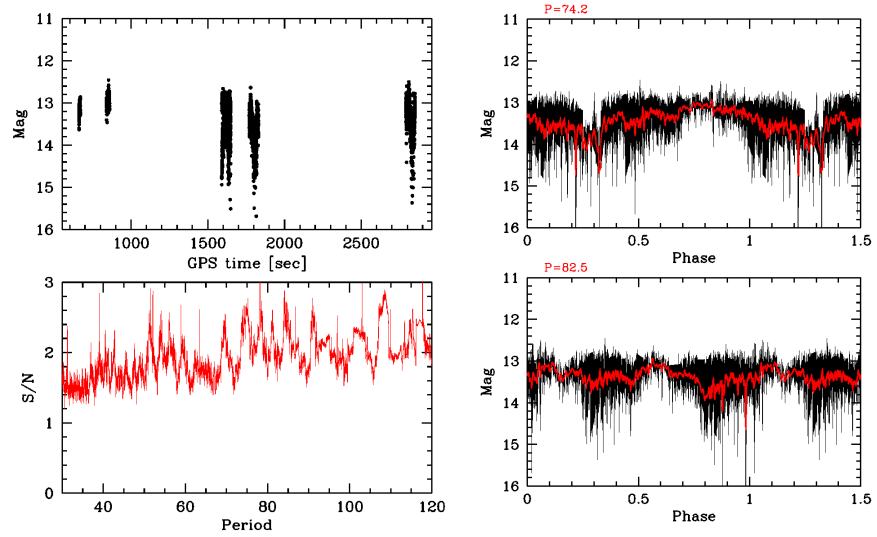


Figure 3.80: Filter R periodogram analysis of Molniya 1-62.

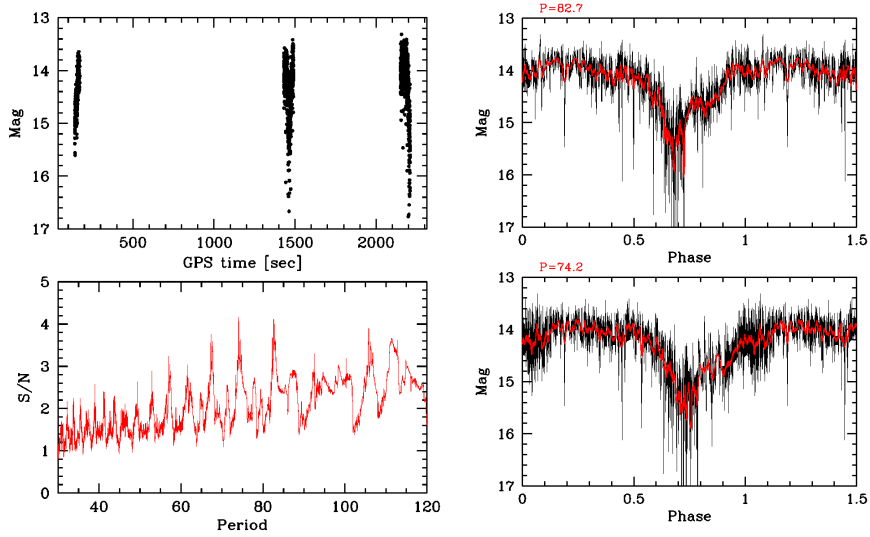


Figure 3.81: Filter V periodogram analysis of Molniya 1-62.

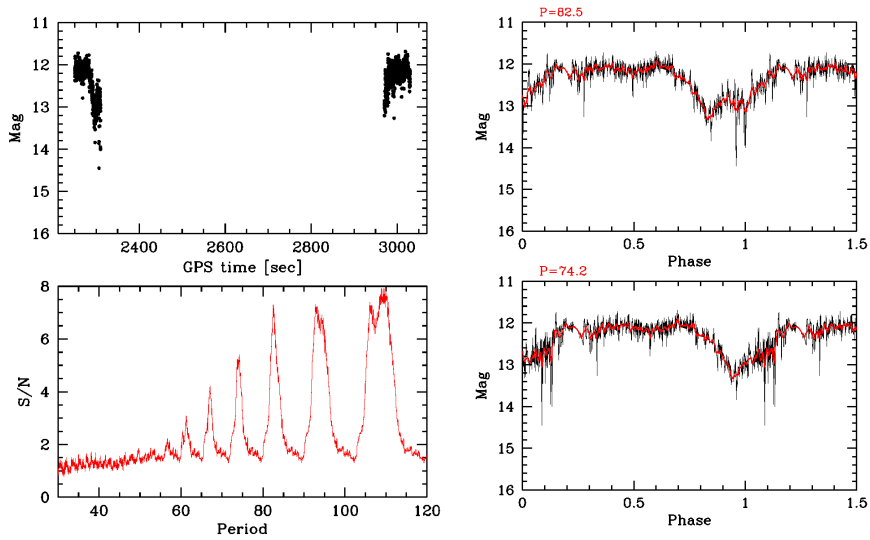


Figure 3.82: Filter I periodogram analysis of Molniya 1-62.

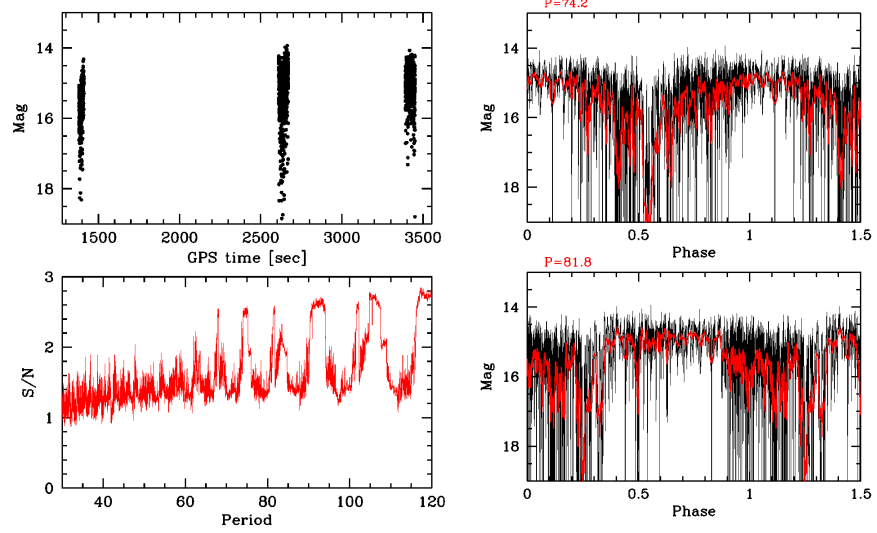


Figure 3.83: Filter B periodogram analysis of Molniya 1-62.

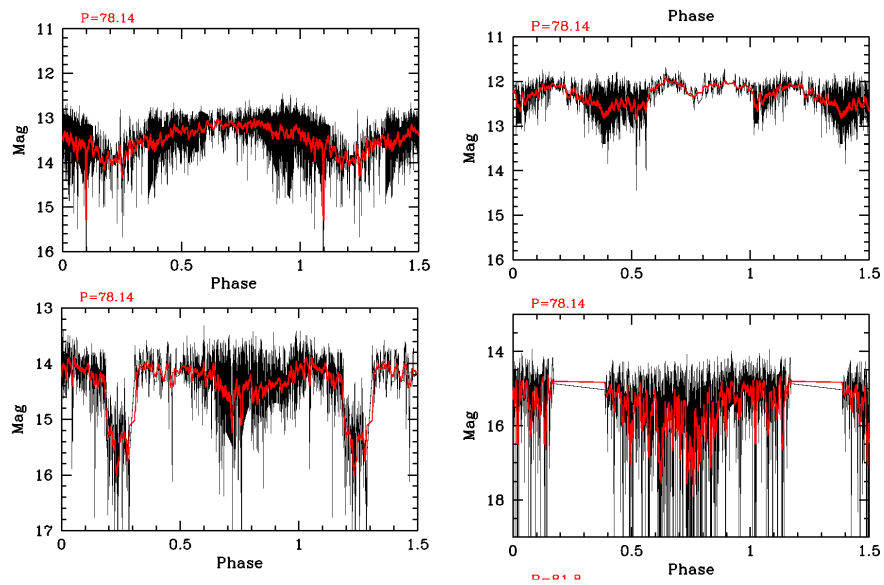


Figure 3.84: Filter R (top left), V (bottom left), I (top right), B (bottom right) fit of Molniya 1-62 light curves with period $P = 78.14$ s.

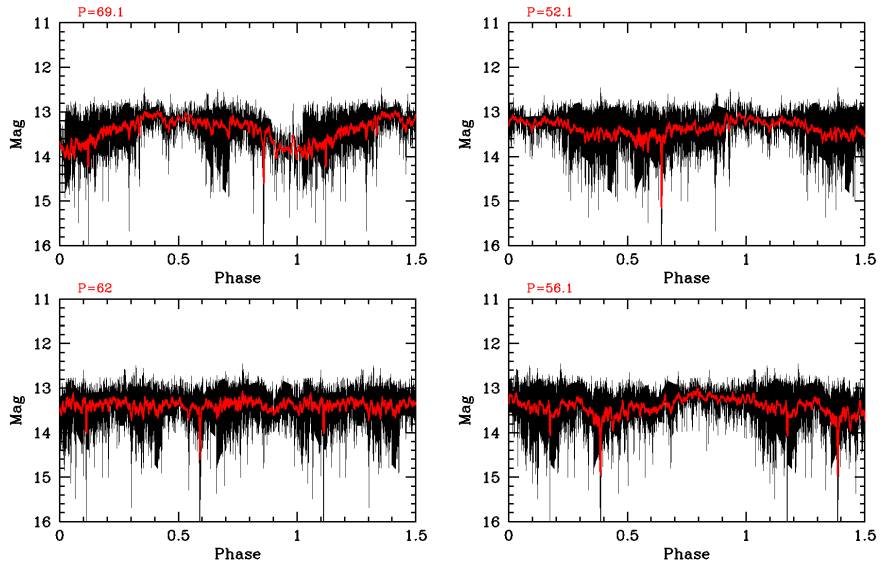


Figure 3.85: Fit of Molniya 1-62 filter R light curves with period $P = 78.14$ s.

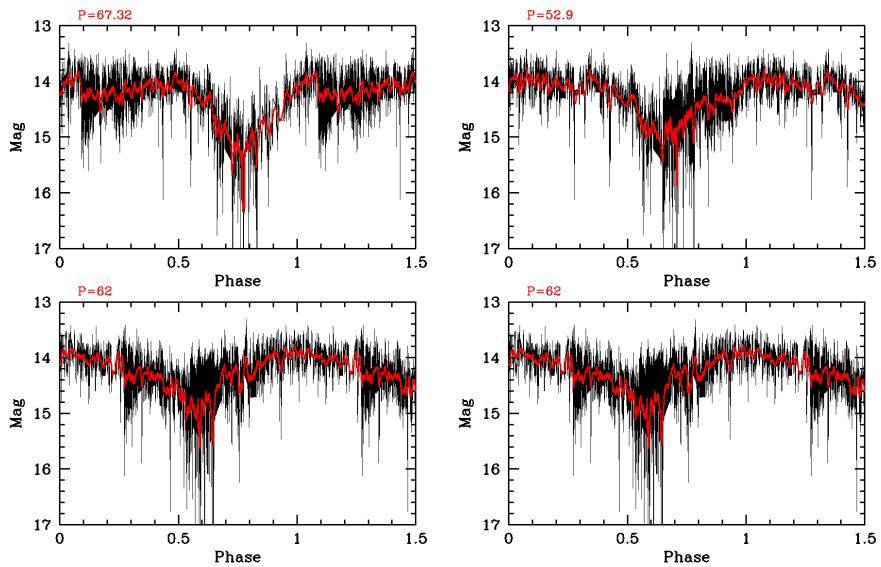


Figure 3.86: Fit of Molniya 1-62 filter V light curves with period $P = 78.14$ s.

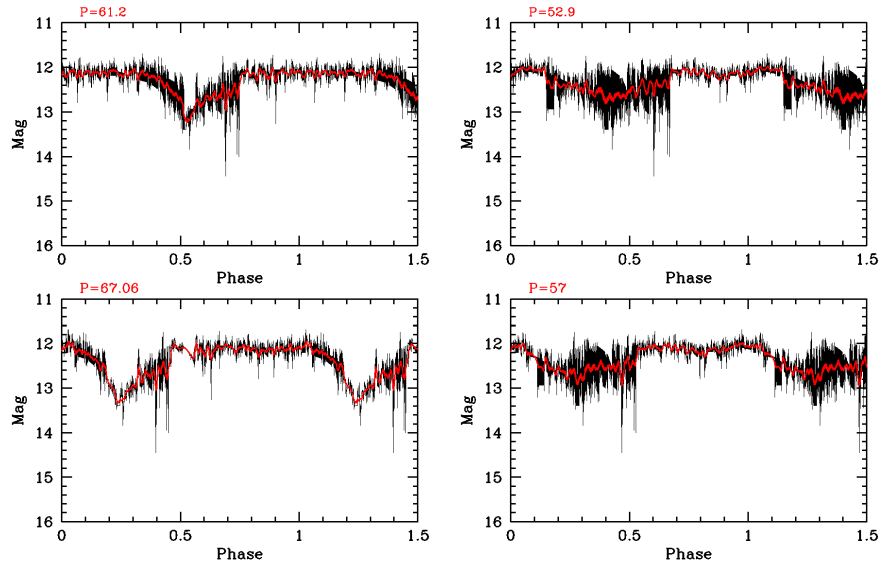


Figure 3.87: Fit of Molniya 1-62 filter I light curves with period $P = 78.14$ s.

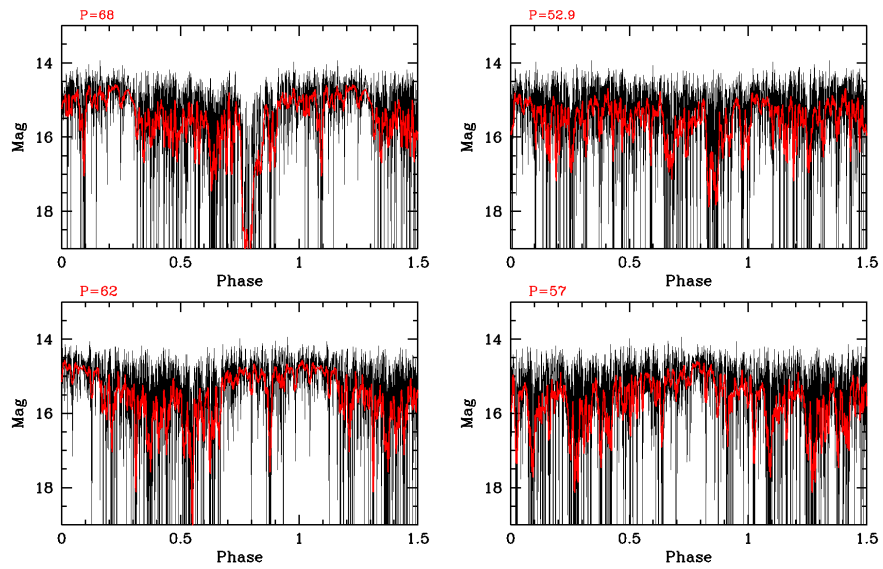


Figure 3.88: Fit of Molniya 1-62 filter B light curves with period $P = 78.14$ s.

3.18 Molniya 1-32

Molniya 1-32 appears in the light curves to be stable (Section A.3, figures A.59,A.60,A.61,A.62,A.63,A.64). Watching the magnitude vs time plot instead it's clear that the satellite is rotating with a very long period (Figure 3.90). The period is so long that with our short time exposures the satellite appears to be stable. Needless to say that the periodogram isn't able to provide any estimate of the period with the few and short exposures available.

Day	UT(start)	Airm	Expt(s)	F	D(Km)	Mag	PA
2016-08-02	21:10:57	1.04	20	V	32901	13.830	72.88
2016-08-02	21:12:53	1.04	20	I	33078	12.128	73.05
2016-08-02	21:38:04	1.05	20	I	35077	12.040	75.12
2016-09-26	18:38:04	1.40	3	R	16993	14.264	110.82
2016-09-26	18:41:01	1.37	3	R	17502	13.690	109.93
2016-09-26	18:43:02	1.35	3	I	17840	13.429	108.64
2016-09-26	18:45:02	1.33	3	V	18177	15.298	107.82
2016-09-26	18:47:01	1.31	3	B	18513	16.458	107.03
2016-09-26	18:48:59	1.30	6	B	18847	16.669	106.27
2016-09-26	18:50:59	1.29	6	R	19180	14.461	105.53
2016-09-26	18:52:59	1.27	6	I	19510	13.424	104.82
2016-09-26	18:54:59	1.26	6	V	19838	14.658	104.13
2016-09-26	18:56:59	1.25	6	B	20165	15.443	103.46
2016-09-26	18:59:59	1.24	12	R	20649	10.651	102.51
2016-09-26	19:01:58	1.23	12	I	20969	12.488	101.9
2016-09-26	19:05:59	1.22	12	V	21601	14.183	100.73
2016-09-26	19:07:59	1.22	12	B	21913	15.682	100.17

Table 3.26: Molniya 1-32 data

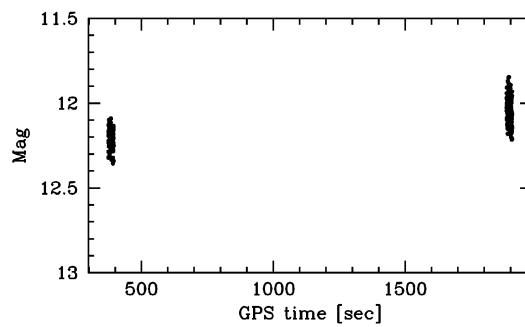


Figure 3.89: Molniya 1-32 magnitude vs time in I, night 2016/08/02-03. There's evidence of a long rotational period.

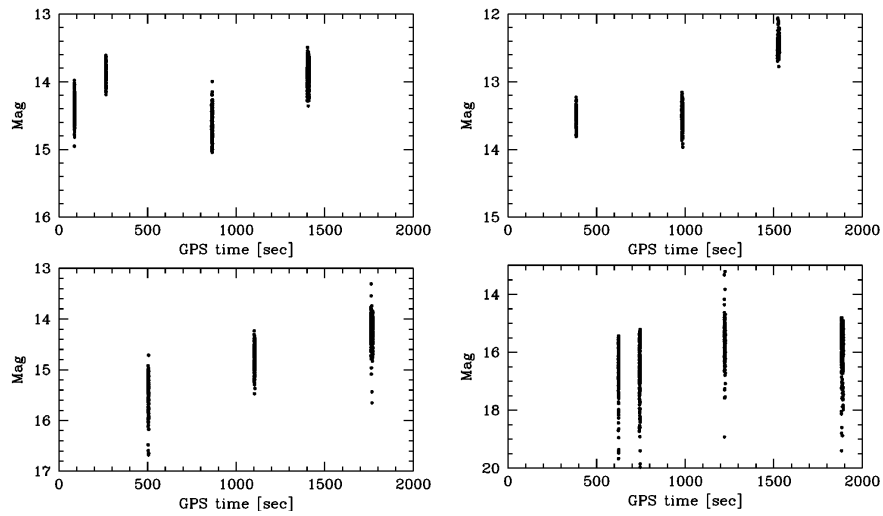


Figure 3.90: Molniya 1-32 magnitude vs time in filter R (top left), V (bottom left), I (top right) and B (bottom right), night 2016/09/26-27. There's a evidence of a long rotational period.

3.19 Molniya 3-40

Molniya 3-40 appears in the light curves to be stable (Section A.3, figures A.65,A.66, A.67,A.68). Watching the magnitude vs time plot instead it's clear that the satellite is rotating with a very long period (Figure 3.91). The period is so long that with our short time exposures the satellite appears to be stable. Once again the periodogram isn't able to provide any estimate of the period with the few and short exposures available.

Day	UT(start)	Airm	Expt(s)	F	D(Km)	Mag	PA
2016-09-26	22:10:56	1.31	20	R	34924	13.050	83.08
2016-09-26	22:13:44	1.3	20	I	35128	12.137	82.56
2016-09-26	22:15:38	1.3	20	V	35261	13.699	82.22
2016-09-26	22:17:39	1.3	20	B	35391	14.851	81.88
2016-09-26	22:19:39	1.3	20	R	35520	12.933	81.54
2016-09-26	22:21:39	1.3	20	I	35646	11.946	81.2
2016-09-26	22:23:39	1.29	20	V	35771	13.688	80.87
2016-09-26	22:25:39	1.29	20	B	35893	15.521	80.54
2016-09-26	22:30:39	1.29	20	R	36189	14.473	79.72
2016-09-26	22:32:38	1.28	20	I	36304	12.916	79.4
2016-09-26	22:36:39	1.28	20	V	36527	14.243	78.76
2016-09-26	22:43:39	1.28	20	B	36898	14.561	77.65

Table 3.27: Molniya 3-40 data

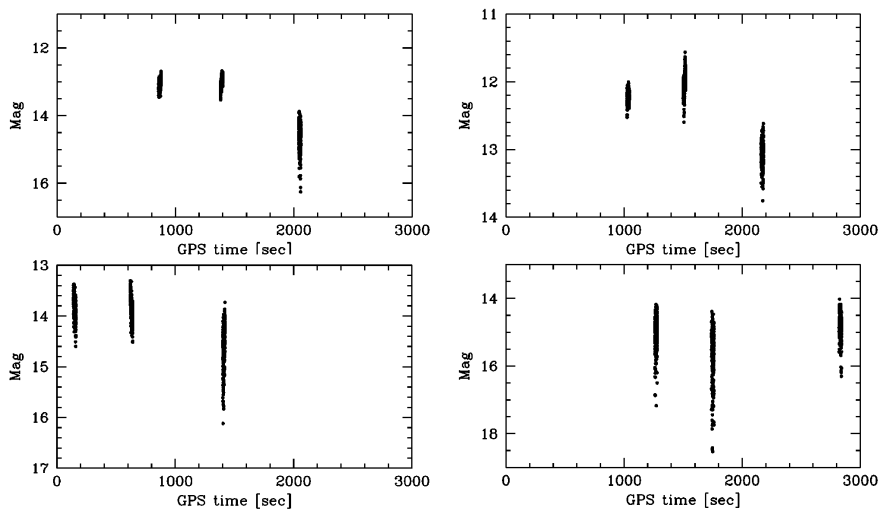


Figure 3.91: Molniya 3-40 magnitude vs time in filter R (top left), V (bottom left), I (top right) and B (bottom right), night 2016/09/26-27. There's a clear presence of a long rotational period.

3.20 Molniya 3-50

Molniya 3-50 appears in the light curves to be stable (Section A.3, figures A.69,A.70, A.71,A.72,A.73; Section A.4, figures A.91,A.92). Watching the magnitude vs time plot instead it's clear that the satellite is rotating with a very long period (Figure 3.91). The period is so long that with our short time exposures the satellite appears to be stable. Once again the periodogram isn't able to provide any estimate of the period with the few and short exposures available.

Day	UT(start)	Airm	Expt(s)	F	D(Km)	Mag	PA
09/26/16	23:53:59	1.34	12	R	25884	13.100	78.47
09/26/16	23:55:59	1.34	12	I	25607	11.824	78.8
09/26/16	23:57:58	1.35	12	V	25327	13.088	79.13
09/26/16	23:59:58	1.35	12	B	25044	15.342	79.47
09/27/16	00:01:59	1.36	12	R	24758	14.457	79.65
09/27/16	00:03:59	1.37	12	I	24469	12.103	80.19
09/27/16	00:06:00	1.37	12	V	24177	13.949	80.56
09/27/16	00:07:58	1.38	12	B	23882	14.655	80.95
09/27/16	00:09:59	1.39	12	R	23584	12.383	81.35
09/27/16	00:11:59	1.39	12	I	23283	10.600	81.76
09/27/16	00:13:58	1.4	12	V	22979	13.319	82.19
09/27/16	00:15:59	1.41	12	V	22672	14.108	82.62
09/27/16	00:17:59	1.42	12	B	22362	15.768	83.08
09/27/16	23:04:00	1.28	20	R	31377	13.743	71.96
09/27/16	23:06:59	1.29	20	I	31059	12.315	72.25
09/27/16	23:09:00	1.29	25	V	30844	13.910	72.45
09/27/16	23:11:59	1.29	25	B	30515	14.283	72.75
09/27/16	23:13:54	1.29	30	R	30293	12.639	72.96

Table 3.28: Molniya 3-50 data

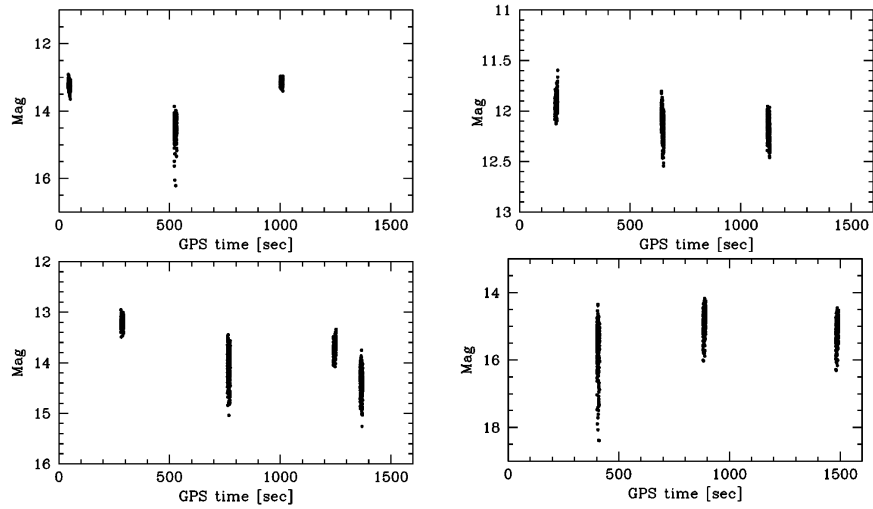


Figure 3.92: Molniya 3-50 magnitude vs time in filter R (top left), V (bottom left), I (top right) and B (bottom right), night 2016/09/26-27. There's a clear presence of a long rotational period.

3.21 Molniya 3-13

We have only three exposures of Molniya 3-13 that are shown in Section A.6, Figure A.155. In filter R and B light curves the satellite seems to be stable, while in Filter V LC there's a clear evidence of the satellite spinning. The period estimate is impossible with this few exposures.

Day	UT(start)	Airm	Expt(s)	F	D(Km)	Mag	PA
2106-12-22	21:04:59	10	1.38	R	35860	12.773	40.04
2106-12-22	21:07:58	20	1.37	B	36079	13.219	40.51
2106-12-22	21:09:59	20	1.37	V	36223	10.271	40.82

Table 3.29: Molniya 3-13 data

3.22 Molniya 1-56

We have only four exposures of Molniya 1-56 that are shown in Section A.4, Figure A.87. In every filter the satellite seems to be stable.

Day	UT(start)	Airm	Expt(s)	F	D(Km)	Mag	PA
2016-09-27	18:19:59	1.1	20	R	31811	11.873	58.7
2016-09-27	18:21:59	1.1	20	I	31995	11.990	58.74
2016-09-27	18:24:58	1.1	20	V	32266	12.872	58.81
2016-09-27	18:26:59	1.1	20	B	32444	14.520	58.84

Table 3.30: Molniya 1-56 data

3.23 Molniya 3-24

We have only four exposures of Molniya 3-24 that are shown in Section A.4, Figure A.97. In filter R,I and B light curves the satellite seems to be stable, while in Filter V LC there's evidence of the satellite spinning. The period estimate is impossible with this few exposures.

Day	UT(start)	Airm	Expt(s)	F	D(Km)	Mag	PA
2016-09-28	01:20:59	1.49	20	R	25955	13.315	98.67
2016-09-28	01:23:59	1.48	20	I	26246	13.340	99.1
2016-09-28	01:26:59	1.48	20	V	26529	13.957	99.52
2016-09-28	01:29:59	1.48	20	B	26807	14.854	99.94

Table 3.31: Molniya 3-13 data

3.24 Molniya 3-51

Periodogram analysis of Molniya 3-51 light curves was a difficult task because of the noisiness of the LC (Section A.1, Figures A.30, A.31, A.32, A.33, A.34, A.35, A.36, A.37). The periodogram results are plotted in figure 3.93 and figure 3.94. As you can see the periodograms show alias phenomena in all filters, and there are many peaks in the signal-to-noise ratio. There is inconsistency in the position of the peaks between different filters. We try to fit the light curves with many different periods but non of the values found was good for all the filters. The failure of the periodogram analysis is ascribable to the noisiness of the light curves. In conclusion we weren't able to find a certain period for Molniya 3-51.

Day	UT(start)	Airm	Expt(s)	F	D(Km)	Mag	PA
2016-08-01	21:39:55	1.445	15	V	24891	15.455	111.36
2016-08-01	21:41:47	1.445	15	R	24647	14.487	111.03
2016-08-01	21:42:38	1.444	15	I	24524	13.498	110.87
2016-08-01	21:43:27	1.441	15	B	24524	16.408	110.7
2016-08-01	21:46:13	1.438	15	I	24023	13.542	110.42
2016-08-01	21:47:02	1.438	15	B	24023	16.402	110.21
2016-08-01	21:48:04	1.438	15	V	23895	15.494	110.04
2016-08-01	21:48:55	1.437	15	R	23767	14.236	109.88
2016-08-01	21:49:46	1.436	15	I	23637	13.498	109.71
2016-08-01	21:50:36	1.435	15	B	23507	16.310	109.55
2016-08-01	22:10:54	1.413	15	V	20702	15.826	106.16
2016-08-01	22:11:46	1.414	15	R	20552	14.801	105.99
2016-08-01	22:12:37	1.414	15	I	20401	14.437	105.81
2016-08-01	22:17:48	1.407	15	V	19633	16.061	104.94
2016-08-01	22:18:39	1.407	15	R	19477	14.378	104.76
2016-08-01	22:19:30	1.407	15	I	19319	14.106	104.59
2016-08-01	22:20:21	1.407	15	B	19161	16.854	104.59

Table 3.32: Molniya 3-51 data

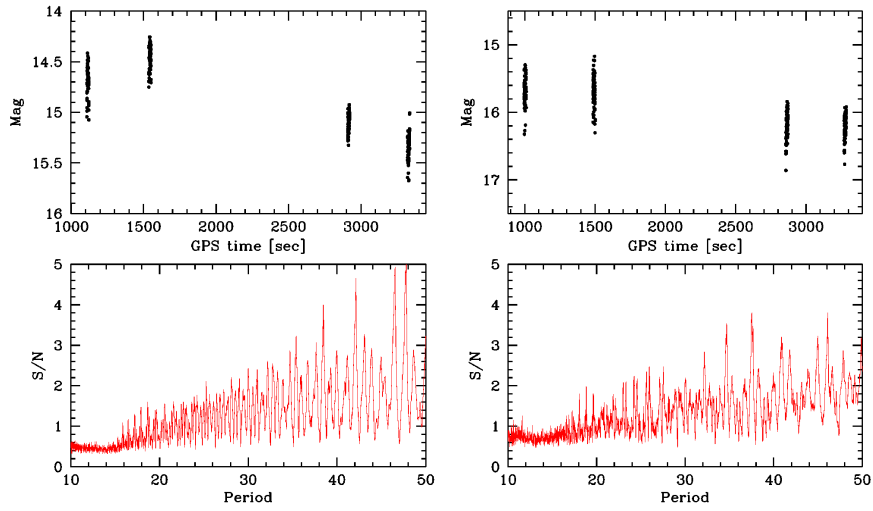


Figure 3.93: Molniya 3-51 periodogram analysis in filter R (left) and V (right)

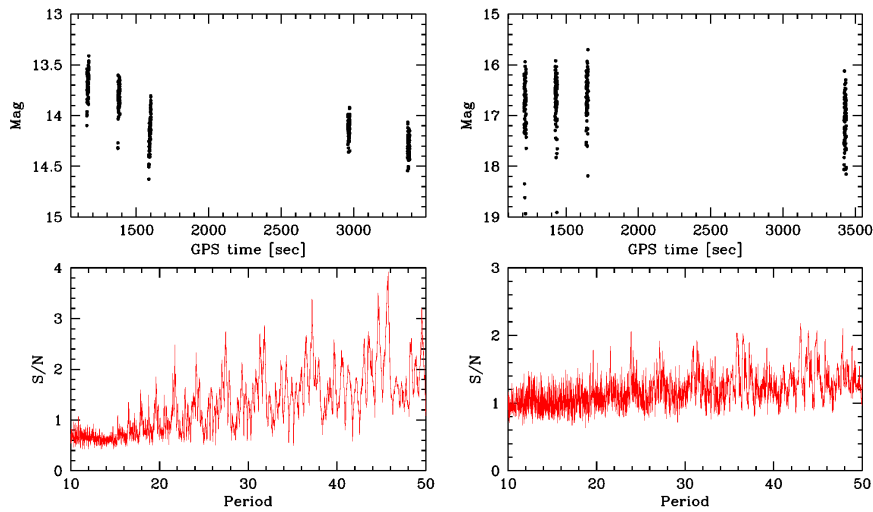


Figure 3.94: Molniya 3-51 periodogram analysis in filter I (left) and B (right)

3.25 Molniya 1-90

Periodogram analysis of Molniya 1-90 light curves was made on the December observations because the November exposures was too short compared to the period to provide some results. The results of periodogram analysis are plotted in figure 3.95, figure 3.96, figure 3.97 and figure 3.98. Periodogram in R filter shows two peaks in the signal to noise ratio near $P = 64.5$ s and $P = 96$ s, the peaks are found also in the other filter even if partially hidden by aliasing phenomena due to the scarce sampling of the light curve. The exact position of the peaks is plotted in Table 3.33. Filter R analysis finds two peaks near $P = 96$, the fit with this two values is plotted in Figure 3.99, the two peaks have similar signal-to-noise ratio and the fit seems to be good for both the values. To provide an estimate of the rotational period we need to decide which one of the two values found ($P \approx 65$ s and $P \approx 96$ s) is the correct one. The signal-to-noise seems to suggest that the higher is the correct one, but the fit especially in R filter seems to be better with $P \approx 65$ s because it reproduces a characteristic pattern that can be seen in the light curves (Section A.7, figures A.192, A.193, A.194, A.195, A.196). As you can see there is a small spike of brightness near the slightest of the light curve, this spike is well reproduced by the fit with $P \approx 65$ s. Anyway more observations are needed to decide with certainty which one of these two values is the correct period for Molniya 1-90.

Filter	Period(s)	Error(s)
R	64.5	1.0
R	95.5/96.1	2.0
I	64.6	1.0
I	96.9	1.0
V	66.5	1.0
V	96	1.0
B	64.7	1.0
B	97.1	1.0

Table 3.33: Molniya 1-90 periods found with periodogram analysis

Day	UT(start)	Airm	Expt(s)	F	D(Km)	Mag	PA
2016-11-26	18:02:58	1.05	5	R	12660	11.653	48.12
2016-11-26	18:04:58	1.05	5	R	13053	11.867	47.44
2016-11-26	18:06:58	1.06	5	I	13441	11.693	46.83
2016-11-26	18:08:58	1.06	5	V	13824	12.122	46.27
2016-11-26	18:10:58	1.07	7	B	14201	13.194	45.77
2016-11-26	18:12:58	1.07	7	R	14573	11.598	45.32
2016-11-26	18:14:57	1.08	7	I	14940	11.734	44.91
2016-11-26	18:16:58	1.08	7	V	15300	12.922	44.54
2016-11-26	18:18:58	1.09	7	B	15655	13.292	44.2
2016-11-26	18:20:57	1.09	7	R	16004	11.474	43.9
2016-11-26	18:22:57	1.1	7	I	16348	11.028	43.63
2016-11-26	18:24:27	1.1	7	V	16517	12.196	43.5
2016-11-26	18:25:58	1.11	7	B	16852	13.272	43.27
2016-12-23	23:07:53	10	1.11	R	25888	11.170	45.63
2016-12-23	23:10:44	30	1.11	R	26396	11.318	45.05
2016-12-23	23:14:39	30	1.1	R	26488	11.960	44.28
2016-12-23	23:17:43	30	1.1	R	26547	11.716	43.72
2016-12-23	23:20:39	30	1.09	R	26599	11.321	43.16
2016-12-23	23:23:39	30	1.09	B	26642	12.538	42.61
2016-12-23	23:26:40	30	1.09	V	26678	12.335	42.06
2016-12-23	23:30:39	30	1.08	R	26713	11.812	41.34
2016-12-23	23:33:40	30	1.08	I	26730	10.871	40.8
2016-12-23	23:36:40	30	1.08	B	26739	12.000	40.27
2016-12-23	23:40:40	30	1.07	V	26739	13.210	39.57
2016-12-23	23:43:39	30	1.07	R	26730	12.181	39.04
2016-12-23	23:46:40	30	1.07	I	26714	10.872	38.53

Table 3.34: Molniya 1-90 data

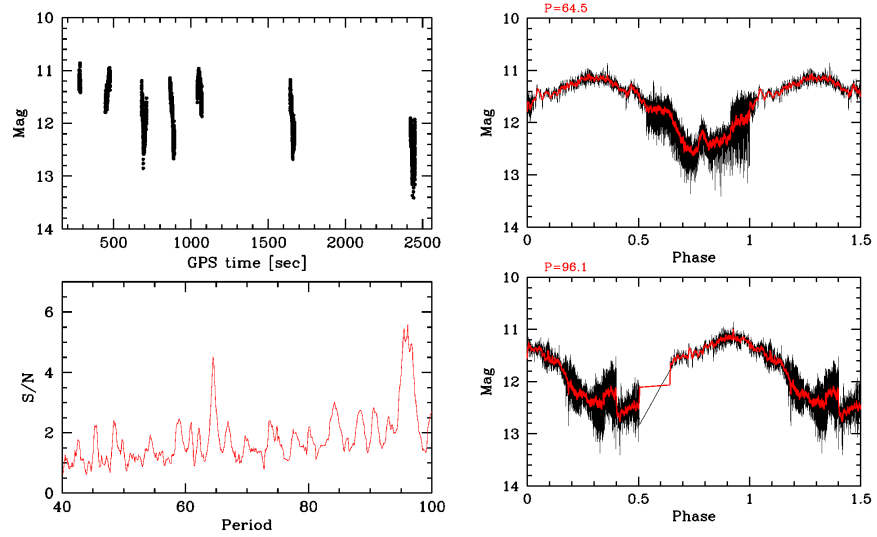


Figure 3.95: Filter R periodogram analysis of Molniya 1-90.

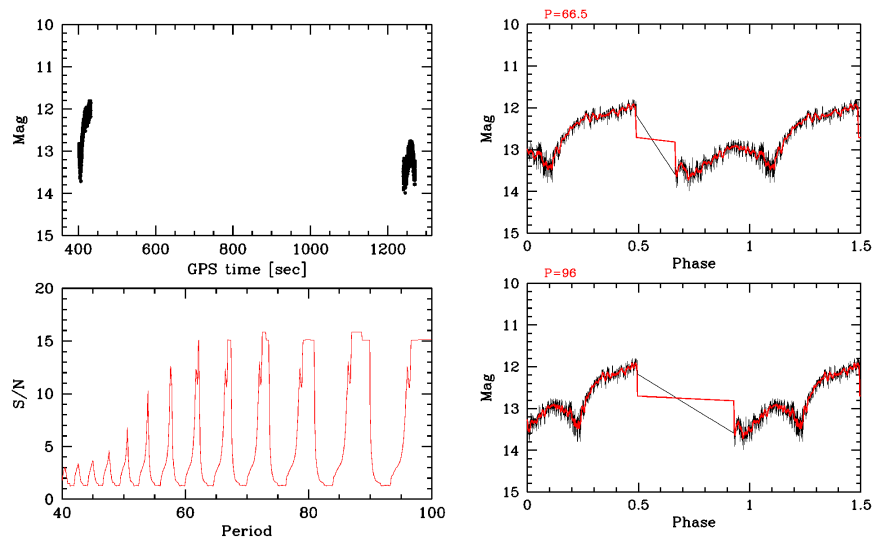


Figure 3.96: Filter V periodogram analysis of Molniya 1-90.

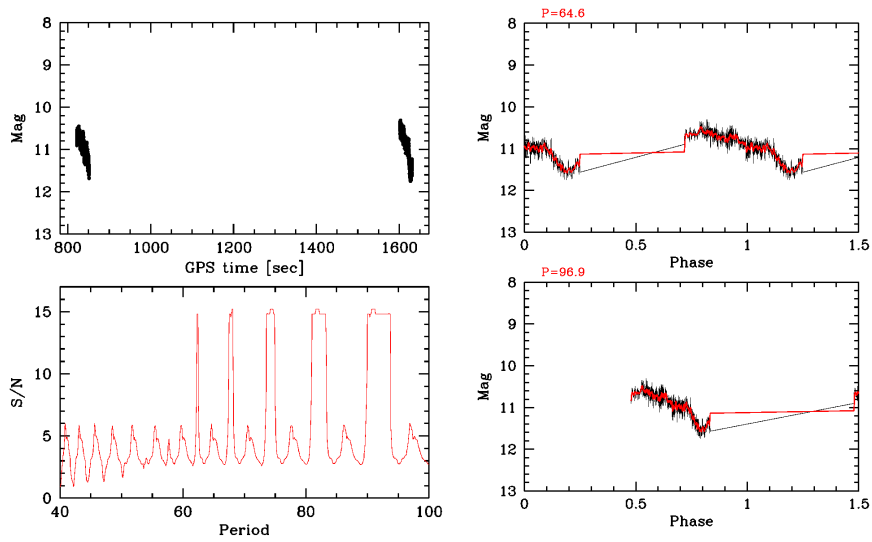


Figure 3.97: Filter I periodogram analysis of Molniya 1-90.

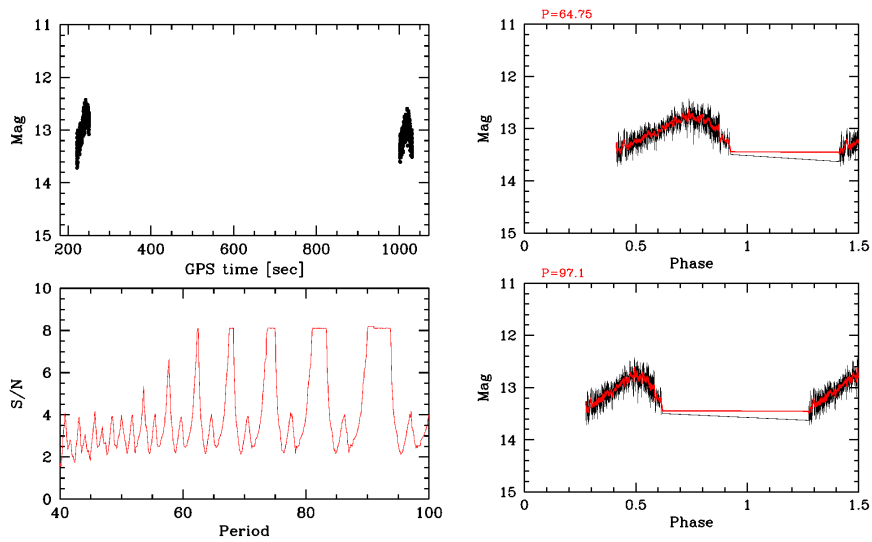


Figure 3.98: Filter B periodogram analysis of Molniya 1-90.

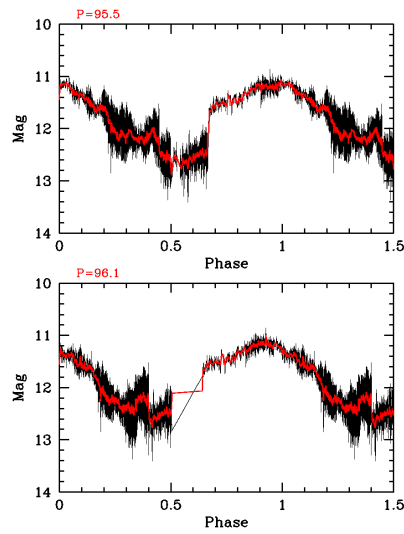


Figure 3.99: Filter R fit of Molniya 1-90 light curves with period $P = 95.5$ s and 96.1 s.

3.26 Molniya 1-80

Watching at the light curves of Molniya 1-80 (Section A.1, figures A.20,A.21 A.22,A.23,A.24, A.25,A.26,A.27,A.28,A.29) the satellite seems to be stable. Watching the magnitude vs time plot (Figure 3.100) instead seems to be evidence of rotation. Anyway the period is too long for our exposures and the periodogram analysis wasn't satisfactory in all filters.

Day	UT(start)	Airm	Expt(s)	F	D(Km)	Mag	PA
2016-08-01	22:27:27	1.205	15	V	18138	13.353	88.46
2016-08-01	22:28:19	1.202	15	R	18307	12.553	88.36
2016-08-01	22:29:10	1.199	15	I	18476	11.723	88.27
2016-08-01	22:30:00	1.196	15	B	18644	14.063	88.17
2016-08-01	22:54:07	1.144	15	V	22455	13.559	86.52
2016-08-01	22:54:57	1.143	15	R	22604	12.755	86.47
2016-08-01	22:55:48	1.142	15	I	22752	11.811	86.42
2016-08-01	22:56:40	1.141	15	B	22899	14.647	86.37
2016-08-01	22:57:40	1.14	15	V	23045	13.663	86.32
2016-08-01	22:58:30	1.139	15	R	23191	13.229	86.28
2016-08-01	22:59:21	1.138	15	I	23191	12.189	86.27
2016-08-02	01:03:05	1.079	40	V	35420	13.119	83.35
2016-08-02	01:04:21	1.079	40	R	35534	12.602	83.34
2016-08-02	01:05:36	1.078	40	I	35591	11.459	83.31
2016-08-02	01:11:33	1.076	40	V	35918	13.599	83.22
2016-08-02	01:12:49	1.075	40	R	35971	12.576	83.21
2016-08-02	01:14:05	1.075	40	I	36022	11.713	83.19
2016-08-02	01:15:21	1.074	40	B	36125	14.387	83.18
2016-08-02	01:41:22	1.064	40	V	37216	13.292	82.81
2016-08-02	01:42:37	1.064	40	R	37289	12.218	82.78
2016-08-02	01:43:53	1.063	40	I	37325	11.316	82.76
2016-08-02	01:45:09	1.062	40	B	37360	14.764	82.75
2016-08-02	01:46:36	1.062	40	V	37428	13.730	82.72
2016-08-02	01:47:52	1.062	40	R	37462	12.818	82.71
2016-08-02	01:49:08	1.061	40	I	37495	11.316	82.7
2016-08-02	01:50:23	1.061	40	B	37559	14.452	82.68

Table 3.35: Molniya 1-80 data

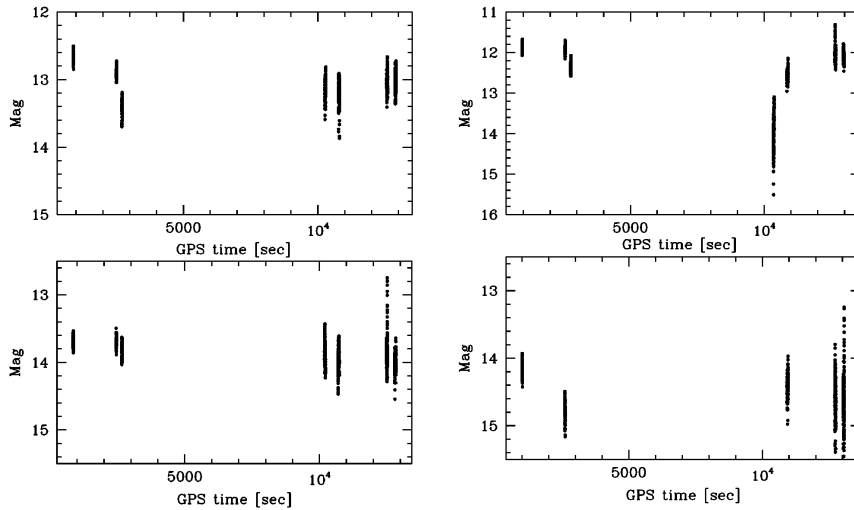


Figure 3.100: Filter R (top left), V (bottom left), I (top right) and B (bottom right) magnitude vs time plot for Molniya 1-90.

3.27 Molniya 1-86

Molniya 1-86 appears in the light curves to be stable (Section A.5, figures A.117,A.118, A.119,A.120). Watching the magnitude vs time plot instead appears that the satellite is rotating with a very long period (Figure 3.101). The period is so long that with our short time exposures the satellite appears to be stable. Once again the periodogram isn't able to provide any estimate of the period with the few and short exposures available.

Day	UT(start)	Airm	Expt(s)	F	D(Km)	Mag	PA
2016-11-26	21:15:59	1.54	1	R	4030	12.529	80.88
2016-11-26	21:19:59	1.26	1	I	4408	11.554	68.57
2016-11-27	03:16:00	1.23	1	B	14371	14.048	79.8
2016-11-27	03:17:51	1.25	10	B	14433	15.519	80.76
2016-11-27	03:19:51	1.28	10	V	14490	13.220	81.72
2016-11-27	03:21:51	1.3	10	R	14543	12.462	82.69
2016-11-27	03:23:51	1.32	10	I	14590	12.865	83.66
2016-11-27	03:25:50	1.35	10	B	14632	13.989	84.63
2016-11-27	03:27:51	1.37	10	V	14670	12.903	85.61
2016-11-27	03:29:50	1.4	10	R	14703	13.139	86.59
2016-11-27	03:31:51	1.43	10	I	14731	11.834	87.58

Table 3.36: Molniya 1-86 data

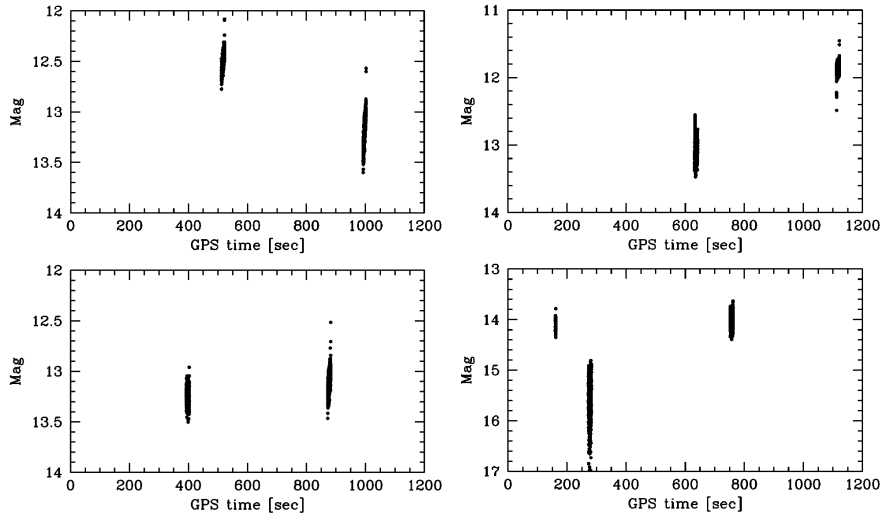


Figure 3.101: Molniya 1-86 magnitude vs time in filter R (top left), V (bottom left), I (top right) and B (bottom right), night 2016/09/26-27. There's a clear presence of a long rotational period.

3.28 Meridian 2

We didn't expect Meridian 2 to rotate since it should still be in operation. Actually watching the light curves in Section A.6, images A.160,A.161,A.162,A.163,A.164, the satellite seems to be stable. The magnitude vs time plot (Figure 3.102) lastly confirms that the satellite isn't rotating.

Day	UT(start)	Airm	Expt(s)	F	D(Km)	Mag	PA
2016-12-23	00:15:55	20	1.03	R	33134	10.344	37.27
2016-12-23	00:18:55	40	1.03	R	33312	10.363	37.74
2016-12-23	00:21:56	40	1.03	B	33485	11.831	38.21
2016-12-23	00:24:01	40	1.03	R	33597	10.434	38.52
2016-12-23	00:27:26	40	1.03	V	33813	11.030	39.35
2016-12-23	00:29:55	40	1.03	I	33918	9.933	39.43
2016-12-23	00:31:55	40	1.03	B	34020	11.897	39.74
2016-12-23	00:33:56	40	1.03	V	34119	11.071	40.03
2016-12-23	00:35:56	40	1.04	R	34217	10.514	40.33
2016-12-23	00:38:03	40	1.04	I	34311	9.948	40.63
2016-12-23	00:39:58	40	1.04	B	34404	11.963	40.92
2016-12-23	00:41:57	40	1.04	V	34494	11.097	41.21
2016-12-23	00:43:59	40	1.04	R	34582	10.561	41.5
2016-12-23	00:47:58	40	1.04	I	34750	10.031	42.08

Table 3.37: Meridian 2 data

3.29 Meridian 4

We didn't expect Meridian 4 to rotate since it should still be in operation. Actually watching the light curves in Section A.6, images A.176,A.177,A.178,A.179, the satellite seems to be stable. The magnitude vs time plot (Figure 3.102) lastly confirms that the satellite isn't rotating.

Day	UT(start)	Airm	Expt(s)	F	D(Km)	Mag	PA
2016-12-23	03:26:57	20	1.49	R	28084	12.453	99.59
2016-12-23	03:29:58	20	1.48	B	28417	14.108	99.42
2016-12-23	03:31:58	20	1.47	V	28637	13.201	99.3
2016-12-23	03:33:58	20	1.47	R	28854	12.515	99.19
2016-12-23	03:35:58	20	1.46	I	29068	11.899	99.08
2016-12-23	03:37:56	20	1.45	B	29280	14.073	98.97
2016-12-23	03:39:56	20	1.45	V	29490	13.327	98.86
2016-12-23	03:41:55	20	1.44	R	29697	12.712	98.75
2016-12-23	03:43:55	20	1.44	I	29490	12.027	98.65

Table 3.38: Meridian 4 data

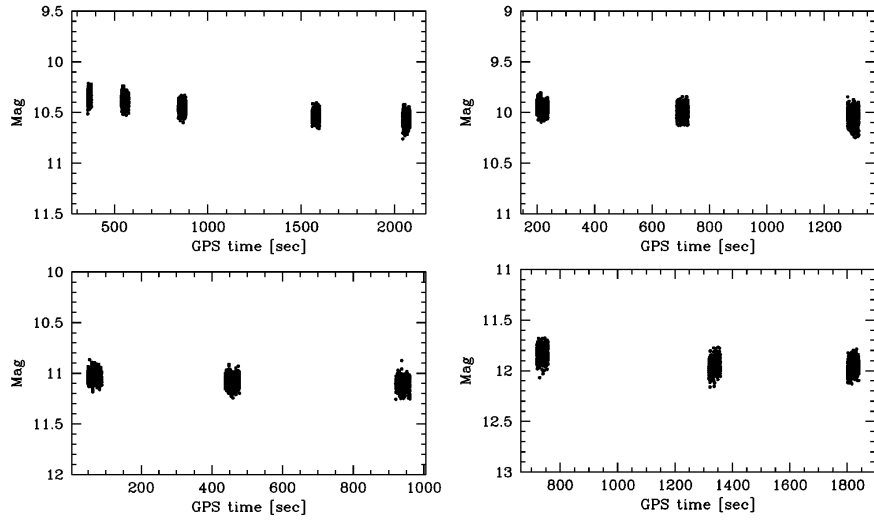


Figure 3.102: Meridian 2 magnitude vs time in filter R (top left), V (bottom left), I (top right) and B (bottom right).

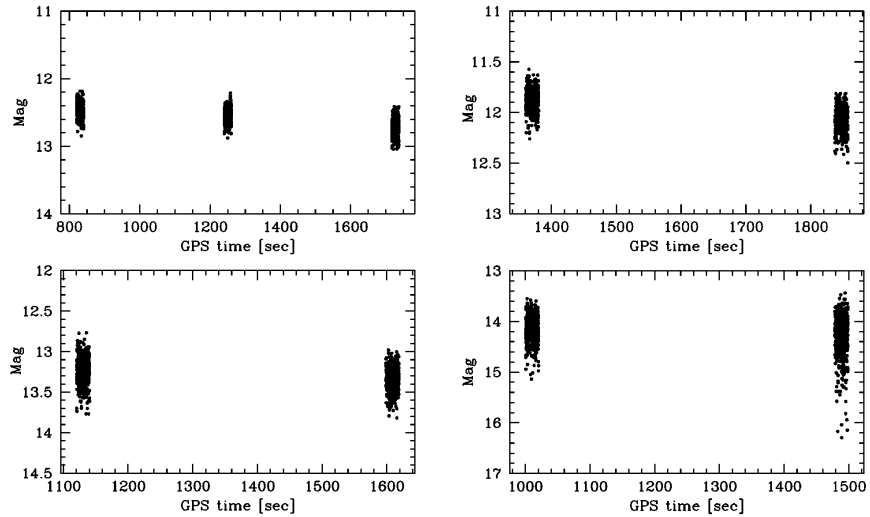


Figure 3.103: Meridian 4 magnitude vs time in filter R (top left), V (bottom left), I (top right) and B (bottom right).

3.30 The special cases of Molniya 1-86 and Molniya 1-44

Molniya 1-86 (launch date May 26, 1993) and Molniya 1-44 (launch date July 31, 1979, decay date October 23, 2017) had in 2016 very peculiar orbits. Both of them has begun their orbital decay process. It's known that the Molniya orbit in the absence of orbital settling maneuvers tends to lead the satellite to orbital decay and to atmospheric re-entry. Molniya 1-44 in the second part of 2016 was orbiting with a period of ≈ 2 hours while Molniya 1-86 was orbiting with a period of ≈ 4 hours and 15 minutes. The orbital characteristics of the two debris updated in December 2016 (using Heavensat) are plotted in Table 3.39.

Satellite	Perigee (km)	Apogee (km)	Inclination (deg)	Period (min)
Molniya 1-86	471.7	13495.0	63.0	256.0
Molniya 1-44	185.2	3089.5	62.0	119.0

Table 3.39: Orbital characteristics of Molniya 1-44 and Molniya 1-86 orbits

You can see that the orbital parameters are different than the typical Molniya orbit parameters. In particular we noticed the Perigee height is much less, so that especially for Molniya 1-44 falls into the satellite atmospheric drag region, this led to the satellite decay happened in October 23, 2017. Molniya 1-86 in 2016 had a Perigee height very close to the drag region, so that we expect that Molniya 1-86 will fall too in the next years. Due to the fast orbital velocity (the orbital period is much smaller than the other orbital periods of Molniya constellation) the apparent velocity of this two object in the sky was higher than that of a typical Molniya debris, for this reason the observation of this two object with the Cassini telescope was difficult (the tracking velocity can not overcome 100000 arcseconds per hour). We were able to observe only Molniya 1-86 and for a very short period of time and with very short exposition time (see Section 3.27), not sufficient to extract a tumbling period. To fill this gap we asked to Alain Figer, a French amateur astronomer and one of the most prominent figures in European amateur astronomy, to give us some of his observations of this two debris. As explained in Section 2.6 Figer images can not be used to study photometric or color indexes aspects, since they are produced with amateur instrumentation which are not equipped with the classic optical astronomical filters and can not be calibrated in magnitude, but are excellent to study the tumbling period of the satellite since Figer instrumentation is provided of a wide field of view, that allows very long time expositions and observation of high apparent velocity objects. Thanks to his images we were able to find a tumbling period for both the satellite. We do not include in the discussion all the images for space reasons (Figer provided us a large amount of images), we only limit ourselves reporting the application of the periodogram to the two best data sets in our possession. The periodogram results are plotted in Figure 3.104. For Molniya 1-44 the periodogram shows a clear peak near $P = 66$ s, tightening the step the periodogram shows that the peak is composed by 3 peaks at $P = 65.06$ s $P = 66.08$ s and 67.03 s, the phasing of light curves however assures us of the correct period is $P = 66.08 \pm 0.5$ s, the error is estimated as always from the peak width. For Molniya 1-86 the periodogram shows a clear

peak near $P = 122$ s, more precisely two peaks at $P = 121.3$ s and $P = 122.2$ s, despite the peak at 121.3 s seems the best of the two the phasing of the light curves sugges (watching expecially the flash phasing) that the correct period is $P = 122.2 \pm 1$ s.

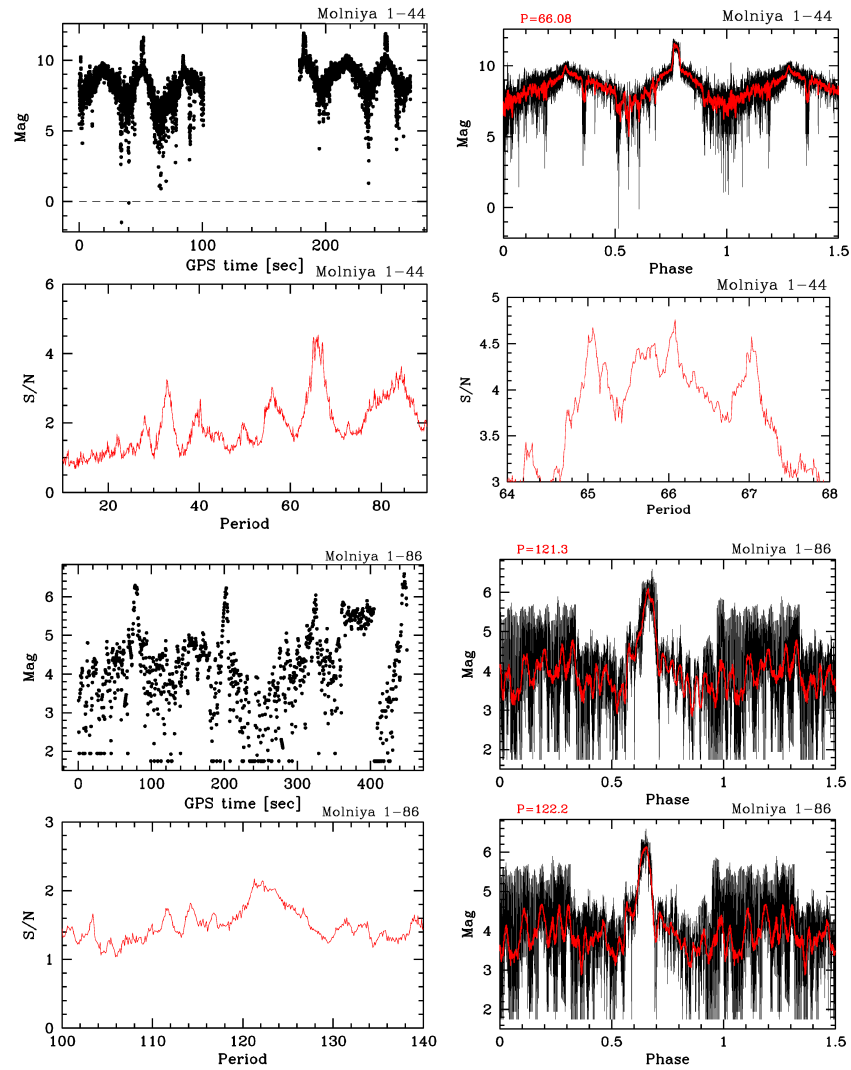


Figure 3.104: Molniya 1-44 (top) and Molniya 1-86 (bottom) periodogram analysis of Figer images, the magnitude in the y axis of the top left plot is not a true magnitude is calculated as the logarithm of the counts multiplied by the number of pixels on which the light curve was mediated.

Chapter 4

Molniya and Meridian constellation general properties

4.1 Phase angle - Magnitude relation

We investigated the relation between the magnitude of the satellites and the phase angle at the time of exposition. To thighten the data and to improve the reliability of the models we add to the data taken in the nights presented in Appendix A other data taken by professor Alberto Buzzoni during 2014,2015 and 2016 at the Osservatorio Astronomico di Loiano and Guillermo Haro Observatory. The magnitude should decrease, to a first approximation, while the phase angle increases. This is obvious because the phase angle (ϕ) represent the portion of the satellite that isn't illuminated by the Sun, or in other words, the portion of the satellite illuminated by the Sun is equal to $180^\circ - \phi$. The plot of our data is presented in Figure 4.1.

As you can see here we find the expected trend, the magnitude decrease with the growth of phase angle. There are nevertheless some points that detach from the principal trend. This is due to the fact that some of the light curves present flashes and drops in magnitude due to the spinning of the satellite. Flashes accours only when the satellite solar panels are oriented exactly in the direction that allows them to reflect light to the observer, in this case the light is reflected and not re-emitted by the satellite. This means that in the equation for magnitude that will be soon presented (4.3,4.4) the albedo term disappears, causing the magnitude to be lower with respect to the normal case (we remind that the lowest is the magnitude the brightest is the observed target). The drop in magnitude are again probably due to peculiar configuration of the satellite with respect to the position of the Sun and the observer, like effects of self-shadowing, that cause a temporary disappearance of the satellite in the light curve. Flashes and drops causes the integrated magnitude of the light curve to be lower or grater respectively, causing the detach of some points from the principal trend in the Phase angle - magnitude plot.

The interpretation of the data involve many different topics of space de-

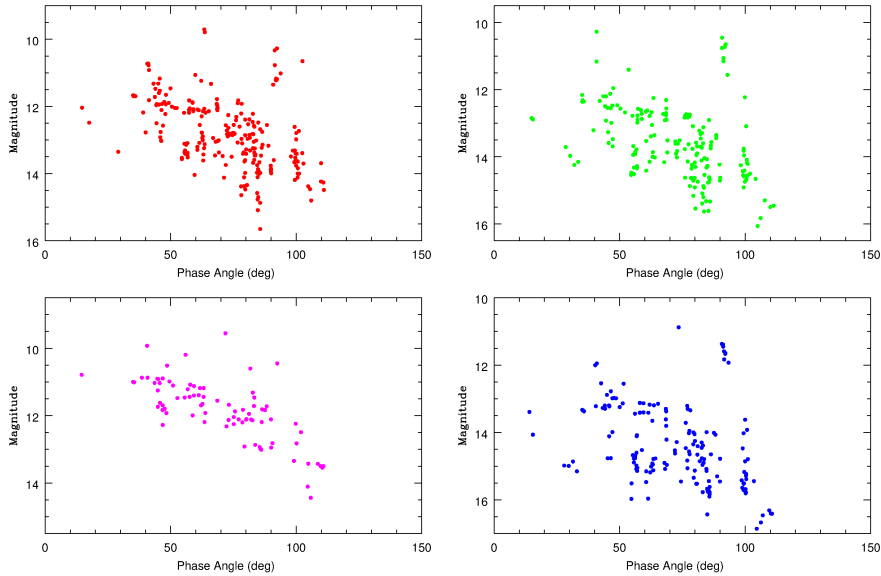


Figure 4.1: Phase angle vs Magnitude plots for observed satellite of Molniya constellation. The magnitude is the integrated magnitude of each light curve, a magnitude calibration and distance correction have been applied. The colors are referred to the filters, blue for filter B, red R, green V and magenta I.

bris science. The first approach was to fit the data with a linear regression $mag = \alpha\phi + \beta$. The linear fit could provide a simple relation (Hejduk (2010)) to describe the trend of the data. The plot of this first fit is presented in Figure 4.2. Obviously the linear fit doesn't lie on a physical model but is only a phenomenological description of the relation. A simple test to check its physical validity could be done focusing on the zero points predicted by the linear fit. With zero point we refer to the predicted magnitude at null phase angle. The zero point is related to the physical properties of the satellite by the following relations derived by equations 4.3,4.4 considering phase function equal to one.

$$mag_{ZP} = M_{AppSun} - 2.5 \cdot \log(F_{reflected}) \quad (4.1)$$

$$F_{ref} = A_{sat} \cdot a / 4\pi d^2 \quad (4.2)$$

The second equation relate the value of the portion of light reemitted by the satellite to its area (A) to the albedo value (a) and to the distance of the satellite from the observer (d). The albedo term and the area are difficult to estimate, the area depends on the shape of the satellite, and since the shape of Molniya debris isn't regular (there are many different features like solar panels) the area depends also on the orientation of the satellite during the exposition. For the most of the expositions the satellites were found spinning for that reason the reflecting area wasn't constant on the exposition. Therefore the A term is in fact an average value of the satellite area during the exposition. For these reasons the estimate of this term is very difficult. The albedo term depends on the material with which the various components of the satellite are built. The specific value is quite impossible to calculate since it should be averaged on the

many different components of the satellite, considering the area of each part and the average exposition time in which these components have been exposed to light. In addition there is the fact that the albedo of the material depends on their age, since in space an effect of deterioration of the materials accours, due to collisions with small debris and the prolonged exposition to the solar radiation (Abercromby et al. (2006)). The determination of the albedo value for Molniya space debris falls outside the scope of our work. Nevertheless a test on the validity of the zero points could be done. In fact knowing the predicted magnitude from the fit we can calculate the corresponding value of A_{eff} (that represent the product of the satellite reflecting area and the albedo value) and compare it with some representative values of area and albedo for Molniya debris. Let's take for example the R filter zero point magnitude calculated with the linear fit of the data. $Mag_R = 10.90419$ corresponds to a A_{eff} value of $\approx 6.86m^2$. As we where saying earlier the reflecting area isn't simple to estimate, since theoretically speaking it varies during the exposition because of the satellite spinning. Even if the satellite is stable it depends on its orientation along the line of sight. An acceptable estimate of this parameter is provided by the satellite RCS (Radar Cross Section) that could be considered as an upper limit for the area value. The RCS value varies from satellite to satellite even if the satellite has the same shape and structure, and for Molniya debris has a typical value of $\approx 15m^2$. Considering the RCS as an estimate of the satellite reflecting area the albedo value results to be $a \approx 0.46$. This value seems to be higher than expected since the average value of albedo for a typicale space debris is ≈ 0.152 (Mulrooney et al. (2008)). Moreover we remind that the RCS value for the reflecting area is an upper limit of the real value for this parameter, which means that the albedo value should be actually $a \geq 0.46$ for filter R images. With the same reasoning we caluclate the lower limits for every filter, we found the following values of albedo term in the respective filer: $a_V \geq 0.5, a_I \geq 2.95$ and $a_B \geq 0.43$.

It's clear that this albedo values are too high considering also that we choose an area that represent an upper limit of the real area value, that because of the spinning of the satellite during the exposition should be smaller than the RCS value, which causes the albedo value to be higher than that calculated with the RCS value. The albedo value for I filter images is higher than the other, it is even greater than one, and since the albedo is by definition between zero and one, the value found with our data is surely wrong. This is due to the lack of data in that filter, in fact the data provided by professor Alberto Buzzoni were only made in filter R,V and B, for this reason the I filter is less sampled. This lack of data causes the flashes points to be more determining in making steeper the slope of the linear regression causing the zero point to be brighter and consequently the albedo value became higher. The flashes generally could affect the slope and the zero points of the linear regression and could be the causes of the linear regression predictions failure. For this reason a cutting of the data has been made to clean the plot from all the unreliable points due to flashes or drops in the light curves. The cutting has been made estimating the

RMS $\sigma = \sqrt{\frac{\sum_{i=1}^{n_{points}} (mag_{true}(i) - mag_{model}(i))^2}{n_{points} - 1}}$ value and by rejecting all the point which detached more than 2σ from the relation. The cutting process has been applied two times before the reevaluation of the fit. The results of this cutting is presented in Figure 4.3.

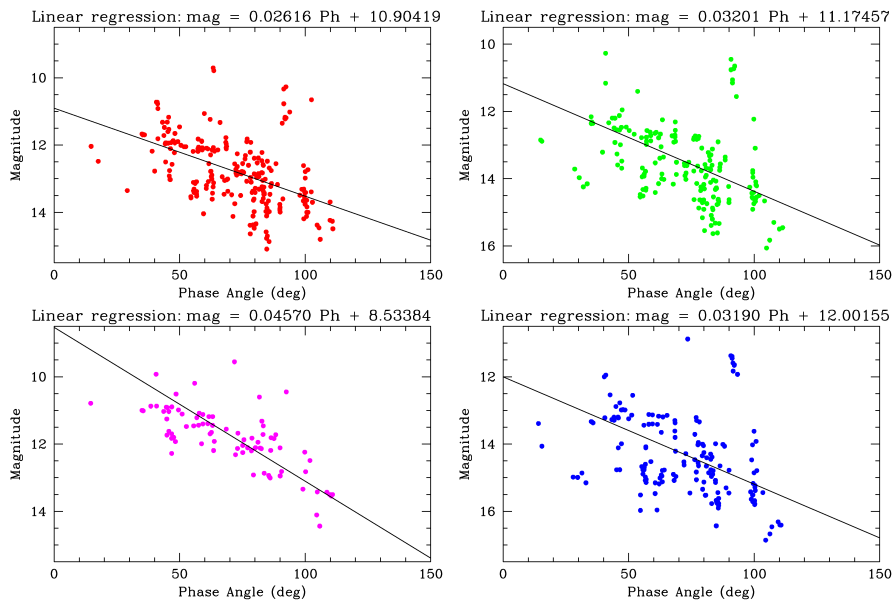


Figure 4.2: Linear regression for Phase angle - magnitude plot.

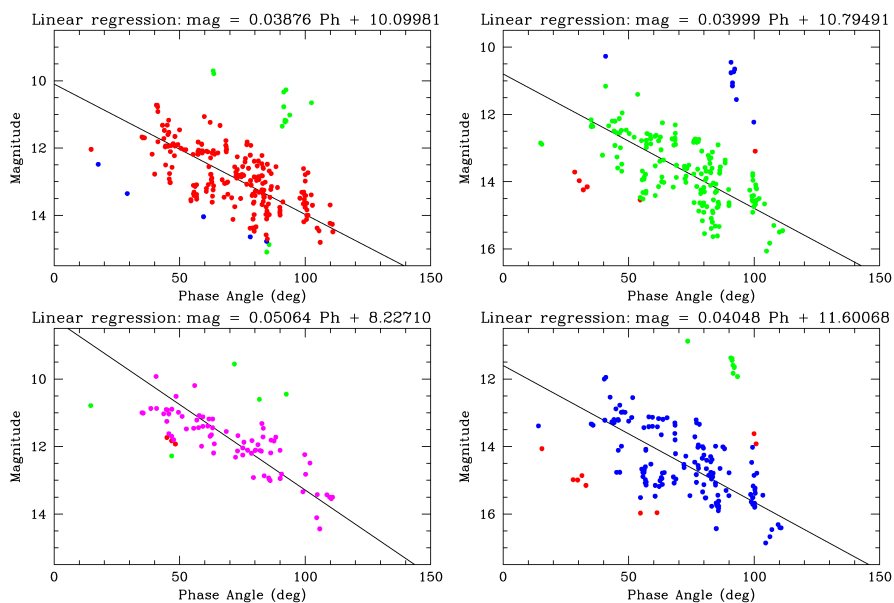


Figure 4.3: Linear regression for Phase angle - magnitude plot after the cutting process, every filter has the point that hasn't been eliminated by the cutting process colored by the filters colour and other two colors that represent the points rejected respectively in the first and in the second implementation of the cutting process.

Contrarily to what we expected the cutting of the data made the zero points even brighter than before, causing the consequent albedo values to be higher than that calculated before the data cleaning. This fact confirmed our suspect that the linear regression isn't the best function to describe this type of data. This could probably be understood watching the plots of the data, especially in filter I there's a evident discrepancy between the data and the model, that overestimate the magnitude at little phase angle and underestimate it at higher phase angle. For these reasons we decided to try to fit the data with four different physical models.

To write our models we referred mainly to three articles Li et al. (2015b), Cognion (2013) and Buratti et al. (2011). Generally the shape of the magnitude-phase angle relation depends on the shape of the satellite, while the magnitude within a certain filter depends on the reflecting area, the albedo, the distance of the satellite and obviously the apparent magnitude of the sun in that filter. The magnitude of the satellite at a given phase angle and with a given filter is described by equations 4.3 and 4.4.

$$mag_{Sat} = M_{AppSun} - 2.5 \cdot \log(F_{reflected}) \quad (4.3)$$

$$F_{ref} = A_{sat} \cdot a \cdot f(\phi) / 4\pi d^2 \quad (4.4)$$

where A is the satellite area, a is the albedo and $f(\phi)$ is the phase function. The phase function is a function ranged from 0 to 1, that represent the portion of the satellite area illuminated by the sun. The phase function depends on the shape of the satellite. Even in this case the arguments previously made for satellite albedo and area apply. For these reason we decide to introduced a new term in equation . The new term is the product of albedo value and satellite area and is called *Aeff* effective area. As we can't estimate properly the value for albedo and area of the satellite, the idea is to build the model leaving the effective area as a free parameter, and then minimizing the RMS (σ) calculated with the Least squares method estimate the best fit vale for *Aeff*. The RMS calculation follows the equation 4.5. Usually in this cases other statistical estimator of the goodness of the fit are used, normally a Chi-squared test should be applied. Sadly the Chi-squared test is applicable if the errors on every mesure are known, and as explained in section 2.4.2 the error on the single exposure is difficult to obtain because it depends on the magnitude calibration error, but also on the presence in the light curves and in the area where the sky is taken of background stars. For these reason we preferred to use the least square method, that represent the average difference between the observed and the predicted value. The best fit is the fit that provides the lower value of RMS.

$$\sigma = \sqrt{\frac{\sum_{i=1}^{n_{points}} (mag_{true}(i) - mag_{model}(i))^2}{n_{points} - 1}} \quad (4.5)$$

In table 4.1 are plotted the phase function of the four models adopted to fit the data. The first model is a lunar model taken from Buratti et al. (2011), that was build to investigate a wavelength dependece of the magnitude-phase angle relation. We choose from the article the values for $C_0, C_1, A_0, A_1, A_2, A_3, A_4$ referring to the Effective Wavelength Midpoint of B,V Johnson and R,I Cousin

Filters. The original function is then corrected with a factor that normalized it to one. The second model is a typical lambertian spherical model (Hejduk (2011), Cognion (2013)). The third is a typical simple lunar model. The fourth is another lambertian model, but models the satellite as a plane, we expected the fourth model to be the worst. In fact we find points in our data at phase angle greater than 90° and a planar structure wouldn't be able to reflect light at phase angle greater than 90° . Since the fourth model can describe the relation until phase angle 90° only, the least square method was applied considering only the points with $\phi < 90^\circ$.

Model	Empirical phase function
Lunar ROLO	$f(\phi) = C_0 \exp(-C_1 \phi) + A_0 + A_1 \phi + A_2 \phi^2 + A_3 \phi^3 + A_4 \phi^4$
Spherical lambertian	$f(\phi) = \frac{2}{3\pi} (\sin(\phi) + (\pi - \phi) \cdot \cos(\phi))$
Lunar brightness	$f(\phi) = \frac{(1 + \cos(\phi))}{2}$
Planar lambertian	$f(\phi) = \cos(\phi)$

Table 4.1: Phase functions employed for the physical models to describe the phase angle - magnitude relation.

The Least squares analysis provides us sixteen different values for A_{eff} , this values are plotted in Table 4.2 with the corresponding albedo value calculated considering an average RCS of the satellite ($A_{sat} = 15m^2$) and with the corresponding RMS value.

Model	Filter	A_{eff} best fit(m^2)	a (with $A_{sat} = 15m^2$)	σ
Lunar ROLO	B	2.25	0.15	1.14
Spherical lambertian	B	1.62	0.11	1.13
Lunar brightness	B	1.18	0.08	1.14
Planar lambertian	B	2.68	0.18	1.28
Lunar ROLO	I	5.35	0.36	0.71
Spherical lambertian	I	4.53	0.30	0.64
Lunar brightness	I	3.35	0.22	0.71
Planar lambertian	I	8.2	0.55	0.79
Lunar ROLO	R	3.14	0.21	0.97
Spherical lambertian	R	2.56	0.17	0.92
Lunar brightness	R	1.87	0.12	0.94
Planar lambertian	R	4.59	0.31	1.15
Lunar ROLO	V	2.5	0.17	1.13
Spherical lambertian	V	1.61	0.11	1.05
Lunar brightness	V	1.17	0.08	1.07
Planar lambertian	V	3.11	0.21	1.03

Table 4.2: Least square A_{eff} , albedo and RMS values

In Figures 4.4,4.5,4.6,4.7 are plotted the four models for every filter. Generally the worst fit as expected is provided by the Planar lambertian model, this

is true watching at the RMS values for filter B,I and R. In filter V instead the worst fit is provided by the Lunar ROLO model, and the other models have similar RMS values. According to the RMS value the best model to fit the data seems to be the spherical lambertian model. This suggests us that the probable best simple model of Molniya debris shape is a simple spherical model, or in other words, that the peculiar shape of Molniya debris is more like a spherical object than a diskly object. We expect this result since the intrinsic shape of Molniya debris is known, and surely is not a disk like object. Since the Lunar ROLO model is a spherical model that unlike that lambertian takes account of the self shadowing effect due to moon ground altitudes, the fact that the spherical lambertian model better fit the data with respect to the Lunar ROLO model could suggest us that in the case of Molniya debris there is little presence of self shadowing effects. This isn't an obvious statement because the intrinsic shape of Molniya debris suggest a large presence of self shadowing effects due to the presence of solar panels. Another check on the model is provided by the albedo value calculated considering $A_{sat} = 15m^2$, we notice that generally the Planar Lambertian model provide an albedo value that is higher than expected, moreover if we consider that the albedo value calculated with this method represent a lower limit for the real value. The albedo values found with the other models are acceptable for filter R,B and V but are too high for filter I. Once again the lack of data of filter I analysis increases the efficacy of flashes point to move the zero point towards brighter magnitudes.

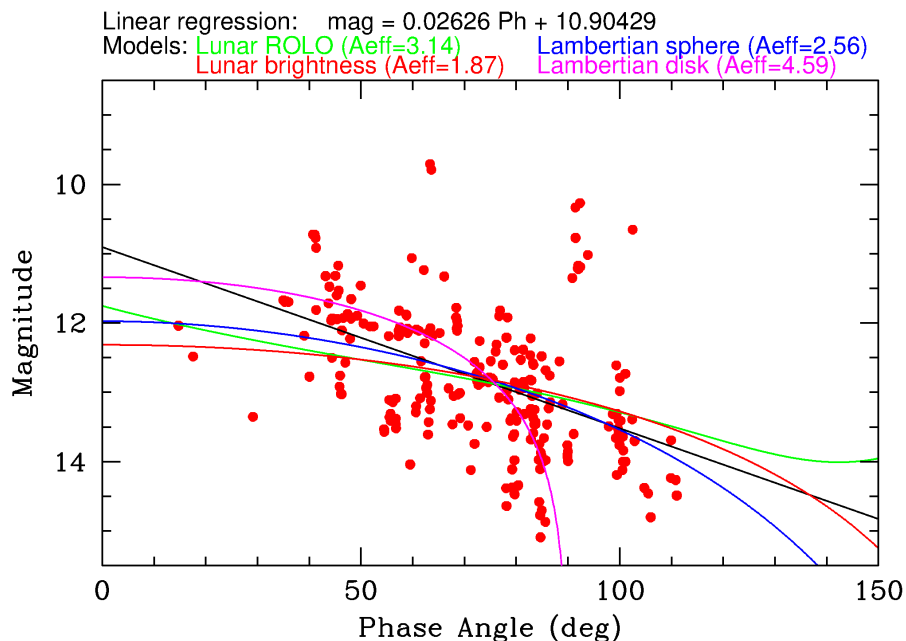


Figure 4.4: Modeling for Phase angle - magnitude relation in Filter R.

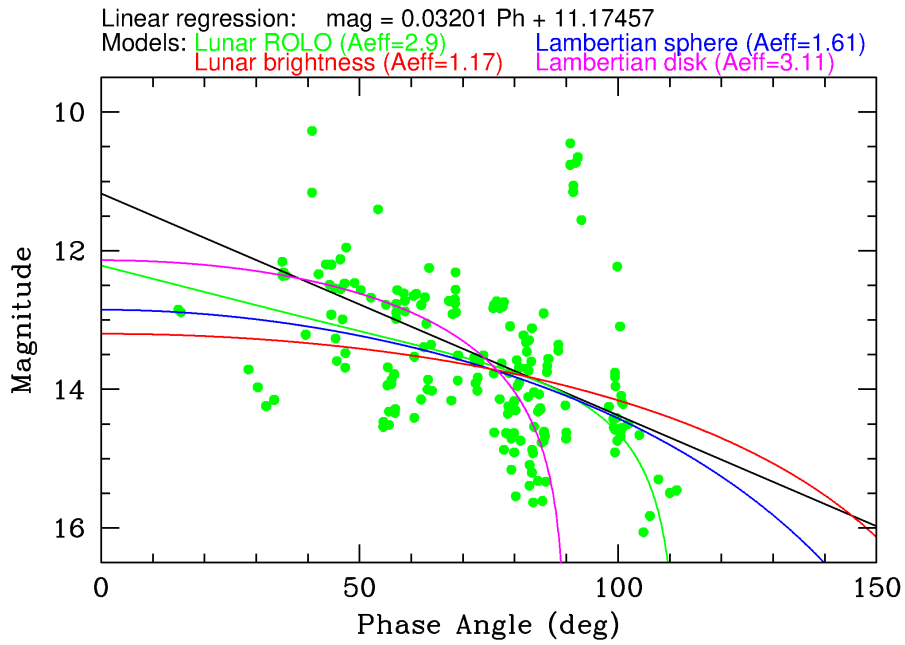


Figure 4.5: Modeling for Phase angle - magnitude relation in Filter V.

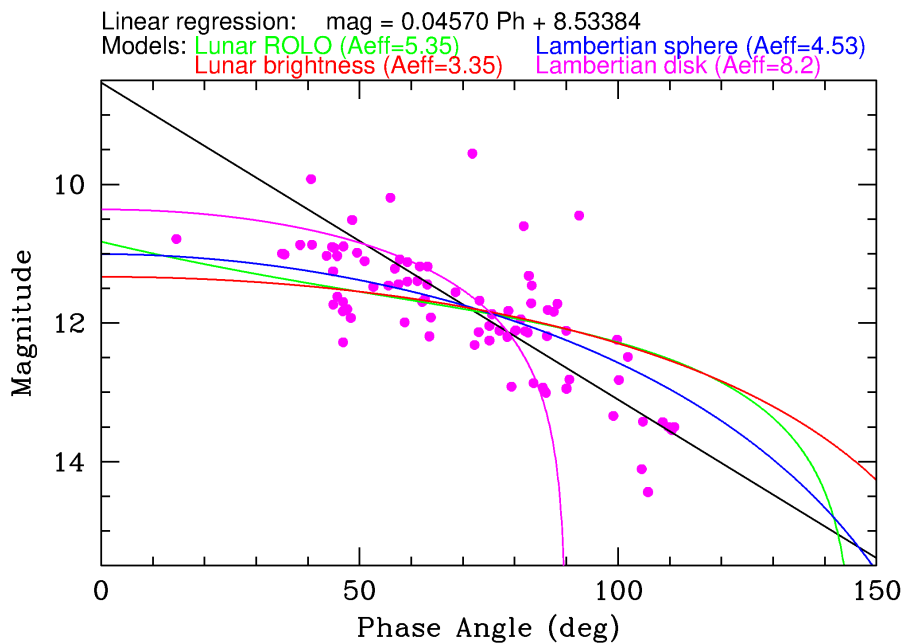


Figure 4.6: Modeling for Phase angle - magnitude relation in Filter I.

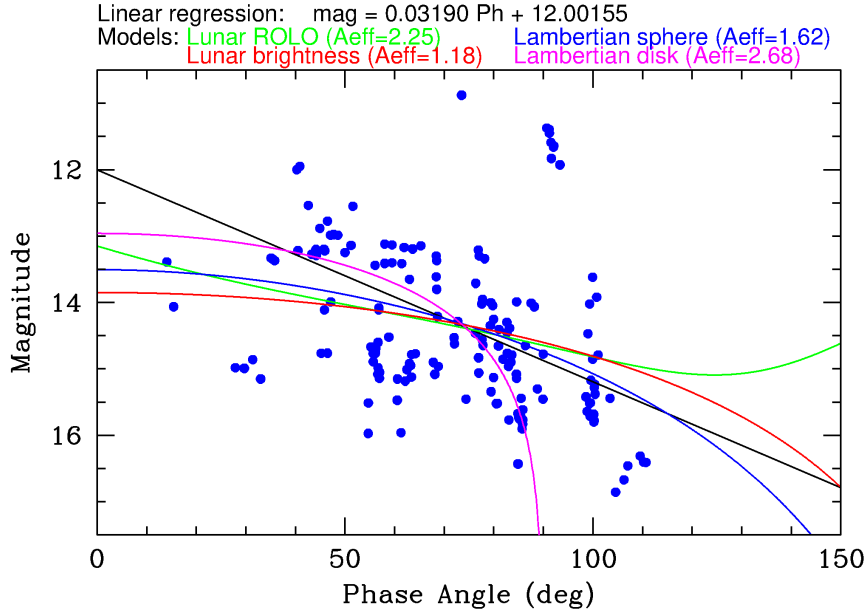


Figure 4.7: Modeling for Phase angle - magnitude relation in Filter B.

To avoid the problem of flashes and drops in magnitude and to check the goodness of the labertian model with respect to the Lunar ROLO model another cutting of data similar to that made for linear regression has been made. For every model and every filter the points that detached more than 2σ from the model have been rejected. The process has been applied two times. In Table 4.3 are plotted the new A_{eff} of the best fit, the new albedo value calculated considering $A_{\text{sat}} = 15m^2$ and the new RMS value of the fit for every model in every filter calculated for the cleaned data. The results of the cutting process and the new best fit models are plotted in figures 4.8,4.9,4.10,4.11.

After the cutting process appears watching at the RMS values that the best model to fit the data is the spherical lambertian model. This is true in every filter exsept filter V where the lunar ROLO model has the same RMS of the spherical lambertian model. The cutting process helped us to improve the predictions of the albedo value. The albedo value has decreased in every filter reaching more acceptable values. Only in filter I the albedo values seem to remain to high. In this case we have to consider the possibility that the prediction is correct and that Molniya debris are actually more efficient in reflecting I filter light. In conclusion it appears that the best model to reproduce the data is the spherical lambertian model, which means that probably for Molniya debris the selfshadowing effect ins't an efficient process or accours only at phase angle greater then $\approx 120^\circ$ where we don't have data to analyse, or most likely that, since most of the observed satellites are tumbling, the self-shadowing effect accours at every phase angle, and therefore it is not visible because it is present in all the points of the analyzed plots. We can fix an lower limit to the albedo value, that axepting the spherical labertian model as the best model, is $a \geq 0.09$ for B filter, $a \geq 0.28$ for I, $a \geq 0.15$ for R and $a \geq 0.10$ for V filter.

Model	Filter	A_{eff} best fit(m^2)	a (with $A_{sat} = 15m^2$)	σ
Lunar ROLO	B	1.84	0.12	0.83
Spherical lambertian	B	1.32	0.09	0.77
Lunar brightness	B	0.96	0.06	0.84
Planar lambertian	B	2.33	0.15	0.85
Lunar ROLO	I	5.08	0.33	0.52
Spherical lambertian	I	4.28	0.28	0.42
Lunar brightness	I	3.18	0.21	0.53
Planar lambertian	I	6.99	0.47	0.58
Lunar ROLO	R	2.89	0.19	0.68
Spherical lambertian	R	2.31	0.15	0.60
Lunar brightness	R	1.68	0.11	0.67
Planar lambertian	R	3.86	0.25	0.74
Lunar ROLO	V	2.80	0.19	0.70
Spherical lambertian	V	1.57	0.10	0.70
Lunar brightness	V	1.15	0.08	0.74
Planar lambertian	V	2.85	0.19	0.75

Table 4.3: Least square A_{eff} , albedo and RMS values for every model and filter after the cutting process.

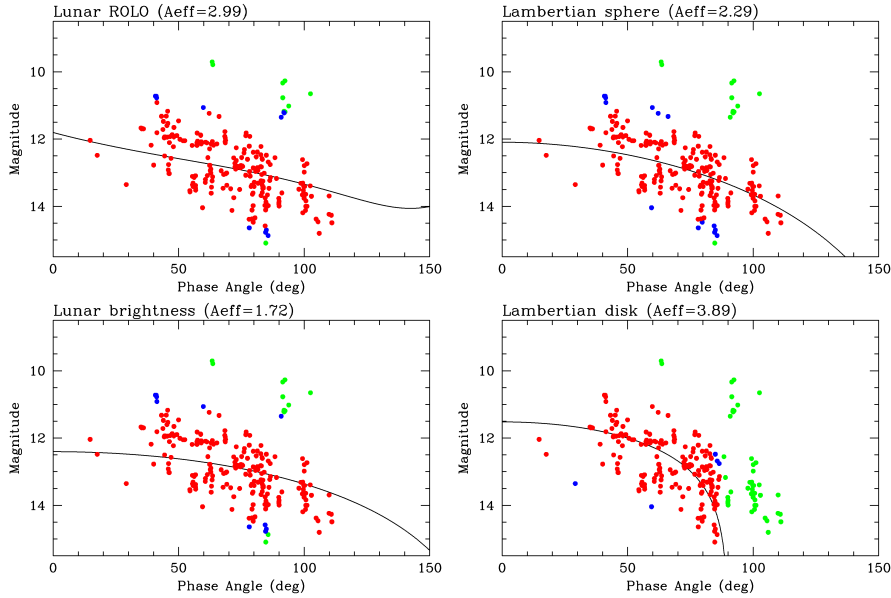


Figure 4.8: Models for Phase angle - magnitude plot after the cutting process in filter R, every point that hasn't been eliminated by the cutting process is colored in red, in green and blue are plotted the points rejected respectively in the first and in the second implementation of the cutting process.

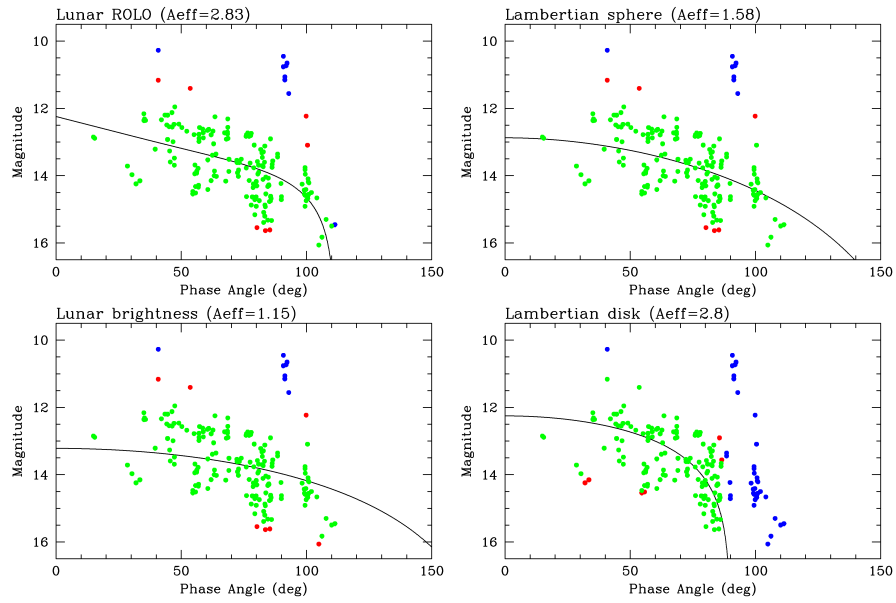


Figure 4.9: Models for Phase angle - magnitude plot after the cutting process in filter V, every point that hasn't been eliminated by the cutting process is colored in green, in blue and red are plotted the points rejected respectively in the first and in the second implementation of the cutting process.

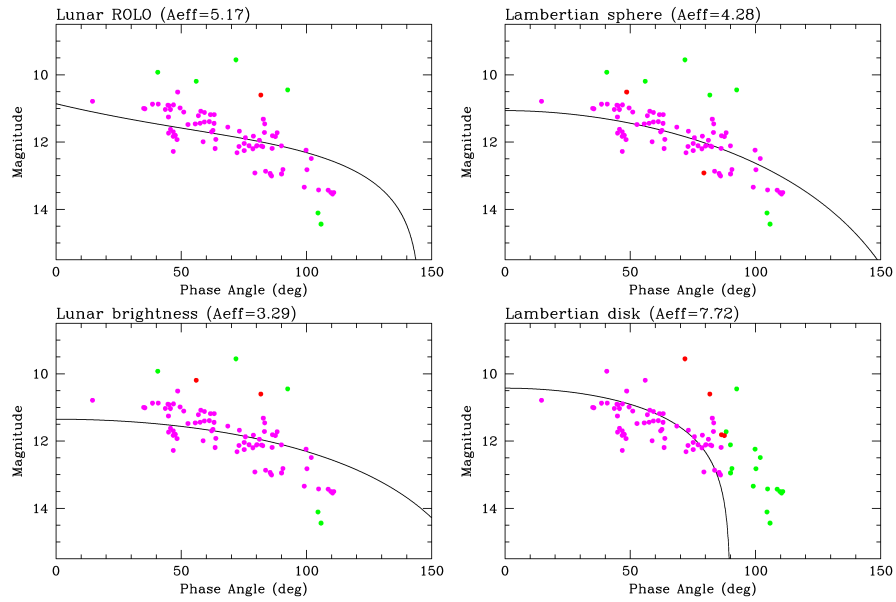


Figure 4.10: Models for Phase angle - magnitude plot after the cutting process in filter I, every point that hasn't been eliminated by the cutting process is colored in magenta, in green and red are plotted the points rejected respectively in the first and in the second implementation of the cutting process.

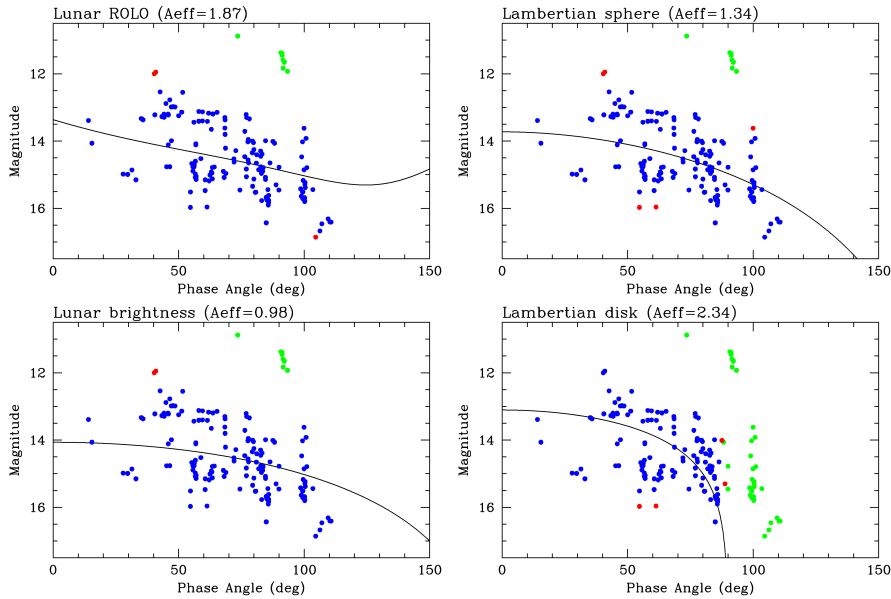


Figure 4.11: Models for Phase angle - magnitude plot after the cutting process in filter B, every point that hasn't been eliminated by the cutting process is colored in blue, in green and red are plotted the points rejected respectively in the first and in the second implementation of the cutting process.

4.2 Photometric and Spectral analysis of Molniya and Meridian constellation

In this section we discuss the analysis of the color indexes and spectra of Molniya constellation.

4.2.1 Color indexes analysis

For what concerns the color indexes, first of all we had to calculate them for every satellite. The calculation technique depended on the observation characteristics. In fact to calculate properly the color indexes is important to compare photometric data at similar phase angle. Although we have shown in the previous section that all filters show a magnitude decrease as the phase angle increases following a pattern common to all filters, and therefore color indexes should not show dependencies on the phase angle, a check on this statement remains necessary, so we preferred to compare data at similar phase angles. Another important consideration is to compare magnitudes in various filters being careful, if in a given filter many data are available, to the time evolution of the photometric data in the same filter. We have shown in Chapter 3 that many of these satellites, indeed almost all, are tumbling. If the tumbling period is short, and a single exposure contains many periods, there's no problem. In this case in fact the integrated magnitude is well representative of the satellite average magnitude in time, and the color index can be calculated averaging the magnitudes of every exposition (taken at similar phase angle) in a given filter,

and subtracting the two mean magnitudes to obtain a given color index. In some cases however the tumbling period is very long, so that the light curve samples only a small portion of the entire period. In this case it is necessary to keep in mind that some magnitudes may have been obtained at peak points and others in the minimum points of the light curve. For this reason in these cases is important to calculate the color indexes in the following way: we connect each point in a given filter (for example R) with the temporally adjacent one through a straight line, and for every point of another filter (for example V) the color index is calculated as the difference between the magnitude in that filter (V), and the magnitude calculated on the straight line connecting the two R magnitude points, at the time of the exposure of the V filter point. Then the various color index measurements obtained in this way, are averaged to obtain a mean color index. In some cases we had only one exposition in each filter so the color index has been calculated simply subtracting the magnitudes. Once the color indexes for all observed satellites has been calculated we proceed with the creation of the color-color diagrams, presented in Figure 4.12.

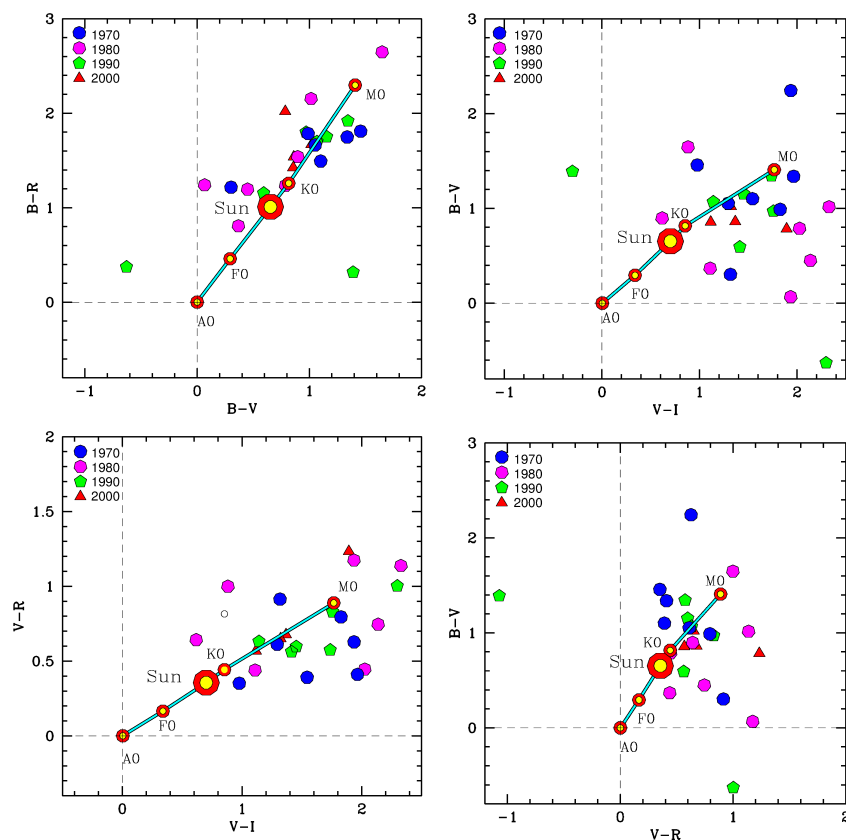


Figure 4.12: Color-color diagrams for Molniya and Meridian satellite constellation. The different colors are referred to the launch year, blue for satellites that has been launched between 1970 and 1980, magenta between 1980 and 1990, green between 1990 and 2000 and red for satellites that has been launched after 2000.

As we expected the constellation is on average more brilliant in filter I, followed in the filter R, filter V and filter B in this order. We notice that satellites are almost always in the most red areas with respect to the Sun's position. This suggests that the materials of which they are composed are in general excellent reflectors of the I-band radiation, and lose their reflection capacity as the radiation moves at higher frequencies in band R, then V and then B. This result partly confirms the albedo estimates made in the previous section, where the maximum value of albedo has been found in band I ($a_I = 0.27$), followed by the band R ($a_R = 0.15$), then V ($a_V = 0.10$) and then B ($a_B = 0.08$). As you can see in the color-color diagrams we plotted the satellites coloring them according to the launch year, this has been made to highlight possible trends with age. In fact we would expect to see a phenomenon of redness due to material deterioration because of solar radiation and collisions with small debris (Abercromby et al. (2006)). However, the diagrams do not show, at least apparently, evident trends with age. To check the lack of age trends and to check the previous supposition of independence of color indexes from phase angle, two more graphics have been created. This plots are presented in Figures 4.13 and 4.14 respectively.

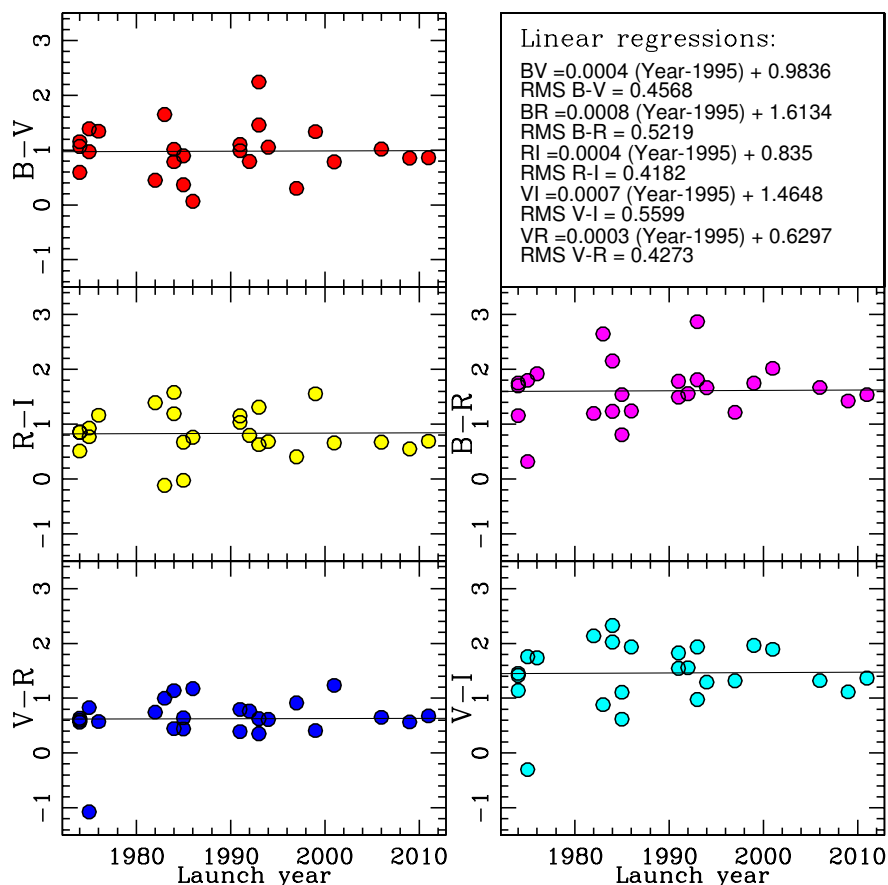


Figure 4.13: Color vs launch year.

The first is the plot of the color indexes versus launch year, the second is the plot of colour indexes versus phase angles. All the plots have been fitted with a linear regression. In the case of plot with age, the linear regression coefficients confirms what previously supposed. The color indexes do not present any trend with age, in contradiction to what space debris science suggests the deterioration and redness effects of the materials are not visible with regard to Molniya space debris. In the second case, however, we note for the color indexes B-V and B-R a slight reddening as the phase angle increases. But comparing the parameter b of the linear regression with the RMS value it is difficult to determine whether this trend is effective or due to fluctuations in the layout of the points. The fact that this trend is only observed in the color indexes that consider filter B, could suggest that filter B actually drops more in brightness than other filters as the phase angle increases. Also R-I and V-I color indexes present soft increasing trends with phase angle increase, even if softer than filter B color indexes. Even in this case it is worth the previous argument, considering however that the observed growth is very slight.

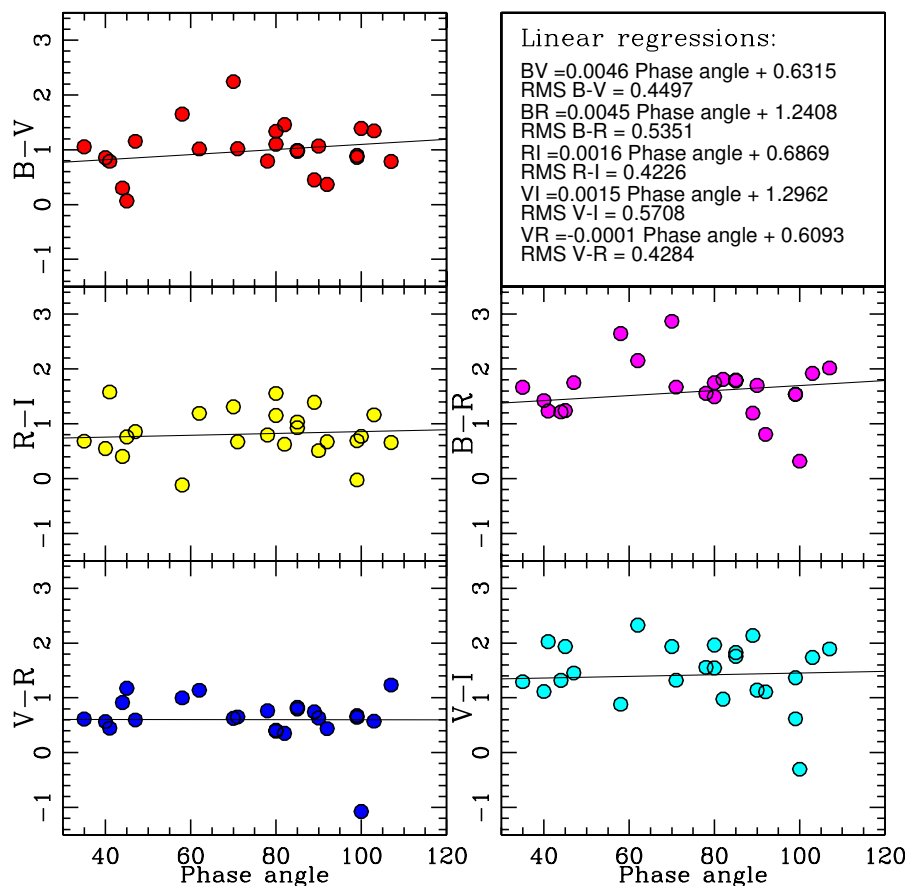


Figure 4.14: Color vs phase angle.

To complete the color indexes characterization of Molniya and Meridian debris, we have tried to compare the observed photometric indexes with those

expected from the laboratory measurements of the photometric response to the sunlight of the materials of which the satellites are built. We took the laboratory data from Cowardin et al. (2010). In their work Cowardin et al. (2010) have measured in laboratory the photometric response of fragments or materials acquired through ground-tests of scaled-model satellites and rocket bodies, exposed to a 75-watt Xenon arc lamp, used as a solar simulator. The resultant colour indexes were then corrected to solar values, to compare them with the telescopic data. For comparison of laboratory measurements with our data we decided to use the diagram B-R versus R-I which seems to be the best to look for correlations. Plotted laboratory data refer to ten different materials listed in the following bulleted list with the corresponding acronym insert in the diagram.

- Beta cloth: a type of fireproof silica fiber cloth used in the manufacture of many spacecraft.
- Intact SC: spacecraft-facing intact Multi-layered insulation (MLI)
- Intact Space: space-facing intact Multi-layered insulation (MLI)
- Cu Kapton SP: space-facing copper-colored Kapton. Kapton is a polyimide that remains stable across a wide range of temperatures used in thermal blankets used on spacecraft, satellites, and various space instruments.
- Cu Kapton SC: spacecraft-facing copper-colored Kapton
- Mylar: Polyethylene terephthalate, common thermoplastic polymer resin of the polyester family. Used in spacecrafts for insulation.
- Al Kapton SP: space-facing aluminized Kapton
- Al Kapton SC: spacecraft-facing aluminized Kapton
- Lab solar panel 1: JPL sample composed of standard solar panel material with gallium arsenide solar cells
- Lab solar panel 2: solar panel taken from a spacecraft, the details of the material type were not released

The B-R versus R-I for laboratory measurements and for Molniya and Meridian space debris is plotted in Figure 4.15. A part of the satellites are between the Mylar and the solar panels 2, while the other are in the regions more towards the red with respect to the Mylar and the solar panels 2. The other materials do not seem to reproduce well the data for Molniya and Meridians. The color redness with respect to mylar and solar panels 2 could suggest a reddening effect due to material deterioration. Just before we have however seen that there are no trends with age, which would seem to exclude this hypothesis. We note also that our results are in good agreement with that found by Cowardin et al. (2010) for stable GEO object, less with that found for GEO flasher. This also amazes us because our satellites are all or almost spinning and many have flash in the light curves. We would also have expected a good agreement with aluminum data, but there seems to be no correlation. In conclusion the comparison of telescope data with laboratory data does not seem to have produced any great

results, no agreement was generally reached between the analyzed materials and the satellites, which tend to position itself toward reddest colors with respect to laboratory measurements. Color indexes analysis instead has suggested a general lack of trend with age and aging effects of materials. Also the phase angle does not seem to have much influence on color indexes, confirming Section 4.1 results, which provide a common model for the drop in magnitude as the phase angle increases for all filters.

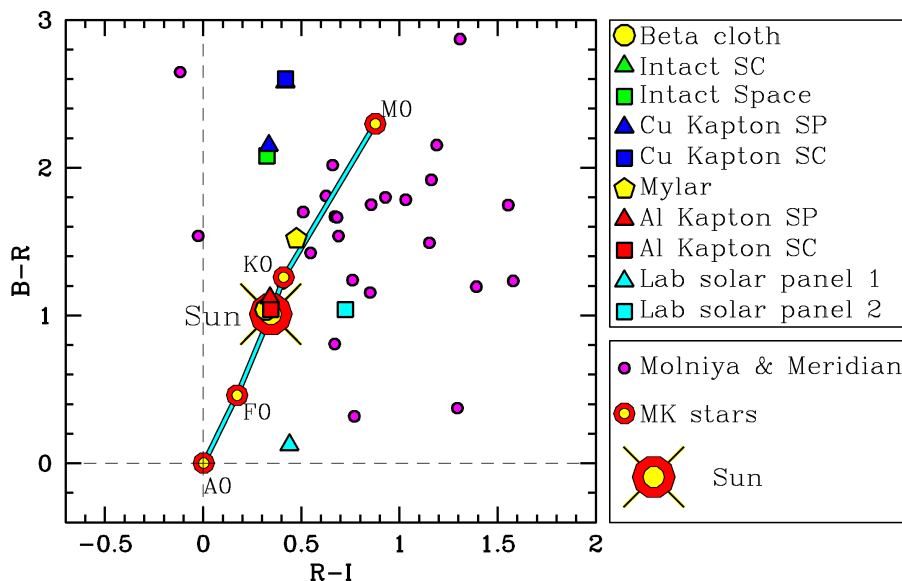


Figure 4.15: B-R versus R-I diagram for Molniya and Meridian satellites and laboratory data.

4.2.2 Spectral analysis

To complete the colors characterization of Molniya and Meridian satellites a spectral analysis has been carried out. The first step of the spectral analysis was to verify the scientific validity of the spectra in our possession. As already explained in section 1.5 spectra are higher quality information than photometry but they also have pitfalls that can compromise their validity. In particular there's the danger that during the exposure the satellite will come out of the slit, if this happens the blue or the red part of the image will escape first (depending on the exit direction), due to differential refraction of Earth atmosphere, and therefore the resultant spectrum will be distorted. There's no way to check if the satellite remains in the slit during the exposure, the only possible check is a posteriori. In fact, it is possible to check that the calibrated spectrum respects photometry data. Practically the spectra and photometry (appropriately converted into flux) are plotted in the same graph and is checked if the spectrum meets the photometric points. The conversion from magnitude to flux for photometry data has been made using Table 1 of Buzzoni (2005). In particular the adopted conversion equation is:

$$\log(flux) = -0.4Mag_f + cost(f) \quad (4.6)$$

Where Mag_f is the magnitude in a given filter and $cost(f)$ is a constant depending on the filter, the value of which can be found in the Table 1 of Buzzoni (2005). When more than one spectrum of a single object was present, the spectra were mediated by weighing on exposure time. In some cases when photometry reflected the spectral trend but there was divergence in flux value, little flux shift were allowed (justifiable by possible small errors in spectral flux calibration). The only exception to this rule has been made for Molniya 3-27 spectrum, in fact for this spectrum the shift in flux was substantial. It's probable that the satellite during the exposition quickly escaped the slit, causing the significant loss of observed flux and the noisiness of the spectrum, but the escape has been so sudden that it did not cause distortion in the spectrum. The results of the check made us classify the spectra in three categories: those who passed the test, those who don't passed the test, and those whose have only one photometry point which differs significantly from the spectrum, in particular the discrepancies were found for the filter I in which photometry systematically overestimate the spectrum flux. An exaple of approved spectrum, rejected for I photometry spectrum, and rejected spectrum is plotted in Figure 4.16, Figure 4.17, and Figure 4.18 respectively. Errors on photometry points are estimated considering the magnitude calibration errors, the errors on the conversion constant and the noise of the light curves (from the periodogram analysis). This errors are probably upper limits, and not real errors, but an estimation should be done, since we can not estimate precisely the error on each mesure, as explained before. Photomery points are the result of an average made on all the expositions in a given filter, making sure that the exposures have taken place at similar phase-angle, to avoid shift due to the phase-angle magnitude relation (see section 4.1). In Table 4.4 are plotted the results of the check.

Approved spectra	Not approved for I photometry	Not approved spectra
Meridian 1	Molniya 3-03	Molniya 1-32
Meridian 2	Molniya 1-53	Molniya 1-56
Meridian 4	Molniya 1-63	Molniya 1-62
Molniya 1-S	Molniya 1-80	Molniya 1-69
Molniya 2-09	Molniya 1-88	Molniya 1-87
Molniya 2-10	Molniya 2-17	Molniya 1-90
Molniya 3-27	Molniya 3-40	Molniya 2-13
	Molniya 3-42	Molniya 3-50
	Molniya 3-51	

Table 4.4: Molniya and Meridian spectra photometry check

The results plotted in Table 4.4 suggest that surely in most cases the acquisition of the spectrum has failed. This is probably due, in the case of spectra discarded for I filter dicrepancies, to the inaccuracies of the Cassini telescope tracking system that was not designed for this type of observation. This inaccuracies could cause the differential exit from the slit, by getting out first the

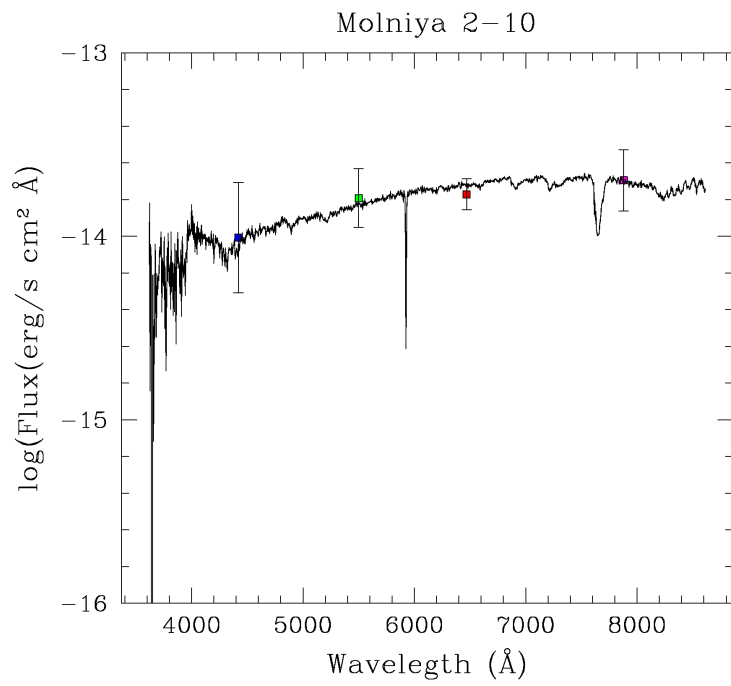


Figure 4.16: Example of approved spectrum

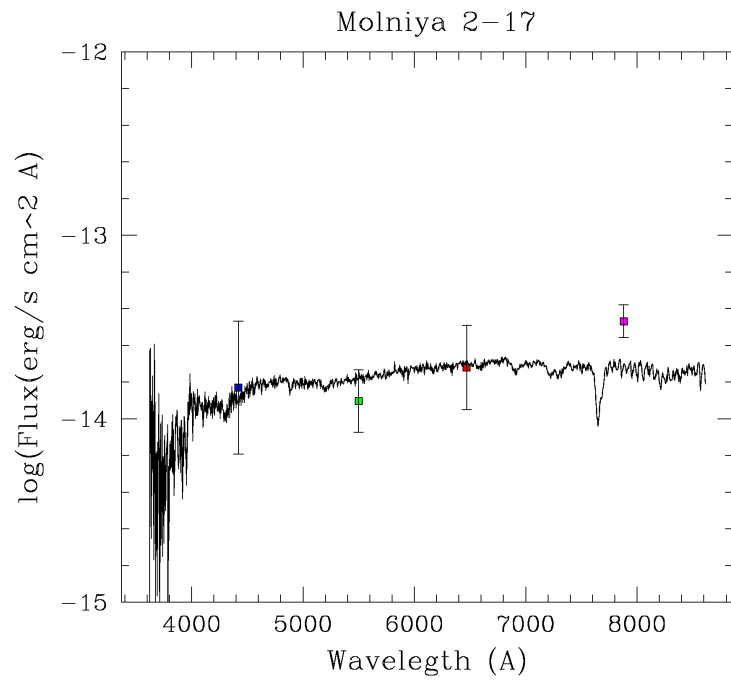


Figure 4.17: Example of rejected for I photometry spectrum

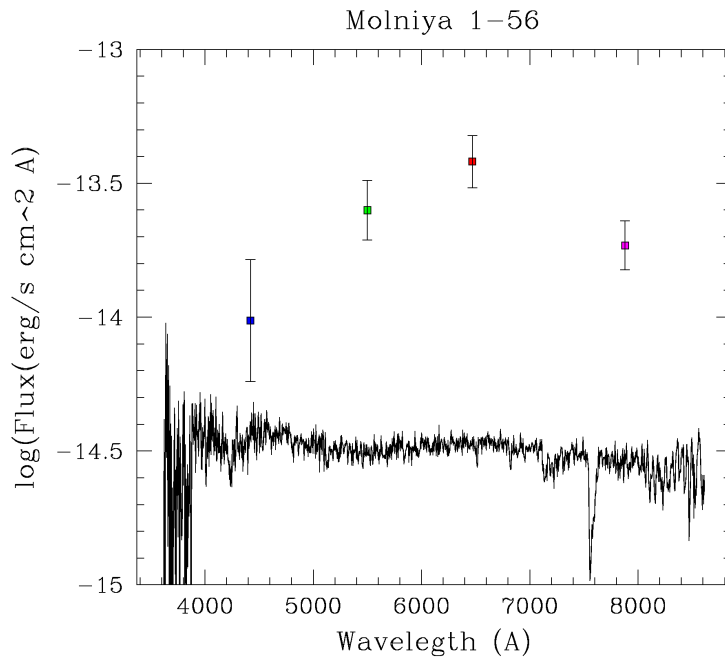


Figure 4.18: Exaple of rejected spectrum

part of the satellite radiation at low energies and then the high one, thus explaining the missing part of the I band. Future observations of this type should be made with greater tracking precision. Spectra that clearly detach from the photometry in every filter may have many failure causes. Errors in the extraction phase (some of the spectra were just recognizable when the extraction has been made, so it is possible even if unlikely that the spectrum of the satellite has been confused with that of a star, or that a star has passed during the exposure exactly above the satellite image distorting the spectrum), calibration errors, scarce photometry, slight phase angle differences between photometry and spectra that may have affected the flash of the satellite (slight angular movements may cause flashes to appear or disappear), the satellite is tumbling with a very long period so it could be that during photometric and spectral exposition the satellite was in different phases. As already said spectrum acquisition is a delicate process and has many possible sources of error.

Let's focus now on the spectra that passed the photometry test. We have anyway analyzed also the spectra rejected for I photometry, but separately. The analysis was carried forward following the approach found in the article written by Seitzer et al. (2012). The spectra were smoothed to 10 Å resolution. Then we divided each spectra by solar spectrum to obtain the wavelength dependent reflectance of Molniya and Meridian. The reflectance was then normalized to its value at 7000 Å, this is the only difference from what has been done in the work of Seitzer et al. (2012), where the reflectance is normalized in the wavelength region 7500 to 8000 Angstroms. We chose to normalize at 7000 Å because in the region between 7500 and 8000 Å we have in our spectra strong atmospheric absorption lines of oxygen, the result, however, should not vary much, since we

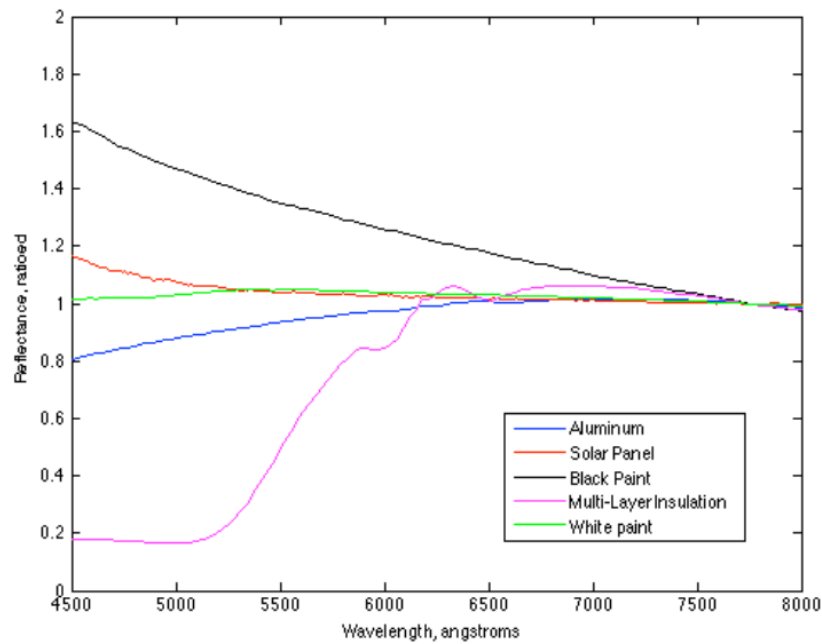


Figure 4.19: Laboratory measurements treated as telescopic observations, and normalized in the wavelength region 7500 to 8000 Angstroms, taken from Seitzer et al. (2012).

are limited to a qualitative analysis. This has been made to compare reflectance of satellite with reflectance properties of the materials taken in laboratory (Figure 4.19). We also searched for the lack of trends with age to confirm the color indexes results of the previous section. The results of this operation are plotted in Figures 4.20, 4.21, and 4.22.

As for the color indexes analysis, none of the analyzed spectra seems to match with the laboratory measurements plot. There's a strong disagreement with alluminium pattern. All the satellite in fact, except Molniya 3-27 and Molniya 1-63, shows a steeper slope with respect to that of alluminium reflectance. We see furthermore that spectra are brighter in band B and V than the pattern of solar panels. In other words the Molniya reflectance function is positioned in an intermediate area between aluminum and solar panels functions, which suggests that the observed one is probably the sum of these two components. The lack of evident trends with age confirms the color indexes results. The only possible observed trend is that of Molniya 3-27 that is younger than the Molniya 1S, 209 and 210, and better reflect blue light. But Molniya 3-27 spectrum has had a particular analysis history and is therefore the less reliable of the spectra presented. Molniya 1-63 shows also larger capacity to reflect blue light with respect to the other, but isn't the younger of the satellite analyzed in its plot. Satellites seems to have common properties of reflection regardless of age, in general they better reflect red radiation than blue, as the color indexes had already demonstrated.

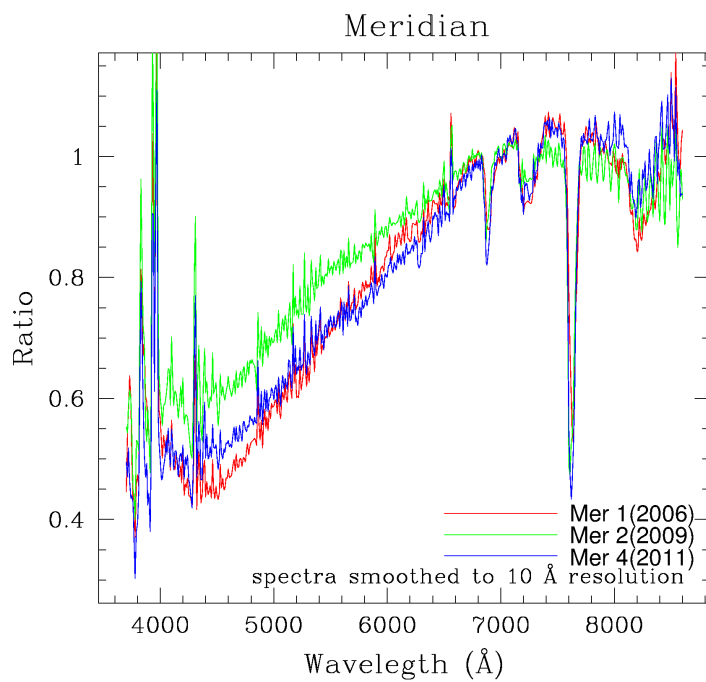


Figure 4.20: Meridian spectra after division by solar spectrum and normalized at 7000 Å. In parenthesis there's the launch year.

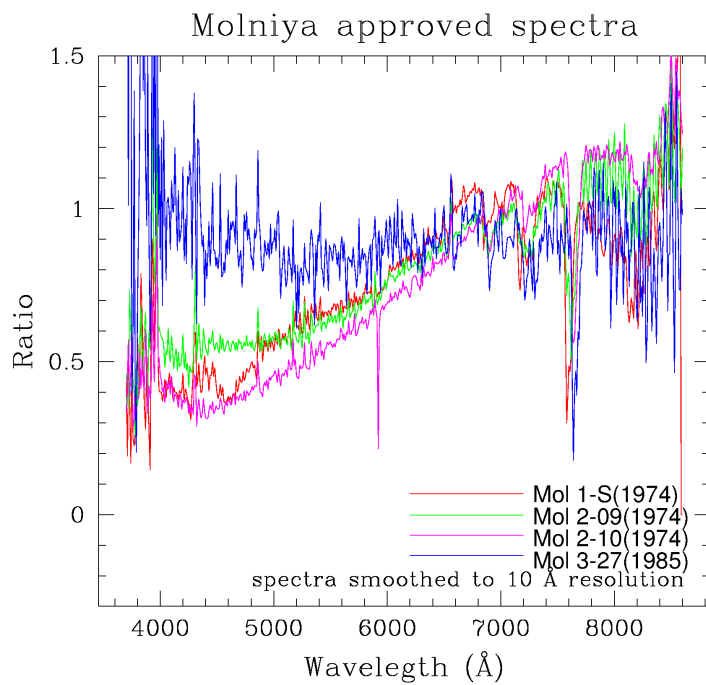


Figure 4.21: Molniya approved spectra after division by solar spectrum and normalized at 7000 Å. In parenthesis there's the launch year.

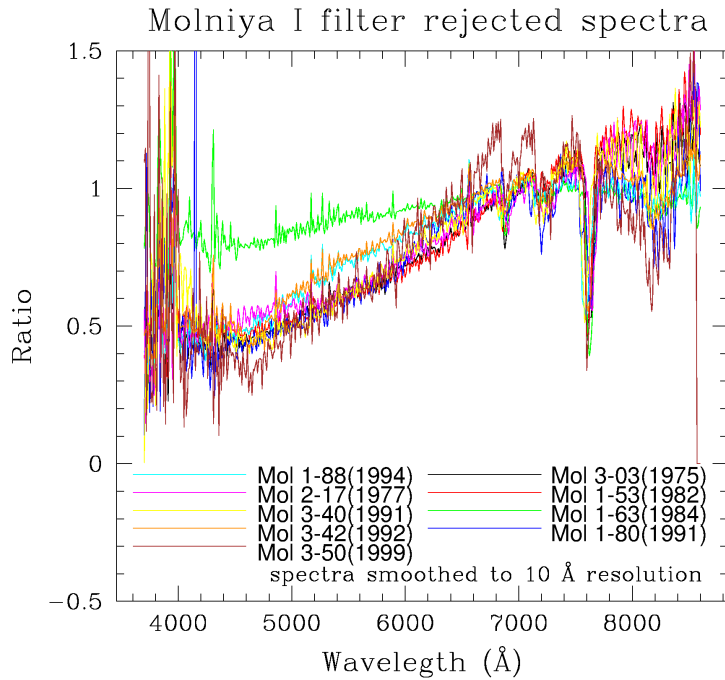


Figure 4.22: Molniya I photometry rejected spectra after division by solar spectrum and normalized at 7000 Å. In parenthesis there's the launch year.

4.3 Tumbling period slowdown model

We know from the literature that the interaction between the space debris and the earth magnetic field should lead to a slowdown of the tumbling period of space debris. The basic principal is that the intensity and direction of earth magnetic field varies in the satellite orbit, these variations create spurious electrical currents in the satellite shell. This currents known as Eddy Currents opposes the rotation. The result of this process leads to a progressive slowdown of the debris tumbling period. The process is described by Equation 4.7 (Gómez and Walker (2015)).

$$P = P_0 \exp\left(\frac{t}{\tau}\right) = P_0 \exp(at) \quad (4.7)$$

The slowdown of the period is exponential with a characteristic time of decay ($\tau = 1/a$) that depends on the satellite characteristics and orbit. The rigorous calculation of the characteristic time of decay is very complex and requires the knowledge of the satellite rotational axis (to calculate the moment of inertia we need to know on which axis the debris is rotating) and orientation, combined with earth magnetic field direction and intensity along the orbit and the knowledge of the satellite building materials. Our approach was to fit the data with a simple exponential function to find the best fit value for τ .

We will discuss the complete fitting process after a short review of the data situation.

After the periodogram analysis has been made the situation of our knowledge of Molniya debris rotational periods is plotted in Table 4.5. These are the results obtained from our observation made with the Cassini telescope in the final part of 2016 and with Figer images (2015). To study the time evolution of rotational periods we need to compare our observation with previous observations if available.

Satellite	Launch date	Tumbling period (s)	Observation date
Molniya 2-9	1974-04-26	15 ± 1	2016-09-27
Molniya 2-10	1974-07-23	41.255 ± 0.15	2016-11-26
Molniya 1-S	1974-07-29	25.83 ± 0.05	2016-08-01/02
Molniya 2-13	1975-07-8	unknown	2016-11-26
Molniya 3-3	1975-11-14	10.175 ± 0.02	2016-12-22
Molniya 1-32	1976-01-22	unknown	2016-08-01/09-26
Molniya 2-17	1977-02-11	54.5 ± 1	2016-09-26/27
Molniya 3-8	1977-10-28	14.36 ± 1	2016-12-23
Molniya 3-13	1980-07-18	unknown	2016-12-22
Molniya 1-53	1982-02-26	12.68 ± 0.1	2016-12-22
Molniya 1-56	1983-03-16	unknown	2016-09-27
Molniya 1-62	1984-08-24	unknown	2016-09-26
Molniya 1-63	1984-12-14	4.10 ± 0.13	2016-12-23
Molniya 3-27	1985-12-24	32.9 ± 0.03	2016-09-27
Molniya 3-24	1985-05-29	unknown	2016-09-27
Molniya 1-69	1986-11-15	65 ± 0.5	2016-11-26
Molniya 1-80	1991-02-15	unknown	2016-08-01/11-26
Molniya 3-40	1991-03-22	unknown	2016-09-26
Molniya 3-42	1992-10-14	4.807 ± 0.002	2016-11-26
Molniya 1-87	1993-12-22	unknown	2016-09-27/12-22
Molniya 1-86	1993-05-26	122.2 ± 1	Figer(25-10-2015)
Molniya 1-88	1994-12-14	3.583 ± 0.002	2016-12-22
Molniya 1-90	1997-09-24	$\approx 65 \pm 1$	2016-12-23
Molniya 3-50	1999-07-8	unknown	2016-09-26/27
Molniya 3-51	2001-07-20	unknown	2016-08-01
Molniya 1-44	1979-07-31	66.08 ± 0.5	Figer(05-09-2015)
Meridian 1	2006-12-24	30.18 ± 0.2	2016-11-26
Meridian 2	2009-05-21	stable	2016-12-22
Meridian 4	2011-05-04	stable	2016-12-22

Table 4.5: Molniya tumbling periods

We searched in the nights of observation made by professor A.Buzzoni during 2014,2015 and 2016 at the Cananea and Loiano observatory for rotational periods to compare with the periods found in the nights made at the Loiano observatory in the final part of 2016. We found five Molniya debris of which we know two different periods at different time.

- Molniya 3-08: $P = 14.36 \pm 1s$ (2016-12-23) and $P = 16 \pm 0.5s$ (2016-03-10)
- Molniya 2-09: $P = 15 \pm 1s$ (2016-09-27) and $P = 14.5 \pm 0.2s$ (2015-09-20)

- Molniya 1-88: $P = 3.583 \pm 0.002s$ (2016-12-22) and $P = 3.5 \pm 0.1s$ (2016-03-10)
- Molniya 1-49: $P = 7.19 \pm 0.03s$ (2016-03-07) and $P = 6.83 \pm 0.02s$ (2014-08-04)
- Molniya 3-42: $P = 4.807 \pm 0.002s$ (2016-11-26) and $P = 4.5 \pm 0.2s$ (2014-10-17)

You can see that all the satellite except Molniya 3-08 comply the expected trend. Molniya 3-08 for some reason don't show the expected slowdown of the period, on the contrary shows an acceleration of the rotational period, for this reason it will be discussed separately. A physical model that takes into account the properties of Molniya debris characteristics and orbit is very complex to build because of the lack of informations on the rotational axis and the precise direction and intensity of the Earth magnetic field along the orbit, and goes out of the purpose of this work. Anyhow we are interested in the experimental aspect, for this reason we decided to fit the data with an exponential function to calculate a common value of the characteristic time for Molniya type debris.

The first step is to fit the periods of every satellite taken individually, since for every satellite we have two points in the time vs period plot we don't need a statistical test to find the best fit model, since through two points passes only one exponential. The zero point of the relation (P_0) is the first period found in order of time (for each satellite). The results of this first step are plotted in Figures 4.23, 4.24, 4.25, 4.26 and 4.27.

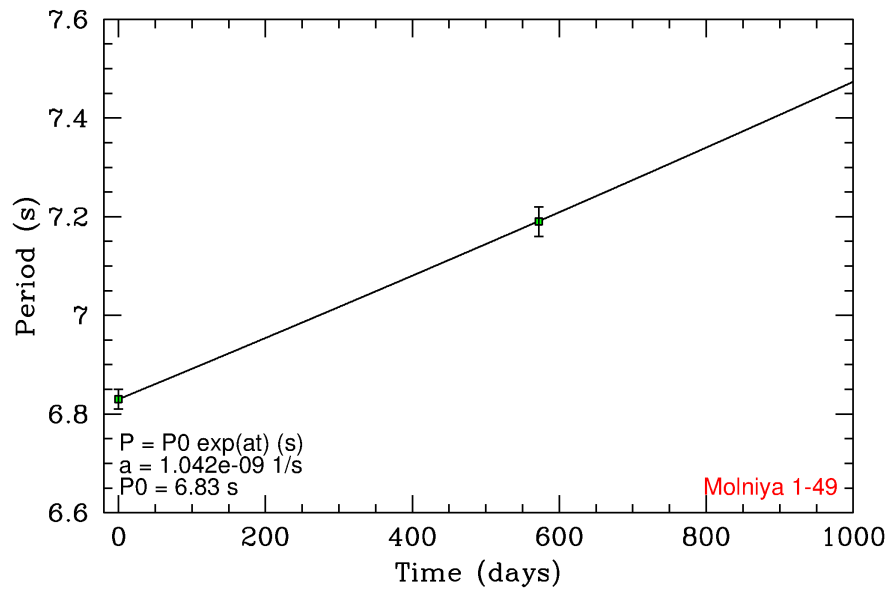


Figure 4.23: Exponential model of the time vs period relation for Molniya 1-49

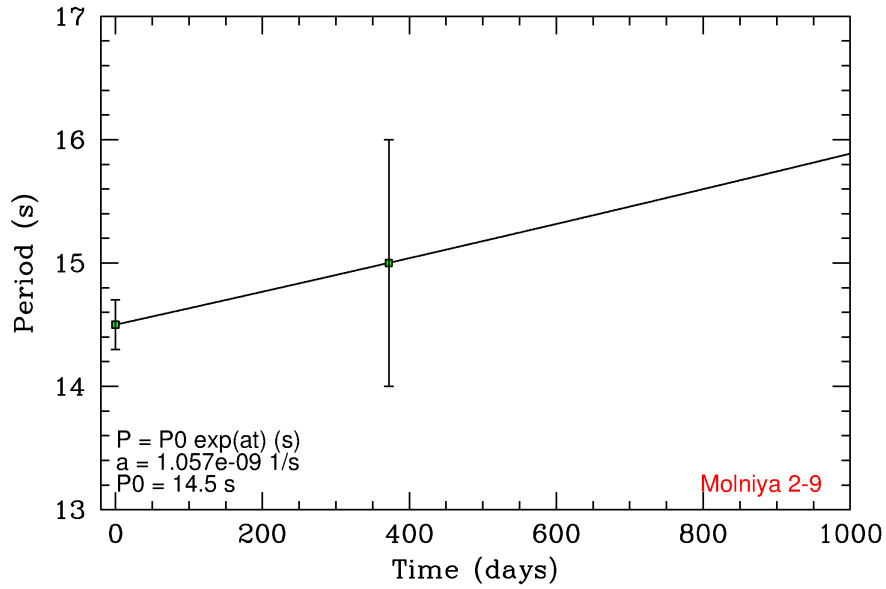


Figure 4.24: Exponential model of the time vs period relation for Molniya 2-09

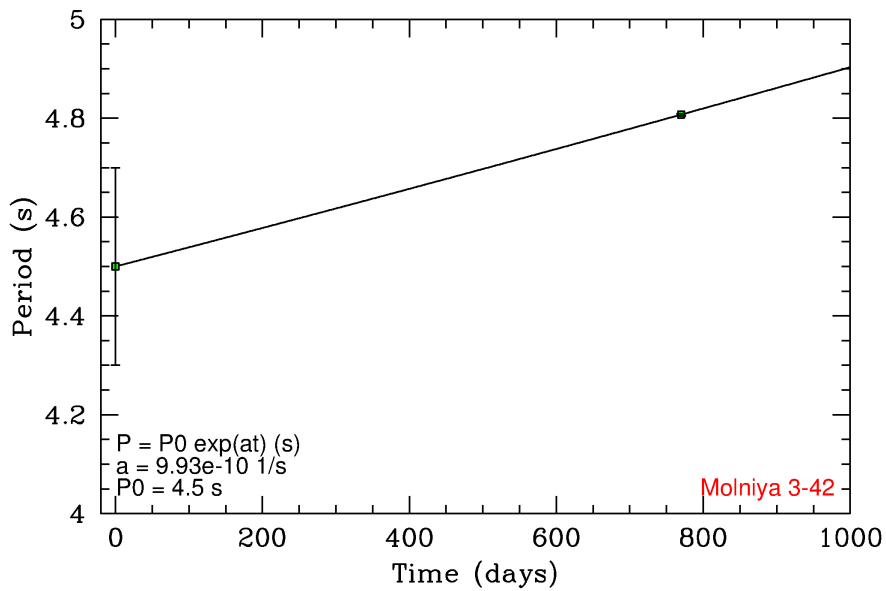


Figure 4.25: Exponential model of the time vs period relation for Molniya 3-42

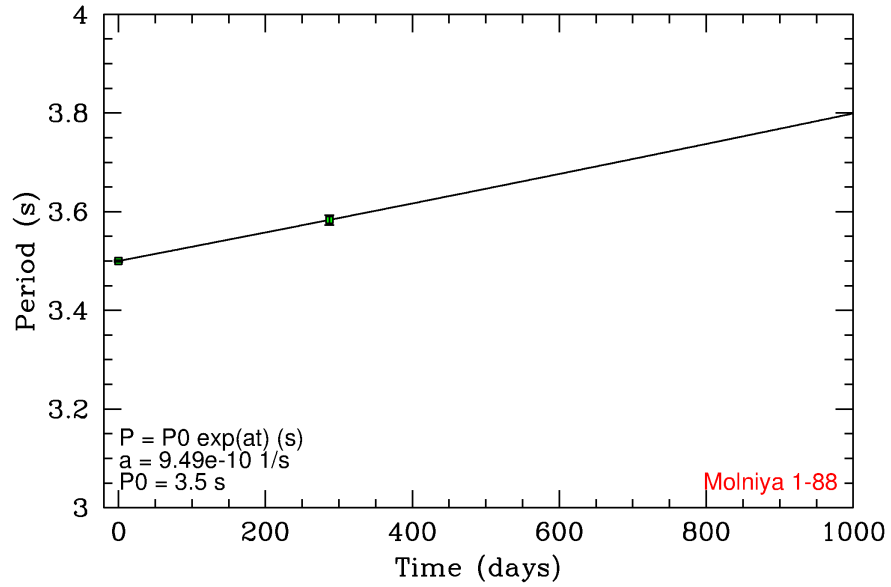


Figure 4.26: Exponential model of the time vs period relation for Molniya 1-88

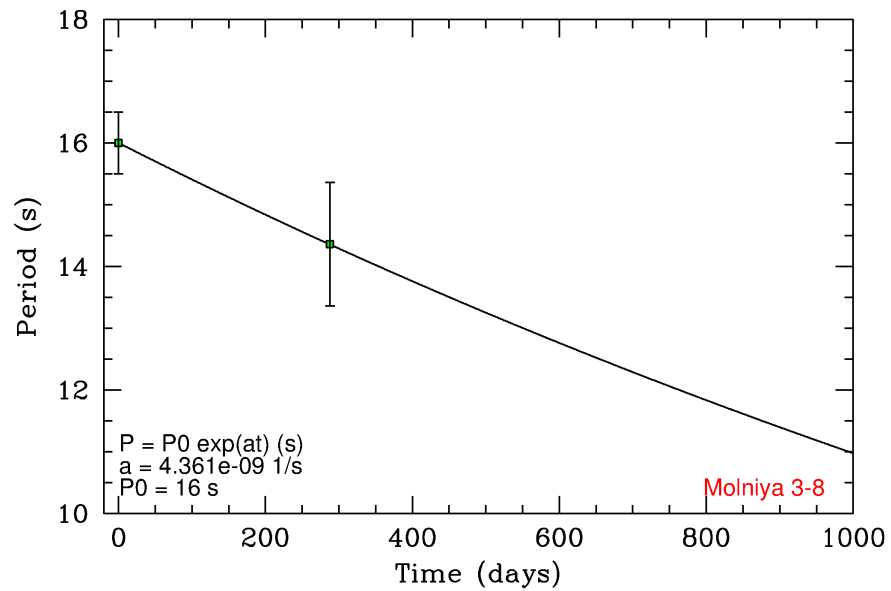


Figure 4.27: Exponential model of the time vs period relation for Molniya 3-08

The four satellites that follow the expected trend show consistency in the characteristic times ($\tau = 1/a$). The four value of the a parameter obtained are plotted in Table 4.6.

Satellite	$a(1/s)$	τ (s)	τ (days)	τ (years)
Molniya 1-49	1.04210^{-9}	953288846,5	11033	30.2
Molniya 2-09	1.05710^{-9}	946073793,7	10949	30.0
Molniya 3-42	9.9310^{-10}	1007049345,4	11655	31.9
Molniya 1-88	9.4910^{-10}	1053740779,7	12196	33.4
Molniya 3-08	4.36110^{-9}	229305205,2	2654	7.3

Table 4.6: Molniya characteristic time of decay

In the plots the trend seems to be linear insted of exponential, this is due to the little value of the a parameter, or the high value of the characteristic time. The mean value of the characteristic time is $\tau = 31.39$ years. The model is however incomplete since we can't calculate a common zero point to study all the periods as they were taken from a single satellite. This would allow us to better characterise the model parameter. All Molniya satellite are equal in dimension and shape, and also the orbits are similar. Then in theory should be possible to study all the rotational period as they were taken from a single debris at different times, to reconstruct a common evolution law for Molniya type debris. This has been made using the derivative of the period (dP/dt).

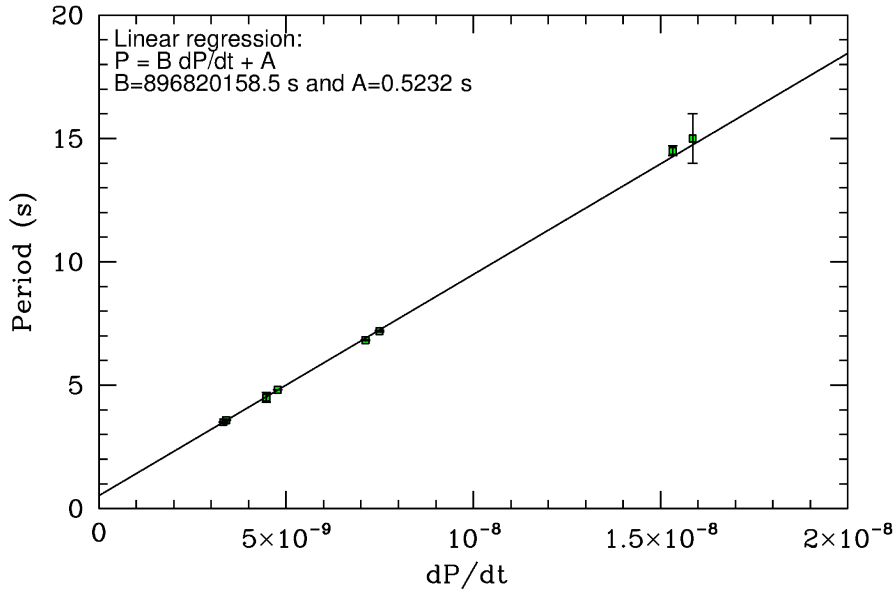


Figure 4.28: P vs dP/dt diagram for the period slowdown model.

For every point has been calculated the value of the derivative as:

$$\frac{dP}{dt} = aP_0 \exp(at) \quad (4.8)$$

and a diagram P vs dP/dt has been build.

Given the exponential form of the relation we expected that the points on the P vs dP/dt plot to be placed on a straight line. The result of this step is plotted in Figure 4.28.

The approach here was to fit the new plot with a standard deviation to calculate the relation between the period and it's derivative, and once discovered the straight line that ties the two quantities reconstruct a common zero point P_0 for all the satellite. The straight line found with the linear regression is:

$$P = B \left(\frac{dP}{dt} \right) + A \quad (4.9)$$

where $A = 0.5232$ s e $B = 896820158.5$ s = 28.44 years are the two coefficient of the linear regression. The parameter B represent the characteristic time expressed in seconds while the A parameter represents the common zero point of the relation (P_0). In other words a common model for all the Molniya debris involved in this section (except Molniya 3-08) can be written as follows:

$$P = A \exp \left(\frac{t}{B} \right) \quad (4.10)$$

The final plot of the period slowdown model for Molniya debris is plotted in Figures 4.29, 4.30.

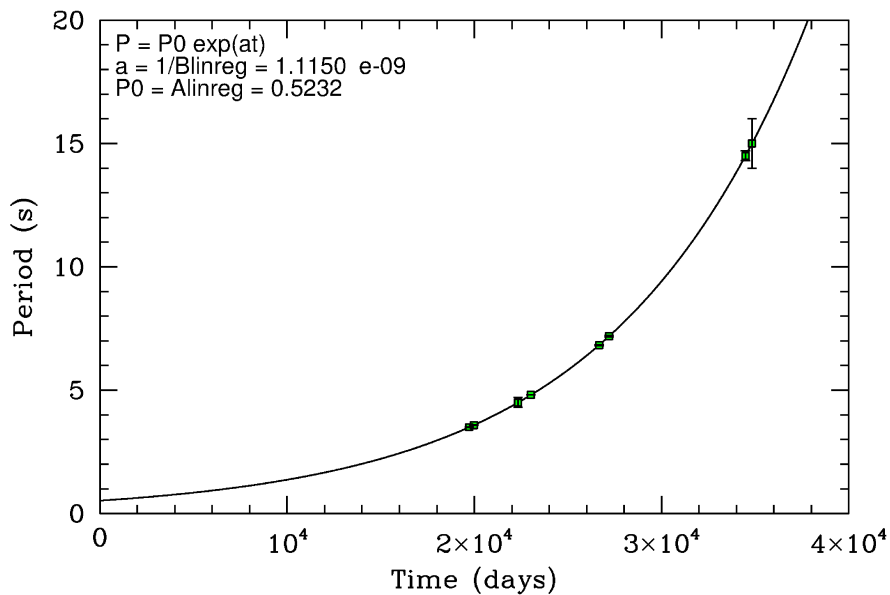


Figure 4.29: Final plot of the period slowdown model for Molniya debris.

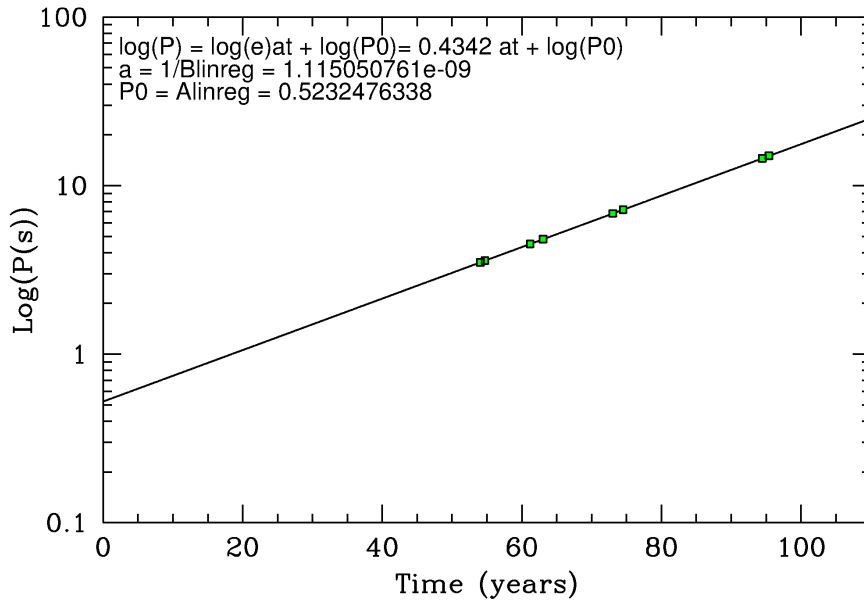


Figure 4.30: Final logarithmic plot of the period slowdown model for Molniya debris.

The zero point P_0 founded with this method should not be interpreted as a physical zero point, this is obvious watching at the time scale of Figure 4.30 and the lunch date column of Table 4.5. Let's take as example Molniya 1-88, lunched in 1994 and observed in 2016, its points are plotted at $t \approx 55$ years, considering that after the lunch Molniya type satellite remain operative typically for 7 – 8 years, it's impossible that the period has started from P_0 to evolve to the observed value, since it has had approximately 15 years insted of 55. It's probable that Molniya 1-88 first tumbling period was higher than P_0 , close to a value of about 2s. The zero point P_0 should therefore be interpreted as an mathematical artifice to reconstruct a common relation for Molniya type debris.

In conclusion we can affirm that the tumbling period slowdown of Molniya space debris follows the expected trend, well descibed by an exponential increase with time of the tumbling period, with a characteristic time of 28.44 years. More observation will be neede to check if the relation founded would be still valid in the future. A possible future development of this work might be to build a physically valid model to interpretate the characteristic time foud in term of Molniya debris charcteristics and orbits.

4.3.1 The case of Molniya 3-08

Molniya 3-08 (Figure 4.27) unlike others Molniya debris doesn't show a slow-down of the tumbling period, instead the period speeds up from $P = 16$ s (2016-03-10) to $P = 14.36$ s (2016-12-23). The fitting of the two points with a decreasing exponential function ($P = P_0 \exp(-t/\tau)$) provides a characteristic time that is completely different form the other characteristic times found for the other Molniya debris (Table 4.6). Although it's not the first time that such

a behavior is observed, for example the payload MIDAS 6, 63- 14 A shows a similar exponential acceleration¹, or in the case of Rocket Intercosmos 11 which shows a rapid acceleration of the period in the early phase of its orbital life (Boehnhardt et al. (1989)). The causes of this acceleration are still unknown. The acceleration could be due to a fuel leak (like in the case of Rocket Intercosmos 11, but a bit improbable for Molniya debris, since in theory the fuel lack is the cause of the satellite tumbling, and the fuel is used to maintain the satellite attitude as long as it's possible, that is, as long as there's fuel), or a thermal or radiation effect, or due to collision with small debris that could accelerate the spinning of the satellite. We can make suppositions about the speed and mass that this body should have to cause a similar period variation. Approximating the shape of the Molniya satellite to a cylinder with radius $r = 0.7$ m and length $L = 4.4$ m which rotates around one of the smaller axes, we can calculate its moment of inertia as:

$$I = \frac{1}{12}M(3r^3 + L^2) \approx 3000kgm^2 \quad (4.11)$$

where M is the mass of the satellite. The variation of angular velocity is:

$$\Delta\omega = \frac{2\pi}{P_f} - \frac{2\pi}{P_i} \quad (4.12)$$

where P_f and P_i are the final and initial tumbling period. Using now the conservation of the angular momentum:

$$\Delta L = I\omega_f - I\omega_i = m_{deb}v_{deb}R_{impact} \quad (4.13)$$

where m_{deb} and v_{deb} are mass and velocity of the small debris $R_{impact} = 8$ m is the distance to which the impact with respect to the axis of rotation occurred (we suppose that the small debris hit the satellite in the outside of the solar panels). In equation 4.13 we are ignoring the fact that the final moment of inertia of satellite should be different from the initial one due to mass added by the impact, we can do it because we are assuming that the mass of bullet is negligible compared to the mass of the satellite. From equation 4.13 it is easy to get the product value between mass and speed of the small debris, which turns out to be $m_{deb}v_{deb} \approx 35$ kg m/s. Considering the typical velocity of orbiting debris even a small mass object could be responsible for the observed acceleration of the period, if we suppose for exaple a velocity of about 1 km/s the mass of the debris is 35 grams. Of course, all this is true only if the satellite survives the impact without breaking. It's anyway impossible, with two only observations to confirme or exclude the impact supposition, it's however clear that if in future observations the satellite will be found tumbling faster then the last observation, the hypotesis of collision with small debris would no longer be valid, because the last hypotesis can explain a sudden acceleration and not a durable one in time.

4.4 The fallen

The last section of this chapter is dedicated to the decayed Molniya satellite, in particular those satellite which have fallen to the ground (in a figurative sense,

¹<http://www.satobs.org/tumble/expresfpm.html> , Fig11

this kind of satellites burns completely into the atmosphere without reaching the ground) in recent times: Molniya 1-44 decayed on 2017-10-23, Molniya 1-93 decayed on 2016-04-16, and Molniya 3-51 decayed on 2016-12-19 (three months after we observed it). The process that brings satellites with a Molniya-type orbit to the re-entry in atmosphere has been thoroughly studied in the work of Kolyuka et al. (2009). In particular in this work it is highlighted how the models show that the major factor influencing the lifetime of a space vehicle in a Molniya-type orbit is the gravitational attraction from the Moon and the Sun. We did not want to go into modeling the various gravitational perturbations to which these satellites are subjected, we limit ourselves to report the most important and to analyze the trend of the orbital parameters of the three considered objects during their orbit lifetime. There are at least four perturbation that can influence Molniya orbit:

- non-central part of the Earth gravity field,
- luni-solar gravitational attraction,
- solar radiation pressure,
- aerodynamical drag of the Earth's atmosphere.

as mentioned, of these four the second is the most important as far as the Molniya orbits are concerned. The lifetime of these objects however depends also, according to the models of Kolyuka et al. (2009), on the initial values of the longitude of ascending node Ω and also on the value of argument of perigee ω_0 of the orbit. Let us now see what are the perturbative effects due to the various perturbations always according to the models of Kolyuka et al. (2009), we will then try to find them in the plots of evolution of orbital parameters of the three satellites we are considering.

- Preferential influence of the Earth gravity field causes a secular variation of Ω and ω_0 , the rate of this variations depends on the inclination i and eccentricity e . The rate of variation of Ω drift exceeds the rate of ω_0 due to the peculiar inclination of the orbit that suppresses the perturbations on ω_0 (see section 1.2).
- Eccentricity e and perigee distance r_π variation are due to solar-lunar perturbations much more than Earth oblateness perturbations.
- The solar-lunar perturbation causes the drift of the inclination, the velocity of this process depends on Ω and ω_0 , that also varies because of Earth oblateness.
- ω_0 varies because of two perturbations: solar-lunar that cause a secular drift whose intensity depends on Ω , and influence of a non-central part of the Earth gravity field that also causes a secular drift which depends on inclination i and eccentricity e .
- The variation velocity of perigee distance r_π caused by the solar-lunar perturbations depends on Ω and ω_0 as shown in Figure 4.31.

- The variations of perigee distance can bring the satellite into the atmospheric drag zone that can accelerate the process causing the fall of the satellite to the ground and the end of the satellite life in orbit.

As you can see the evolution of orbital parameters is very complex as each one evolves in a way dependent on the others, we will nevertheless try to analyze the evolution in accordance with what has been said so far. First of all, let's see now how the orbital parameters evolve in the plots presented in Figure 4.32, Figure 4.33, and Figure 4.34. The plotted data were provided by Heavensat.

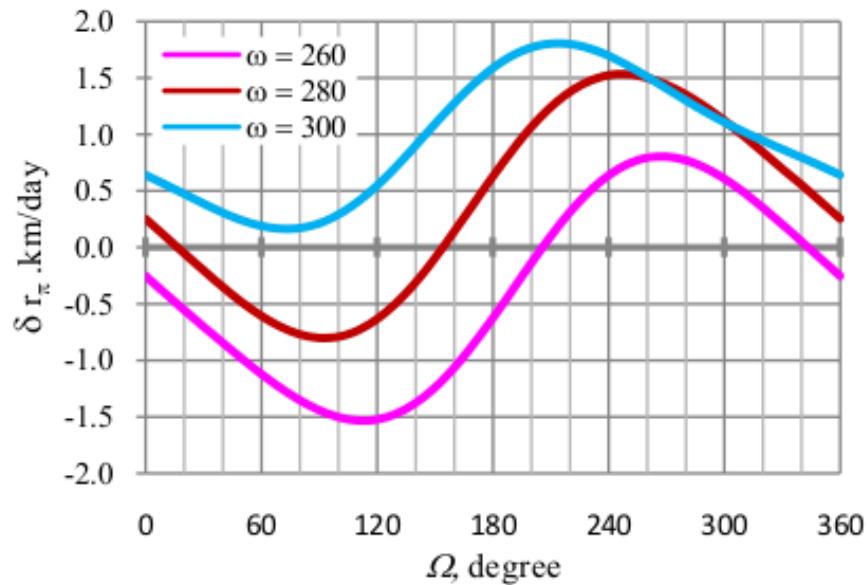


Figure 4.31: Velocity of changing of parameter r_π of the “Molniya” type orbit depending on Ω and ω_0 , image from Kolyuka et al. (2009)

If we consider the first ten years, the evolution of the orbital parameters is similar for all the three satellites. We note that the parameter Ω is strongly affected by the perturbations while parameter ω_0 as expected does not vary significantly. The Apogee height remains constant in this initial period (and consequently also the semi-major axis), this is also an expected result since satellites in these early years should be operational. Even eccentricity and inclination do not undergo significant variations, as well as the orbital period. We also note that the evolution of the perigee height depends heavily, except for slight oscillations, on the parameter Ω , when $\Omega > \approx 180^\circ$ the perigee height increases, when $\Omega < \approx 180^\circ$ decreases. This behavior is easily understandable looking at Figure 4.31 taken by the aforementioned article (Kolyuka et al. (2009)) and considering ω_0 values of the three satellites during this first phase. The evolution after the first ten or twelve years however differs considerably between Molniya 1-44 and Molniya 1-93 and 3-51. The first in fact has had a very long lifetime, remaining in orbit for nearly forty years. The other two instead have lasted for a short time, it is evident in fact looking at the evolution of the height of the perigee that the perturbations on the latter led them into the atmospheric drag

zone. This happened for Molniya 3-51 about twelve years after launch, and about eleven years after launch for Molniya 1-93. Neither of them managed to recover from the encounter with Earth atmosphere. Molniya 1-93 decayed immediately after the first entry in the atmospheric drag region, we see how apogee height, semi-major axis, eccentricity and orbital period collapse quickly to zero after the perigee reaches about two hundred kilometers height. Molniya 3-51 didn't decay immediately, in fact it lived another period of growth of the perigee height, settling on an orbit characterized by height of the apogee ≈ 32000 km, orbital period ≈ 9.5 h, and eccentricity and inclination unchanged. However, the return of the parameters Ω to angles lower than 180° has brought the perigee height in the atmosphere drag zone causing the rapid collapse of the orbit and the re-entry into atmosphere. Molniya 1-44 has had a very particular orbital life, in fact, unlike the other two has been able to remain in orbit despite the perigee proximity to the earth's atmosphere. This success is probably attributable to the evolution of parameter ω_0 which at some point began to evolve, probably because of the inclination which has dropped to $\approx 62^\circ$ no longer guaranteeing the cancellation of the perturbation term due to the oblateness of the Earth, which becomes null with inclination angle $i = 63.4^\circ$. The evolution of the argument of the perigee ω_0 has contributed to soften perigee height perturbations. In fact, in the final stages it seems that is ω_0 to condition the evolution of the perigee height, while Ω , which varies very quickly, seems to be responsible for the observable oscillations in the evolution of the perigee height. This is not surprising given the strong dependence of the evolution of perigee height from both Ω and ω_0 (Figure 4.31). We note that perigee height decrease for small values of the argument of the perigee and increase or at least remain constant for high values. The satellite is therefore survived to a complete cycle of the parameter ω_0 from 0° to 360° . Once the second cycle started, the small values of ω_0 brought the satellite in the atmospheric drag zone, causing finally the re-entry into atmosphere. In conclusion we can say that the predictions of Kolyuka et al. (2009) models are fully respected by the three decayed Molniya debris.

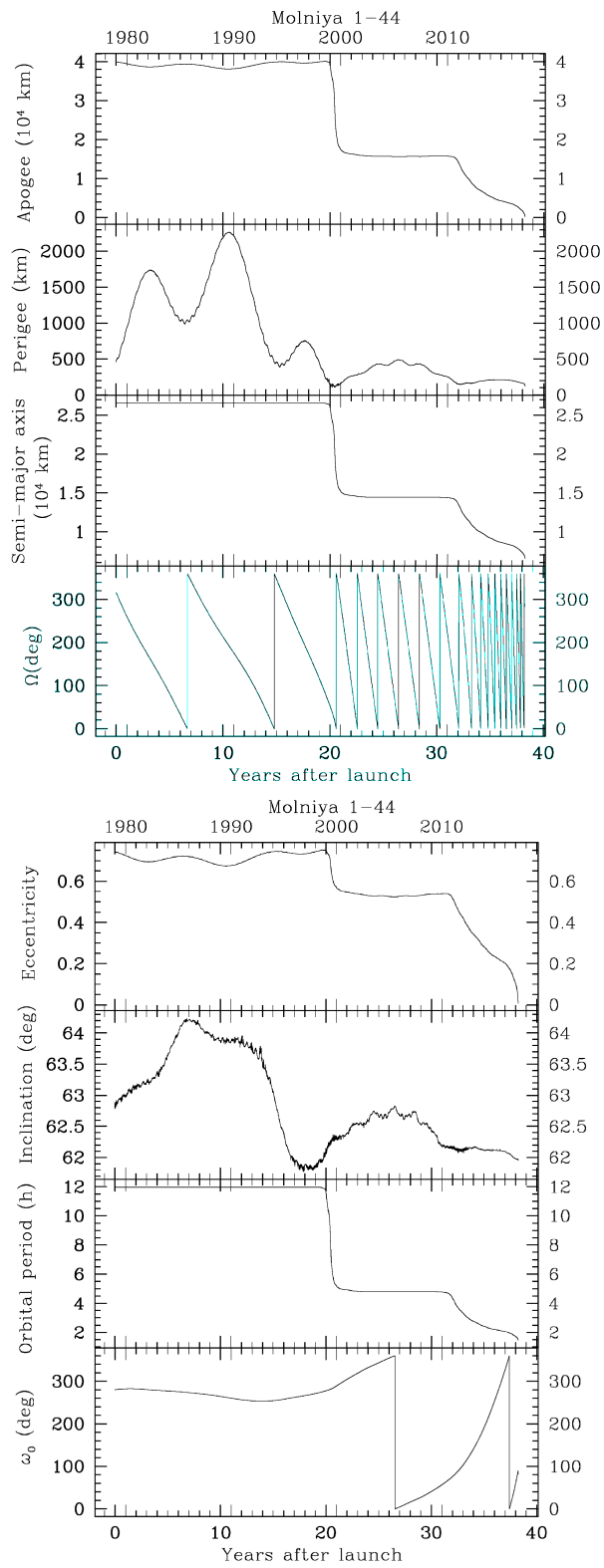


Figure 4.32: Orbital parameter evolution for Molniya 1-44

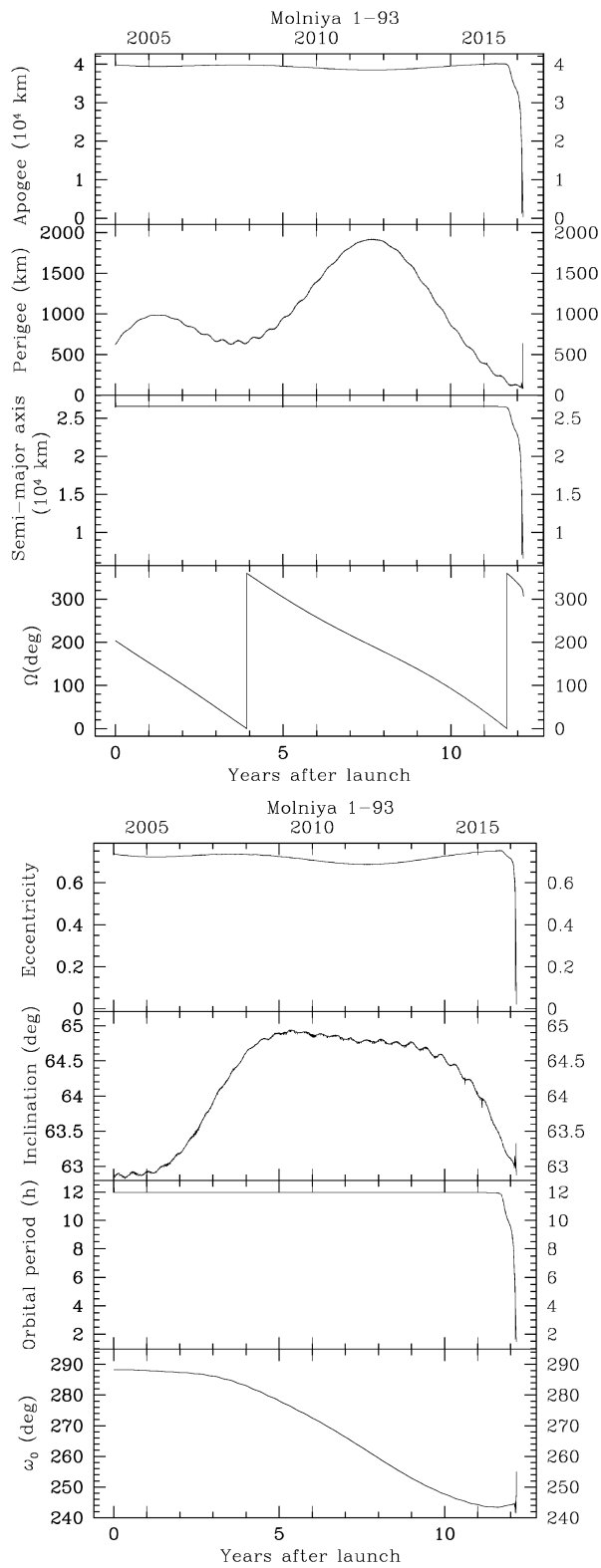


Figure 4.33: Orbital parameter evolution for Molniya 1-93

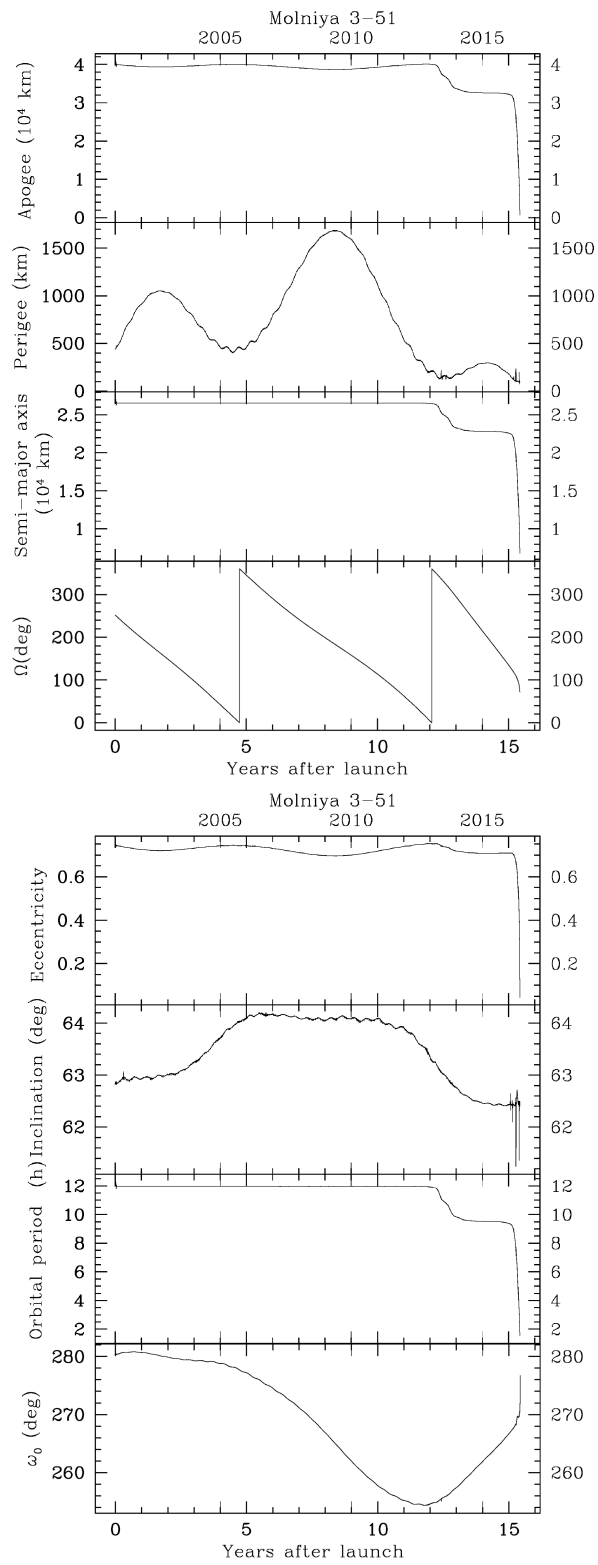


Figure 4.34: Orbital parameter evolution for Molniya 3-51

Chapter 5

Conclusions

This work falls within the scope of the science of space debris. Space debris science is the science that deals with studying the temporal evolution of man made satellites that ended their operation and have remained in orbit without the possibility of control by man. The study of these objects is becoming more and more important in recent years due to Kessel syndrome, a scenario in which the density of objects in low earth orbit (LEO) is high enough that collisions between objects could cause a cascade process where each collision generates space debris that increases the likelihood of further collisions. This process would lead to the impossibility of using satellites for a very long time because of too frequent collisions that would quickly suppress any attempt to keep satellites in orbit. In order to prevent this syndrome from beginning, it is important to study the behavior of these objects and their instabilities, and to develop recognition methods that allow to start cataloging and tracking those objects (such as old rocket or stage) of which the orbital evolution was not followed from the beginning. Object of which consequently no name and origin are known, but that remain in orbit representing a danger to other satellites and especially to space stations. These are necessary condition to start thinking about possible solutions of the Kessel syndrome problem. In this work, we went into the spectrophotometric analysis of the constellation of satellites Molniya and Meridian, russian military communications satellites, starting with a series of observations made with the Cassini telescope in the second part of 2016. Our aim was to obtain a as complete as possible characterization of the properties of these objects. To make this we made two type of images, photometry and spectra. The first has many possible usages, in fact it can be used to study satellites colours and their variations related to the variations of other parameters as it was done for the phase angle, but also to study the rotational instabilities that Molniya type satellite tend to develop once out of control. The spectra instead are powerful tools to characterize the colour properties and the reflectance of these satellite, allowing, at least theoretically, to understand the materials of which these objects are made of, and therefore represent a powerful tool for the purpose of cataloging forgotten objects. Our analysis has led us to investigate various aspects of the constellation which can be divided into two categories. The first regards the instabilities to which these satellites are exposed. We have investigated two aspects. Orbital instabilities and balance instabilities.

Regarding orbital instability we have tested the results of the article written

by Kolyuka et al. (2009). To do this we have analyzed the orbital history of the three fallen Molniya debris, namely Molniya 3-51, Molniya 1-93 and Molniya 1-44. Orbital history wasn't extracted from our images, but we were entrusted with the same tool that allowed the observation, Heavensat, a software that provided ephemeris of all observed satellite. The results of this analysis have confirmed the predictions of Kolyuka et al. (2009). In particular about the role played by the two orbital parameters Ω and ω_0 (longitude of ascending node and argument of the perigee) in conditioning the evolution of the height of the perigee, and therefore the time needed to bring the satellite in contact with the atmospheric drag zone, and trigger the process of atmosphere re-entry. Also forecasts on Ω and ω_0 evolution, conditioned by eccentricity and above all by the inclination, have been confirmed, the first parameter undergoes a secular variation, the second instead does not vary because of the peculiar inclination of the molniya orbit. Slight variations in inclination are however sufficient to trigger the variation of the parameter ω_0 and consequently completely change the orbital evolution, as seen in Molniya 1-44 case, that has remained in orbit much longer than the other two.

The second instability examined is that of the balance of these satellites. From the beginning we said that these satellites once out of control tend to develop a spinning motion. However, the causes of development of this motion are not clear. What can be done is to study the temporal evolution. In fact the tumbling period should vary with time because of the action of Earth magnetic field. The magnetic field variation along the orbit creates inside the satellite electrical currents, which in turn create magnetic fields. These magnetic fields oppose rotation creating a braking effect. The braking effect should be exponential with time. To study this phenomenon we started from photometric images, analyzing the track left by satellites on the CCD. From the footprint we have trace back, with the use of a periodogram and the putting in phase of several light curves, to the spin period of the satellites in all the cases where it was possible. To study the evolution of a phenomenon, however, it is necessary to have two observations at different times, for this reason we went out to look for satellite tumbling periods in prior observations taken by professor Buzzoni in 2014, 2015 and 2016. In some cases where we were not able to observe the satellites because of their peculiar orbit, we were helped by Figer who provided us with the missing data. After this long research and analysis we managed to get the periods, referred to two different times, of five satellites. This allowed us to create an evolutionary model that was able to reproduce the observed time evolution. The resulting model is actually an exponential model characterized by a characteristic time of 28.44 years. Only in one case the model did not work, in fact one of the satellites showed an acceleration of the tumbling period. This acceleration can have many causes but we could not verify them. For a check in fact future observations will be needed to see if the acceleration was an occasional event or due to a phenomenon that lasts in time.

The second category is a spectrophotometric characterization of these objects. In particular we studied two aspects: the relation that exists between the magnitude of the satellite and the phase angle to which it is observed, and the spectral and color indexes properties. To study the phase angle - magnitude relation we considered the integrated magnitude of every light curves we had. As expected, the magnitude drops with the phase angle. The way magnitude drops however is closely related to the shape of the object being analyzed, therefore

phase angle - magnitude relation is another aspect that could give information on the nature of a unknown object. For this reason we tried to fit the data with four different models: a lunar model taken from Buratti et al. (2011), that was build to investigate a wavelength dependece of the magnitude-phase angle relation for the Moon that takes into account lunar roughness, a lambertian spherical model, a simple lunar model, and a planar lambertian model. The goodness of fit was evaluated with a Least Square method in every photometric filter and for every model. In all the filter analyzed the best model to fit the data was the lambertian spherical model. The best fit model allowed us to fix a lower limit to albedo value for Molniya debris. The minimum value of albedo was found to be $a_{min} = 0.09$ for B filter, $a_{min} = 0.28$ for I filter, $a_{min} = 0.15$ for R filter and $a_{min} = 0.10$ for V filter.

The color indexes analysis was carried out building the color-color diagram for the satellites constellation. A check for possible dependencies of the color indexes on age and phase angle has been made. Neither of them has been found to significantly affect colors indexes. The color-color diagram have shown that in general satellites colors are redder than Sun colors, and consequently satellites of Molniya type have different responses to radiation based on the wavelength. In particular they are excellent band I reflectors. Their reflective capacities decrease at the wavelength drops by moving from band R to V and finally to B. This has also partially confirmed the albedo values found with the magnitude phase angle models, which describe a situation consistent with what found in the case of color indexes. Finally a comparison was made in the color-color diagram B-R R-I between the colors of the satellites and the colors of the materials of which they are composed measured in laboratory. Satellites tend to present redder colors than those of the analyzed materials, the materials closest to the observed colors of the satellites are the Mylar and the solar panels. To complete the color characterization of Molniya and Meridian space debris a spectral analysis was carried out. The first step of spectral analysis was to check the spectra reliability comparing its flux with that calculated with photometry. This check was necessary because of the difficulties and the many possible causes of error that may occur while capturing a spectrum, and made us reject some of the spectra. The spectral analysis then was carried forward dividing the satellite spectra by solar spectrum to obtain the reflectance wavelength dependence. The reflectance was than normalized to 7000 Å. So we searched in the spectra the imprints of the materials of which the Molniya are made, but without success. Even in this case there were no agreement between satellites patterns and material patterns. The Molniya reflectance function is positioned in an intermediate area between aluminum and solar panels functions, which suggests that the observed one is probably the sum of these two components. Any age trend was founded, confirming photometry predictions.

In conclusion we have obtained a satisfactory characterization of Molniya-type satellites. Molniya type orbits present gravitational instabilities that tend to lead the satellite to the re-entry in Earth atmosphere. The orbiting satellites on this orbit tend to develop an dynamical instability that forces the satellite to begin to tumble. The tumbling periods evolve with time following an exponential law with characteristic time 28.44 years. The various photometric tests showed a good agreement between them. Even spectra, with all their uncertainties has confirmed photometric predictions. Molniya and Meridian constellation have differential reflectance properties with wavelength, their reflective capacity drops

with decreasing wavelength. The colour properties, unlike previously supposed, do not show age dependencies. The phase angle conditions the magnitude in every filter following a spherical lambertian model, the color indexes therefore do not depend on the phase angle.

The future prospects of this study are many and can take many directions. Surely it would be important to continue observing these satellites to deepen the functioning of evolution of the tumbling period, to test with new data if the model continues to be reliable, especially with regard to the characteristic time of the process. Could also be interesting to build a model that is not only qualitative, but attempts to describe the data relying on physical considerations on the moment of inertia of these satellites and on the Earth's magnetic field. Likewise regarding magnitude-phase angle relation, it would be interesting to build a model based on the physical characteristics of the satellites, considering the shape and the presence of solar panels. Another thing that has not been done but may be interesting is to see under what phase angle conditions the satellites flash, these could provide informations on which is the axis on which the satellite is tumbling, providing a useful tool for building a better evolutionary model.

Appendix A

Observations

All the magnitudes presentes in the tables of this Chapter are not distance calibrated.

A.1 Night 2016/08/01-02

- Clear non photometric sky
- Operator: Ivan Bruni
- JD:2457602.5

UT(start)	Object	Airmass	Exptime(s)	Filter/Grism	Mag	Phase Angle
19:48:40	Molniya 1-S	2.323	25	V	13.45	15.44
19:52:17	Molniya 1-S	2.318	30	V	13.41	14.91
19:53:22	Molniya 1-S	2.317	30	R	12.60	14.73
19:54:28	Molniya 1-S	2.304	30	I	11.35	14.56
19:56:44	Molniya 1-S	2.298	30	B	13.95	14.06
21:39:55	Molniya 3-51	1.445	15	V	15.05	111.36
21:41:47	Molniya 3-51	1.445	15	R	14.06	111.03
21:42:38	Molniya 3-51	1.444	15	I	13.06	110.87
21:43:27	Molniya 3-51	1.441	15	B	15.97	110.70
21:46:13	Molniya 3-51	1.438	15	I	13.06	110.42
21:47:02	Molniya 3-51	1.438	15	B	15.92	110.21
21:48:04	Molniya 3-51	1.438	15	V	15.00	110.04
21:48:55	Molniya 3-51	1.437	15	R	13.73	109.88
21:49:46	Molniya 3-51	1.436	15	I	12.98	109.71
21:50:36	Molniya 3-51	1.435	15	B	15.78	109.55
21:56:03	Molniya 3-51	1.429	120	GR4	-	108.71
22:04:16	Molniya 3-51	1.421	120	GR4	-	108.71
22:10:54	Molniya 3-51	1.413	15	V	15.02	106.16

Table A.1: Logbook 2016/08/01-02

UT(start)	Object	Airmass	Exptime(s)	Filter/Grism	Mag	Phase Angle
22:11:46	Molniya 3-51	1.414	15	R	13.98	105.99
22:12:37	Molniya 3-51	1.414	15	I	13.60	105.81
22:17:48	Molniya 3-51	1.407	15	V	15.14	104.94
22:18:39	Molniya 3-51	1.407	15	R	13.44	104.76
22:19:30	Molniya 3-51	1.407	15	I	13.15	104.59
22:20:21	Molniya 3-51	1.407	15	B	15.88	104.59
22:27:27	Molniya 1-80	1.205	15	V	12.26	88.46
22:28:19	Molniya 1-80	1.202	15	R	11.48	88.36
22:29:10	Molniya 1-80	1.199	15	I	10.67	88.27
22:30:00	Molniya 1-80	1.196	15	B	13.03	88.17
22:54:07	Molniya 1-80	1.144	15	V	12.93	86.52
22:54:57	Molniya 1-80	1.143	15	R	12.14	86.47
22:55:48	Molniya 1-80	1.142	15	I	11.21	86.42
22:56:40	Molniya 1-80	1.141	15	B	14.06	86.37
22:57:40	Molniya 1-80	1.14	15	V	13.09	86.32
22:58:30	Molniya 1-80	1.139	15	R	12.67	86.28
22:59:21	Molniya 1-80	1.138	15	I	11.63	86.27
23:30:22	Molniya 1-S	1.786	15	V	13.01	44.21
23:31:13	Molniya 1-S	1.786	15	R	12.45	44.45
23:32:05	Molniya 1-S	1.786	15	I	11.42	44.69
23:32:56	Molniya 1-S	1.786	15	B	13.40	44.93
23:34:23	Molniya 1-S	1.784	25	V	13.06	45.17
23:35:24	Molniya 1-S	1.781	25	R	12.46	45.42
23:36:25	Molniya 1-S	1.781	25	I	11.55	45.66
23:37:26	Molniya 1-S	1.779	25	B	13.74	45.90
23:38:39	Molniya 1-S	1.776	40	V	13.07	46.38
23:39:55	Molniya 1-S	1.776	40	R	12.44	46.62
23:41:10	Molniya 1-S	1.776	40	I	11.41	46.86
23:42:26	Molniya 1-S	1.772	40	B	13.50	47.10
23:44:22	Molniya 1-S	1.771	40	V	12.99	47.10
23:45:37	Molniya 1-S	1.768	40	R	12.45	48.07
23:46:53	Molniya 1-S	1.768	40	I	12.44	48.31
23:48:09	Molniya 1-S	1.763	40	B	13.50	48.55
23:49:53	Molniya 1-S	1.763	40	V	12.98	49.04
23:51:10	Molniya 1-S	1.762	40	R	12.41	49.28
23:52:26	Molniya 1-S	1.762	40	I	11.50	49.52
23:53:41	Molniya 1-S	1.757	40	B	13.76	50.01
23:55:06	Molniya 1-S	1.757	40	V	13.08	50.25
23:56:23	Molniya 1-S	1.755	40	R	12.52	50.49

Table A.2: Logbook 2016/08/01-02

UT(start)	Object	Airmass	Exptime(s)	Filter/Grism	Mag	Phase Angle
23:57:38	Molniya 1-S	1.755	40	I	11.62	50.98
23:58:54	Molniya 1-S	1.754	40	B	13.65	51.22
00:01:16	Molniya 1-S	1.747	240	R	12.56	51.70
00:11:02	Molniya 1-S	1.738	120	GR4	-	54.13
00:23:30	Molniya 1-S	1.723	40	V	13.08	57.30
00:24:46	Molniya 1-S	1.723	40	R	12.57	57.54
00:26:01	Molniya 1-S	1.723	40	I	11.59	57.78
00:27:17	Molniya 1-S	1.723	40	B	13.63	58.03
00:29:28	Molniya 1-S	1.717	40	V	13.12	58.51
00:30:44	Molniya 1-S	1.717	40	R	12.59	59.00
00:32:01	Molniya 1-S	1.717	40	I	11.63	59.25
00:33:17	Molniya 1-S	1.717	40	B	13.64	59.49
00:39:04	Molniya 1-S	1.708	40	V	13.13	60.95
00:40:20	Molniya 1-S	1.708	40	R	12.62	61.20
00:41:36	Molniya 1-S	1.708	40	I	11.69	61.68
00:42:50	Molniya 1-S	1.708	40	B	13.68	61.93
00:45:48	Molniya 1-S	1.702	40	V	13.18	62.66
00:47:04	Molniya 1-S	1.702	40	R	12.65	62.91
00:48:21	Molniya 1-S	1.702	40	I	11.69	63.15
00:49:36	Molniya 1-S	1.702	40	B	13.70	63.64
01:03:05	Molniya 1-80	1.079	40	V	13.48	83.35
01:04:21	Molniya 1-80	1.079	40	R	12.97	83.34
01:05:36	Molniya 1-80	1.078	40	I	11.83	83.31
01:11:33	Molniya 1-80	1.076	40	V	13.99	83.22
01:12:49	Molniya 1-80	1.075	40	R	12.97	83.21
01:14:05	Molniya 1-80	1.075	40	I	12.11	83.19
01:15:21	Molniya 1-80	1.074	40	B	14.79	83.18
01:25:01	Molniya 1-80	1.070	120	GR4	-	83.03
01:41:22	Molniya 1-80	1.064	40	V	13.76	82.81
01:42:37	Molniya 1-80	1.064	40	R	12.69	82.78
01:43:53	Molniya 1-80	1.063	40	I	11.79	82.76
01:45:09	Molniya 1-80	1.062	40	B	15.24	82.75
01:46:36	Molniya 1-80	1.062	40	V	14.21	82.72
01:47:52	Molniya 1-80	1.062	40	R	13.30	82.71
01:49:08	Molniya 1-80	1.061	40	I	11.80	82.70
01:50:23	Molniya 1-80	1.061	40	B	14.94	82.68
02:16:04	Molniya 1-32	1.065	120	GR4	-	

Table A.3: Logbook 2016/08/01-02

Object	V	B-V	V-R	V-I
PG2213+006	14.124	-0.217	-0.092	-0.203
PG2213+006 A	14.178	0.673	0.406	0.808
PG2213+006 B	12.706	0.749	0.427	0.829
PG2213+006 C	15.109	0.721	0.426	0.830
PG2331+055	15.182	-0.066	-0.092	-0.044
PG2331+055 A	13.051	0.741	0.419	0.821
PG2331+055 B	14.774	0.819	0.480	0.935

Table A.4: Standard stars magnitudes and color indexes from Landolt (1992)

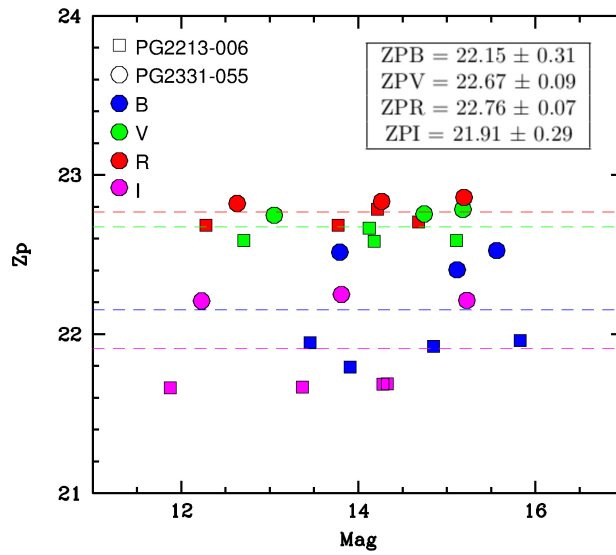


Figure A.1: Photometric zero points 2016/08/01-02, magnitudes from Landolt (1992)

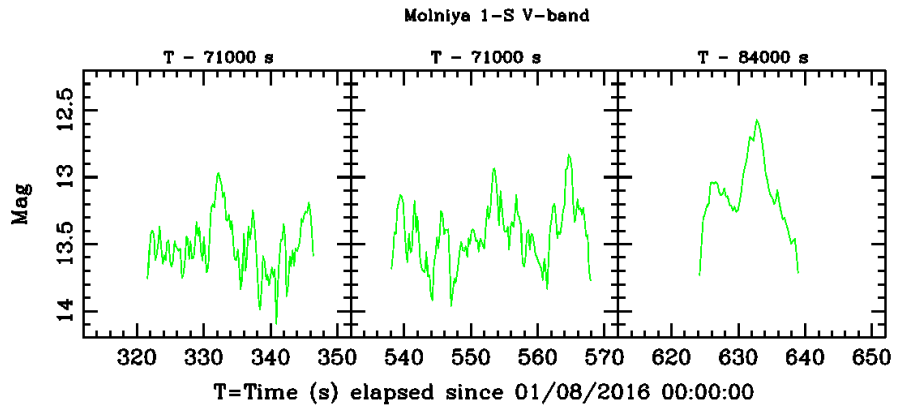


Figure A.2: Molniya 1-S filter V light curves

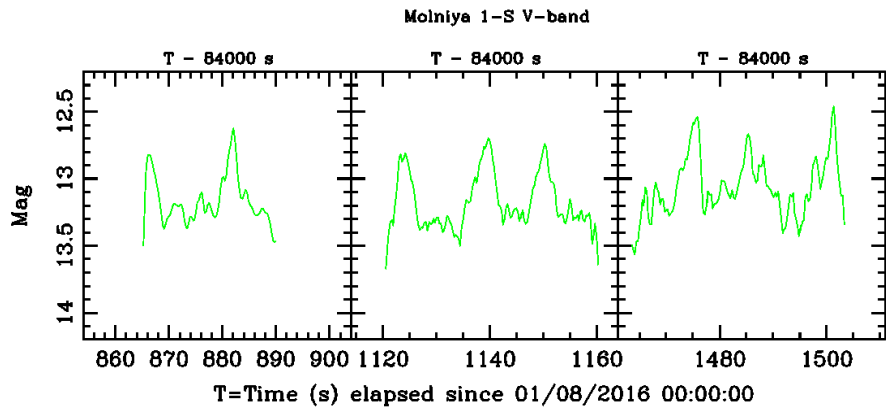


Figure A.3: Molniya 1-S filter V light curves

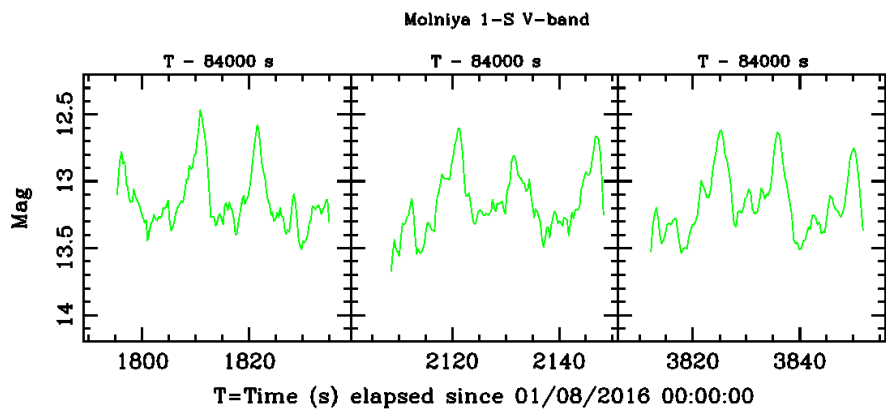


Figure A.4: Molniya 1-S filter V light curves

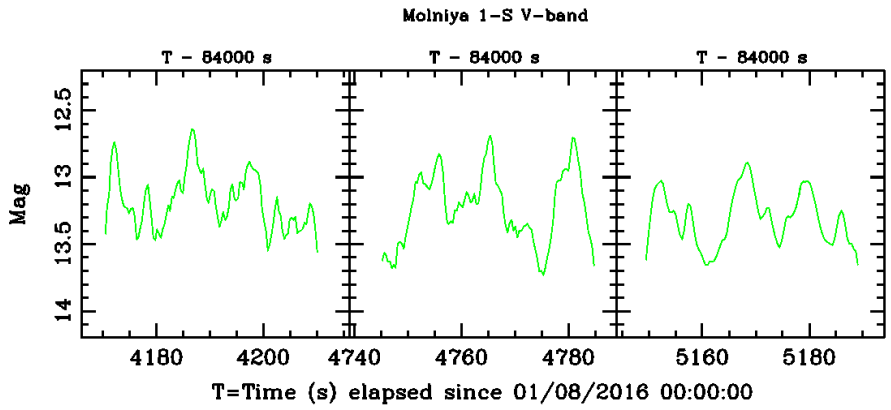


Figure A.5: Molniya 1-S filter V light curves

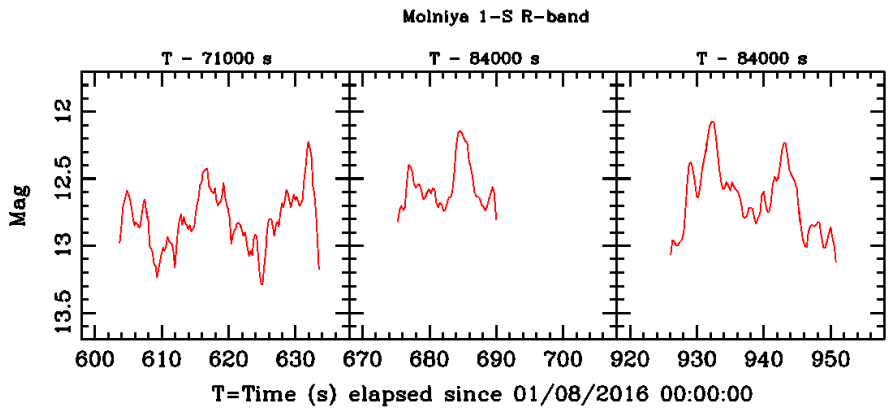


Figure A.6: Molniya 1-S filter R light curves

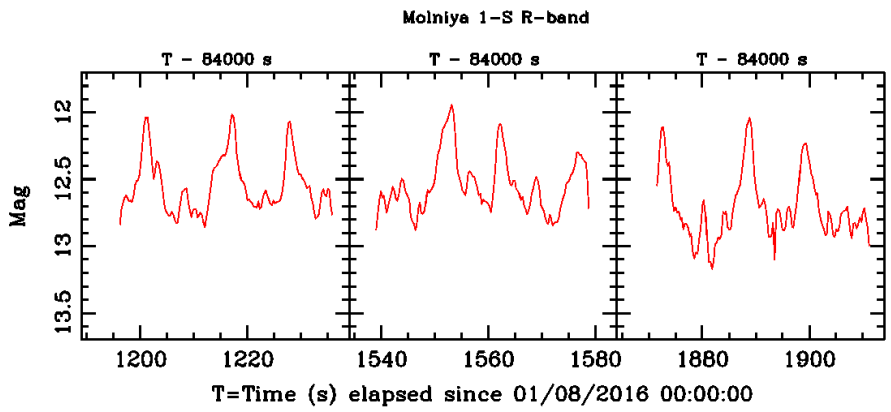


Figure A.7: Molniya 1-S filter R light curves

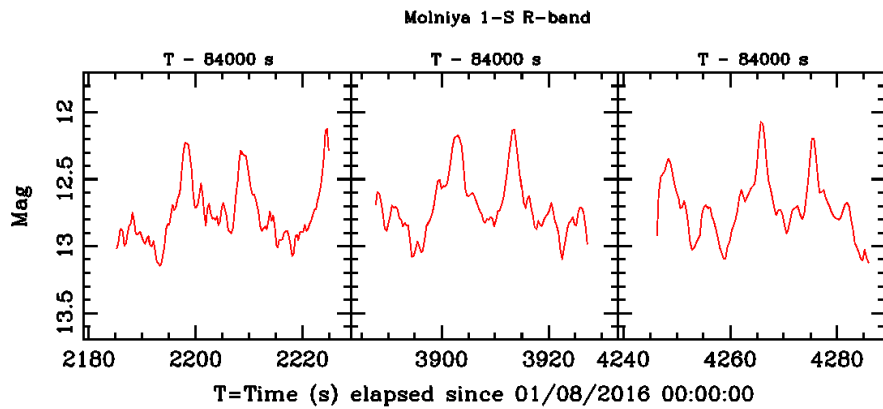


Figure A.8: Molniya 1-S filter R light curves

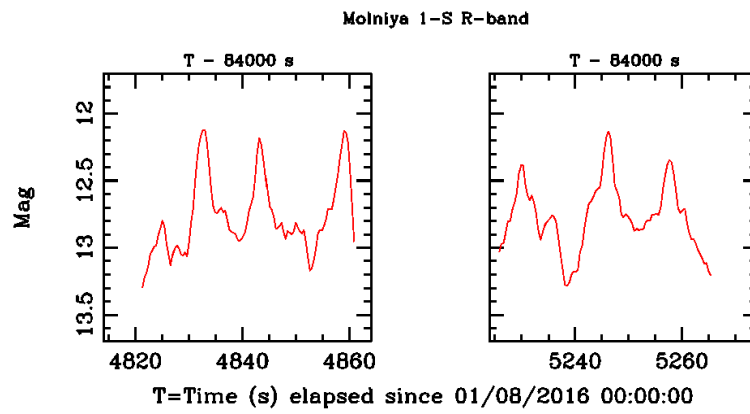


Figure A.9: Molniya 1-S filter R light curves

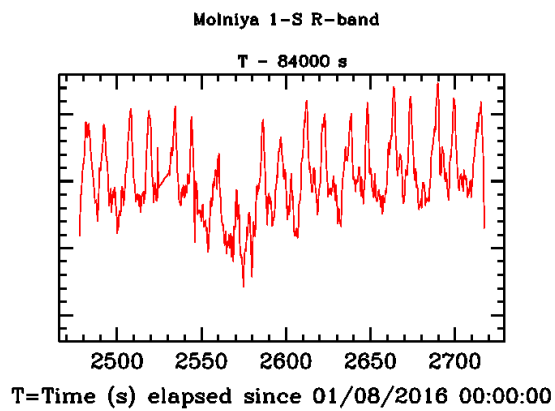


Figure A.10: Molniya 1-S filter R light curves

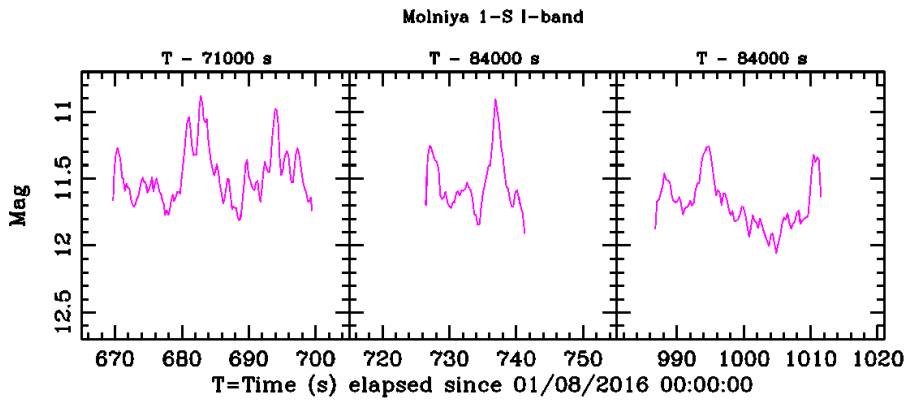


Figure A.11: Molniya 1-S filter I light curves

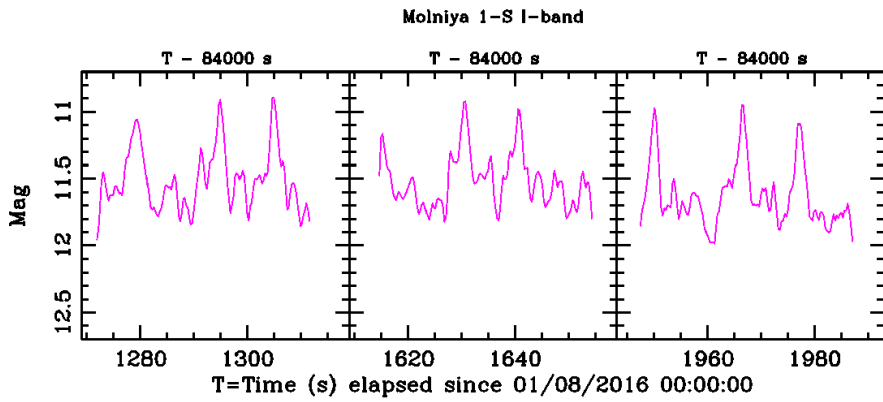


Figure A.12: Molniya 1-S filter I light curves

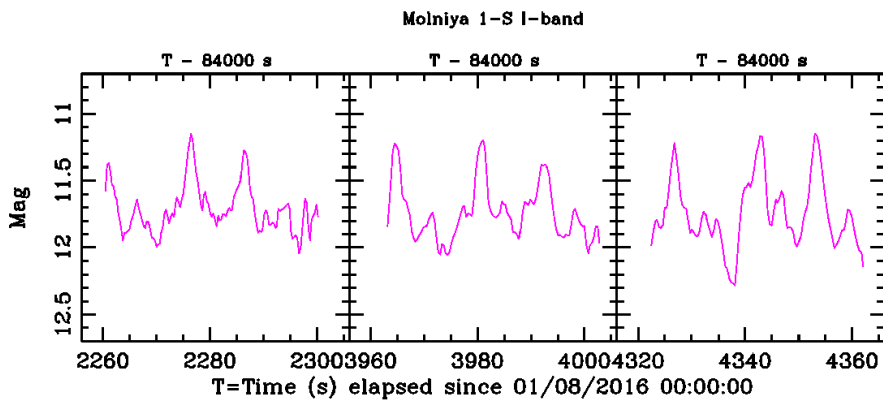


Figure A.13: Molniya 1-S filter I light curves

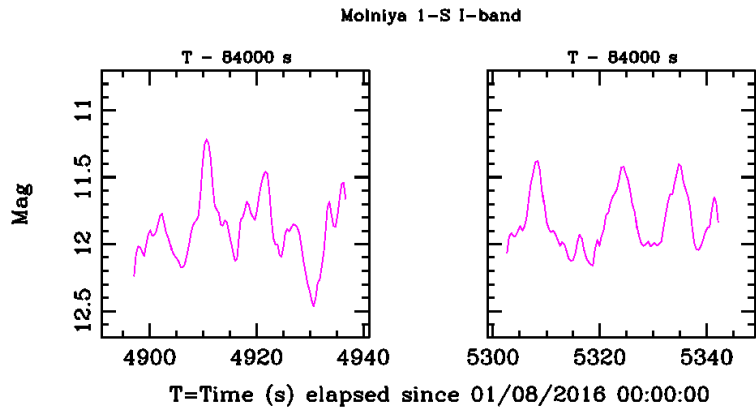


Figure A.14: Molniya 1-S filter I light curves

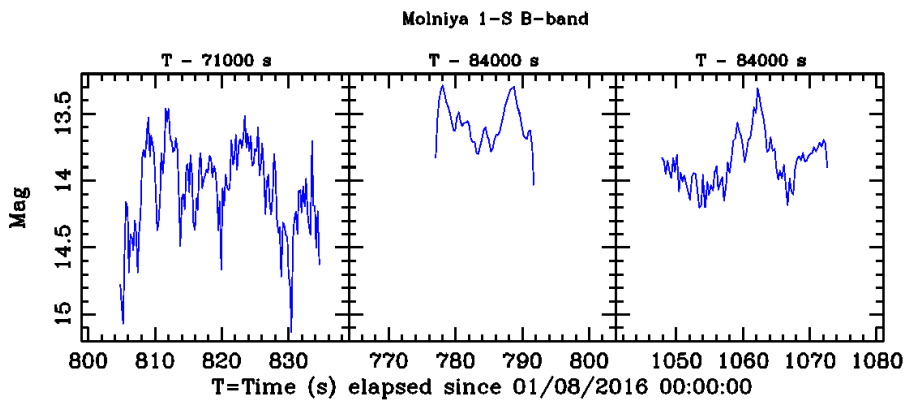


Figure A.15: Molniya 1-S filter B light curves

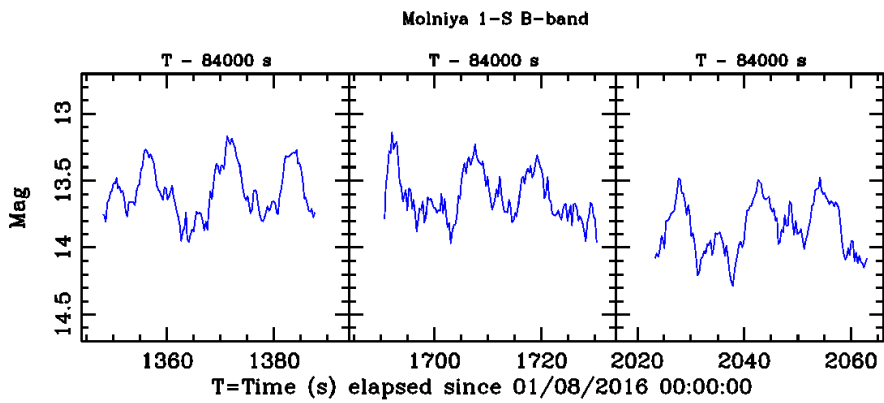


Figure A.16: Molniya 1-S filter B light curves

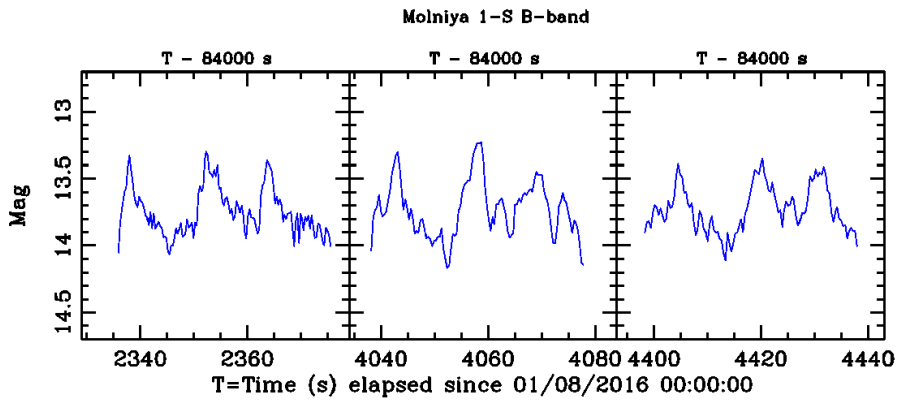


Figure A.17: Molniya 1-S filter B light curves

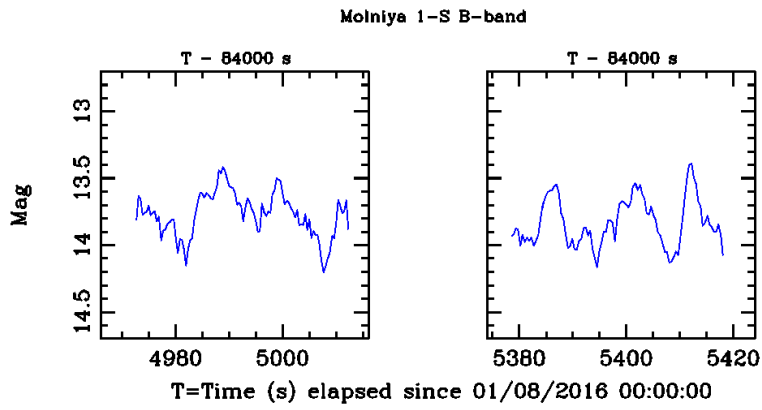


Figure A.18: Molniya 1-S filter B light curves

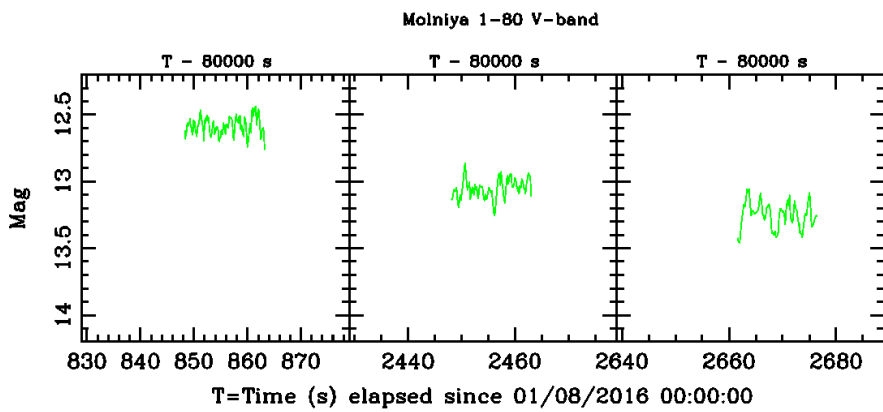


Figure A.19: Molniya 1-80 filter V light curves

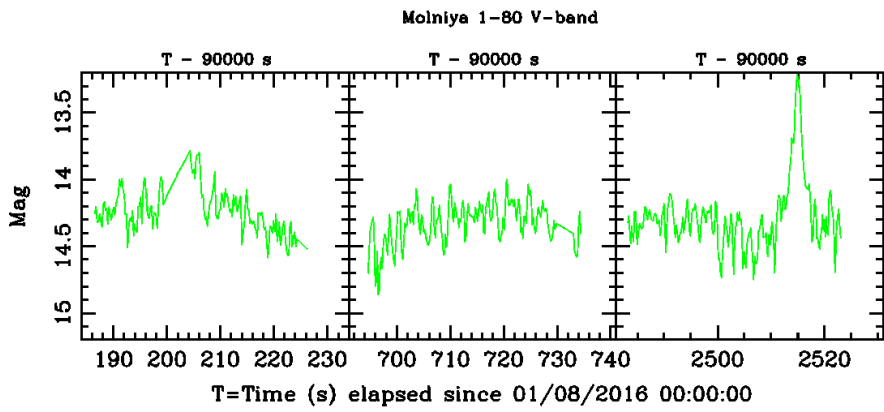


Figure A.20: Molniya 1-80 filter V light curves

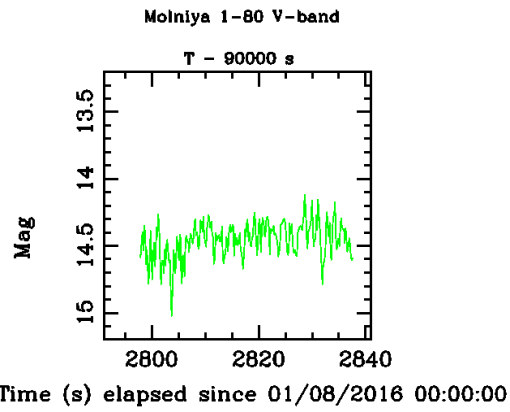


Figure A.21: Molniya 1-80 filter V light curves

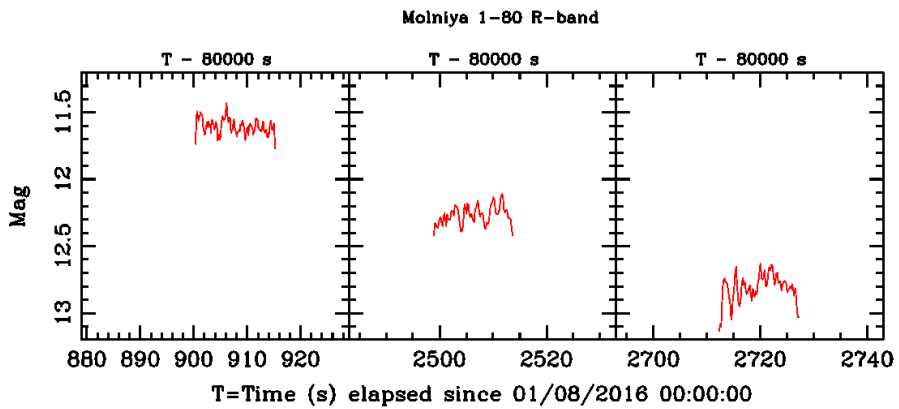


Figure A.22: Molniya 1-80 filter R light curves

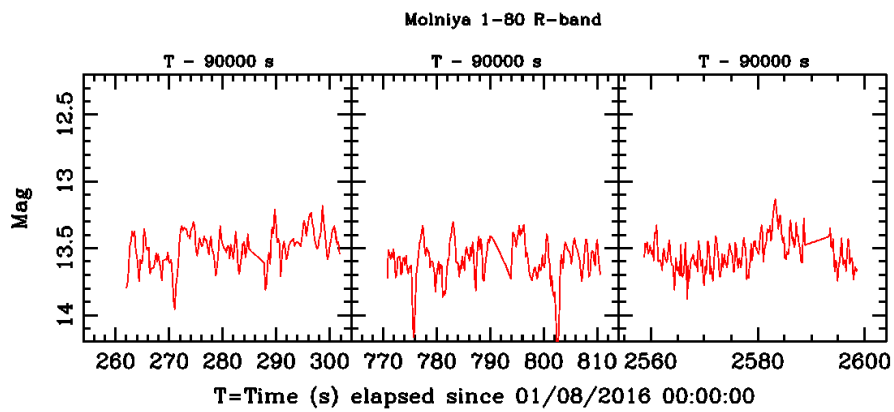


Figure A.23: Molniya 1-80 filter R light curves

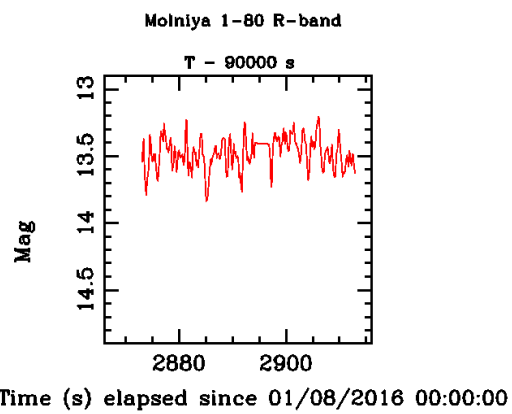


Figure A.24: Molniya 1-80 filter R light curves

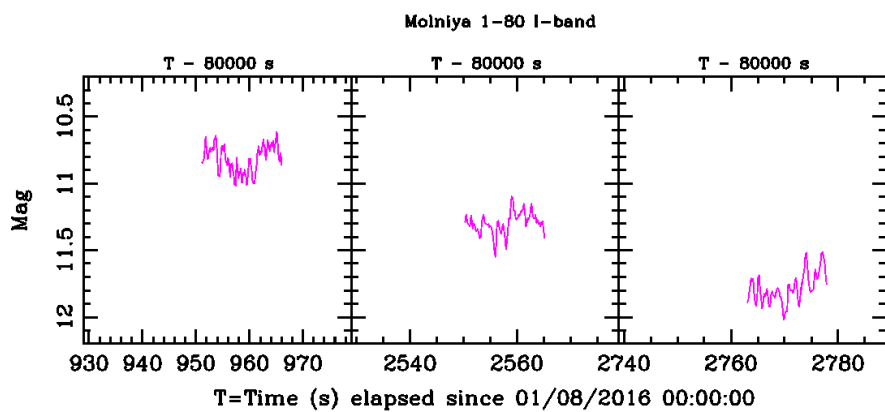


Figure A.25: Molniya 1-80 filter I light curves

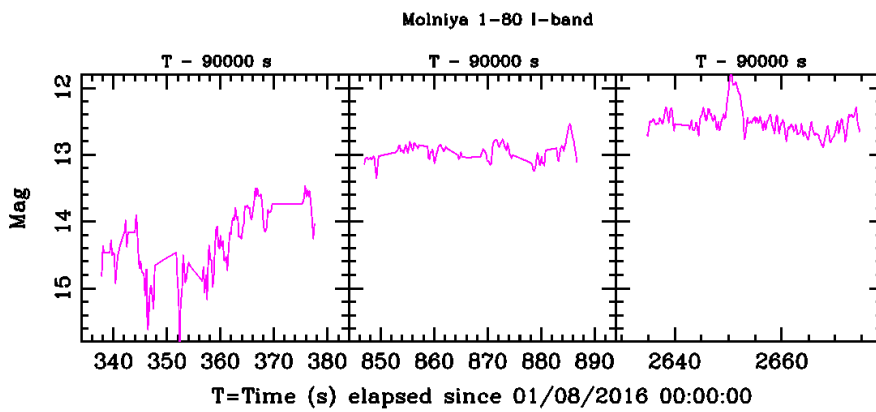


Figure A.26: Molniya 1-80 filter I light curves

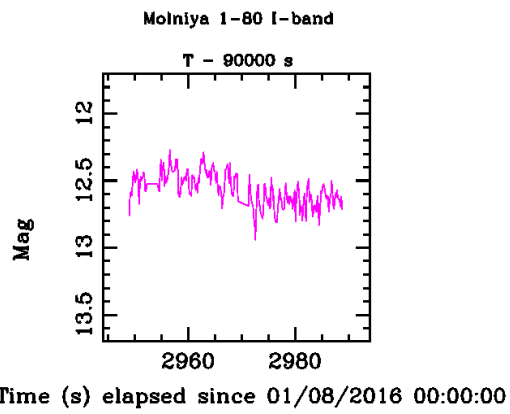


Figure A.27: Molniya 1-80 filter I light curves

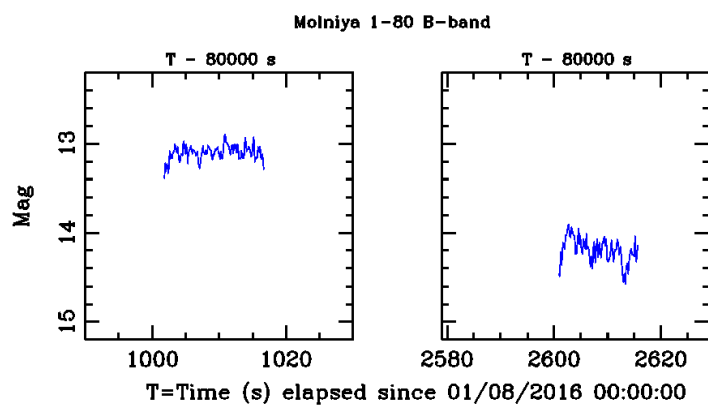


Figure A.28: Molniya 1-80 filter B light curves

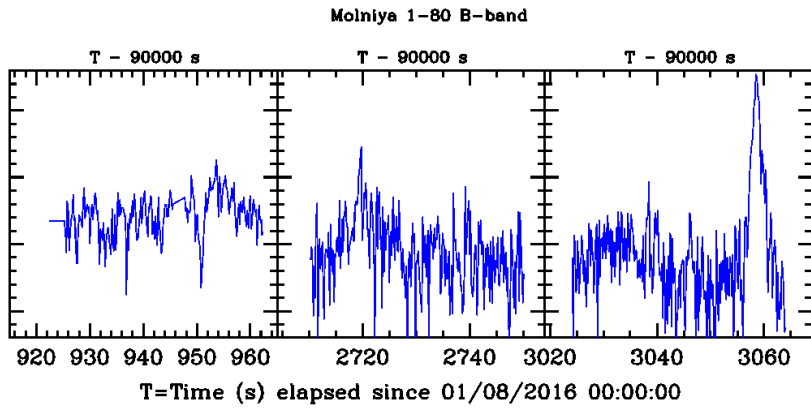


Figure A.29: Molniya 1-80 filter B light curves

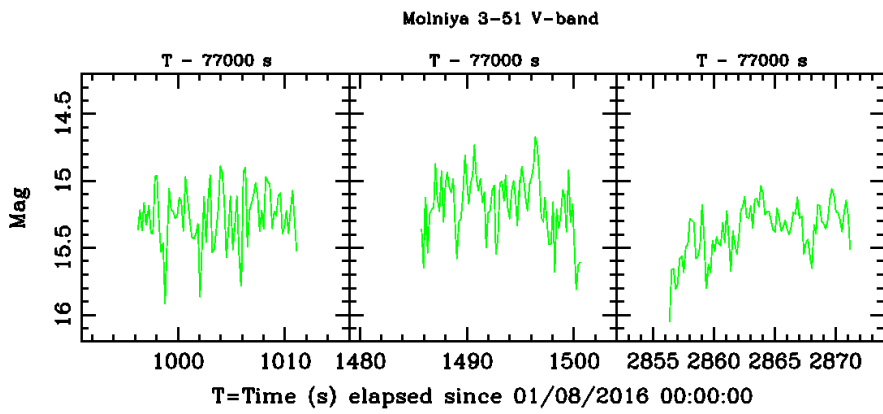


Figure A.30: Molniya 3-51 filter V light curves

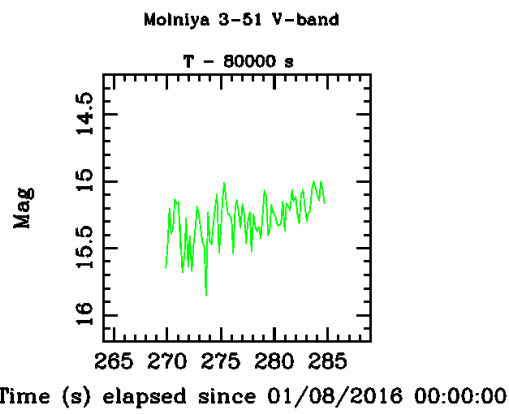


Figure A.31: Molniya 3-51 filter V light curves

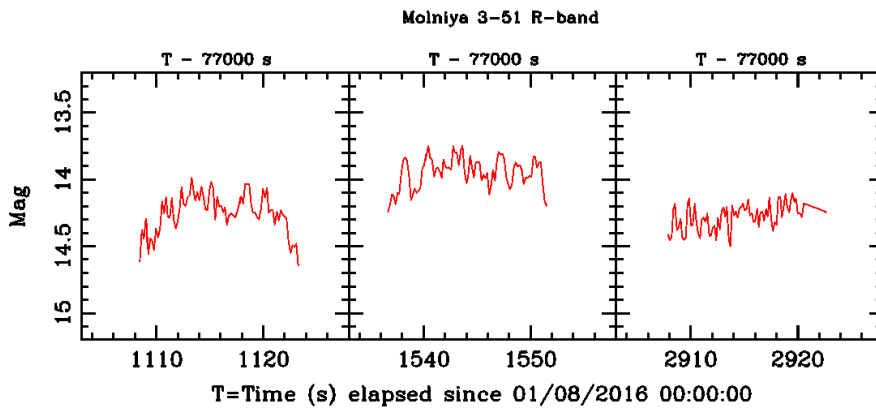


Figure A.32: Molniya 3-51 filter R light curves

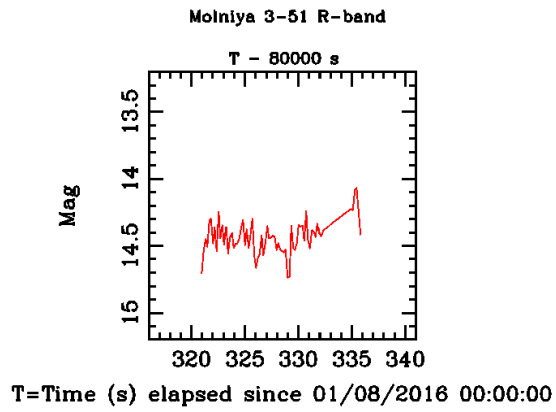


Figure A.33: Molniya 3-51 filter R light curves

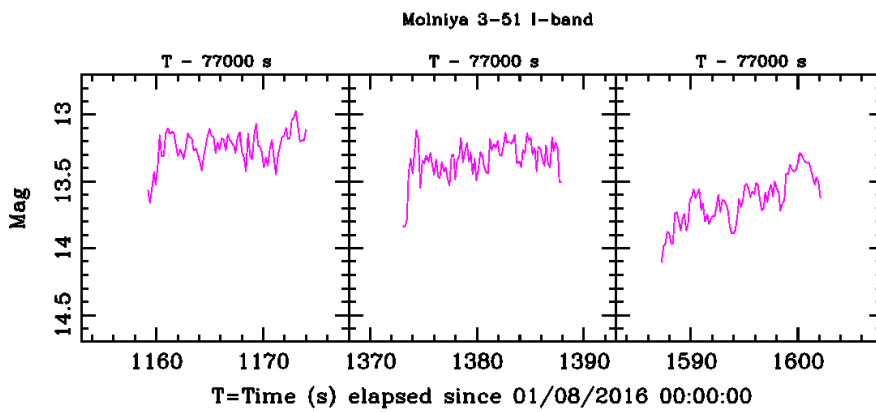


Figure A.34: Molniya 3-51 filter I light curves

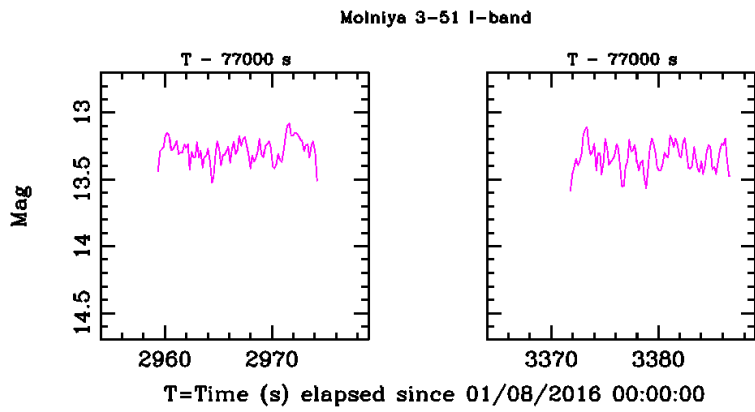


Figure A.35: Molniya 3-51 filter I light curves

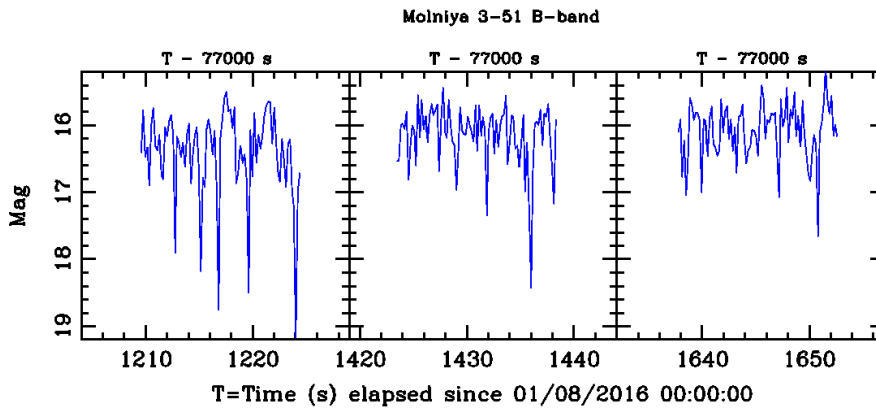


Figure A.36: Molniya 3-51 filter B light curves

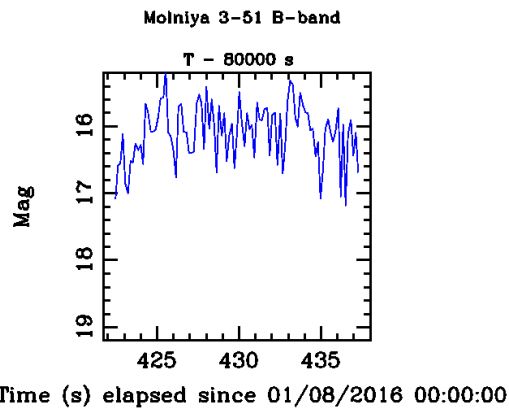


Figure A.37: Molniya 3-51 filter B light curves

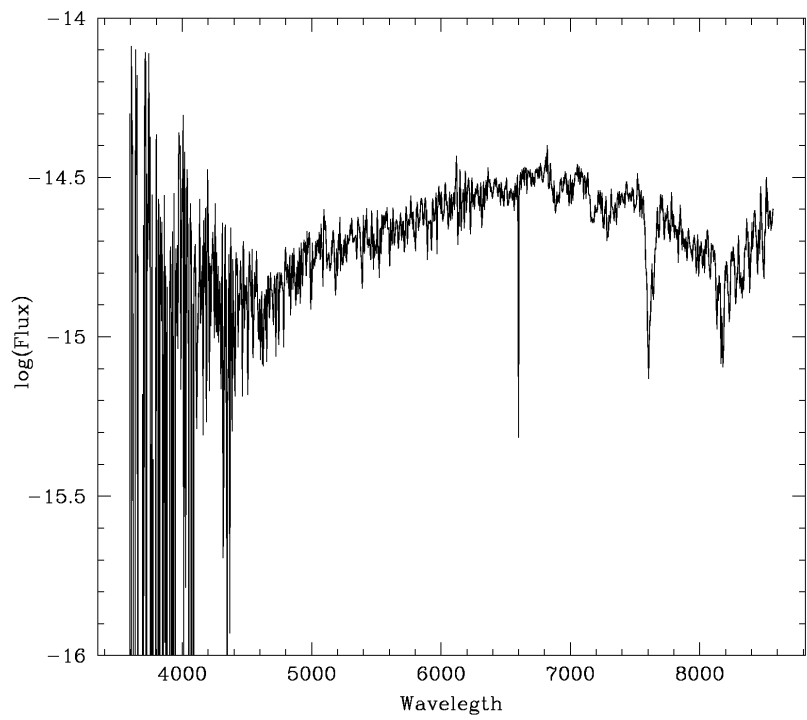
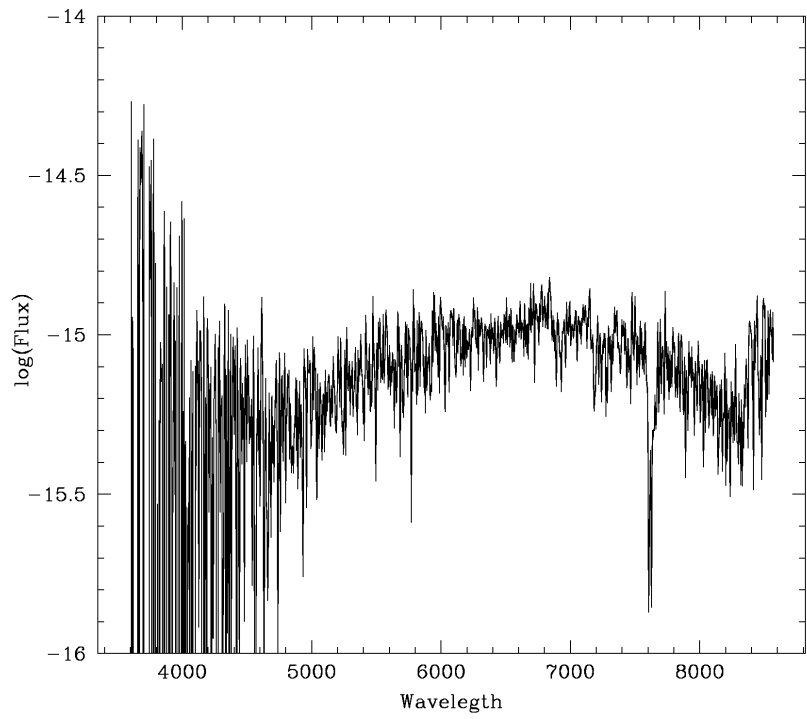


Figure A.38: Molniya 3-51 Spectra

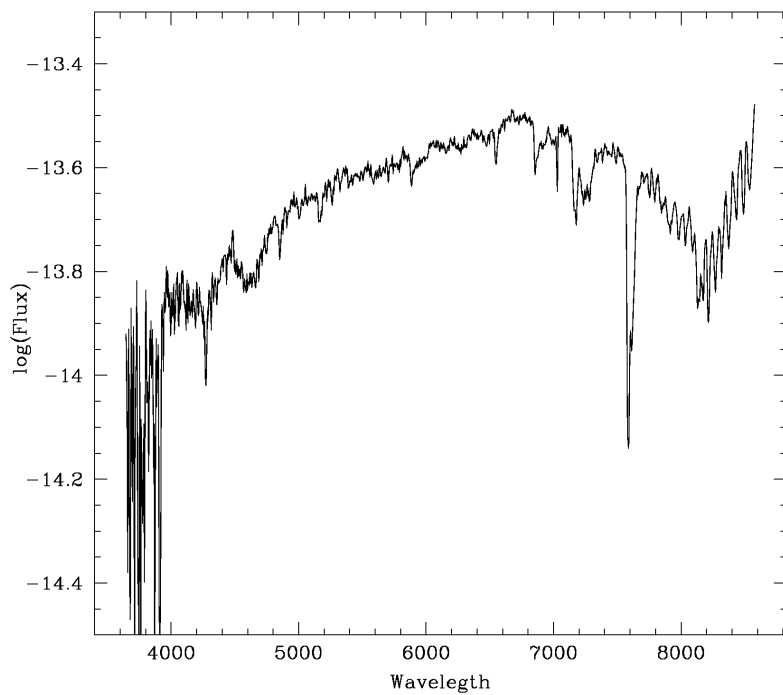


Figure A.39: Molniya 1-S Spectra

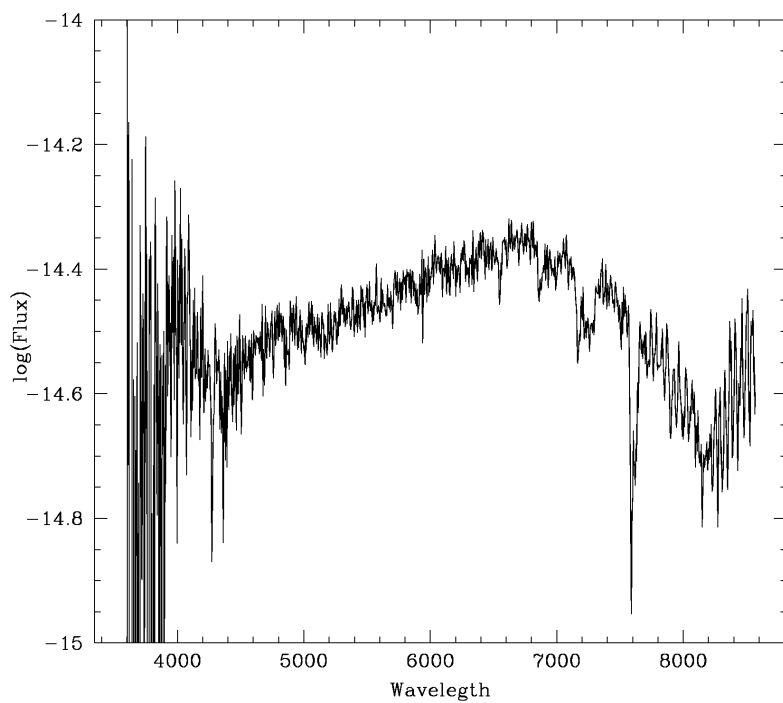


Figure A.40: Molniya 1-80 Spectra

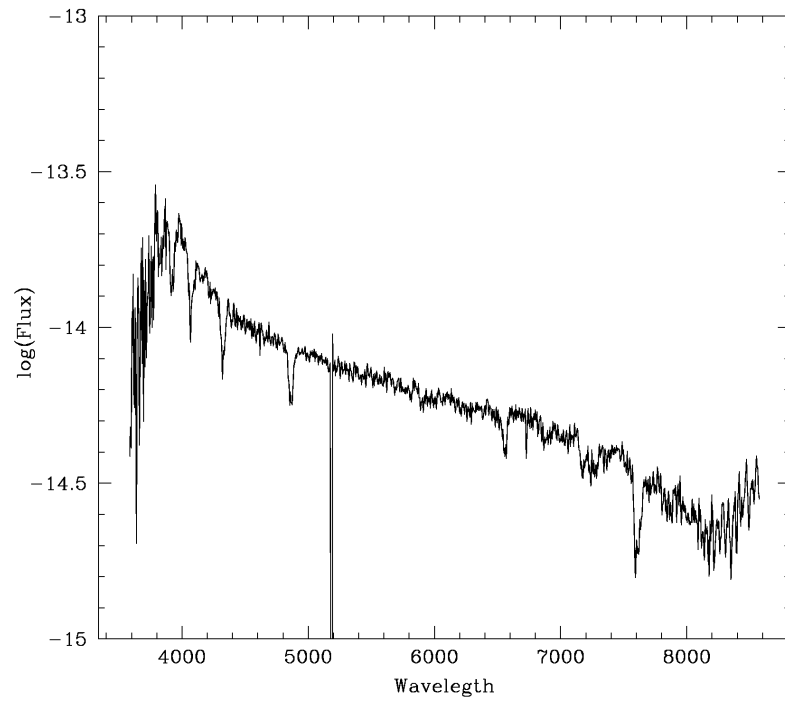


Figure A.41: Molniya 1-32 Spectra

A.2 Night 2016/08/02-03

- Seeing
- Clear non photometric sky
- Operator: Ivan Bruni
- JD:2457603.5

UT(start)	Object	Airmass	Exptime(s)	Filter/Grism	Mag	Phase Angle
21:10:57	Molniya 1-32	1.042	20	V	14.03	72.88
21:12:53	Molniya 1-32	1.042	20	I	12.34	73.05
21:38:04	Molniya 1-32	1.048	20	I	12.38	75.12
22:36:38	Molniya 1-75	1.276	120	GRV		
23:09:21	Molniya 2-17	1.114	120	GRV		
00:02:51	Molniya 1-S	1.752	40	V	13.19	52.19
00:04:07	Molniya 1-S	1.752	40	R	12.56	52.43
00:05:22	Molniya 1-S	1.752	40	I	11.99	52.68
00:14:47	Molniya 1-S	1.732	40	V	13.29	55.11
00:16:04	Molniya 1-S	1.731	40	R	12.70	55.35
00:17:20	Molniya 1-S	1.731	40	I	11.97	55.59
00:18:36	Molniya 1-S	1.730	40	B	13.95	56.08
00:22:53	Molniya 1-S	1.724	40	V	13.28	57.05
00:24:10	Molniya 1-S	1.723	40	R	12.70	57.30
00:25:27	Molniya 1-S	1.722	40	I	11.95	57.54
00:26:43	Molniya 1-S	1.722	40	B	13.92	58.03
00:29:34	Molniya 1-S	1.717	40	V	13.23	58.76
00:30:51	Molniya 1-S	1.717	40	R	12.65	59.00
00:32:07	Molniya 1-S	1.716	40	I	11.91	59.25
00:33:24	Molniya 1-S	1.716	40	B	13.91	59.49
00:36:42	Molniya 1-S	1.711	50	V	13.16	60.47
00:38:09	Molniya 1-S	1.710	50	R	12.60	60.71
00:39:37	Molniya 1-S	1.709	50	I	11.90	61.20
00:41:03	Molniya 1-S	1.709	50	B	13.92	61.44
00:43:02	Molniya 1-S	1.708	50	V	13.29	61.93
00:44:29	Molniya 1-S	1.707	50	R	12.80	62.32
00:45:55	Molniya 1-S	1.706	50	I	12.16	62.66
00:47:22	Molniya 1-S	1.706	50	B	14.16	63.01
00:50:47	Molniya 1-S	1.699	300	R	12.69	63.88
00:56:23	Molniya 1-S	1.696	300	R	12.65	65.20
01:04:48	Molniya 1-S	1.691	240	V	13.23	67.30

Table A.5: Logbook 2016/08/02-03

Object	V	B-V	V-R	V-I
PG2213+006	14.124	-0.217	-0.092	-0.203
PG2213+006 A	14.178	0.673	0.406	0.808
PG2213+006 B	12.706	0.749	0.427	0.829
PG2213+006 C	15.109	0.721	0.426	0.830

Table A.6: Standard stars magnitudes and color indexes from Landolt (1992)

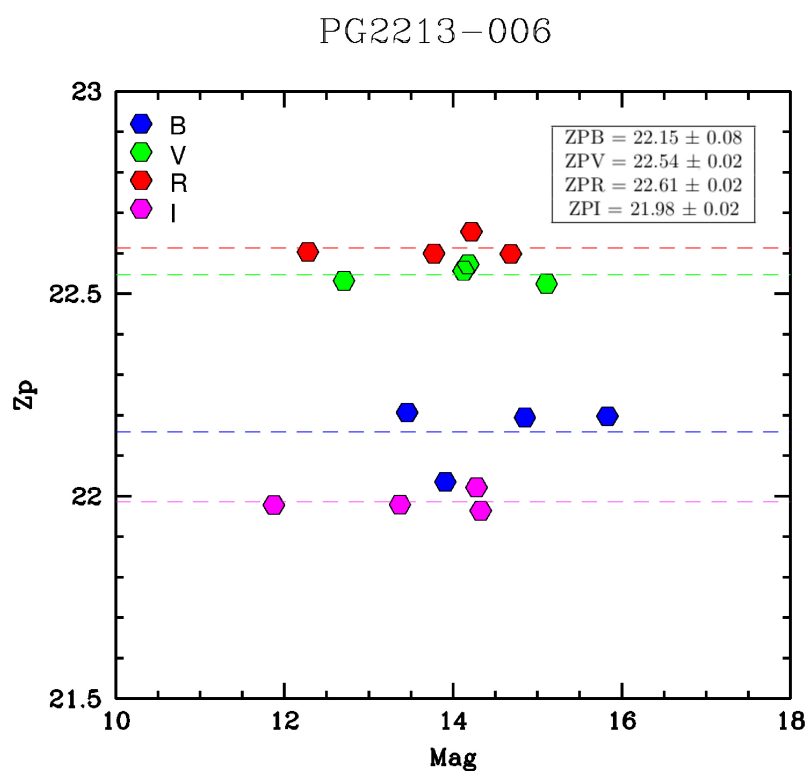


Figure A.42: Photometric zero points 2016/08/02-03, magnitudes from Landolt (1992)

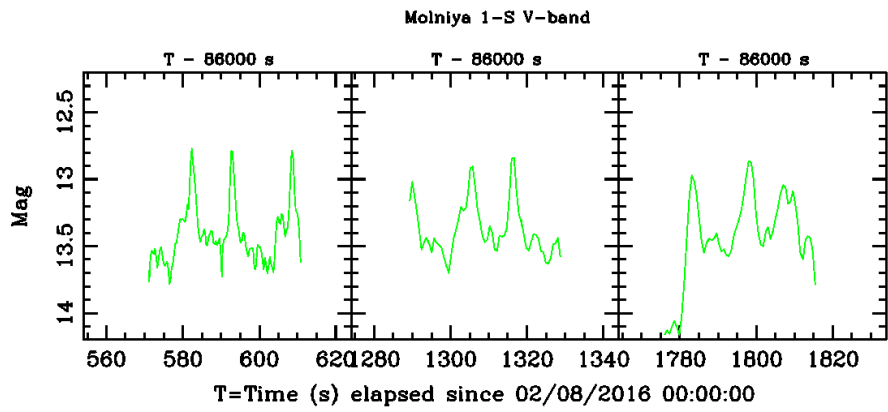


Figure A.43: Molniya 1-S filter V light curves

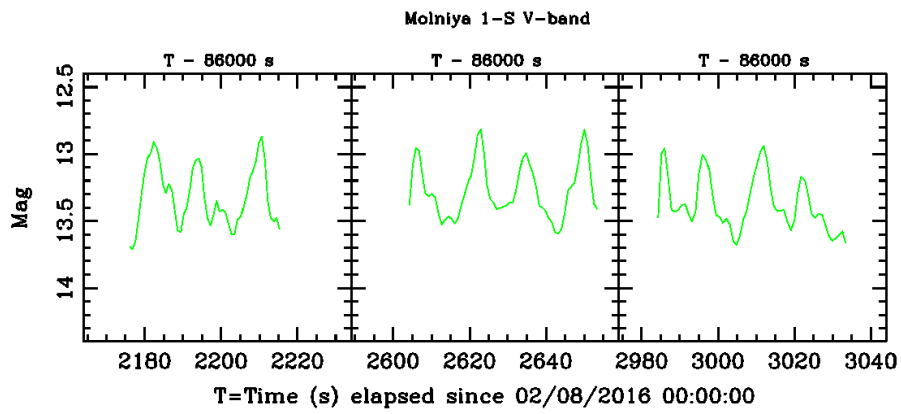


Figure A.44: Molniya 1-S filter V light curves

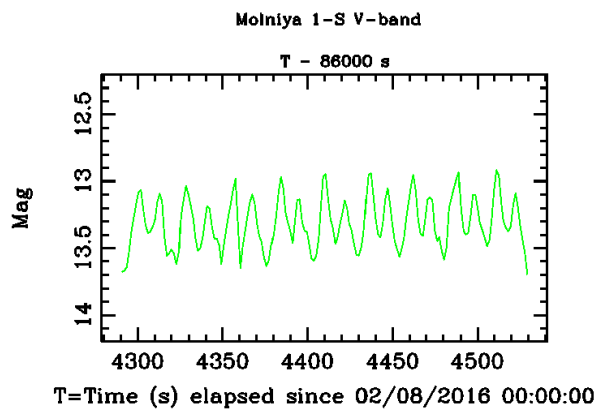


Figure A.45: Molniya 1-S filter V light curves

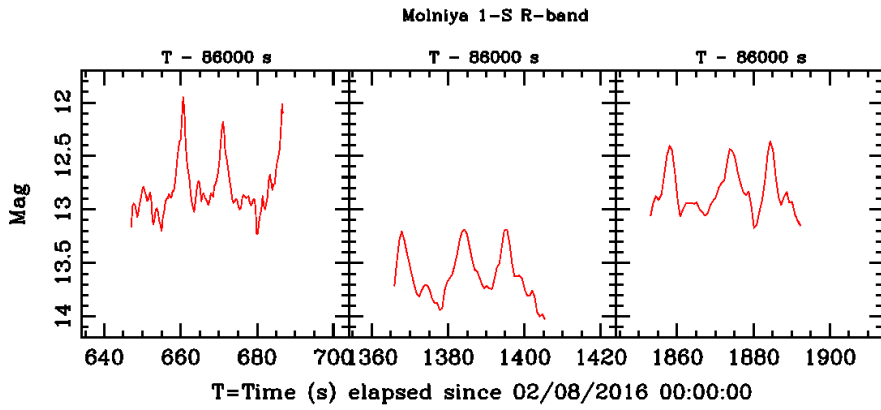


Figure A.46: Molniya 1-S filter R light curves

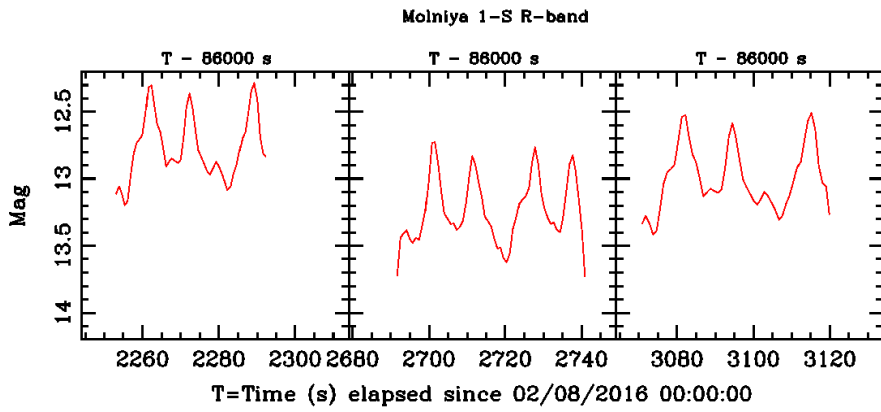


Figure A.47: Molniya 1-S filter R light curves

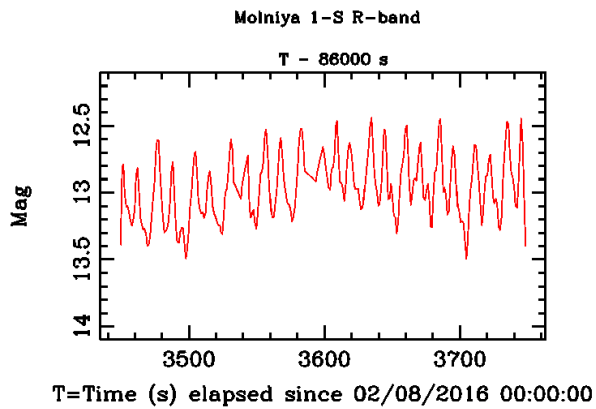


Figure A.48: Molniya 1-S filter R light curves

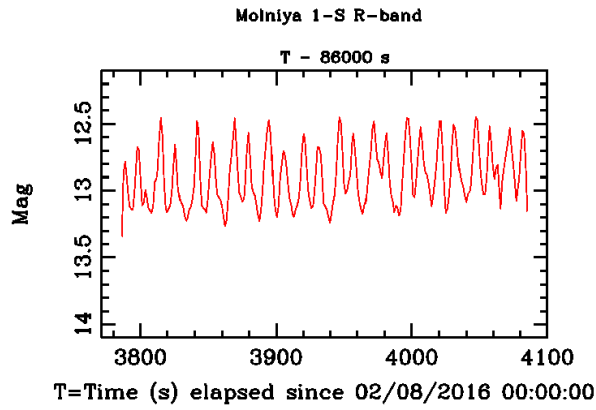


Figure A.49: Molniya 1-S filter R light curves

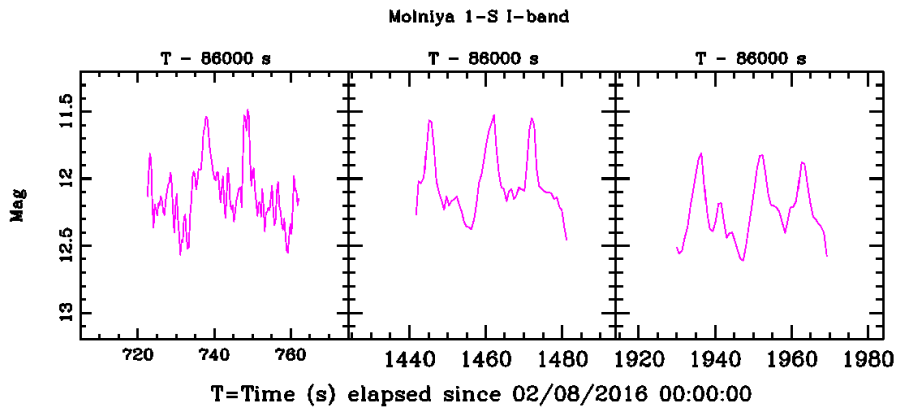


Figure A.50: Molniya 1-S filter I light curves

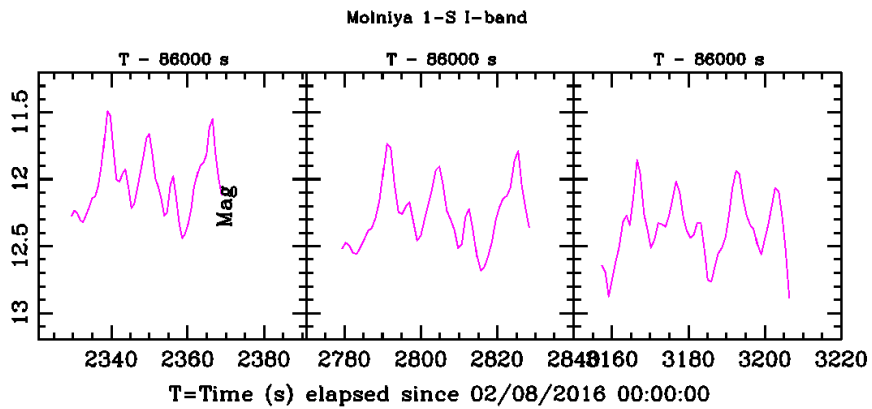


Figure A.51: Molniya 1-S filter I light curves

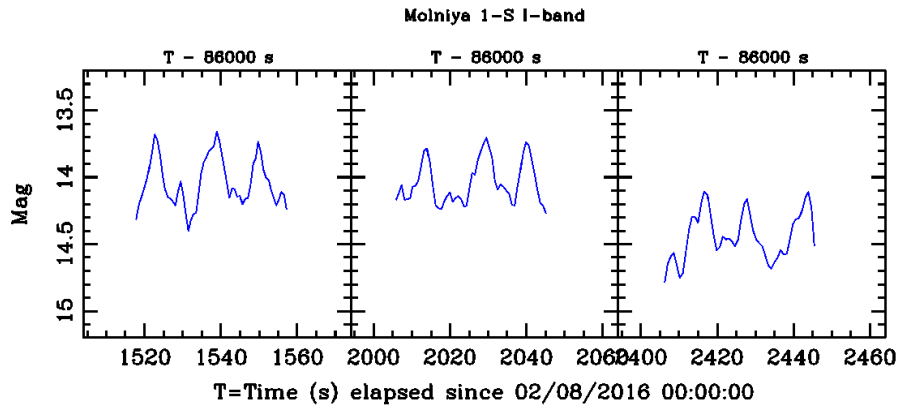


Figure A.52: Molniya 1-S filter B light curves

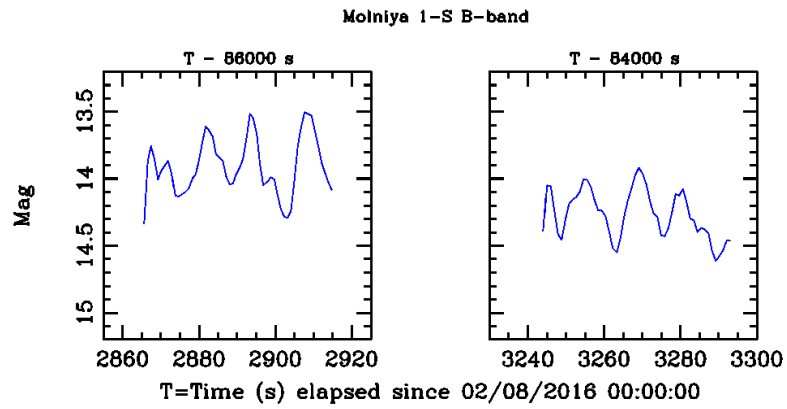


Figure A.53: Molniya 1-S filter B light curves

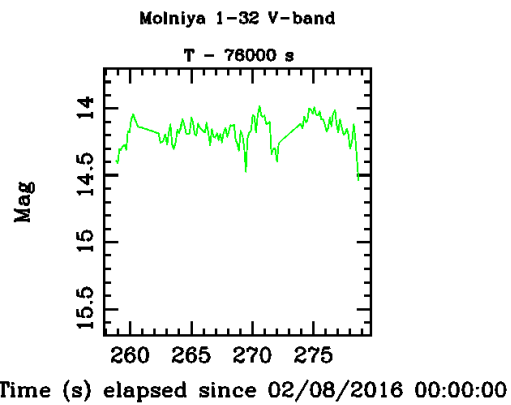


Figure A.54: Molniya 1-32 filter V light curves

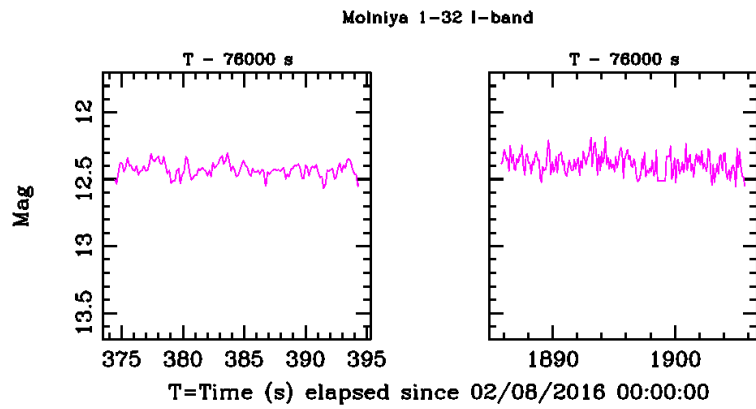


Figure A.55: Molniya 1-32 filter I light curves

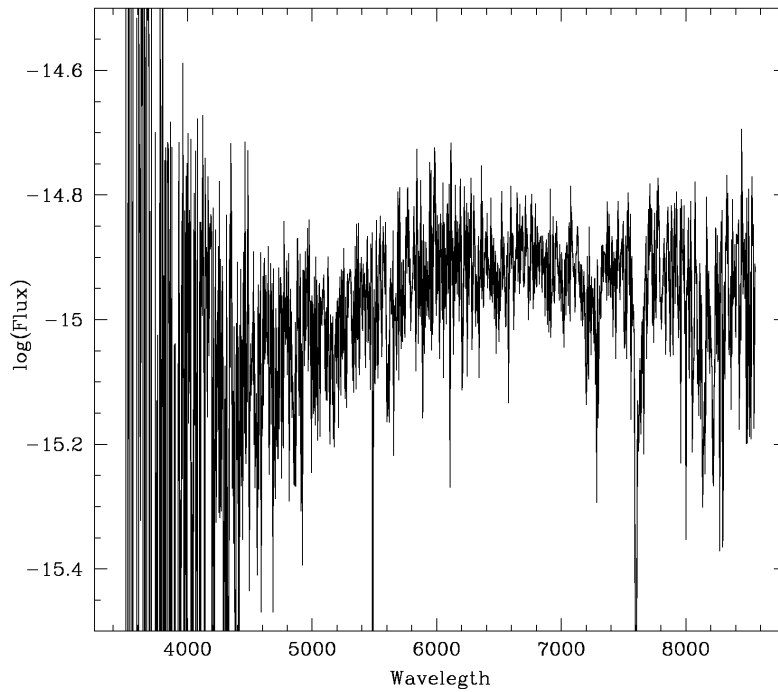


Figure A.56: Molniya 1-75 Spectra

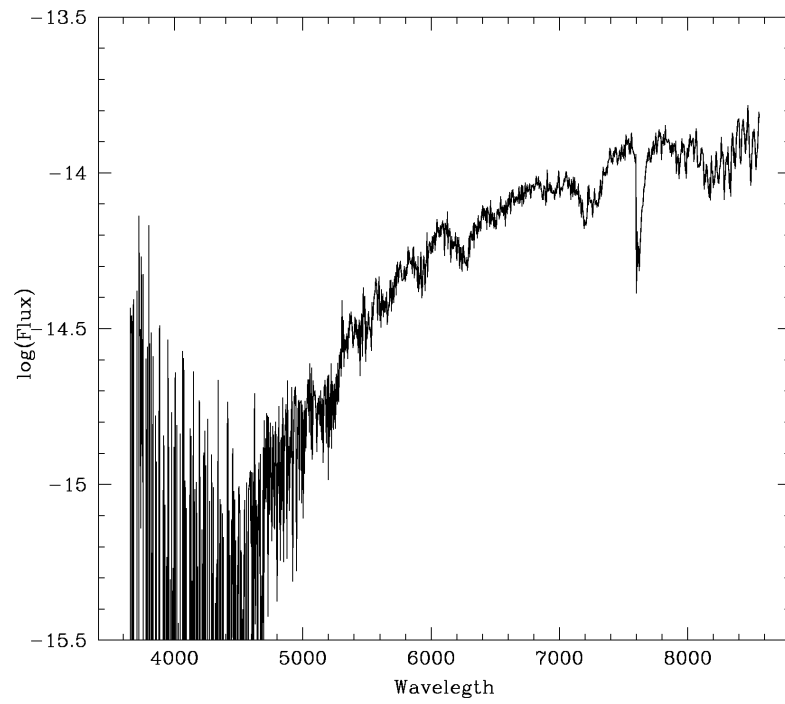


Figure A.57: Molniya 2-17 Spectra

A.3 Night 2016/09/26-27

- Seeing 1.5"
- Clear photometric sky
- Operator: Ivan Bruni
- JD:2457657.5

UT(start)	Object	Airmass	Exptime(s)	Filter/Grism	Mag	Phase Angle
18:38:04	Molniya 1-32	1.40	3	R	13.03	110.82
18:41:01	Molniya 1-32	1.37	3	R	12.52	109.93
18:43:02	Molniya 1-32	1.35	3	I	12.30	108.64
18:45:02	Molniya 1-32	1.33	3	V	14.21	107.82
18:47:01	Molniya 1-32	1.31	3	B	15.41	107.03
18:48:59	Molniya 1-32	1.30	6	B	15.66	106.27
18:50:59	Molniya 1-32	1.29	6	R	13.49	105.53
18:52:59	Molniya 1-32	1.27	6	I	12.49	104.82
18:54:59	Molniya 1-32	1.26	6	V	13.76	104.13
18:56:59	Molniya 1-32	1.25	6	B	14.58	103.46
18:59:59	Molniya 1-32	1.24	12	R	9.84	102.51
19:01:58	Molniya 1-32	1.23	12	I	11.71	101.90
19:05:59	Molniya 1-32	1.22	12	V	13.47	100.73
19:07:59	Molniya 1-32	1.22	12	B	15.00	100.17
20:51:23	Molniya 1-32	1.17	60	GR4	-	83.20
21:45:15	Molniya 1-32	1.19	60	GR4	-	78.20
22:10:56	Molniya 3-40	1.31	20	R	13.38	83.08
22:13:44	Molniya 3-40	1.30	20	I	12.48	82.56
22:15:38	Molniya 3-40	1.30	20	V	14.05	82.22
22:17:39	Molniya 3-40	1.30	20	B	15.21	81.88
22:19:39	Molniya 3-40	1.30	20	R	13.30	81.54
22:21:39	Molniya 3-40	1.30	20	I	12.32	81.20
22:23:39	Molniya 3-40	1.29	20	V	14.07	80.87
22:25:39	Molniya 3-40	1.29	20	B	15.91	80.54
22:30:39	Molniya 3-40	1.29	20	R	14.88	79.72
22:32:38	Molniya 3-40	1.28	20	I	13.33	79.40
22:36:39	Molniya 3-40	1.28	20	V	14.67	78.76
22:43:39	Molniya 3-40	1.28	20	B	15.01	77.65

Table A.7: Logbook 2016/09/26-27

UT(start)	Object	Airmass	Exptime(s)	Filter/Grism	Mag	Phase Angle
22:53:47	Molniya 3-40	1.27	120	GR4	-	76.11
23:08:01	Molniya 3-40	1.26	120	GR4	-	74.01
23:53:59	Molniya 3-50	1.34	12	R	12.78	78.47
23:55:59	Molniya 3-50	1.34	12	I	11.48	78.80
23:57:58	Molniya 3-50	1.35	12	V	12.72	79.13
23:59:58	Molniya 3-50	1.35	12	B	14.95	79.47
00:01:59	Molniya 3-50	1.36	12	R	14.04	79.65
00:03:59	Molniya 3-50	1.37	12	I	11.66	80.19
00:06:00	Molniya 3-50	1.37	12	V	13.48	80.56
00:07:58	Molniya 3-50	1.38	12	B	14.16	80.95
00:09:59	Molniya 3-50	1.39	12	R	11.86	81.35
00:11:59	Molniya 3-50	1.39	12	I	10.05	81.76
00:13:58	Molniya 3-50	1.40	12	V	12.74	82.19
00:15:59	Molniya 3-50	1.41	12	V	13.50	82.62
00:17:59	Molniya 3-50	1.42	12	B	15.13	83.08
00:40:54	Molniya 2-17	1.16	8	R	12.68	71.25
00:42:53	Molniya 2-17	1.18	8	I	8.06	71.83
00:45:54	Molniya 2-17	1.20	8	V	12.44	72.80
00:47:53	Molniya 2-17	1.21	8	B	9.24	73.51
00:49:53	Molniya 2-17	1.23	8	R	11.80	74.28
00:51:53	Molniya 2-17	1.26	7	I	10.43	75.13
00:53:54	Molniya 2-17	1.28	7	V	12.80	76.05
00:57:54	Molniya 2-17	1.36	7	B	11.39	78.15
01:10:59	Molniya 1-62	1.09	10	R	13.71	61.43
01:13:58	Molniya 1-62	1.09	20	R	13.18	61.61
01:18:58	Molniya 1-62	1.09	30	V	14.78	61.92
01:22:59	Molniya 1-62	1.09	30	B	15.82	62.17
01:26:29	Molniya 1-62	1.09	60	R	13.42	62.45
01:29:28	Molniya 1-62	1.09	60	R	13.58	62.60
01:33:28	Molniya 1-62	1.10	60	R	13.65	62.80
01:37:28	Molniya 1-62	1.10	60	I	12.09	63.10
01:40:29	Molniya 1-62	1.10	60	V	14.51	63.25
01:43:28	Molniya 1-62	1.10	60	B	15.77	63.40
01:46:29	Molniya 1-62	1.10	60	R	10.44	63.60
01:49:28	Molniya 1-62	1.10	60	I	12.57	63.80
01:52:28	Molniya 1-62	1.10	60	V	14.67	64.00
01:56:28	Molniya 1-62	1.10	60	B	15.42	64.20
02:29:43	Molniya 1-62	1.11	60	GR4	-	66.27
02:35:32	Molniya 1-62	1.11	60	GR4	-	66.60

Table A.8: Logbook 2016/09/26-27

Object	V	B-V	V-R	V-I
PG0231+051	16.105	-0.329	-0.162	-0.534
PG0231+051 A	12.772	0.71	0.405	0.799
PG0231+051 B	14.735	1.448	0.954	1.951
PG0231+051 C	13.702	0.671	0.399	0.783
PG0231+051 D	14.027	1.088	0.675	1.256
PG0231+051 E	13.804	0.667	0.39	0.757
PG2213+006	14.124	-0.217	-0.092	-0.203
PG2213+006 A	14.178	0.673	0.406	0.808
PG2213+006 B	12.706	0.749	0.427	0.829
PG2213+006 C	15.109	0.721	0.426	0.830

Table A.9: Standard stars magnitudes and color indexes from Landolt (1992)

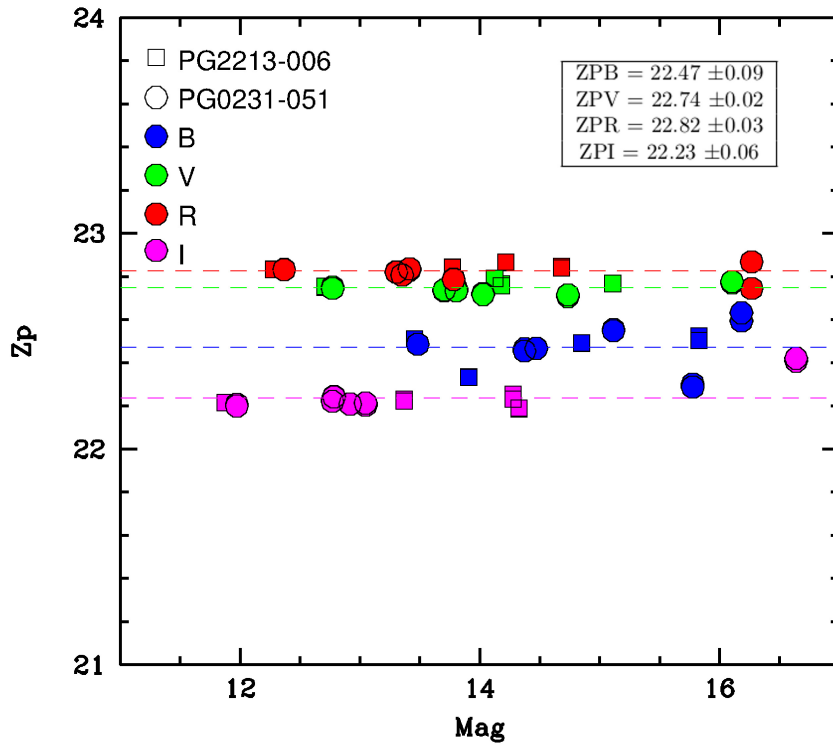


Figure A.58: Photometric zero points 2016/09/26-27, magnitudes from Landolt (1992)

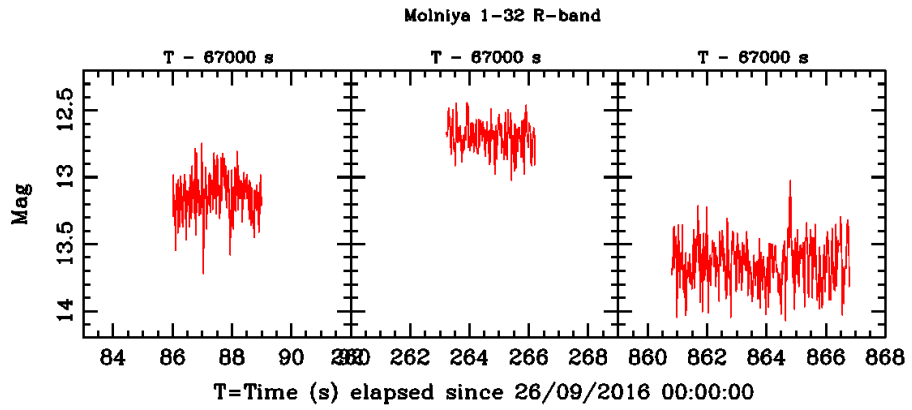


Figure A.59: Molniya 1-32 filter R light curves

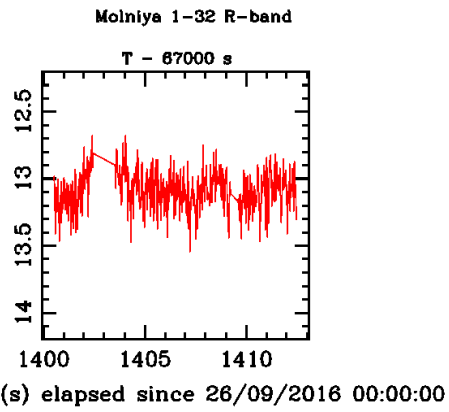


Figure A.60: Molniya 1-32 filter R light curves

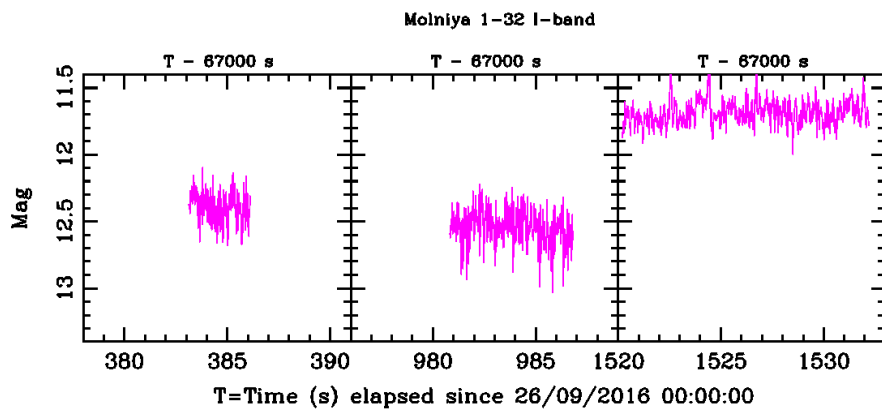


Figure A.61: Molniya 1-32 filter I light curves

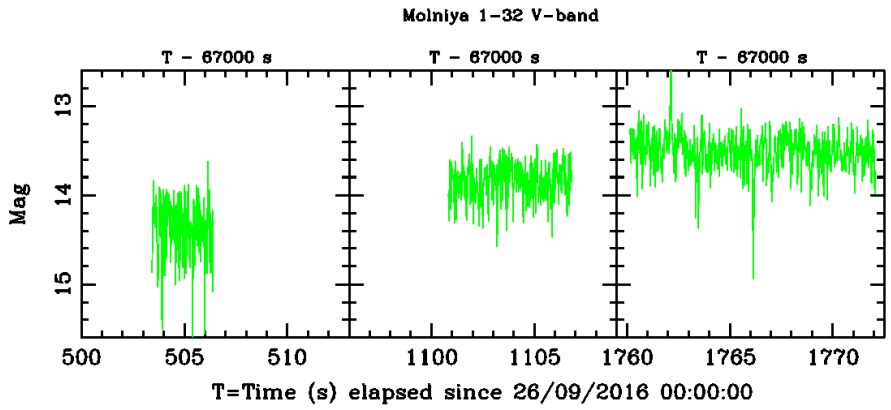


Figure A.62: Molniya 1-32 filter V light curves

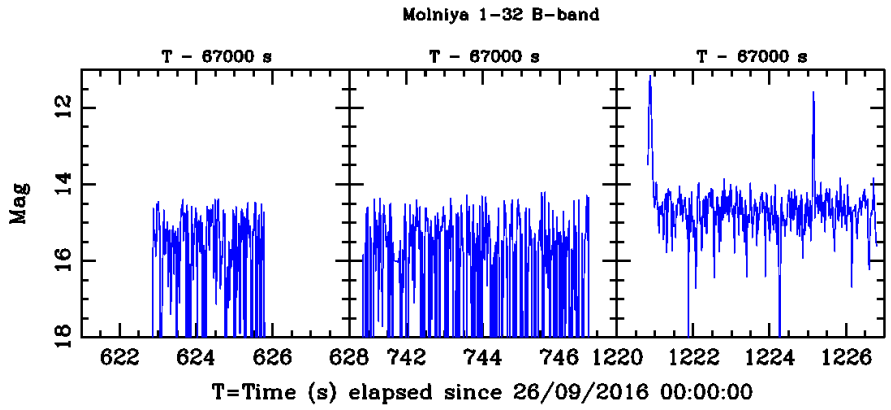


Figure A.63: Molniya 1-32 filter B light curves

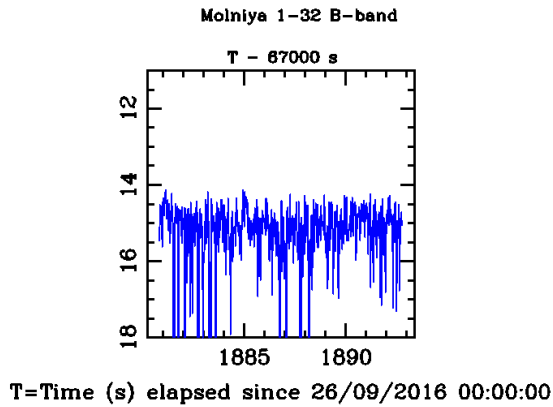


Figure A.64: Molniya 1-32 filter B light curves

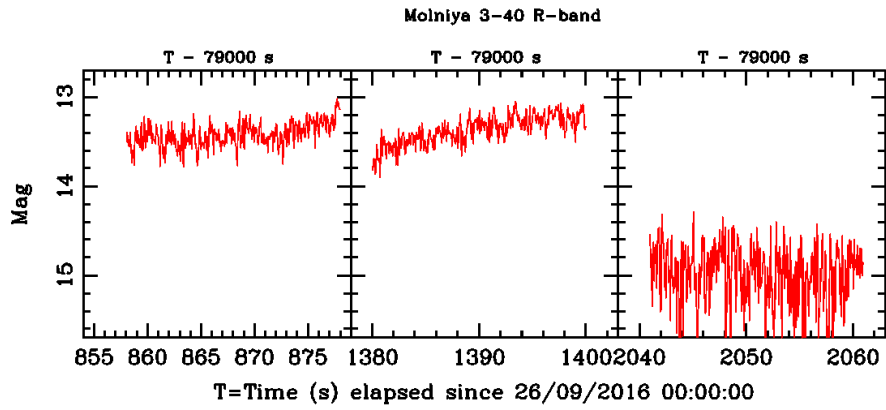


Figure A.65: Molniya 3-40 filter R light curves

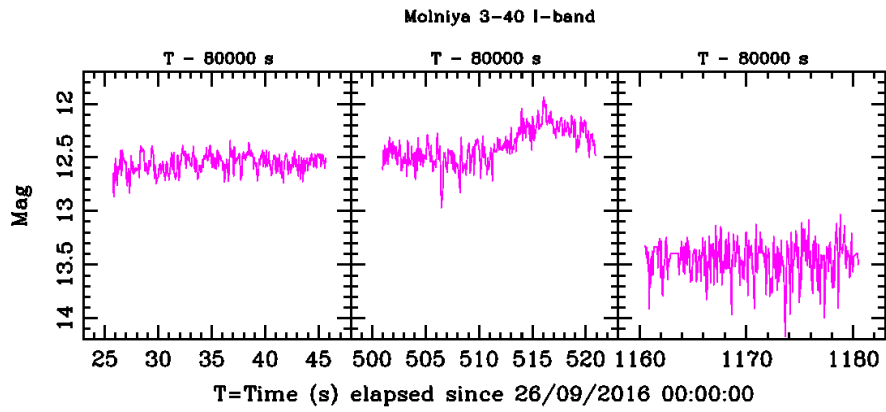


Figure A.66: Molniya 3-40 filter I light curves

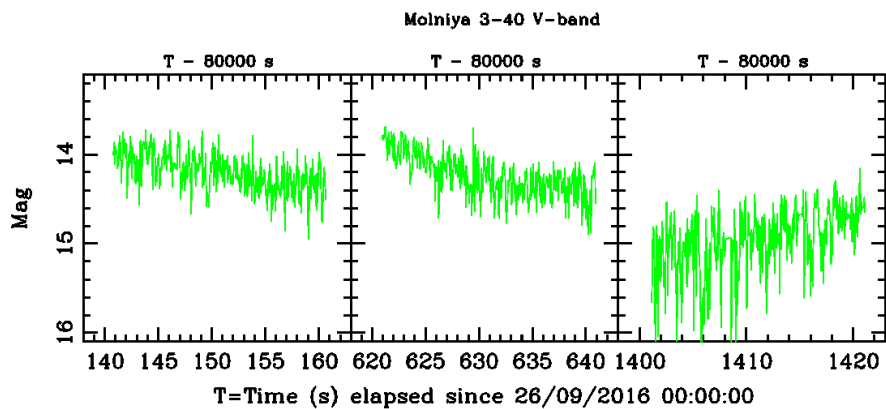


Figure A.67: Molniya 3-40 filter V light curves

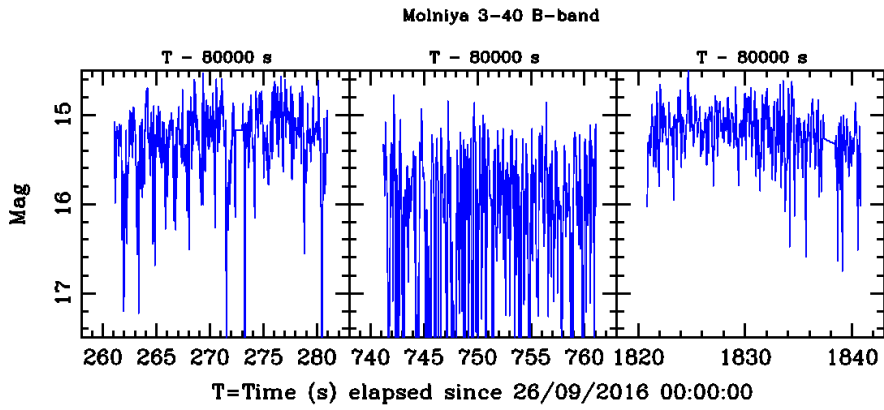


Figure A.68: Molniya 3-40 filter B light curves

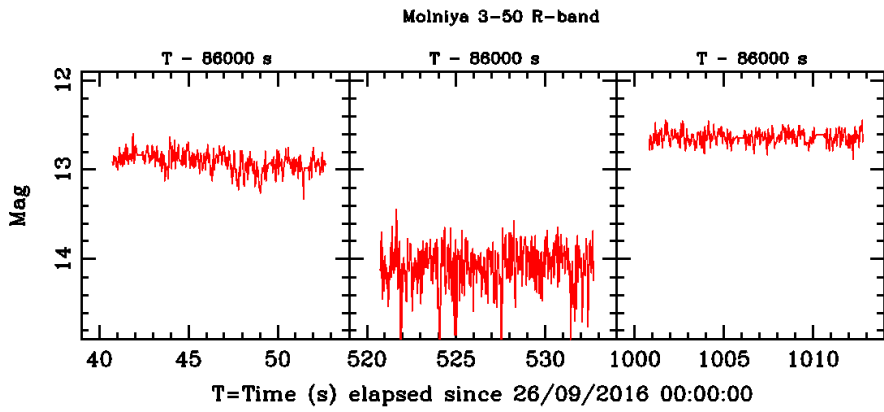


Figure A.69: Molniya 3-50 filter R light curves

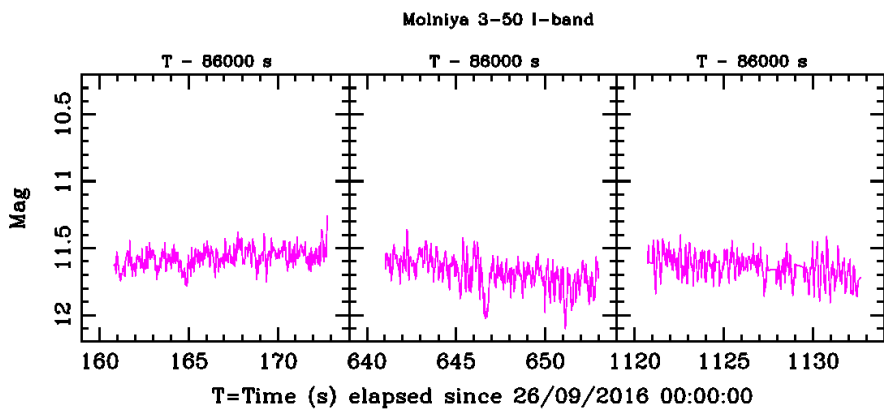


Figure A.70: Molniya 3-50 filter I light curves

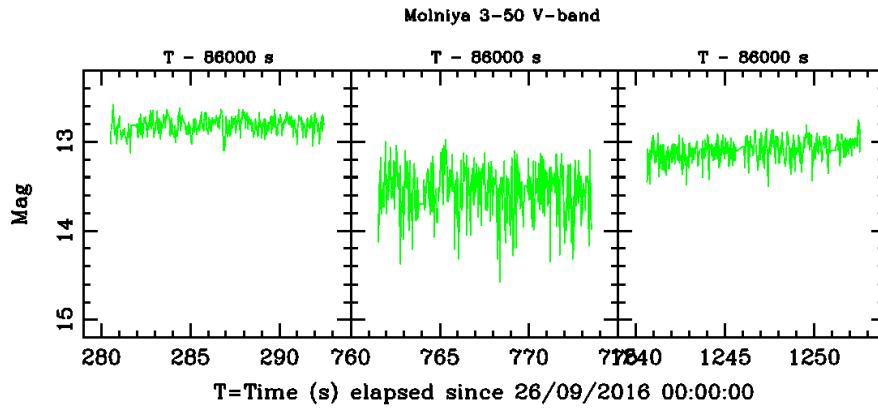


Figure A.71: Molniya 3-50 filter V light curves

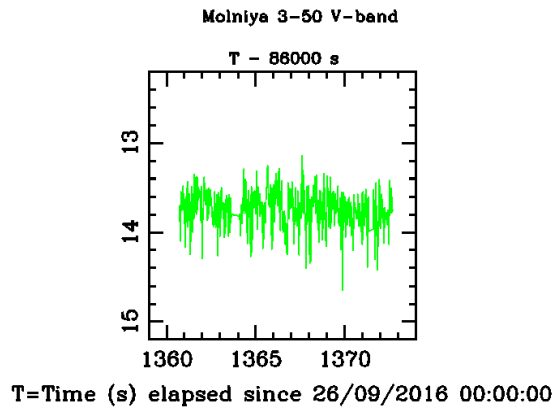


Figure A.72: Molniya 3-50 filter V light curves

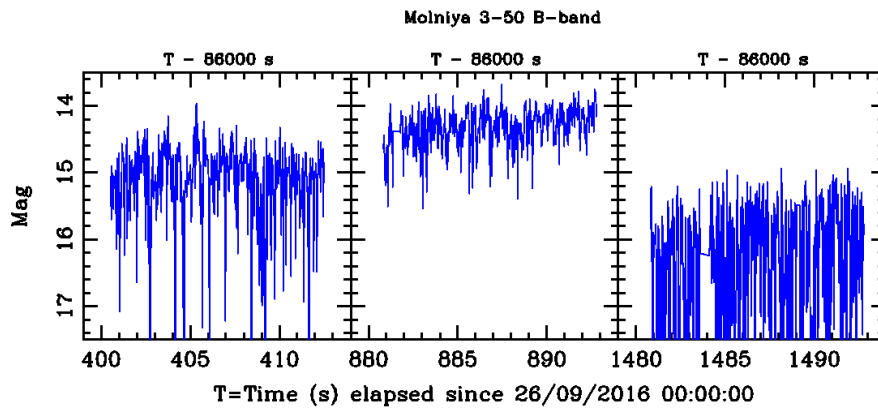


Figure A.73: Molniya 3-50 filter B light curves

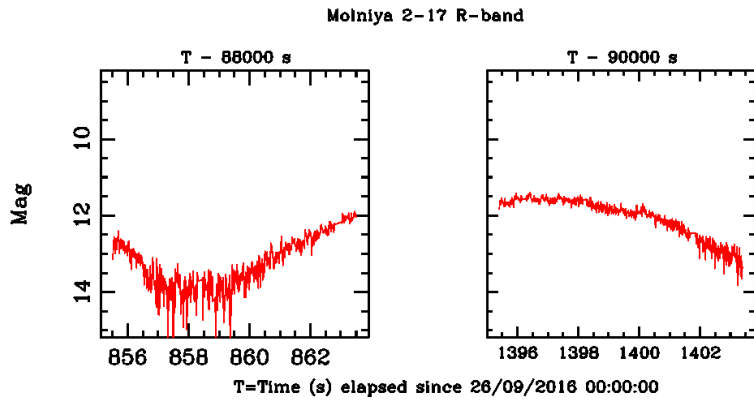


Figure A.74: Molniya 2-17 filter R light curves

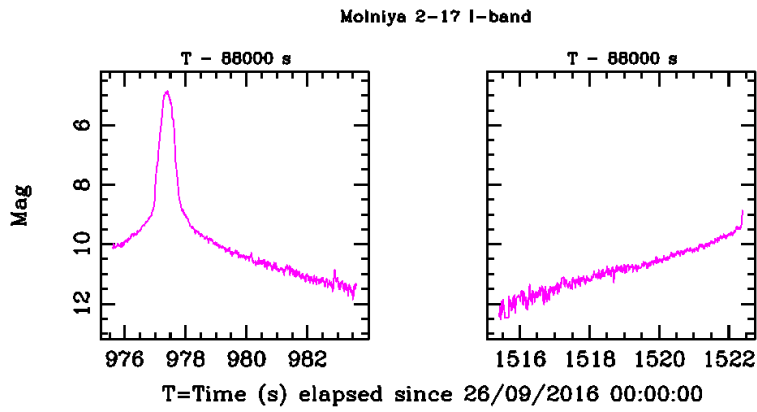


Figure A.75: Molniya 2-17 filter I light curves

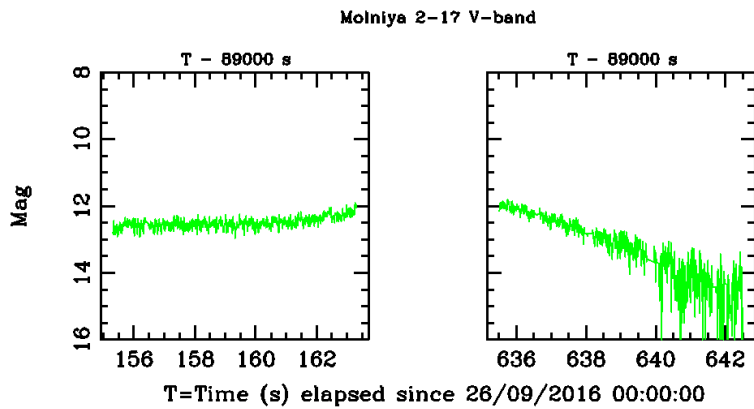


Figure A.76: Molniya 2-17 filter V light curves

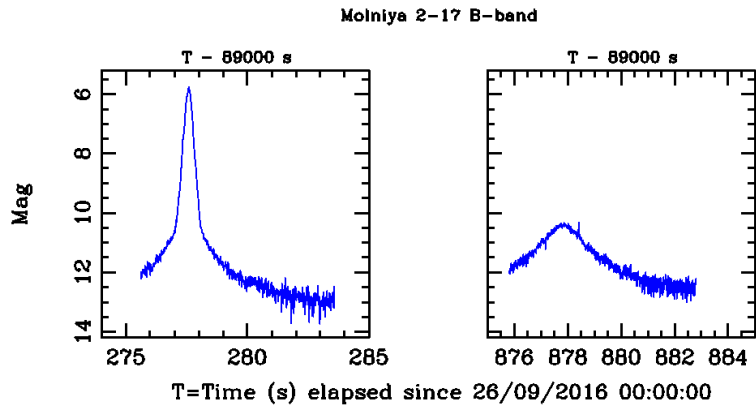


Figure A.77: Molniya 2-17 filter B light curves

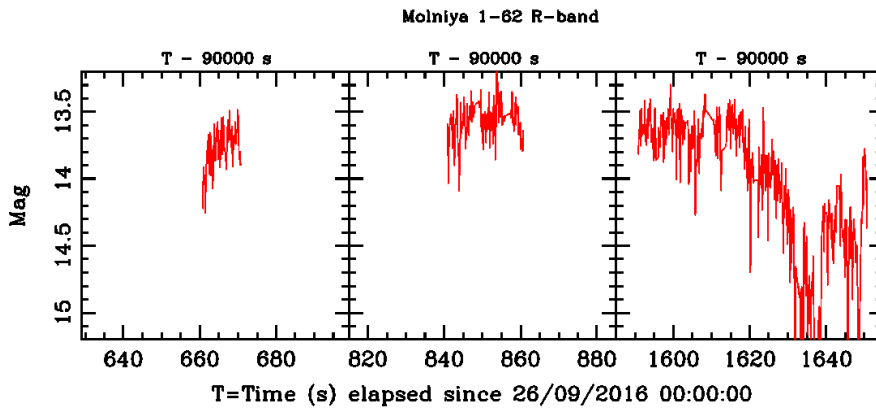


Figure A.78: Molniya 1-62 filter R light curves

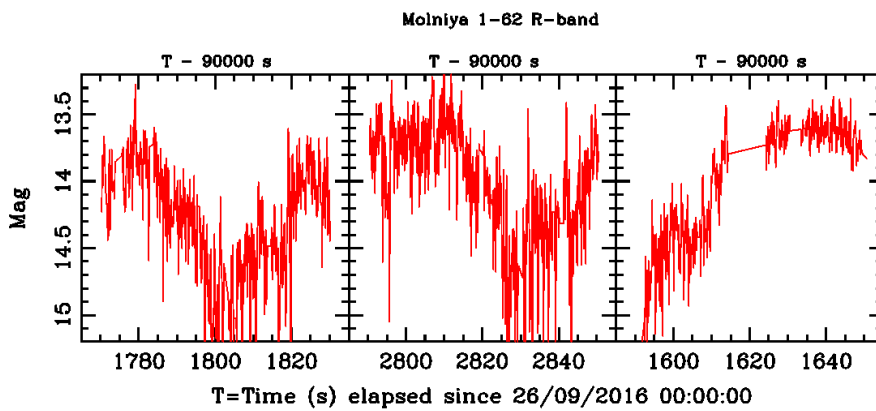


Figure A.79: Molniya 1-62 filter R light curves

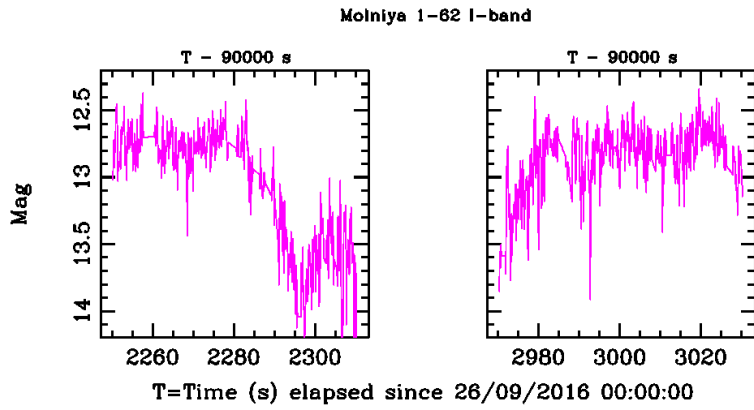


Figure A.80: Molniya 1-62 filter I light curves

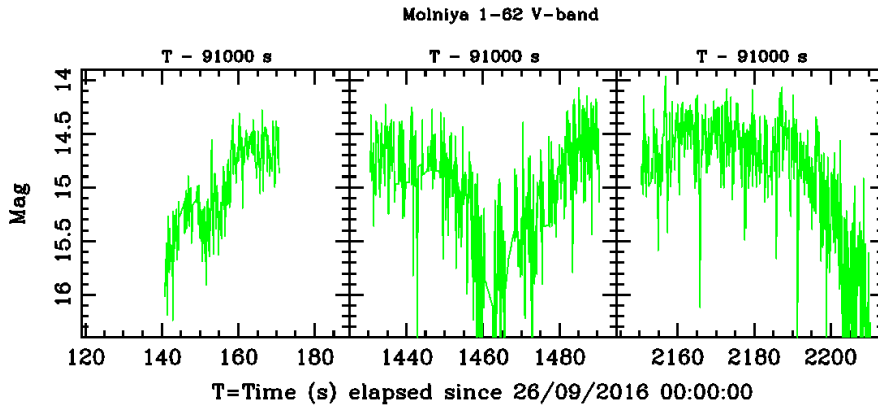


Figure A.81: Molniya 1-62 filter V light curves

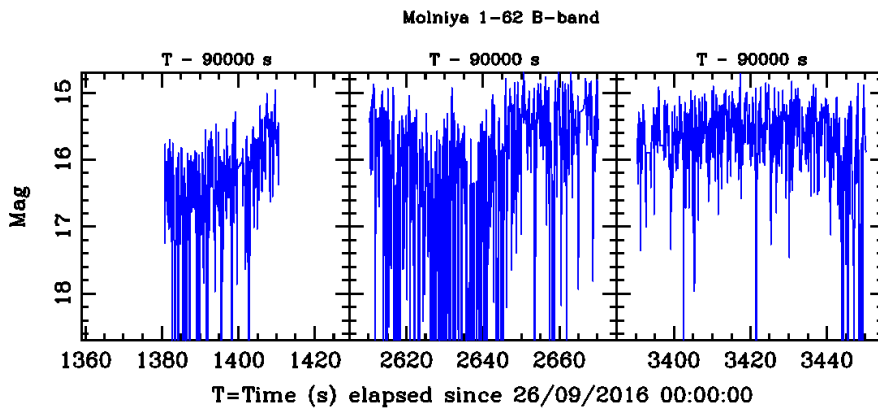


Figure A.82: Molniya 1-62 filter B light curves

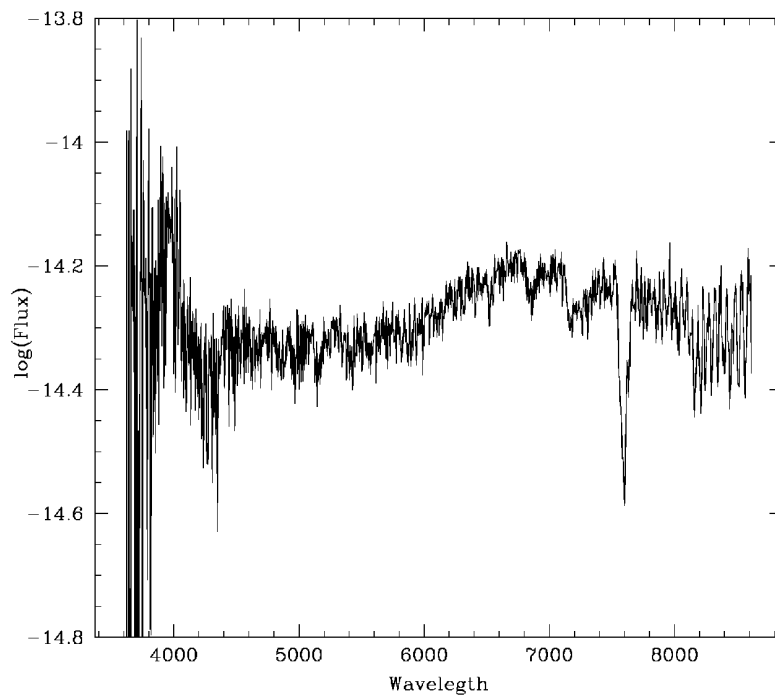
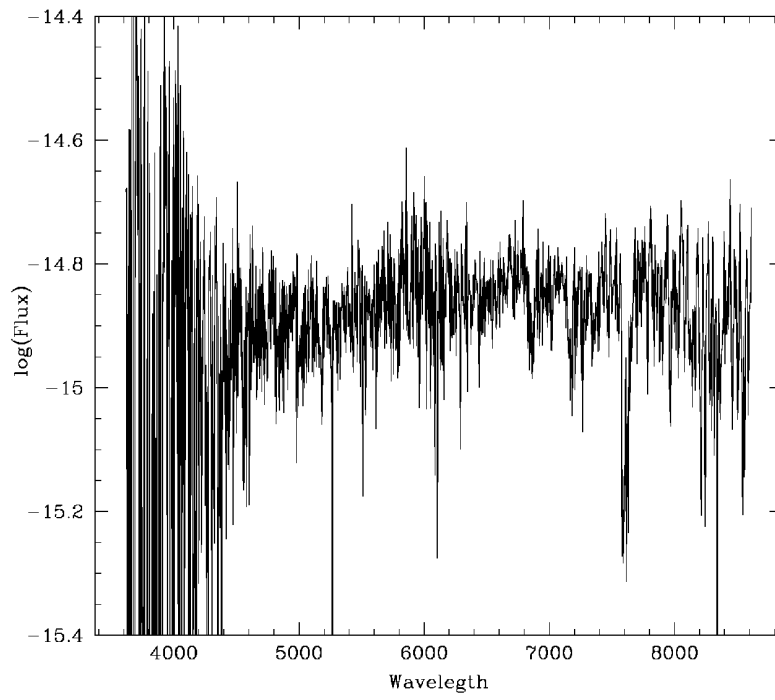


Figure A.83: Molniya 1-32 Spectra

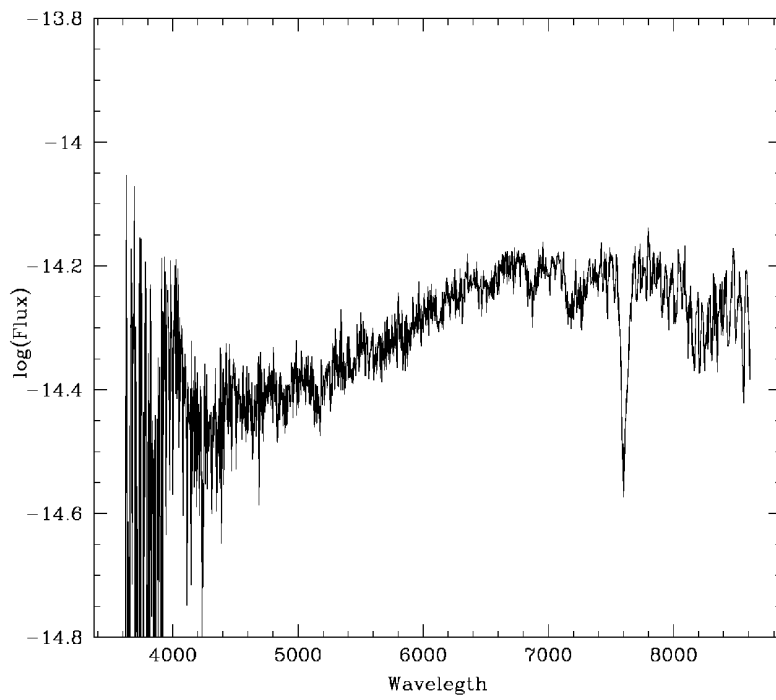
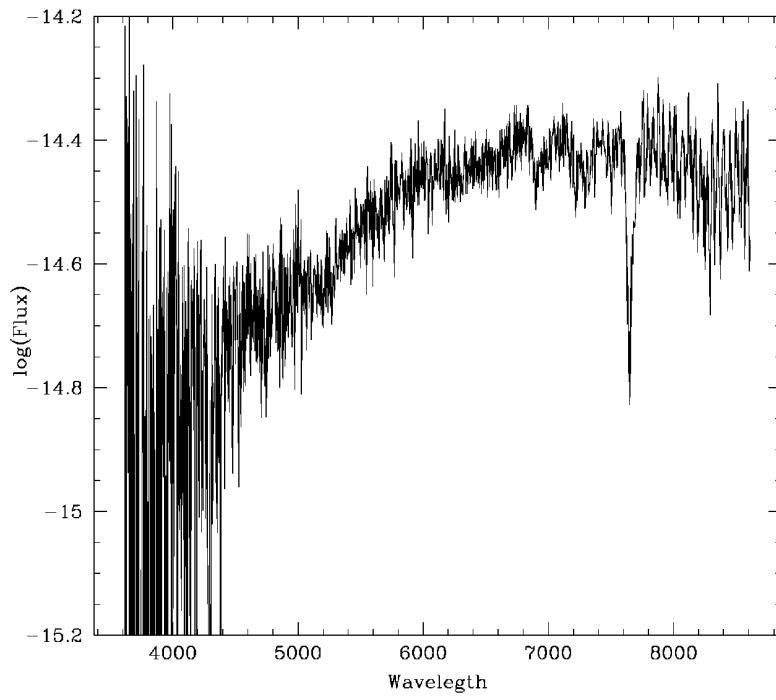


Figure A.84: Molniya 1-62 Spectra

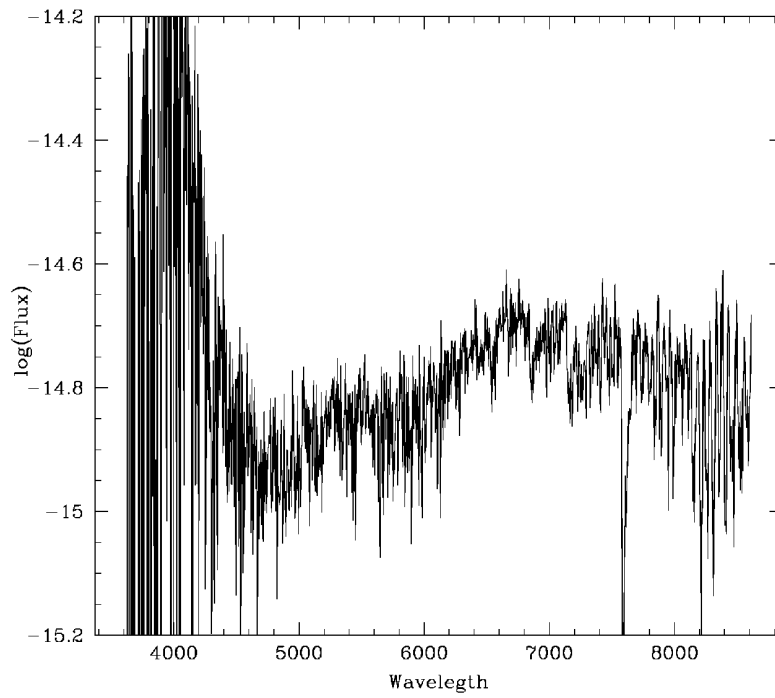
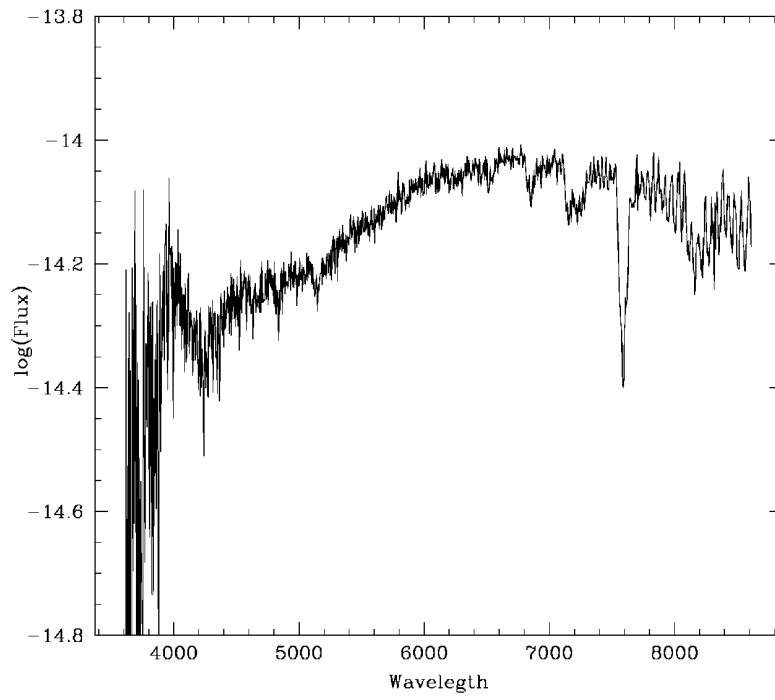


Figure A.85: Molniya 3-40 Spectra

A.4 Night 2016/09/27-28

- Seeing 1.5"
- Clear photometric sky
- Operator: Ivan Bruni
- JD:2457658.5

UT(start)	Object	Airmass	Exptime(s)	Filter/Grism	Mag	Phase Angle
18:19:59	Molniya 1-56	1.10	20	R	12.00	58.7
18:21:59	Molniya 1-56	1.10	20	I	12.13	58.74
18:24:58	Molniya 1-56	1.10	20	V	13.03	58.81
18:26:59	Molniya 1-56	1.10	20	B	14.69	58.84
18:41:03	Molniya 1-56	1.10	60	GR4		59.16
18:50:45	Molniya 1-56	1.10	60	GR4		59.37
18:57:05	Molniya 2-17	1.05	30	R	13.72	63.53
18:59:59	Molniya 2-17	1.05	30	I	12.79	63.5
19:02:59	Molniya 2-17	1.05	30	V	12.85	63.46
19:05:59	Molniya 2-17	1.05	30	B	15.39	63.43
19:08:49	Molniya 2-17	1.05	70	R	12.68	63.41
19:12:49	Molniya 2-17	1.05	70	R	10.32	63.36
19:17:44	Molniya 2-17	1.05	80	R	13.86	63.31
19:41:52	Molniya 2-17	1.05	120	GR4		63.1
19:52:45	Molniya 2-17	1.05	120	GR4		63.01
22:12:45	Molniya 2-9	1.55	20	R	13.38	91.1
22:14:44	Molniya 2-9	1.54	20	I	12.61	90.57
22:17:44	Molniya 2-9	1.52	20	V	14.05	89.8
22:20:45	Molniya 2-9	1.51	20	B	15.14	88.8
22:32:34	Molniya 2-9	1.47	60	GR4		86.19
22:36:46	Molniya 2-9	1.45	60	GR4		85.28
23:04:00	Molniya 3-50	1.28	20	R	13.84	71.96

Table A.10: Logbook 2016/09/27-28

UT(start)	Object	Airmass	Exptime(s)	Filter/Grism	Mag	Phase Angle
23:06:59	Molniya 3-50	1.29	20	I	12.39	72.25
23:09:00	Molniya 3-50	1.29	25	V	13.97	72.45
23:11:59	Molniya 3-50	1.29	25	B	14.32	72.75
23:13:54	Molniya 3-50	1.29	30	R	12.66	72.96
23:19:20	Molniya 3-50	1.30	60	GR4		73.61
23:26:07	Molniya 3-50	1.30	60	GR4		74.42
23:44:50	Molniya 1-87	1.19	10	R	15.76	71.93
23:47:59	Molniya 1-87	1.20	20	R	12.50	72.7
23:49:59	Molniya 1-87	1.20	20	I	11.31	73.2
23:52:59	Molniya 1-87	1.20	20	V	13.18	73.94
23:54:58	Molniya 1-87	1.20	20	B	15.15	74.41
23:57:58	Molniya 1-87	1.21	25	R	12.28	75.11
00:05:57	Molniya 1-88	1.04	10	R	8.76	59.82
00:46:59	Molniya 3-27	1.46	20	R	11.35	92.03
00:49:58	Molniya 3-27	1.46	30	I	10.56	92.47
00:52:55	Molniya 3-27	1.46	30	V	11.65	92.92
00:55:56	Molniya 3-27	1.46	30	B	12.00	93.37
00:58:56	Molniya 3-27	1.47	40	R	11.07	93.84
01:07:50	Molniya 3-27	1.48	60	GR4		95.3
01:20:59	Molniya 3-24	1.49	20	R	13.00	98.67
01:23:59	Molniya 3-24	1.48	20	I	13.05	99.1
01:26:59	Molniya 3-24	1.48	20	V	13.69	99.52
01:29:59	Molniya 3-24	1.48	20	B	14.61	99.94
02:31:46	Molniya 1-80	1.67	60	GR4		60.45
02:45:45	Molniya 1-80	1.70	60	GR4		58.47

Table A.11: Logbook 2016/09/27-28

Object	V	B-V	V-R	V-I
PG2213+006	14.124	-0.217	-0.092	-0.203
PG2213+006 A	14.178	0.673	0.406	0.808
PG2213+006 B	12.706	0.749	0.427	0.829
PG2213+006 C	15.109	0.721	0.426	0.830
PG0231+051	16.105	-0.329	-0.162	-0.534
PG0231+051 A	12.772	0.710	0.405	0.799
PG0231+051 B	14.735	1.448	0.954	1.951
PG0231+051 C	13.702	0.671	0.399	0.783
PG0231+051 D	14.027	1.088	0.675	1.256
PG0231+051 E	13.804	0.667	0.39	0.757

Table A.12: Standard stars magnitudes and color indexes from Landolt (1992)

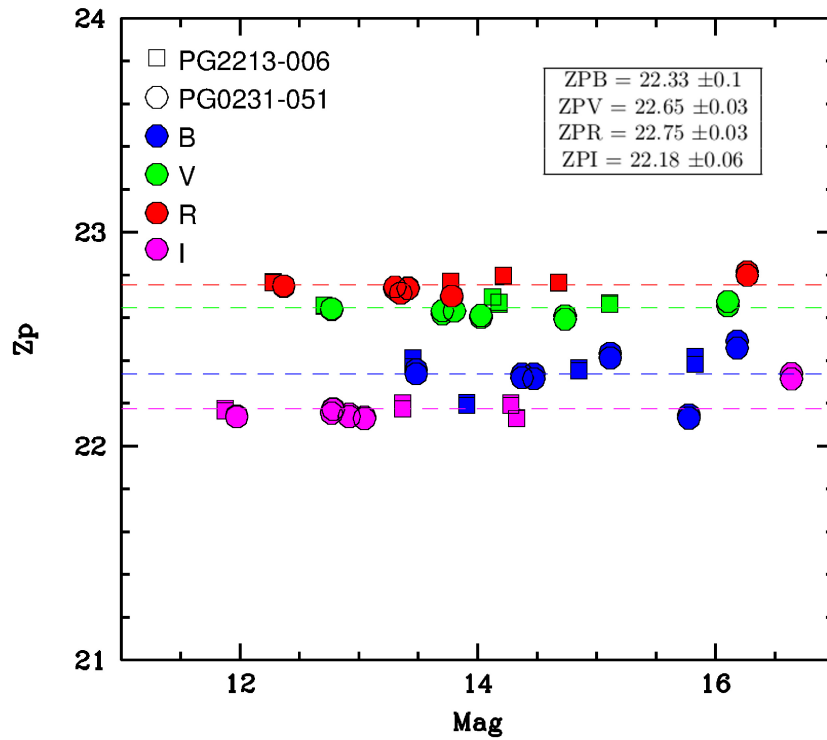


Figure A.86: Photometric zero points 2016/09/27-28, magnitudes from Landolt (1992)

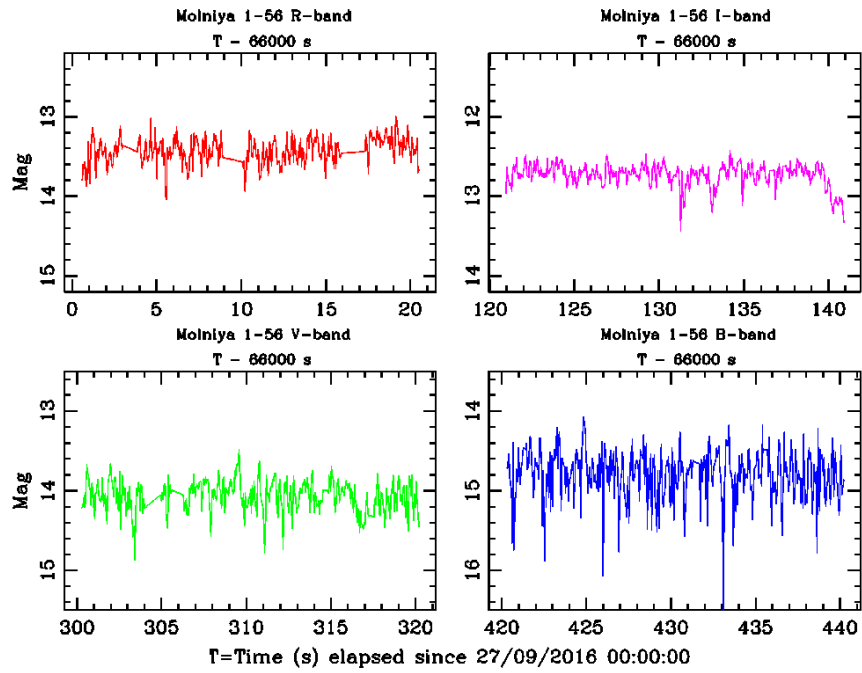


Figure A.87: Molniya 1-56 light curves

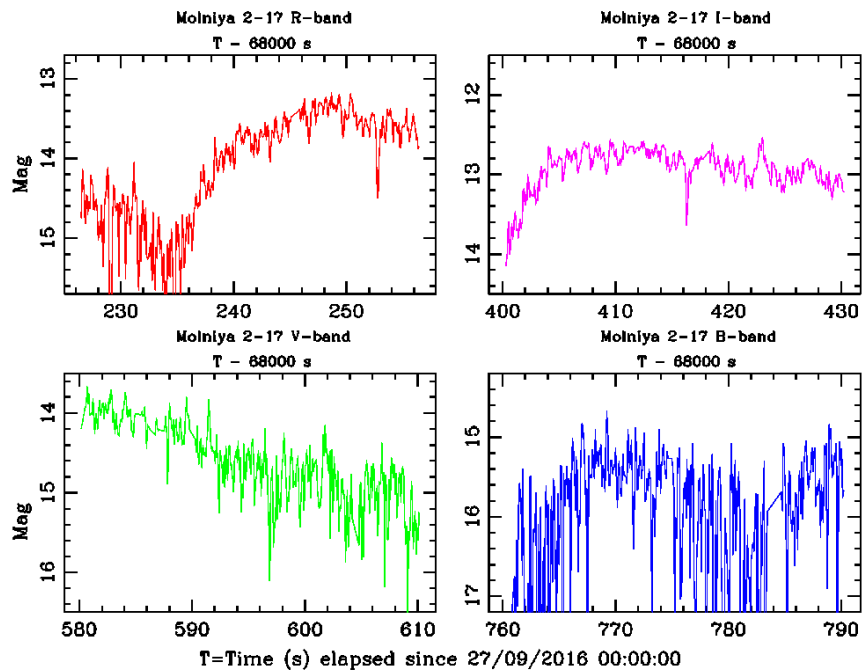


Figure A.88: Molniya 2-17 light curves

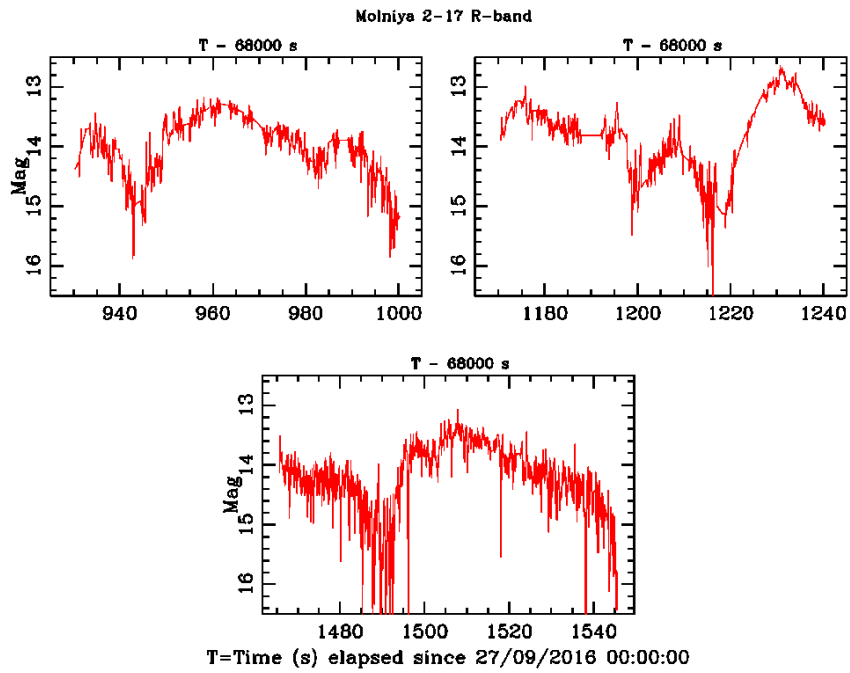


Figure A.89: Molniya 2-17 light curves

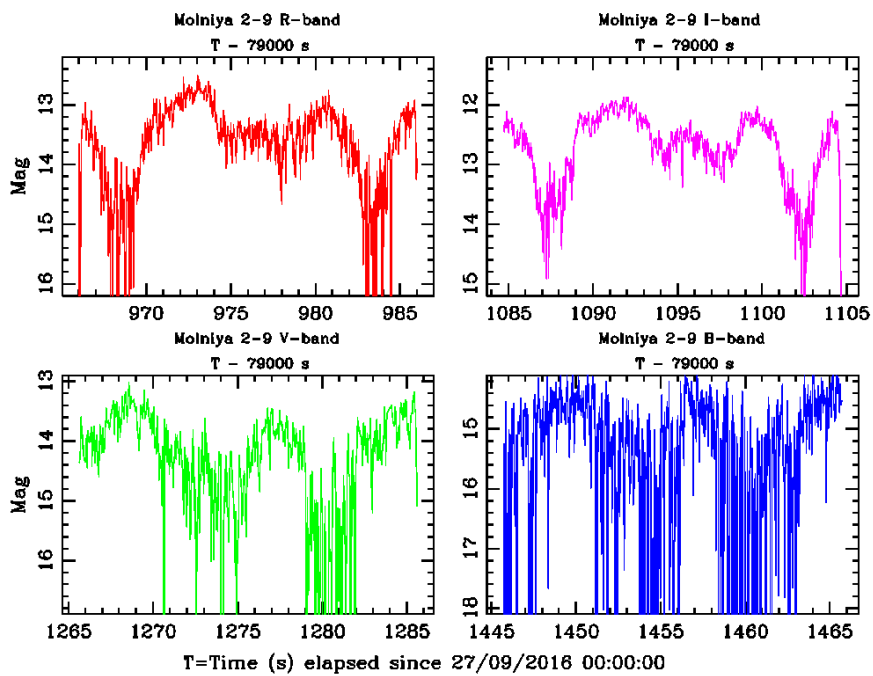


Figure A.90: Molniya 2-9 light curves

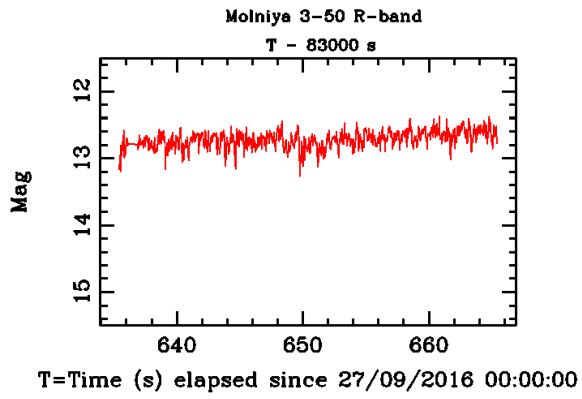


Figure A.91: Molniya 3-50 light curves

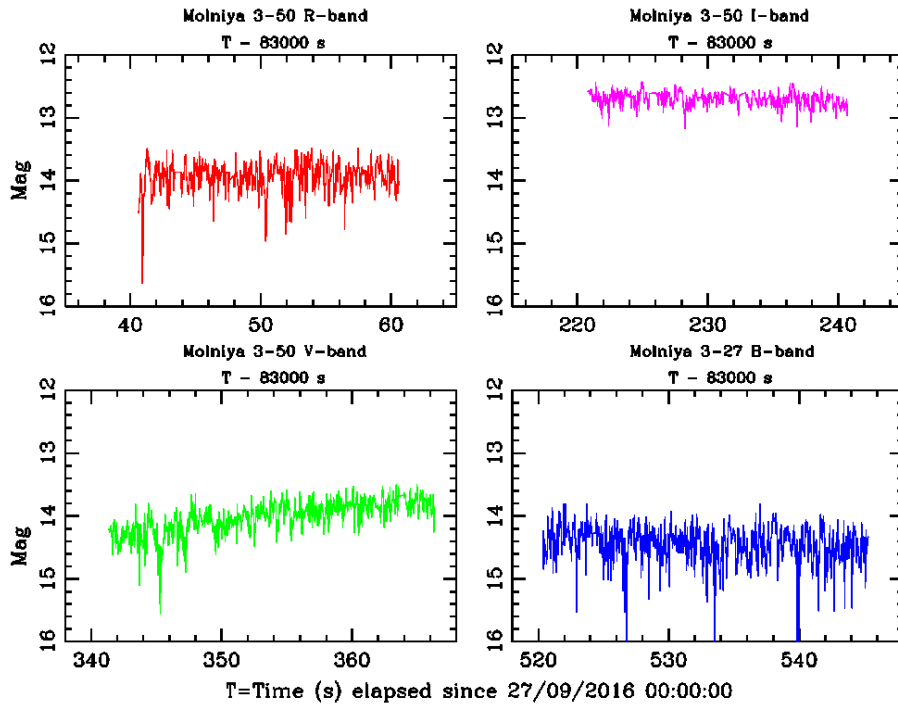


Figure A.92: Molniya 3-50 light curves

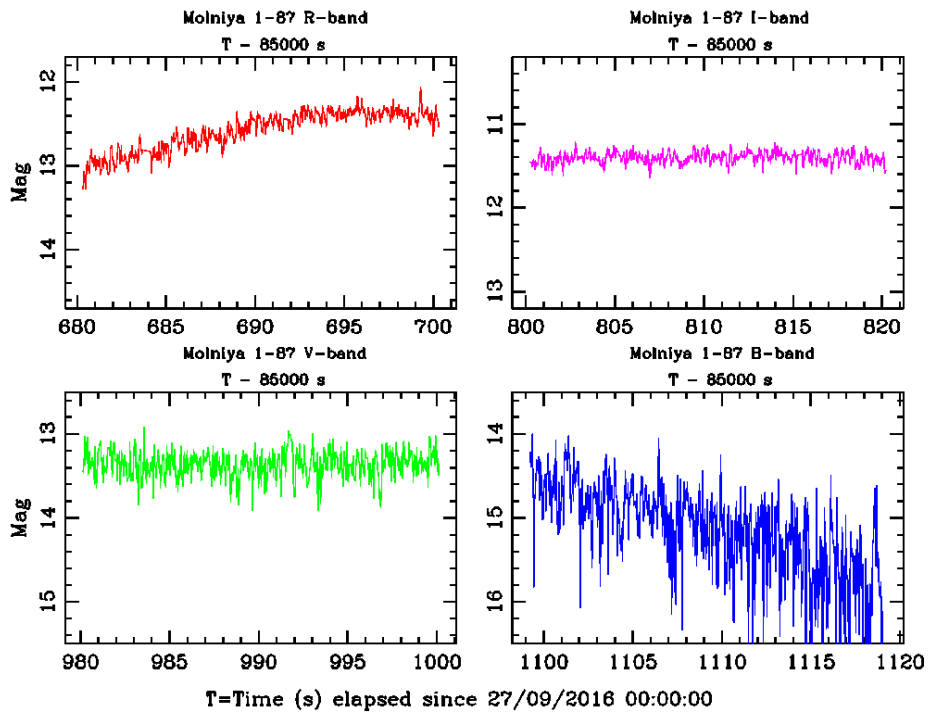


Figure A.93: Molniya 1-87 light curves

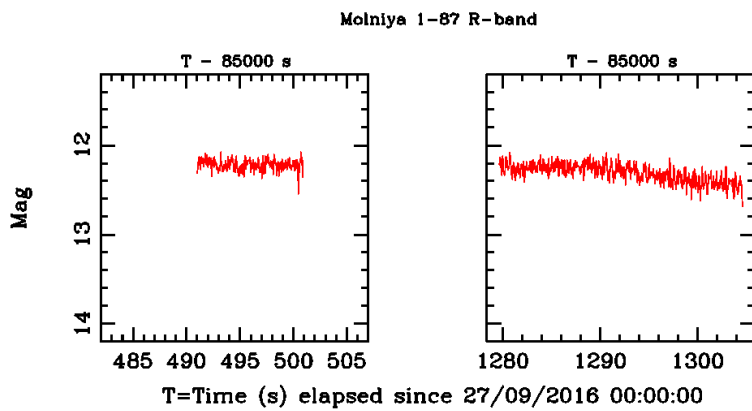


Figure A.94: Molniya 1-87 light curves

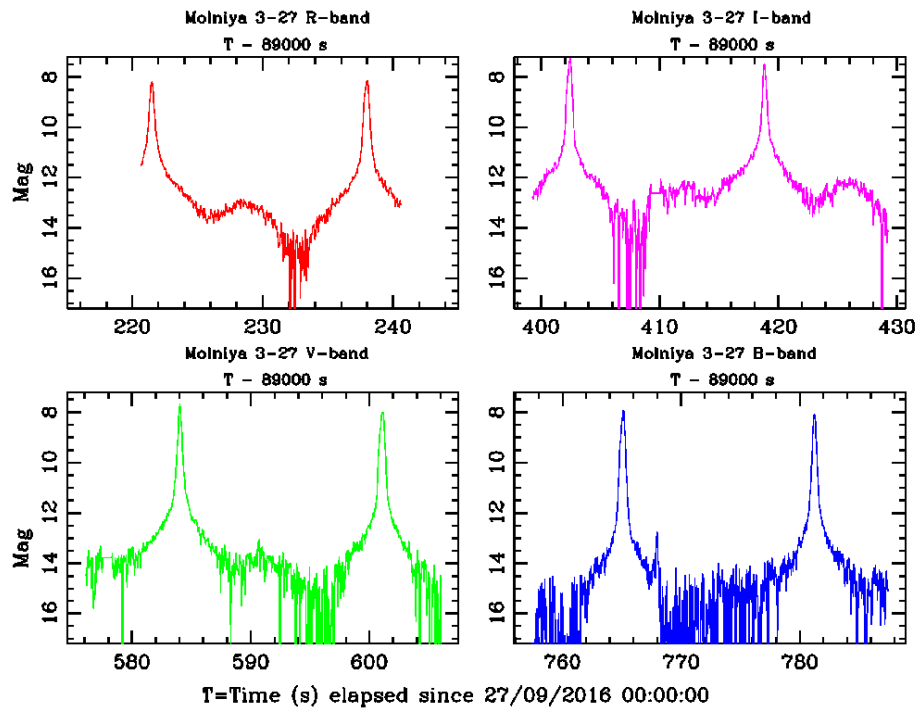


Figure A.95: Molniya 3-27 light curves

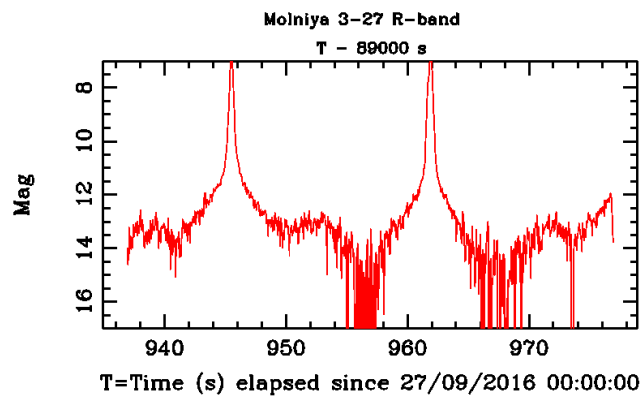


Figure A.96: Molniya 3-27 light curves

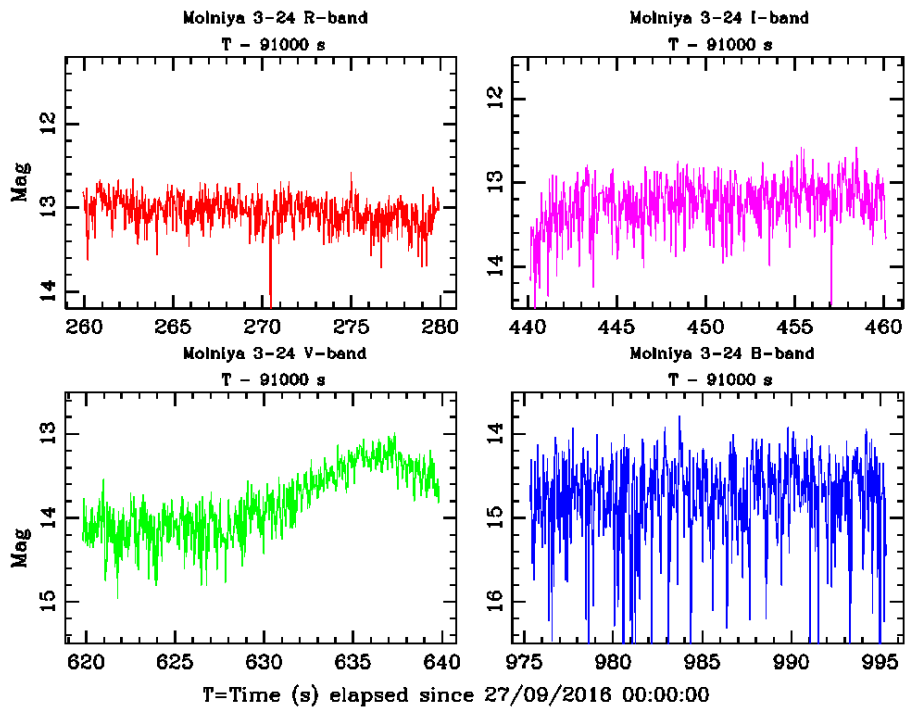


Figure A.97: Molniya 3-24 light curves

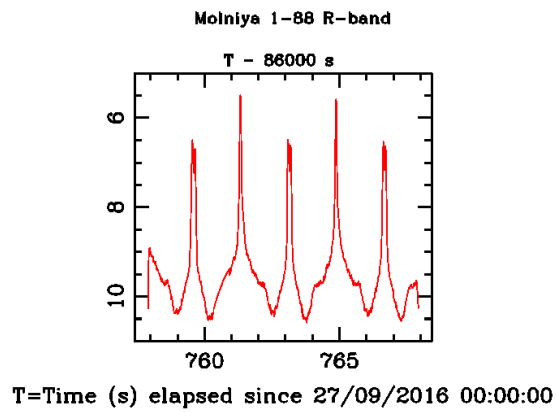


Figure A.98: Molniya 1-88 light curves

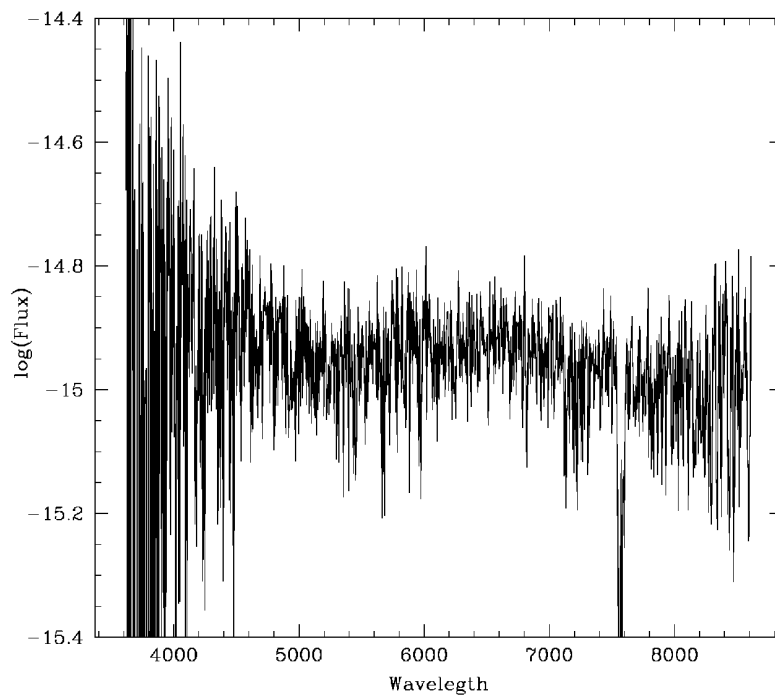
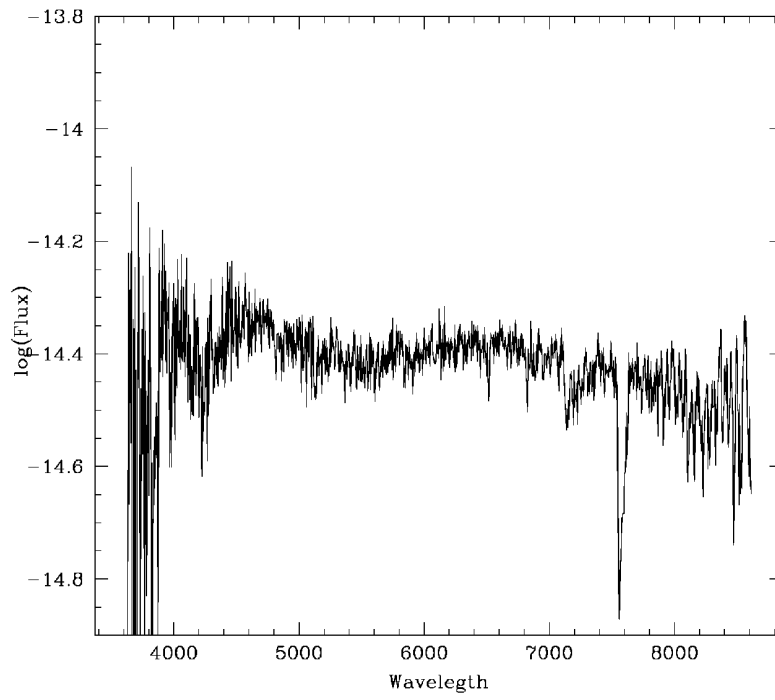


Figure A.99: Molniya 1-56 Spectra

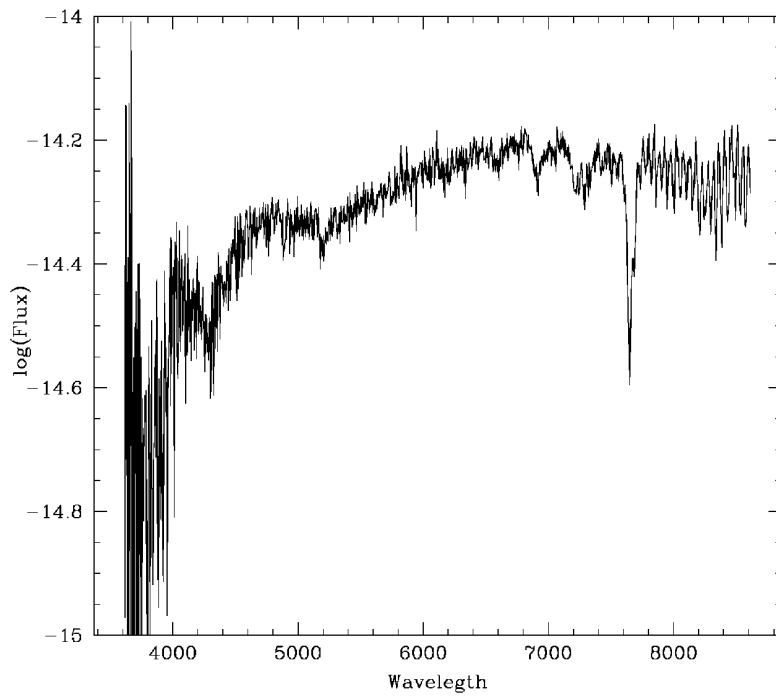
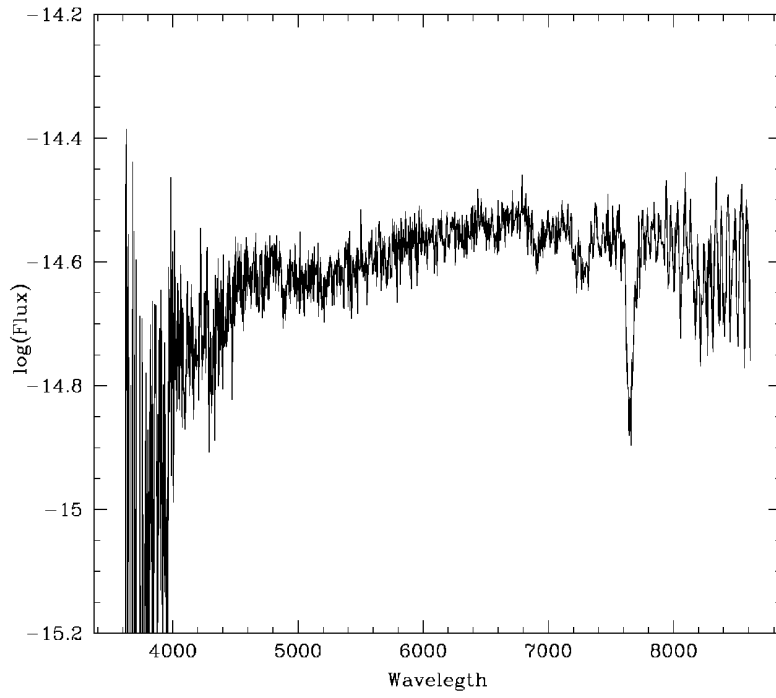


Figure A.100: Molniya 2-17 Spectra

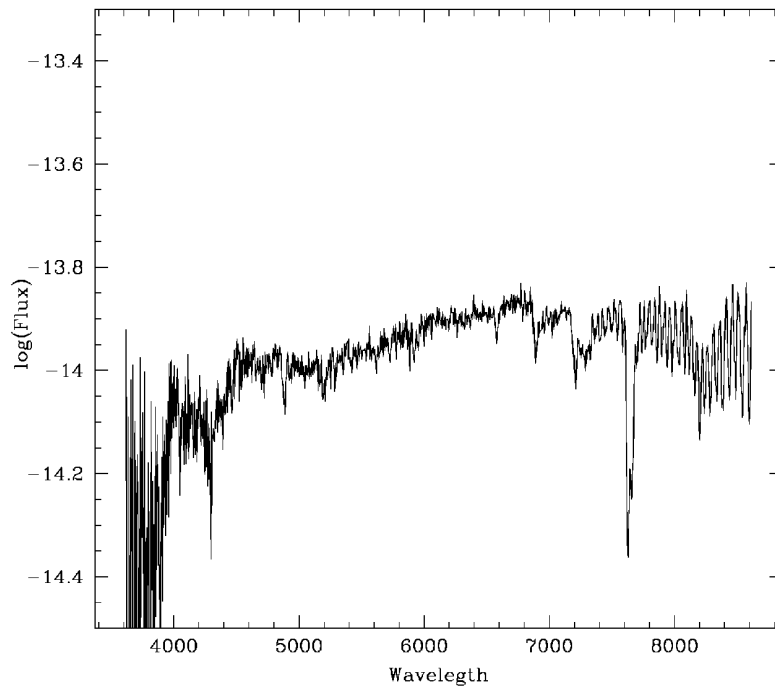
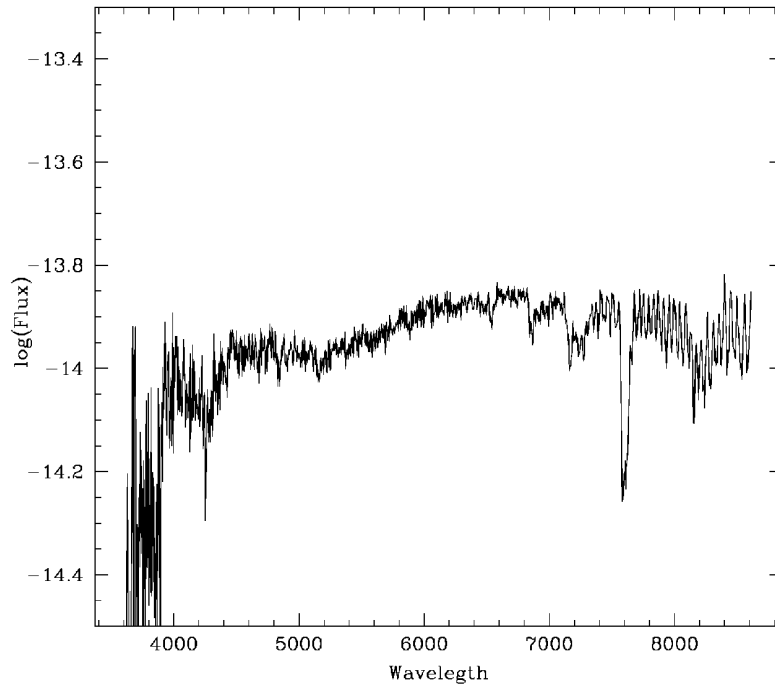


Figure A.101: Molniya 2-9 Spectra

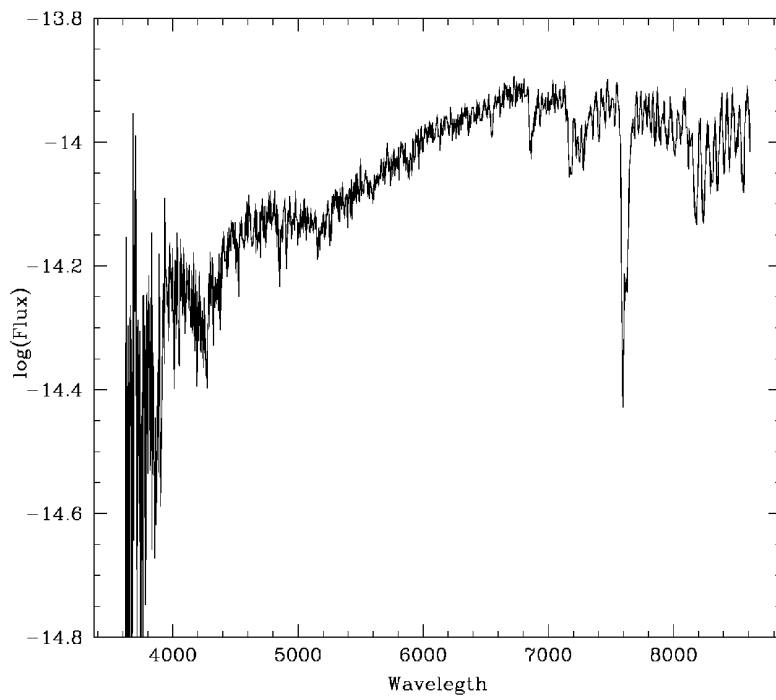
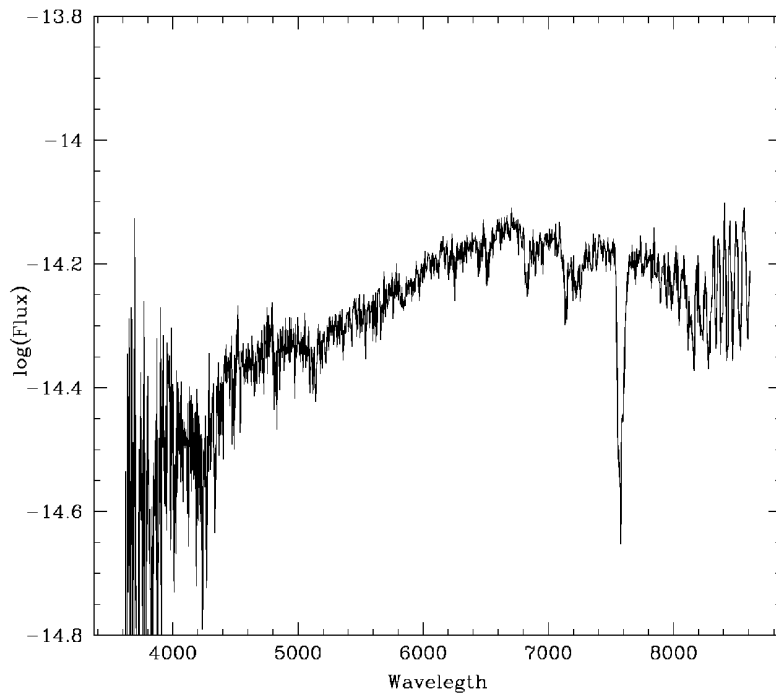


Figure A.102: Molniya 3-50 Spectra

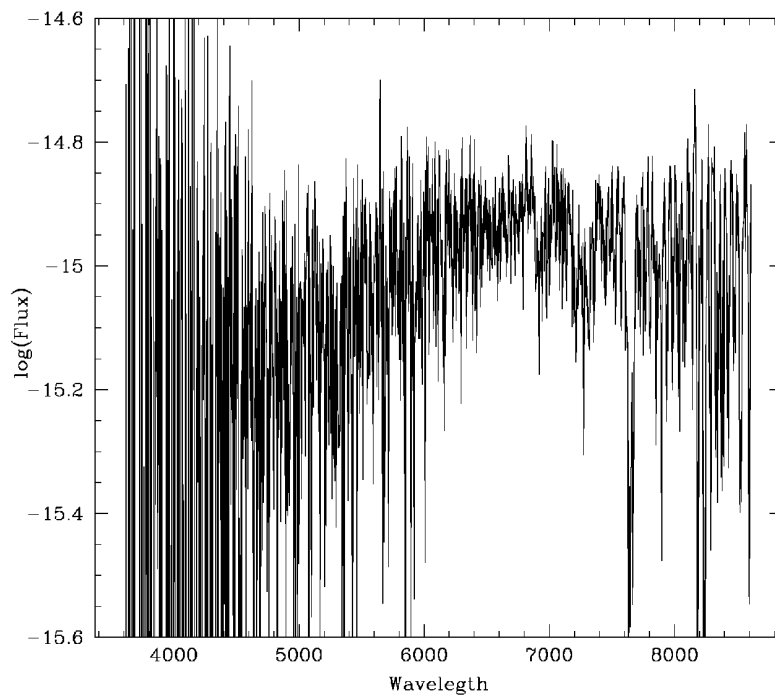
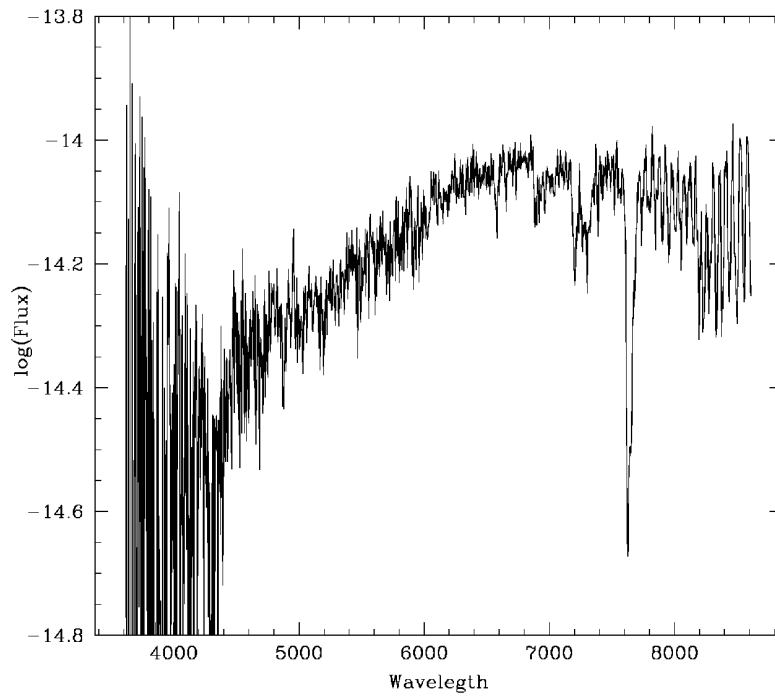


Figure A.103: Molniya 1-80 Spectra

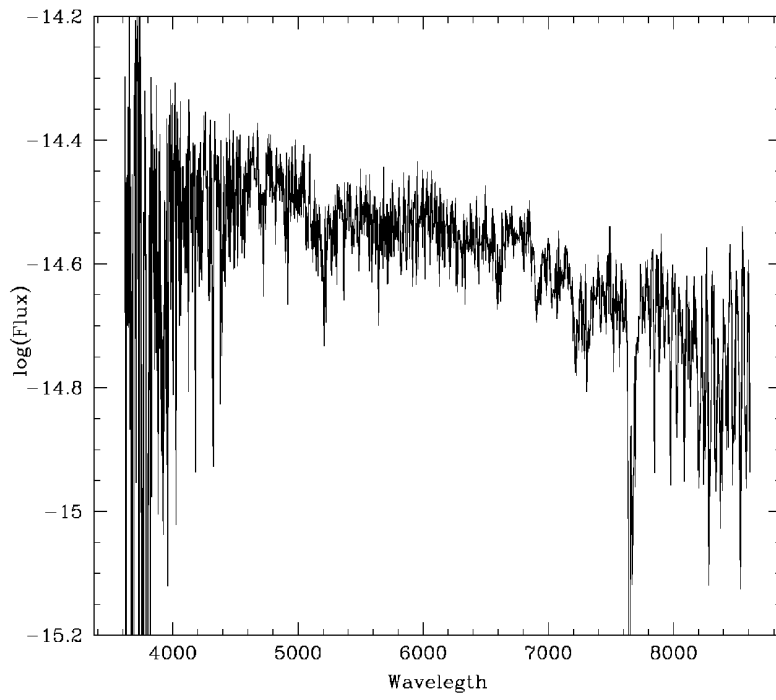


Figure A.104: Molniya 3-27 Spectra

A.5 Night 2016/11/26-27

- Seeing 2.3"
- Clear non photometric sky
- Operator: Roberto Gualandi
- JD:2457719.5

UT(start)	Object	Airmass	Exptime(s)	Filter/Grism	Mag	Phase Angle
18:02:58	Molniya 1-90	1.05	5	R	9.78	48.12
18:04:58	Molniya 1-90	1.05	5	R	10.06	47.44
18:06:58	Molniya 1-90	1.06	5	I	9.95	46.83
18:08:58	Molniya 1-90	1.06	5	V	10.44	46.27
18:10:58	Molniya 1-90	1.07	7	B	11.57	45.77
18:12:58	Molniya 1-90	1.07	7	R	10.03	45.32
18:14:57	Molniya 1-90	1.08	7	I	10.22	44.91
18:16:58	Molniya 1-90	1.08	7	V	11.46	44.54
18:18:58	Molniya 1-90	1.09	7	B	11.88	44.20
18:20:57	Molniya 1-90	1.09	7	R	10.11	43.90
18:22:57	Molniya 1-90	1.10	7	I	9.71	43.63
18:24:27	Molniya 1-90	1.10	7	V	10.90	43.50
18:25:58	Molniya 1-90	1.11	7	B	12.02	43.27
18:42:56	Molniya 1-88	1.09	3	R	7.92	66.09
18:44:56	Molniya 1-88	1.05	3	R	7.94	62.15
18:46:56	Molniya 1-88	1.03	3	R	8.71	58.79
18:48:57	Molniya 1-88	1.01	3	I	7.13	55.96
18:50:57	Molniya 1-88	1.01	3	V	8.46	53.58
18:52:57	Molniya 1-88	1.00	3	B	9.72	51.59
18:54:57	Molniya 1-88	1.01	3	R	8.74	49.94
18:56:57	Molniya 1-88	1.01	3	I	7.90	48.56
18:58:57	Molniya 1-88	1.02	4	V	9.44	47.42
19:00:57	Molniya 1-88	1.03	4	B	10.36	46.47
19:02:56	Molniya 1-88	1.04	5	R	9.21	45.69
19:04:57	Molniya 1-88	1.05	5	I	8.68	45.06
19:06:57	Molniya 1-88	1.06	6	V	10.05	44.54
19:08:57	Molniya 1-88	1.07	6	B	11.13	44.12
19:37:40	Molniya 2-13	1.73	60	GR4		99.26
19:59:39	Molniya 2-13	1.81	60	GR4		99.42

Table A.13: Logbook 2016/11/26-27

UT(start)	Object	Airmass	Exptime(s)	Filter/Grism	Mag	Phase Angle
20:18:59	Molniya 2-13	1.94	7	R	13.12	99.65
20:24:50	Molniya 2-13	1.99	15	R	12.91	99.76
20:27:44	Molniya 2-13	2.02	15	I	11.71	99.82
20:29:44	Molniya 2-13	2.04	15	V	11.67	99.86
20:33:44	Molniya 2-13	2.09	15	B	13.00	99.96
20:35:44	Molniya 2-13	2.11	15	R	12.33	100.01
20:40:44	Molniya 2-13	2.19	15	I	12.09	100.16
21:15:59	Molniya 1-86	1.54	1	R	8.17	80.88
21:19:59	Molniya 1-86	1.26	1	I	7.39	68.57
21:36:19	Molniya 2-10	1.06	20	R	11.64	47.89
21:39:19	Molniya 2-10	1.06	20	I	11.26	47.61
21:43:19	Molniya 2-10	1.06	20	V	12.99	47.27
21:45:20	Molniya 2-10	1.06	20	B	13.53	47.12
21:47:21	Molniya 2-10	1.07	20	R	12.14	46.97
21:49:19	Molniya 2-10	1.07	20	I	11.87	46.83
21:51:19	Molniya 2-10	1.07	20	V	12.61	46.70
21:55:19	Molniya 2-10	1.07	20	B	14.43	46.47
21:58:22	Molniya 2-10	1.07	20	R	12.73	46.30
22:01:19	Molniya 2-10	1.07	30	R	12.76	46.16
22:05:19	Molniya 2-10	1.07	30	R	12.54	45.98
22:08:21	Molniya 2-10	1.07	40	R	12.73	45.86
22:12:19	Molniya 2-10	1.07	40	I	11.47	45.71
22:15:19	Molniya 2-10	1.07	40	V	13.47	45.61
22:31:44	Molniya 2-10	1.08	40	B	14.79	45.20
22:35:41	Molniya 2-10	1.08	120	GR4		45.13
00:57:58	Meridian 1	1.37	20	R	10.77	70.30
01:02:00	Meridian 1	1.34	20	I	10.13	70.37
01:03:59	Meridian 1	1.33	20	V	11.50	70.44
01:06:59	Meridian 1	1.32	20	B	12.47	70.51
01:08:59	Meridian 1	1.31	25	R	10.86	70.56
01:10:57	Meridian 1	1.30	25	I	10.19	70.62
01:13:57	Meridian 1	1.29	25	V	11.55	70.69
01:15:58	Meridian 1	1.28	25	B	12.63	70.75
01:17:54	Meridian 1	1.27	30	R	10.92	70.80
01:19:54	Meridian 1	1.26	30	I	10.27	70.86
01:21:55	Meridian 1	1.26	30	V	11.51	70.92
01:23:53	Meridian 1	1.25	30	B	12.64	70.98
01:25:54	Meridian 1	1.24	30	R	10.95	71.03
01:27:54	Meridian 1	1.24	30	R	11.02	71.09
01:29:54	Meridian 1	1.23	30	R	11.04	71.15
01:31:54	Meridian 1	1.22	30	R	11.07	71.21
01:33:54	Meridian 1	1.22	30	I	10.40	71.27
01:35:54	Meridian 1	1.21	30	V	11.80	71.34
01:37:54	Meridian 1	1.20	30	B	12.78	71.40
01:47:13	Meridian 1	1.18	60	GR4		71.69
01:52:18	Meridian 1	1.17	60	GR4		71.85

Table A.14: Logbook 2016/11/26-27

UT(start)	Object	Airmass	Exptime(s)	Filter/Grism	Mag	Phase Angle
02:06:58	Molniya 3-42	1.28	3	R	10.56	74.58
02:08:58	Molniya 3-42	1.25	3	R	10.57	74.82
02:11:58	Molniya 3-42	1.22	3	R	10.69	75.27
02:13:59	Molniya 3-42	1.20	3	I	9.84	75.60
02:15:58	Molniya 3-42	1.19	3	V	11.81	75.95
02:17:59	Molniya 3-42	1.18	4	B	12.57	76.32
02:19:58	Molniya 3-42	1.17	5	R	11.25	76.69
02:21:59	Molniya 3-42	1.17	5	I	10.35	77.07
02:23:59	Molniya 3-42	1.16	5	V	11.93	77.46
02:25:59	Molniya 3-42	1.16	5	B	13.01	77.84
02:27:59	Molniya 3-42	1.16	7	R	11.39	78.22
02:29:58	Molniya 3-42	1.16	7	I	10.68	78.59
02:31:58	Molniya 3-42	1.16	8	V	12.30	78.96
02:33:58	Molniya 3-42	1.16	8	B	12.94	79.33
02:35:58	Molniya 3-42	1.16	10	R	11.50	79.69
02:37:58	Molniya 3-42	1.16	10	I	10.81	80.05
02:39:58	Molniya 3-42	1.16	10	V	12.32	80.40
02:43:59	Molniya 3-42	1.17	10	B	13.24	81.07
02:46:05	Molniya 3-42	1.17	10	R	11.73	81.40
02:50:05	Molniya 3-42	1.17	10	I	11.08	82.04
02:52:03	Molniya 3-42	1.18	12	V	12.46	82.35
02:54:03	Molniya 3-42	1.18	12	B	13.34	82.66
02:56:03	Molniya 3-42	1.18	14	R	11.91	82.96
03:04:01	Molniya 3-42	1.20	60	GR4		84.09
03:06:40	Molniya 3-42	1.20	60	GR4		84.49
03:16:00	Molniya 1-86	1.23	1	B	12.45	79.80
03:17:51	Molniya 1-86	1.25	10	B	13.93	80.76
03:19:51	Molniya 1-86	1.28	10	V	11.64	81.72
03:21:51	Molniya 1-86	1.30	10	R	10.89	82.69
03:23:51	Molniya 1-86	1.32	10	I	11.30	83.66
03:25:50	Molniya 1-86	1.35	10	B	12.43	84.63
03:27:51	Molniya 1-86	1.37	10	V	11.35	85.61
03:29:50	Molniya 1-86	1.40	10	R	11.59	86.59
03:31:51	Molniya 1-86	1.43	10	I	10.29	87.58
03:36:58	Molniya 1-69	1.15	20	R	12.71	44.39
03:39:59	Molniya 1-69	1.15	20	I	11.48	44.88
03:42:59	Molniya 1-69	1.15	20	V	13.51	45.37
03:45:49	Molniya 1-69	1.15	30	B	14.37	45.84
03:48:39	Molniya 1-69	1.15	40	R	12.38	46.32
03:51:39	Molniya 1-69	1.15	40	I	12.12	46.78
03:54:37	Molniya 1-69	1.15	40	V	13.99	47.23
03:57:42	Molniya 1-69	1.15	40	B	13.29	47.68
04:05:03	Molniya 1-69	1.15	60	GR4		48.72
04:08:54	Molniya 1-69	1.15	60	GR4		49.29

Table A.15: Logbook 2016/11/26-27

Object	V	B-V	V-R	V-I
PG0231+051	16.105	-0.329	-0.162	-0.534
PG0231+051 A	12.772	0.71	0.405	0.799
PG0231+051 B	14.735	1.448	0.954	1.951
PG0231+051 C	13.702	0.671	0.399	0.783
PG0231+051 D	14.027	1.088	0.675	1.256
PG0231+051 E	13.804	0.667	0.39	0.757
Rubin 149	13.866	-0.129	-0.04	-0.108
Rubin 149 A	14.495	0.298	0.196	0.391
Rubin 149 B	12.642	0.662	0.374	0.728
Rubin 149 C	14.425	0.195	0.093	0.222
Rubin 149 D	11.48	-0.037	0.021	0.029
Rubin 149 E	13.718	0.522	0.321	0.637
Rubin 149 F	13.471	1.115	0.594	1.132
Rubin 149 G	12.839	0.541	0.322	0.645

Table A.16: Standard stars magnitudes and color indexes from Landolt (1992)

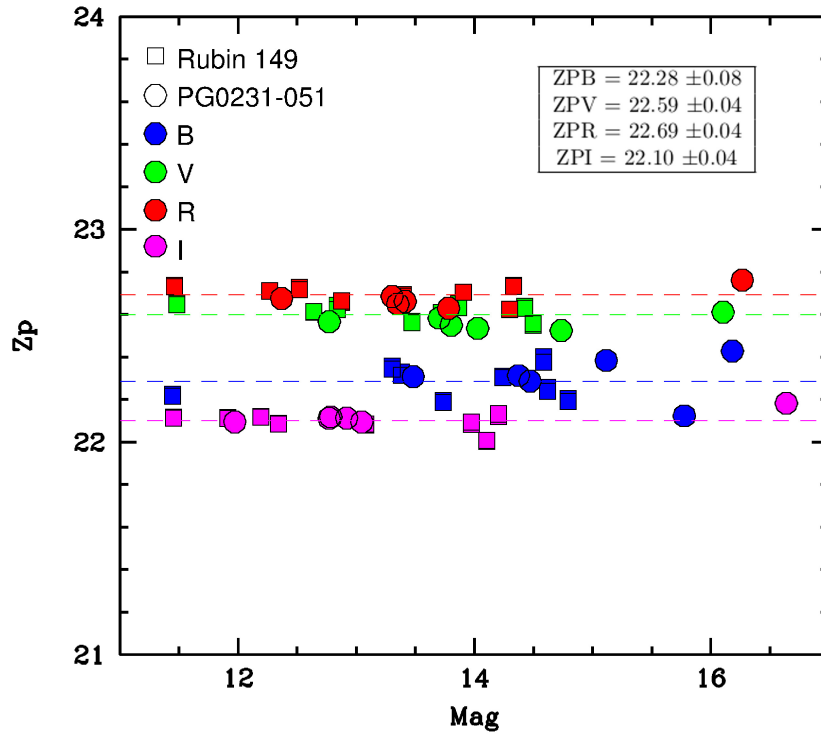


Figure A.105: Photometric zero points 2016/11/26-27, magnitudes from Landolt (1992)

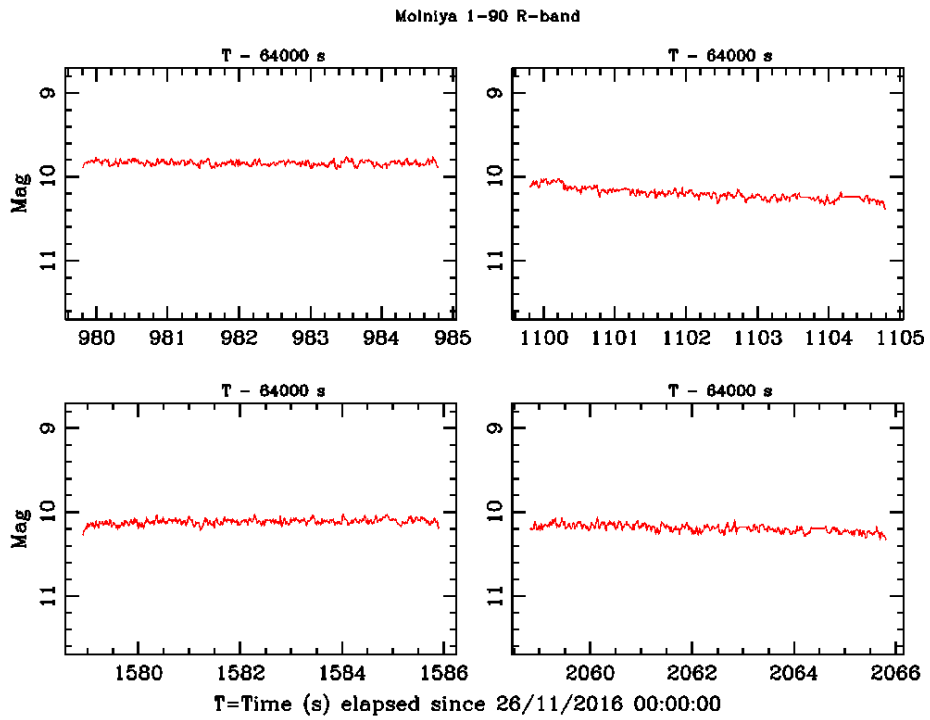


Figure A.106: Molniya 1-90 filter R light curves

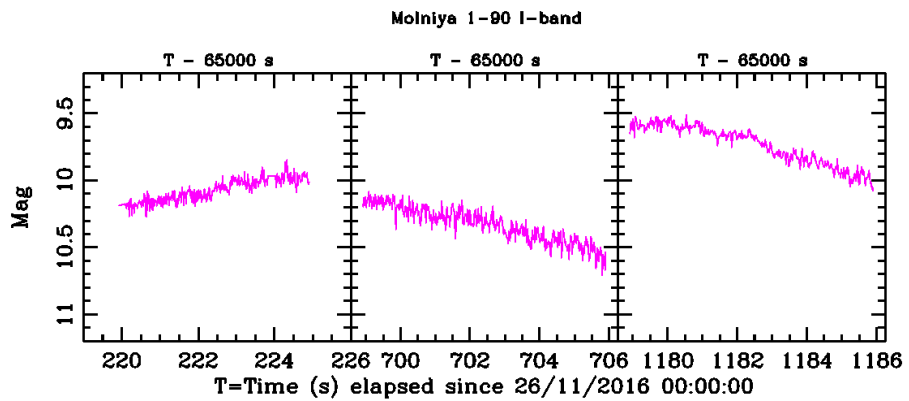


Figure A.107: Molniya 1-90 filter I light curves

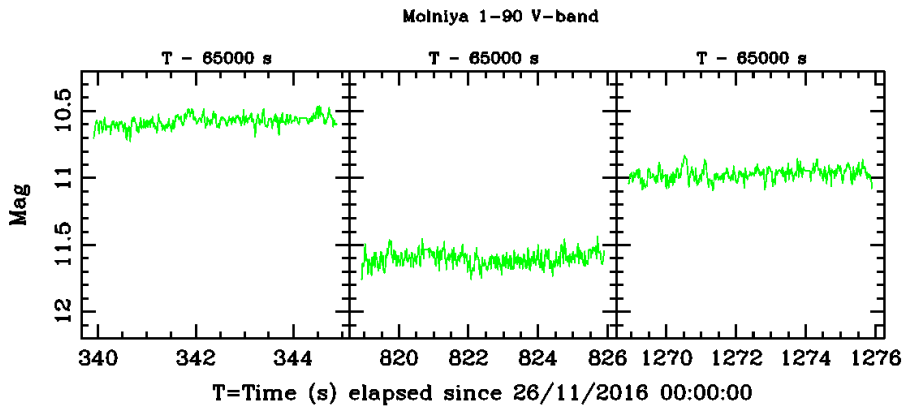


Figure A.108: Molniya 1-90 filter V light curves

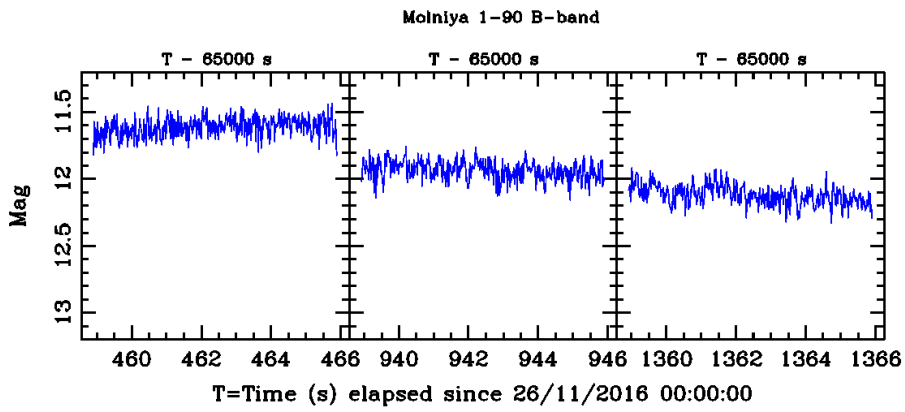


Figure A.109: Molniya 1-90 filter B light curves

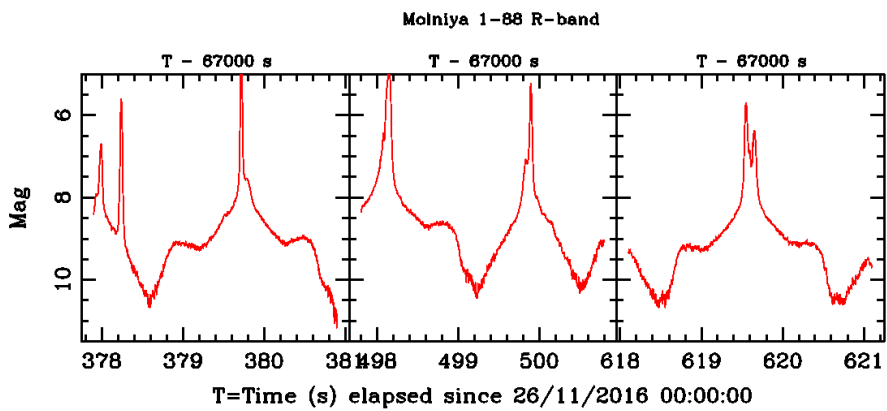


Figure A.110: Molniya 1-88 filter R light curves

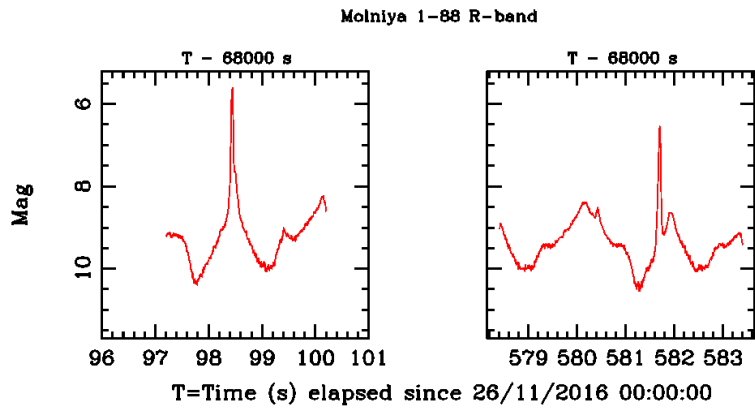


Figure A.111: Molniya 1-88 filter R light curves

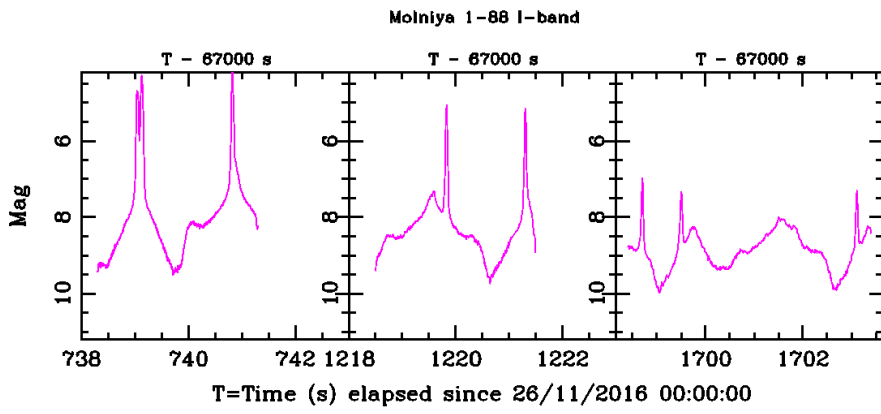


Figure A.112: Molniya 1-88 filter I light curves

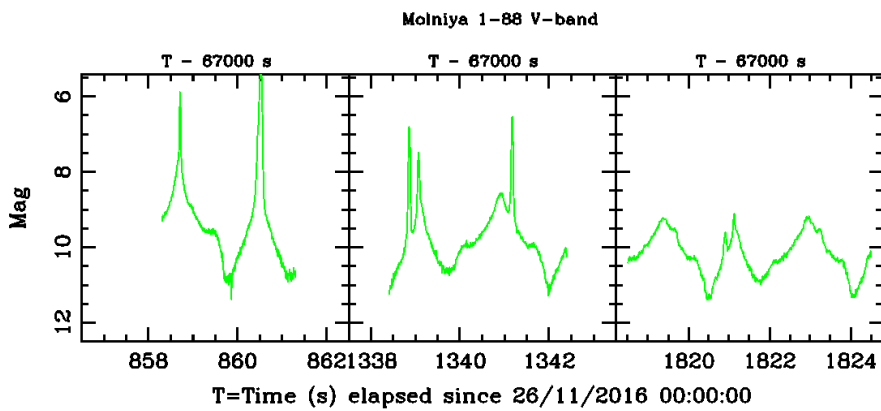


Figure A.113: Molniya 1-88 filter V light curves

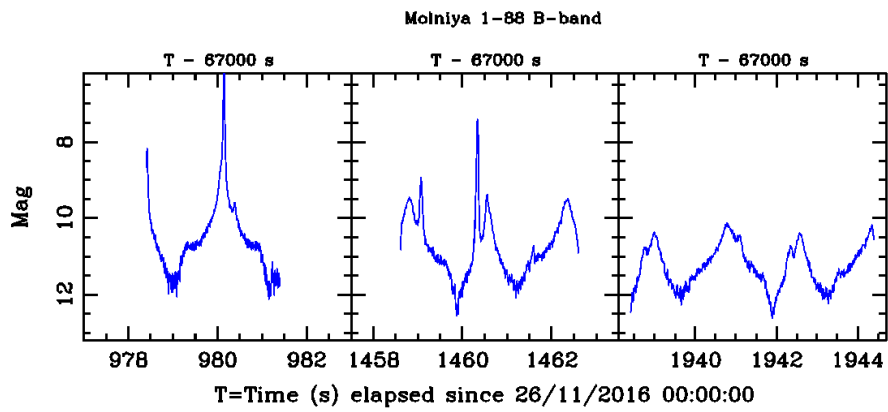


Figure A.114: Molniya 1-88 filter B light curves

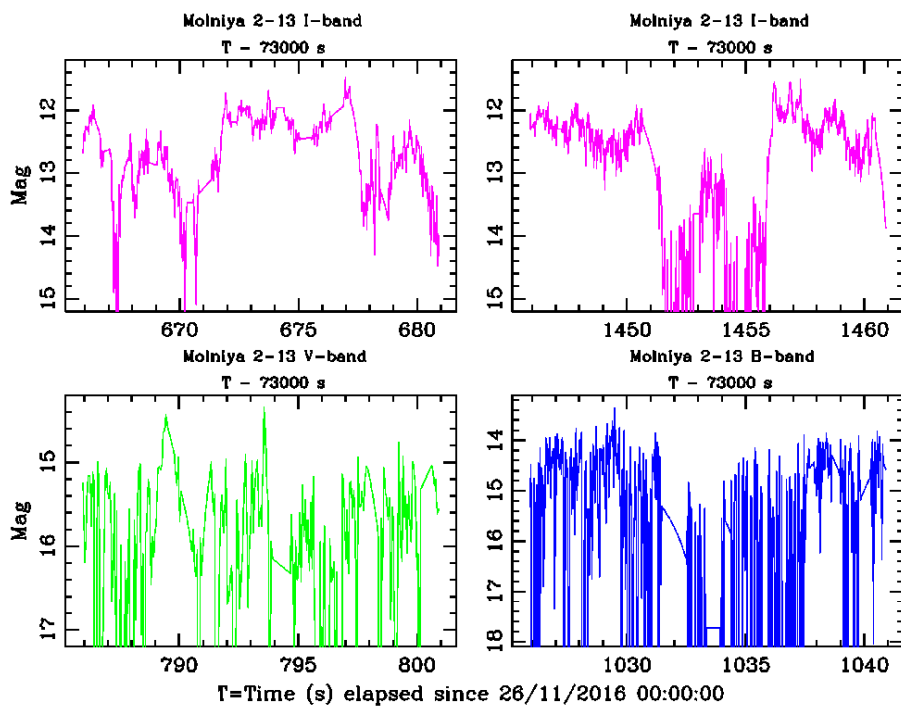


Figure A.115: Molniya 2-13 light curves

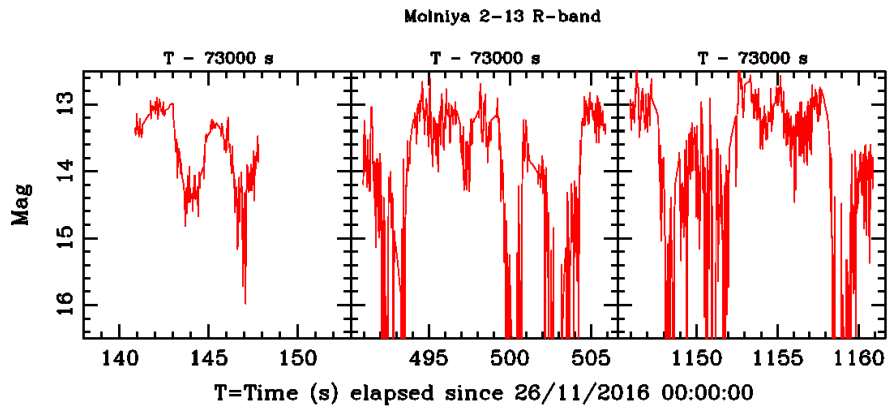


Figure A.116: Molniya 2-13 filter R light curves

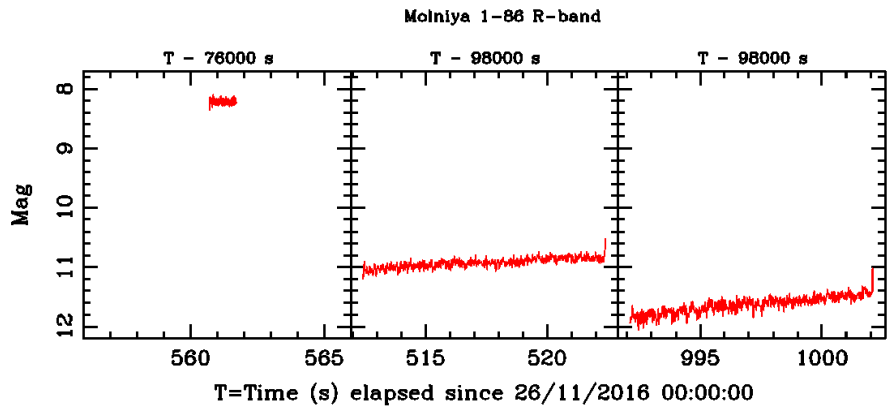


Figure A.117: Molniya 1-86 filter R light curves

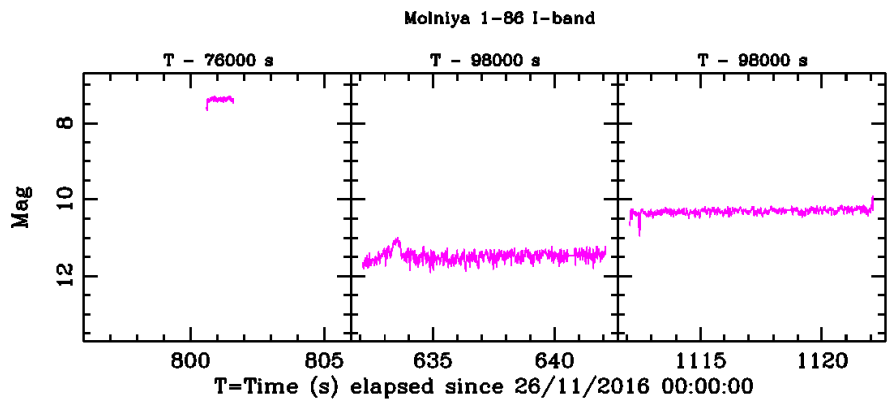


Figure A.118: Molniya 1-86 filter I light curves

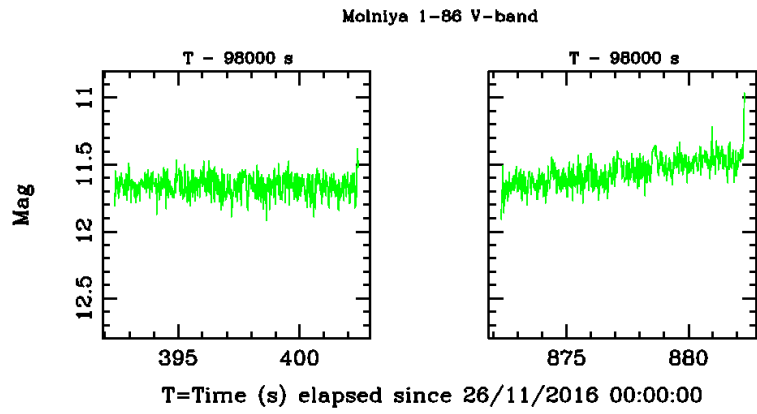


Figure A.119: Molniya 1-86 filter V light curves

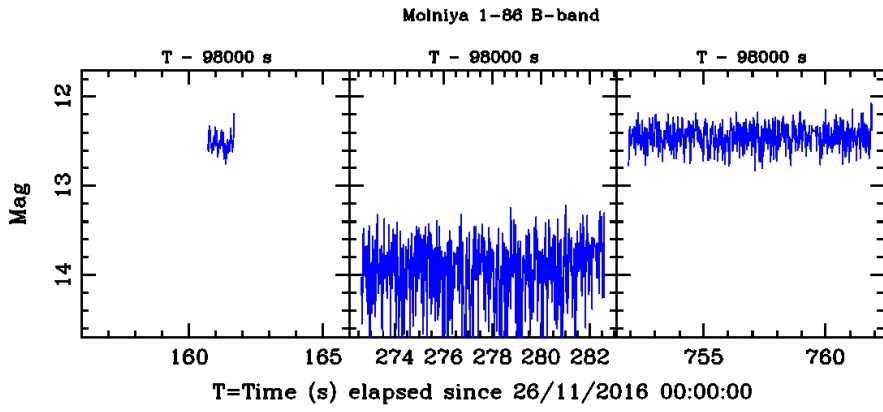


Figure A.120: Molniya 1-86 filter B light curves

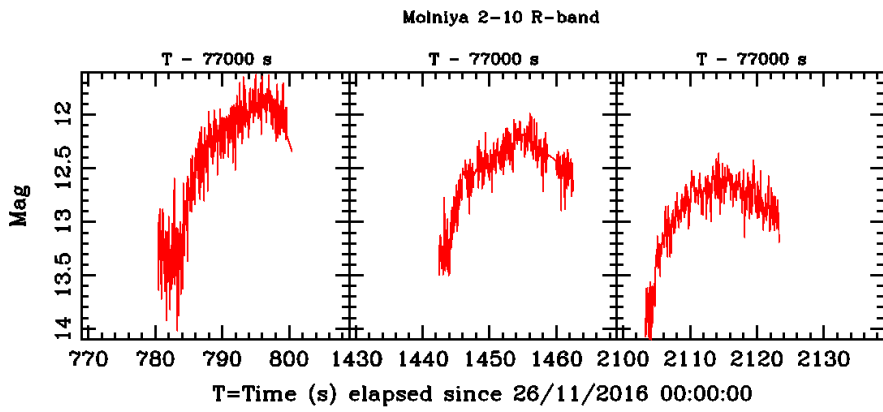


Figure A.121: Molniya 2-10 filter R light curves

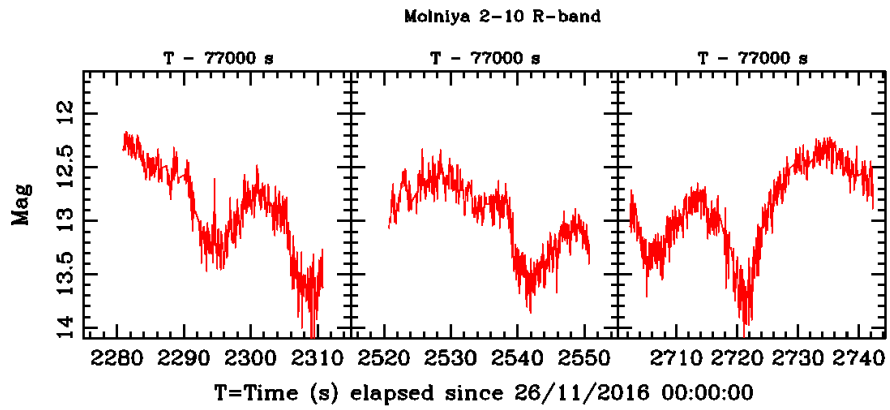


Figure A.122: Molniya 2-10 filter R light curves

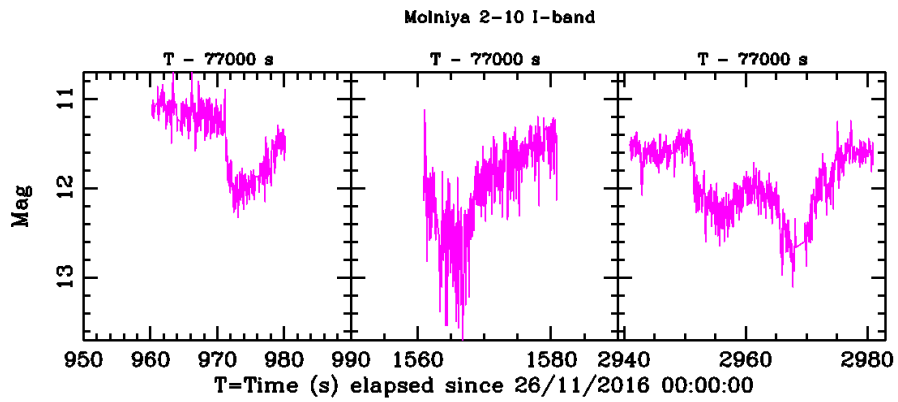


Figure A.123: Molniya 2-10 filter I light curves

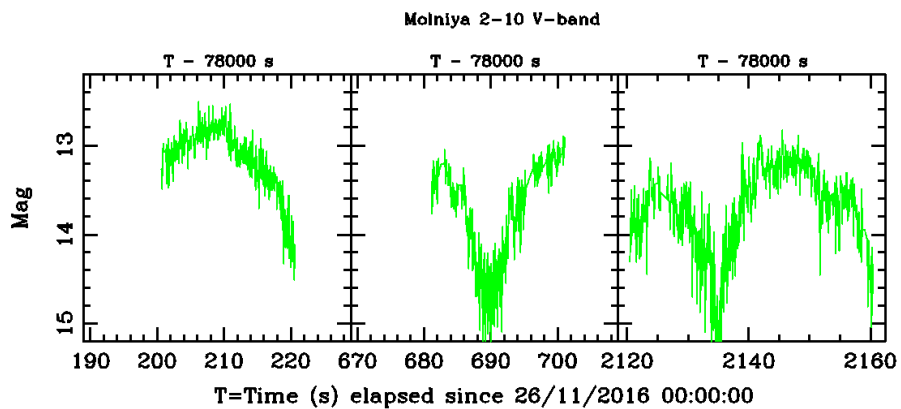


Figure A.124: Molniya 2-10 filter V light curves

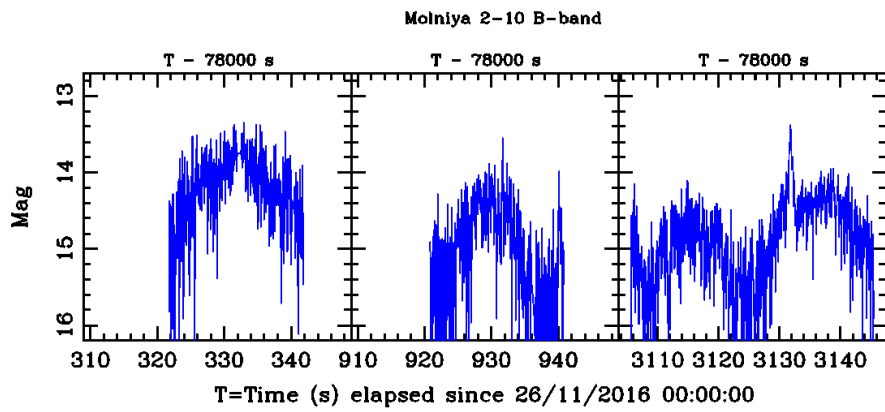


Figure A.125: Molniya 2-10 filter B light curves

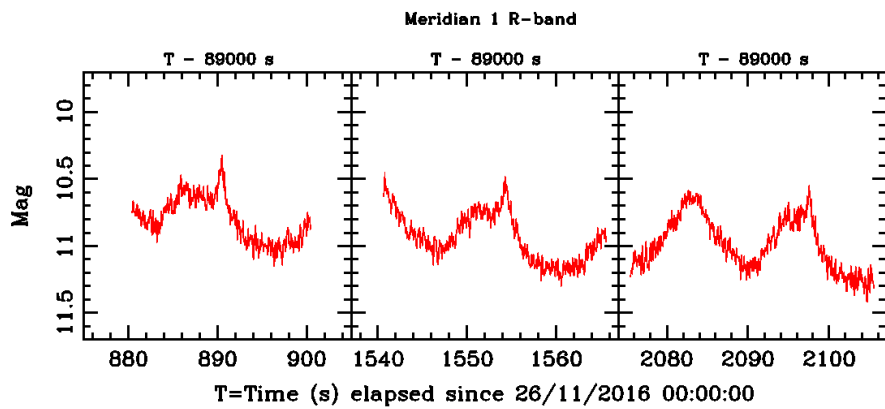


Figure A.126: Meridian 1 filter R light curves

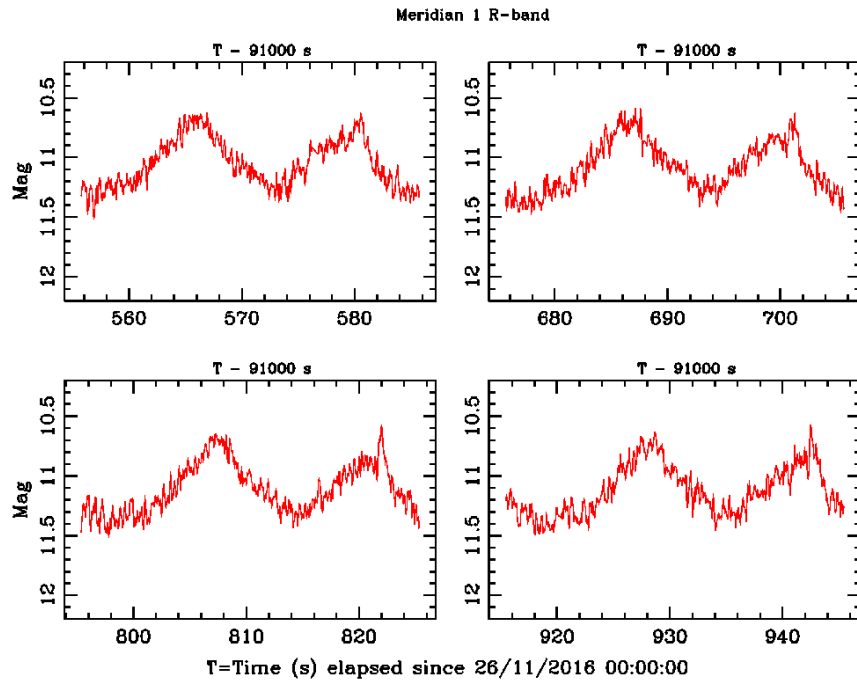


Figure A.127: Meridian 1 filter R light curves

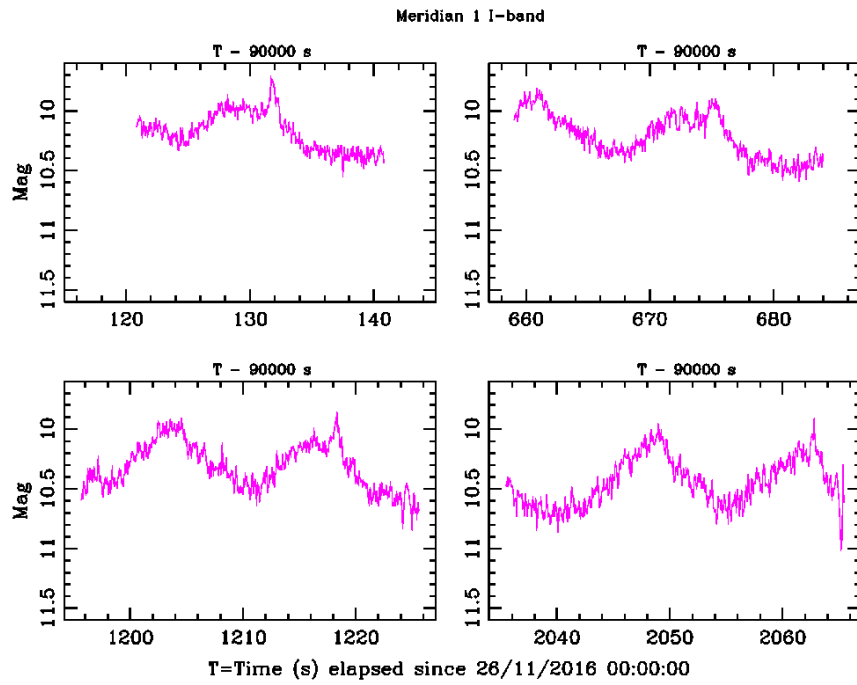


Figure A.128: Meridian 1 filter I light curves

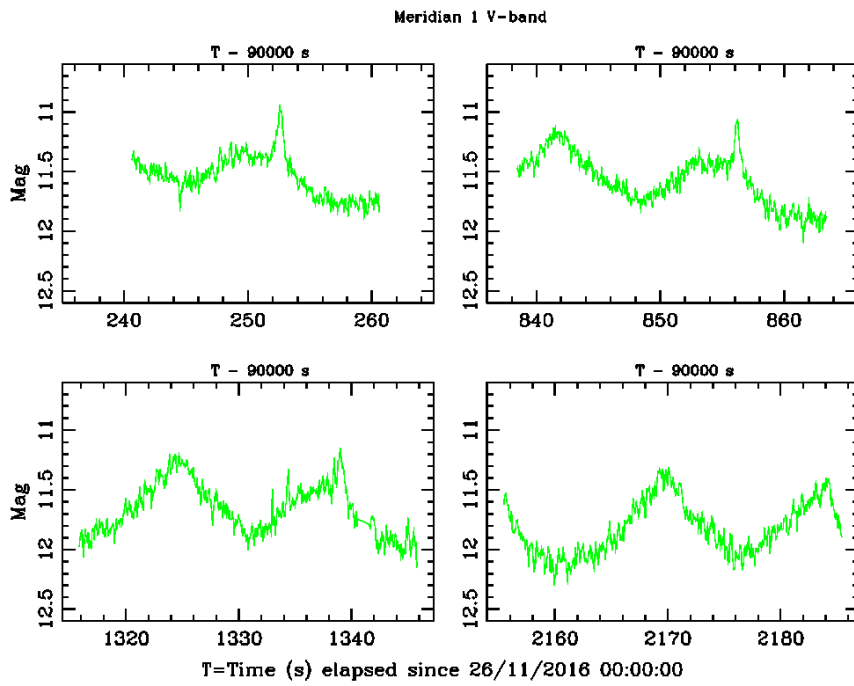


Figure A.129: Meridian 1 filter V light curves

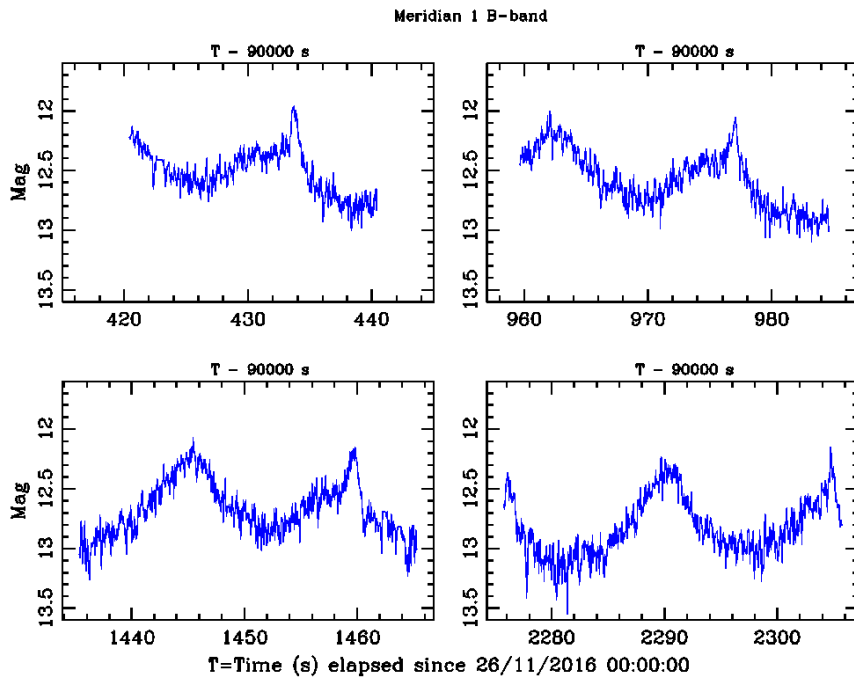


Figure A.130: Meridian 1 filter B light curves

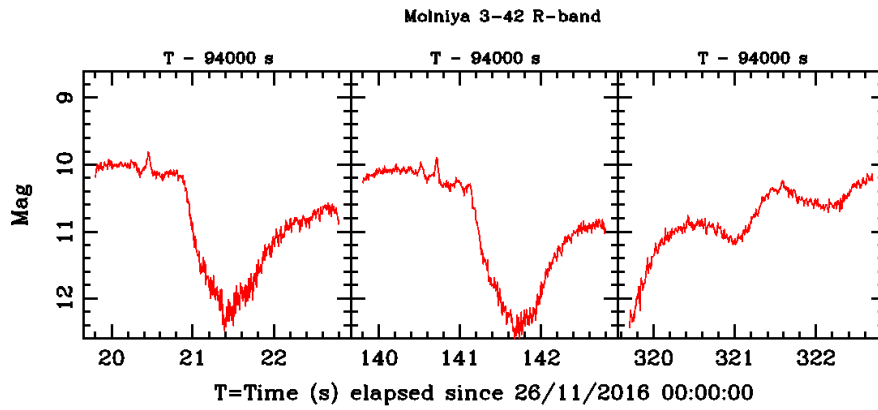


Figure A.131: Molniya 3-42 filter R light curves

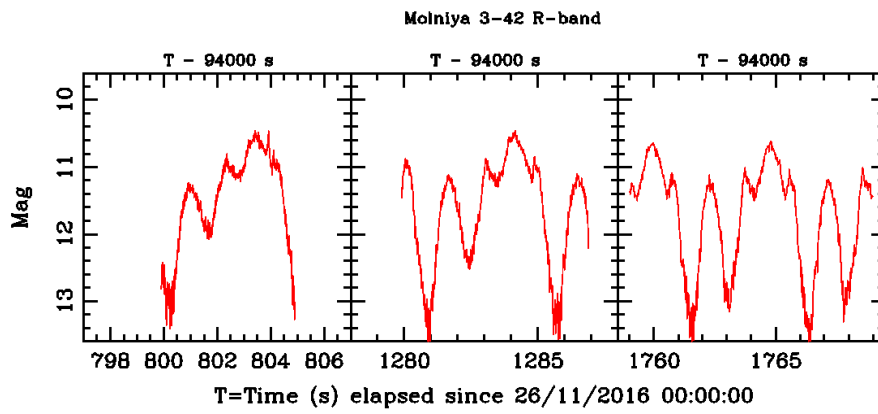


Figure A.132: Molniya 3-42 filter R light curves

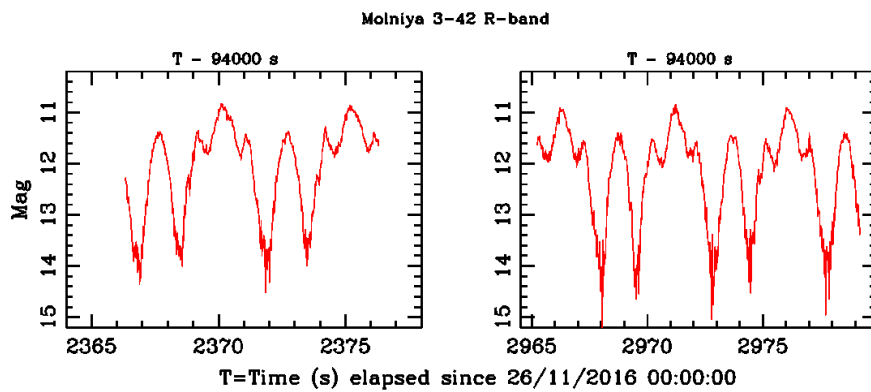


Figure A.133: Molniya 3-42 filter R light curves

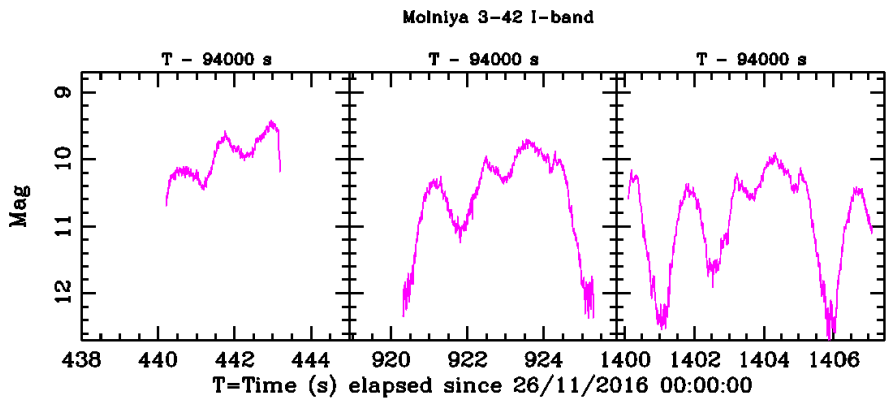


Figure A.134: Molniya 3-42 filter I light curves

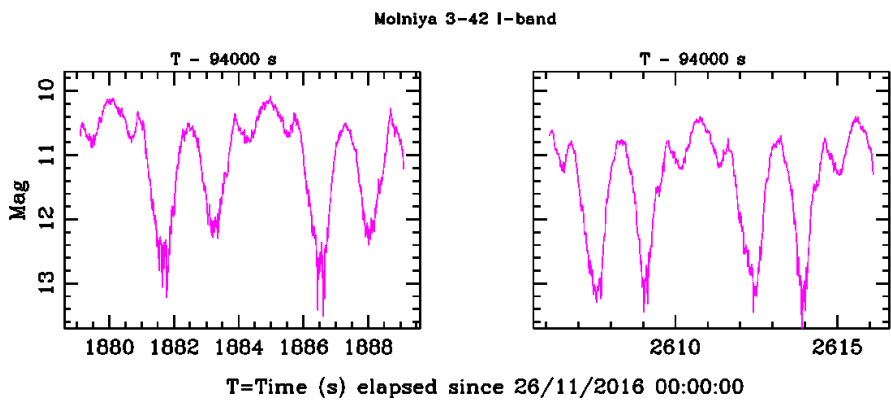


Figure A.135: Molniya 3-42 filter I light curves

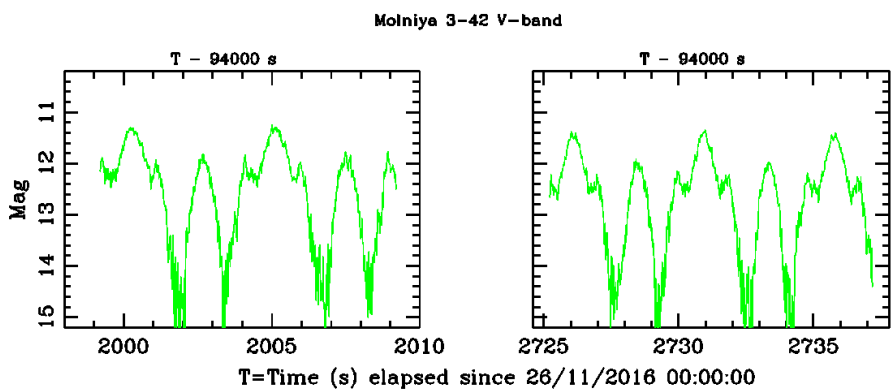


Figure A.136: Molniya 3-42 filter V light curves

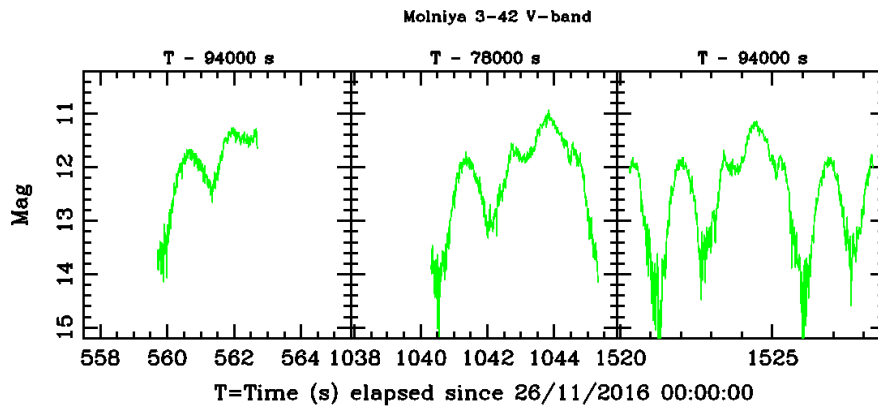


Figure A.137: Molniya 3-42 filter V light curves

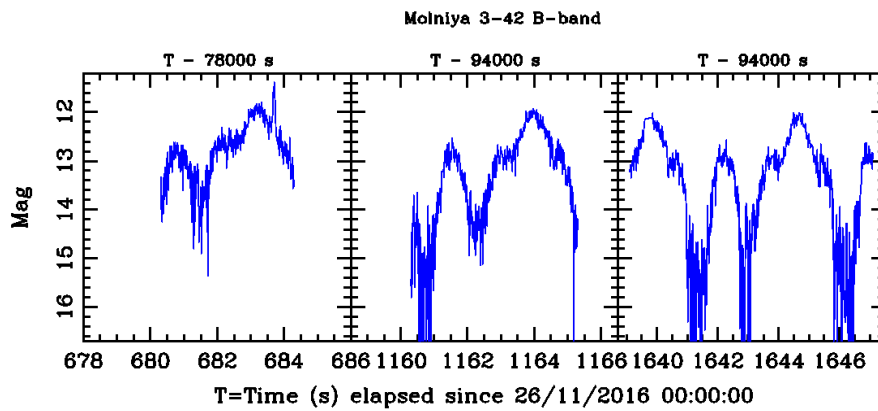


Figure A.138: Molniya 3-42 filter B light curves

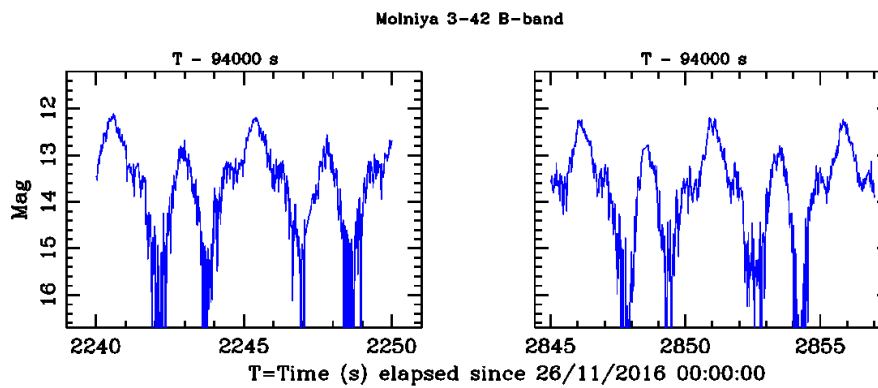


Figure A.139: Molniya 3-42 filter B light curves

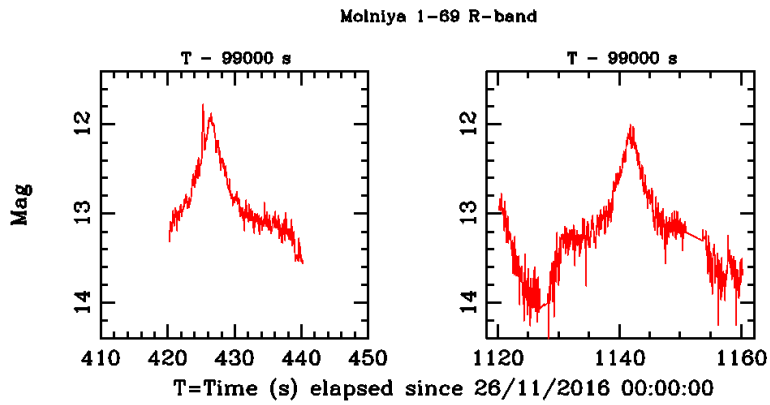


Figure A.140: Molniya 1-69 filter R light curves

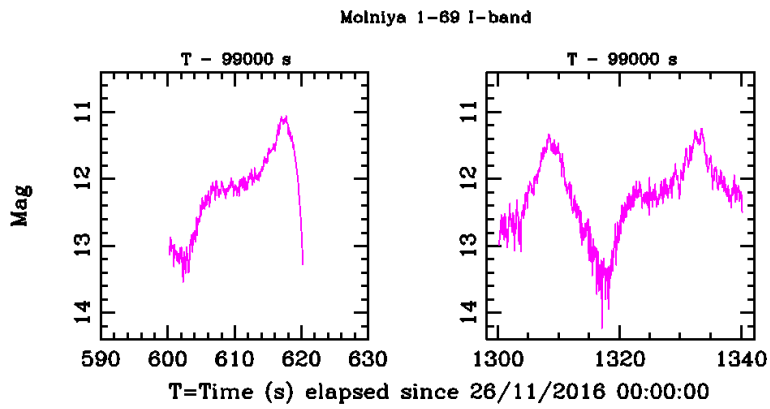


Figure A.141: Molniya 1-69 filter I light curves

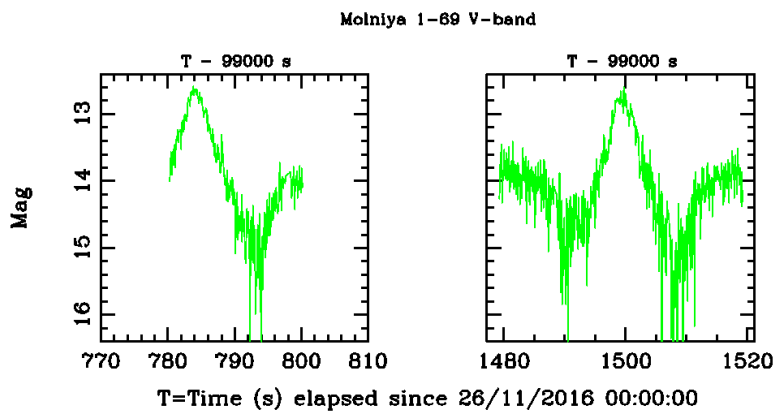


Figure A.142: Molniya 1-69 filter V light curves

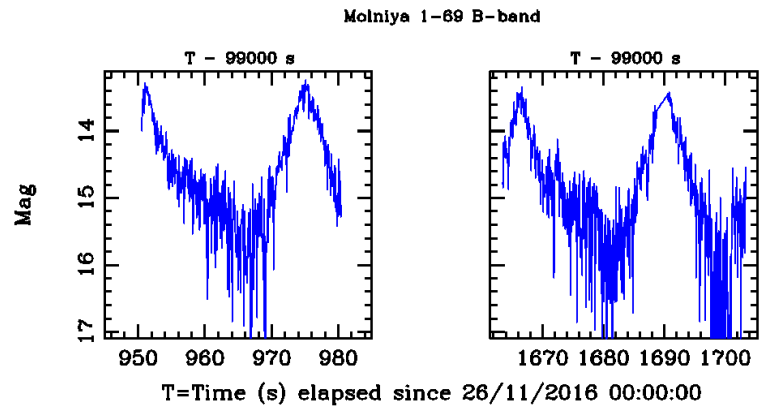


Figure A.143: Molniya 1-69 filter B light curves

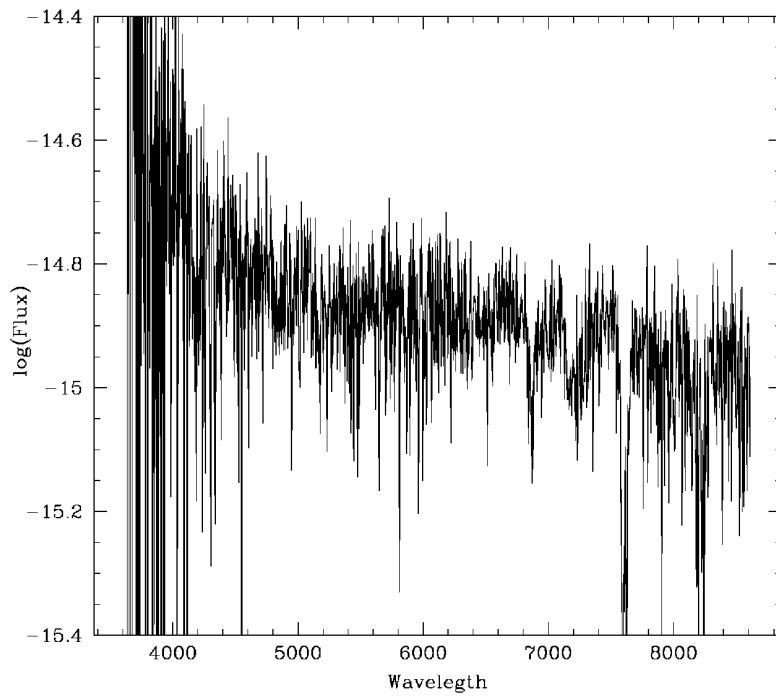
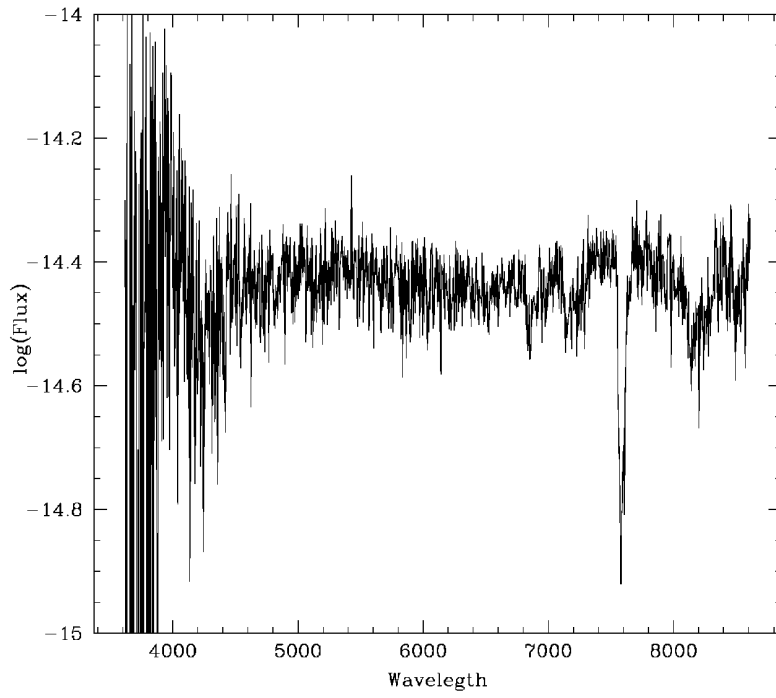


Figure A.144: Molniya 2-13 Spectra

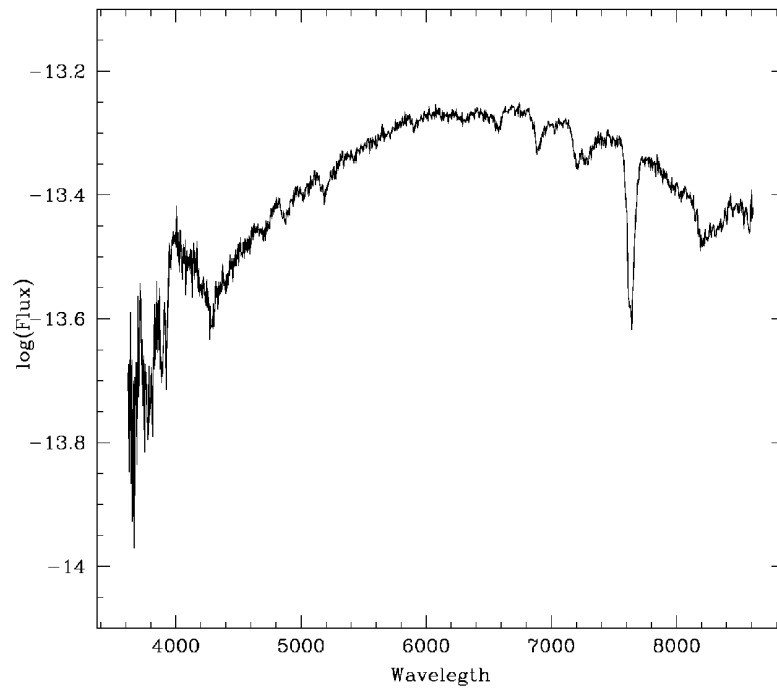
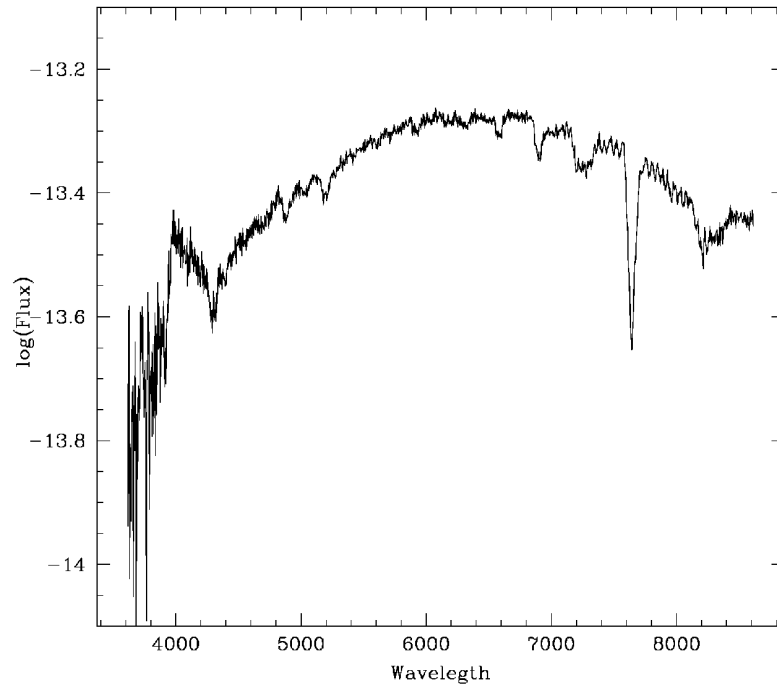


Figure A.145: Meridian 1 Spectra

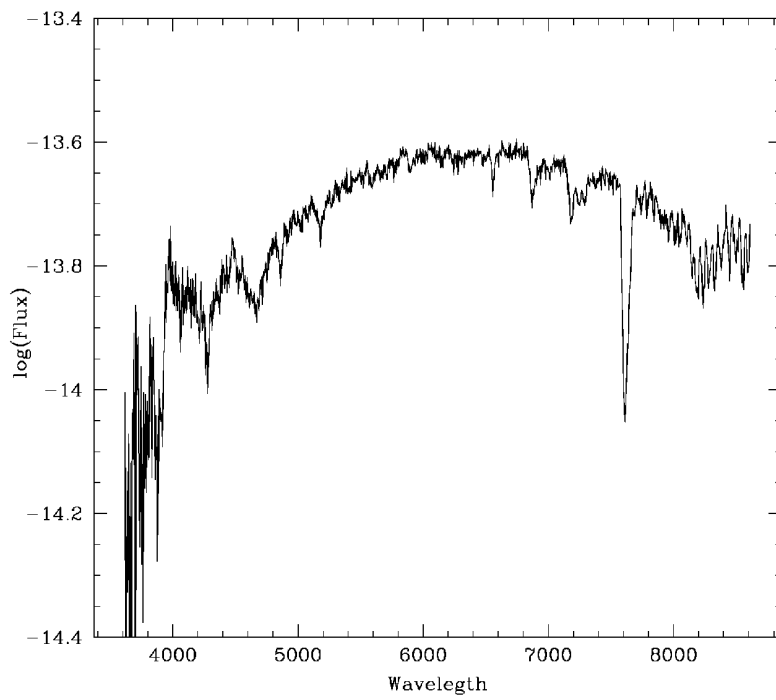
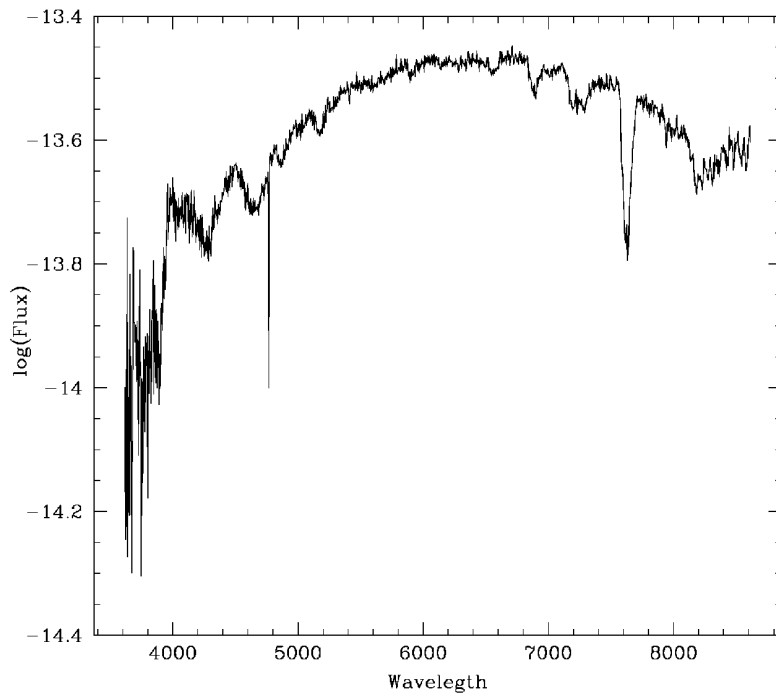


Figure A.146: Molniya 3-42 Spectra

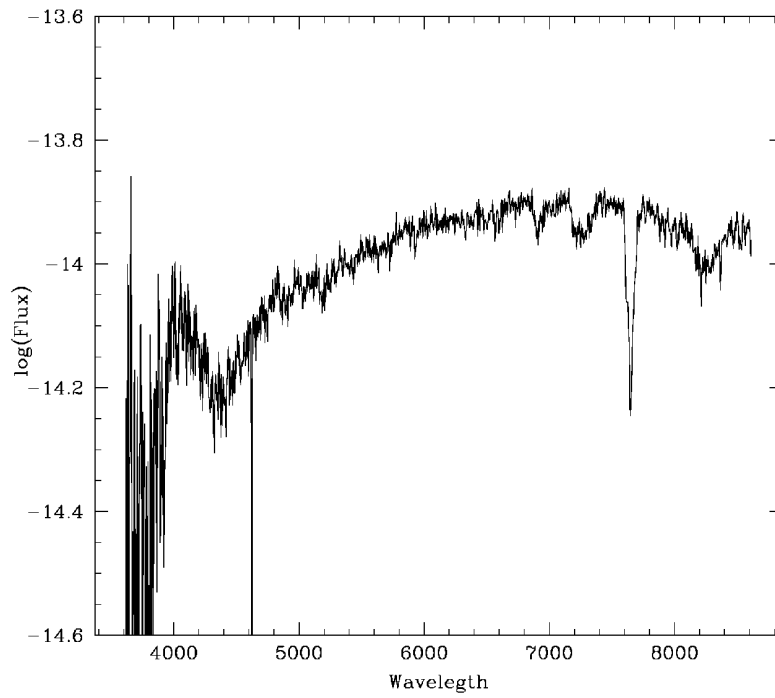
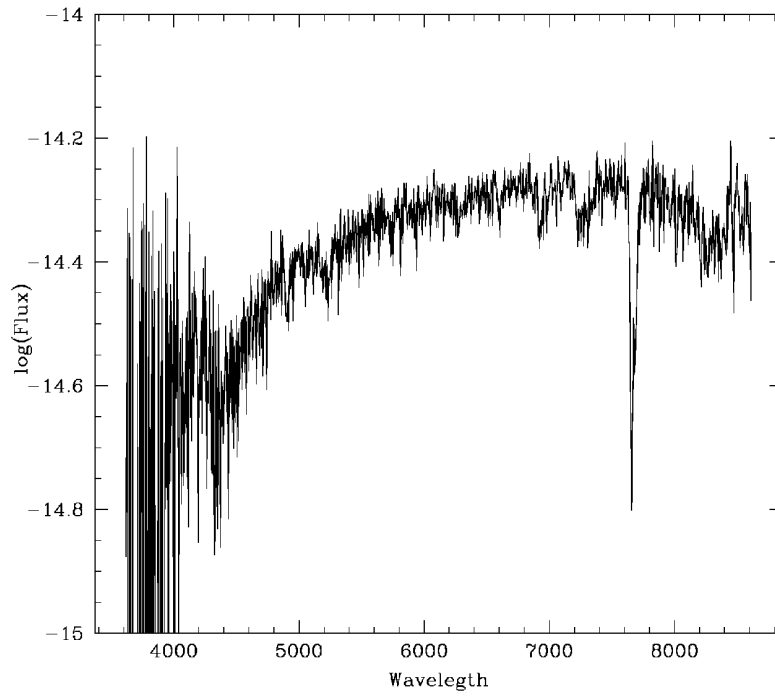


Figure A.147: Molniya 1-69 Spectra

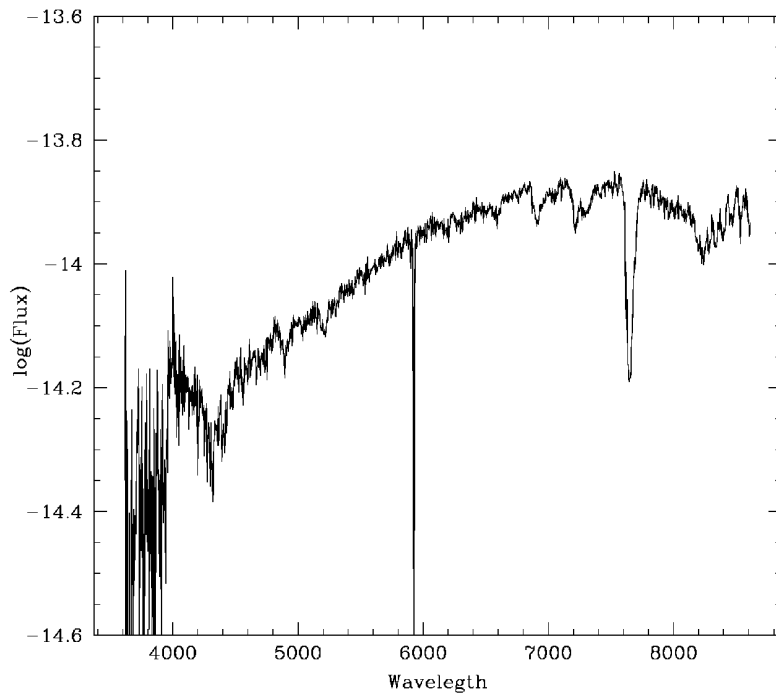


Figure A.148: Molniya 2-10 Spectra

A.6 Night 2016/12/22-23

- Seeing 1.6"
- Clear photometric sky
- Operator: Roberto Gualandi
- JD:2457744.5

UT(start)	Object	Airmass	Exptime(s)	Filter/Grism	Mag	Phase Angle
18:21:59	Molniya 1-87	2	1.12	R	10.60	84.07
18:29:58	Molniya 1-87	3	1.04	R	10.74	75.47
18:32:58	Molniya 1-87	4	1.03	R	10.30	72.94
18:35:57	Molniya 1-87	5	1.02	R	11.63	70.7
18:38:57	Molniya 1-87	5	1.01	R	11.29	68.71
18:41:58	Molniya 1-87	5	1.01	R	11.30	66.92
18:44:58	Molniya 1-87	5	1.01	B	11.60	65.31
18:47:58	Molniya 1-87	5	1.01	V	11.90	63.85
18:49:58	Molniya 1-87	7	1.01	R	12.21	62.96
18:51:57	Molniya 1-87	7	1.01	I	10.35	62.11
18:53:58	Molniya 1-87	7	1.01	B	14.67	61.31
18:55:59	Molniya 1-87	7	1.01	V	12.29	60.57
18:57:58	Molniya 1-87	7	1.01	R	12.85	59.52
19:08:05	Molniya 1-87	7	1.02	I	10.25	56.82
19:42:28	Molniya 1-87	60	1.05	GR4		50.34
20:10:23	Molniya 1-87	60	1.07	GR4		47.23
20:15:18	Molniya 1-87	60	1.07	GR4		46.8
20:50:35	Molniya 3-13	60	1.40	GR4		37.77
20:54:01	Molniya 3-13	60	1.39	GR4		38.44
21:04:59	Molniya 3-13	10	1.38	R	13.16	40.04
21:07:58	Molniya 3-13	20	1.37	B	13.62	40.51
21:09:59	Molniya 3-13	20	1.37	V	10.68	40.82
21:33:57	Molniya 1-88	10	1.18	R	11.29	35.98
21:36:54	Molniya 1-88	15	1.18	B	12.97	35.81
21:38:54	Molniya 1-88	15	1.18	V	11.96	35.71
21:41:53	Molniya 1-88	15	1.18	R	11.29	35.57
21:43:53	Molniya 1-88	15	1.19	I	10.62	35.48
21:45:53	Molniya 1-88	15	1.19	B	12.96	35.41
21:48:53	Molniya 1-88	15	1.19	V	11.93	35.3
21:50:52	Molniya 1-88	15	1.19	R	11.31	35.24

Table A.17: Logbook 2016/12/22-23

UT(start)	Object	Airmass	Exptime(s)	Filter/Grism	Mag	Phase Angle
21:52:53	Molniya 1-88	15	1.19	I	10.62	35.18
21:55:52	Molniya 1-88	15	1.19	B	12.95	35.11
21:57:53	Molniya 1-88	15	1.19	V	11.98	35.08
21:59:52	Molniya 1-88	15	1.19	V	11.78	35.05
22:01:52	Molniya 1-88	15	1.19	R	11.29	35.02
22:03:52	Molniya 1-88	15	1.19	I	10.62	35.01
22:13:56	Molniya 1-88	60	1.19	GR4		35.03
22:30:46	Molniya 1-88	60	1.20	GR4		35.51
00:15:55	Meridian 2	20	1.03	R	10.56	37.27
00:18:55	Meridian 2	40	1.03	R	10.59	37.74
00:21:56	Meridian 2	40	1.03	B	12.07	38.21
00:24:01	Meridian 2	40	1.03	R	10.68	38.52
00:27:26	Meridian 2	40	1.03	V	11.29	39.35
00:29:55	Meridian 2	40	1.03	I	10.20	39.43
00:31:55	Meridian 2	40	1.03	B	12.17	39.74
00:33:56	Meridian 2	40	1.03	V	11.35	40.03
00:35:56	Meridian 2	40	1.04	R	10.80	40.33
00:38:03	Meridian 2	40	1.04	I	10.24	40.63
00:39:58	Meridian 2	40	1.04	B	12.26	40.92
00:41:57	Meridian 2	40	1.04	V	11.40	41.21
00:43:59	Meridian 2	40	1.04	R	10.87	41.5
00:47:58	Meridian 2	40	1.04	I	10.35	42.08
01:10:53	Meridian 2	60	1.05	GR4		45.28
01:13:00	Meridian 2	60	1.05	GR4		45.55
01:26:58	Molniya 3-3	10	1.57	R	13.58	84.35
01:34:54	Molniya 3-3	15	1.53	R	13.81	84.64
01:38:53	Molniya 3-3	15	1.51	R	13.62	84.79
01:41:54	Molniya 3-3	20	1.50	R	12.26	84.9
01:44:51	Molniya 3-3	30	1.49	R	13.77	85.01
01:48:51	Molniya 3-3	30	1.48	B	15.61	85.16
01:51:51	Molniya 3-3	30	1.47	V	14.65	85.23
01:54:51	Molniya 3-3	30	1.46	R	13.88	85.39
01:56:51	Molniya 3-3	30	1.45	I	12.86	85.46
01:58:51	Molniya 3-3	30	1.45	B	15.68	85.54
02:00:51	Molniya 3-3	30	1.44	V	14.71	85.61
02:02:50	Molniya 3-3	30	1.43	R	13.96	85.69
02:04:52	Molniya 3-3	30	1.43	I	12.98	85.76
02:06:51	Molniya 3-3	30	1.42	B	15.63	85.84
02:08:52	Molniya 3-3	30	1.42	V	14.71	85.87
02:10:52	Molniya 3-3	30	1.42	R	13.51	85.98

Table A.18: Logbook 2016/12/22-23

UT(start)	Object	Airmass	Exptime(s)	Filter/Grism	Mag	Phase Angle
02:12:51	Molniya 3-3	30	1.41	I	13.07	86.06
02:20:13	Molniya 3-3	60	1.39	GR4		86.32
02:24:14	Molniya 3-3	60	1.39	GR4		86.46
02:27:28	Molniya 3-3	60	1.38	GR4		86.6
02:48:57	Molniya 1-53	10	1.35	R	13.73	89.88
02:50:57	Molniya 1-53	20	1.35	R	13.92	89.9
02:52:54	Molniya 1-53	30	1.34	R	13.91	89.91
02:55:53	Molniya 1-53	30	1.34	R	13.92	89.93
02:57:54	Molniya 1-53	30	1.33	B	15.49	89.94
02:59:54	Molniya 1-53	30	1.33	V	14.76	89.95
03:01:54	Molniya 1-53	30	1.32	R	13.92	89.97
03:03:54	Molniya 1-53	30	1.32	I	12.19	89.98
03:05:54	Molniya 1-53	30	1.32	B	14.87	89.99
03:07:54	Molniya 1-53	30	1.31	V	14.73	90.01
03:09:54	Molniya 1-53	30	1.31	R	14.11	90.03
03:11:54	Molniya 1-53	30	1.30	I	13.08	90.04
03:17:49	Molniya 1-53	60	1.29	GR4		90.09
03:20:20	Molniya 1-53	60	1.29	GR4		90.12
03:22:33	Molniya 1-53	60	1.29	GR4		90.13
03:26:57	Meridian 4	20	1.49	R	12.31	99.59
03:29:58	Meridian 4	20	1.48	B	13.99	99.42
03:31:58	Meridian 4	20	1.47	V	13.10	99.3
03:33:58	Meridian 4	20	1.47	R	12.43	99.19
03:35:58	Meridian 4	20	1.46	I	11.83	99.08
03:37:56	Meridian 4	20	1.45	B	14.02	98.97
03:39:56	Meridian 4	20	1.45	V	13.29	98.86
03:41:55	Meridian 4	20	1.44	R	12.69	98.75
03:43:55	Meridian 4	20	1.44	I	11.99	98.65
03:49:13	Meridian 4	60	1.43	GR4		98.4
03:51:40	Meridian 4	60	1.42	GR4		98.25
03:54:00	Meridian 4	60	1.42	GR4		98.15

Table A.19: Logbook 2016/12/22-23

Object	V	B-V	V-R	V-I
PG0231051	16.105	-0.329	-0.162	-0.534
PG0231+051 A	12.772	0.71	0.405	0.799
PG0231+051 B	14.735	1.448	0.954	1.951
PG0231+051 C	13.702	0.671	0.399	0.783
PG0231+051 D	14.027	1.088	0.675	1.256
PG0231+051 E	13.804	0.667	0.39	0.757
PG1047+003	13.474	-0.29	-0.132	-0.295
PG1047+003 A	13.512	0.688	0.422	0.84
PG1047+003 B	14.751	0.679	0.391	0.764
PG1047+003 C	12.453	0.607	0.378	0.737

Table A.20: Standard stars magnitudes and color indexes from Landolt (1992)

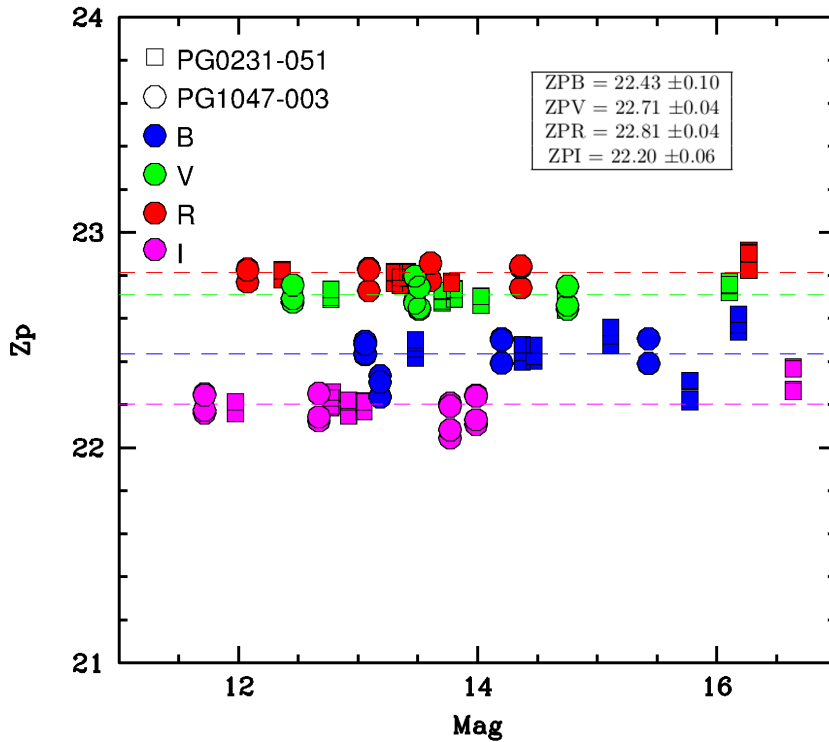


Figure A.149: Photometric zero points 2016/12/22-23-24, magnitudes from Landolt (1992)

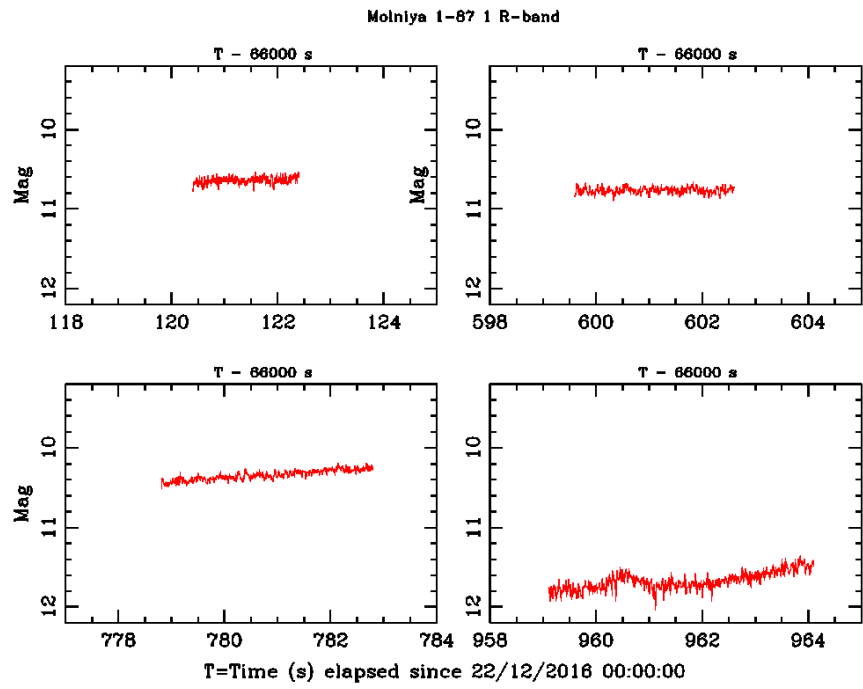


Figure A.150: Molniya 1-87 filter R light curves

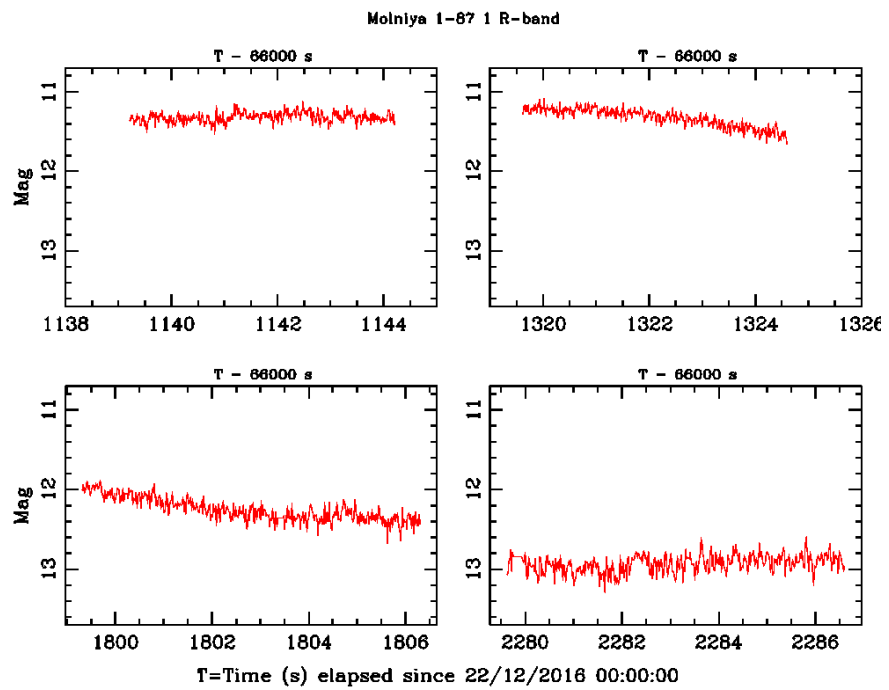


Figure A.151: Molniya 1-87 filter R light curves

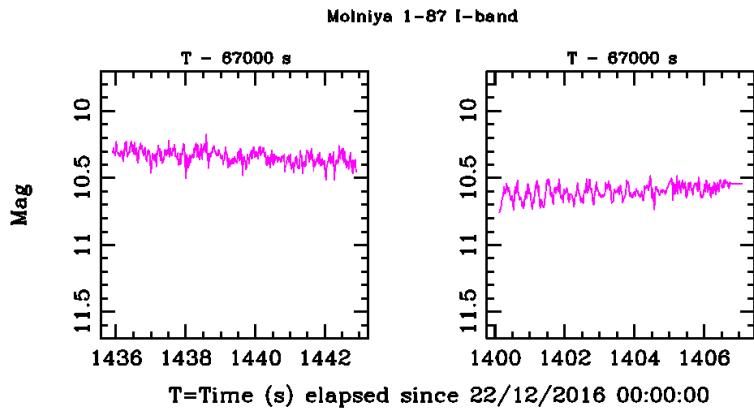


Figure A.152: Molniya 1-87 filter I light curves

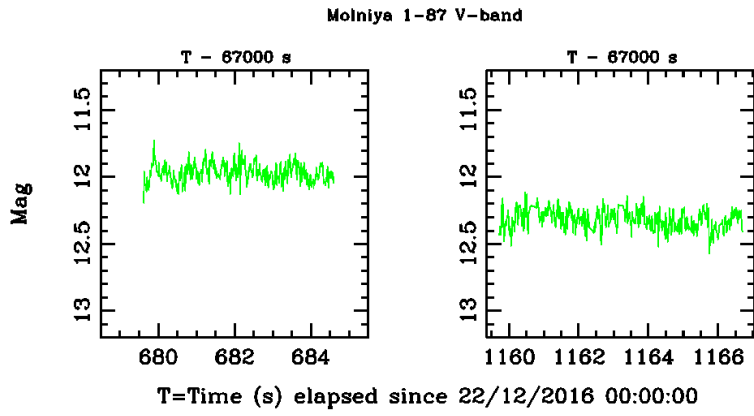


Figure A.153: Molniya 1-87 filter V light curves

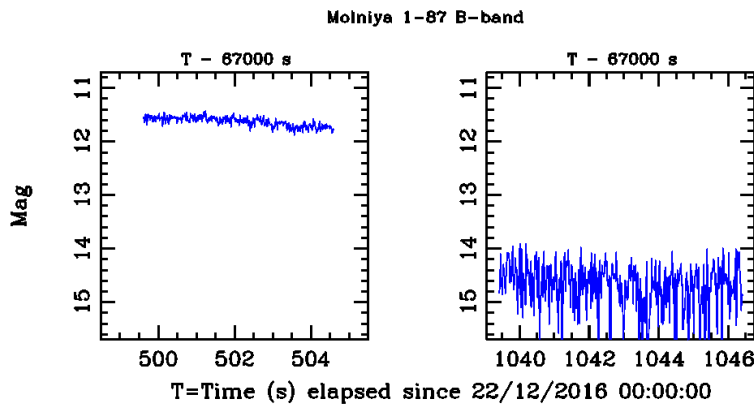


Figure A.154: Molniya 1-87 filter B light curves

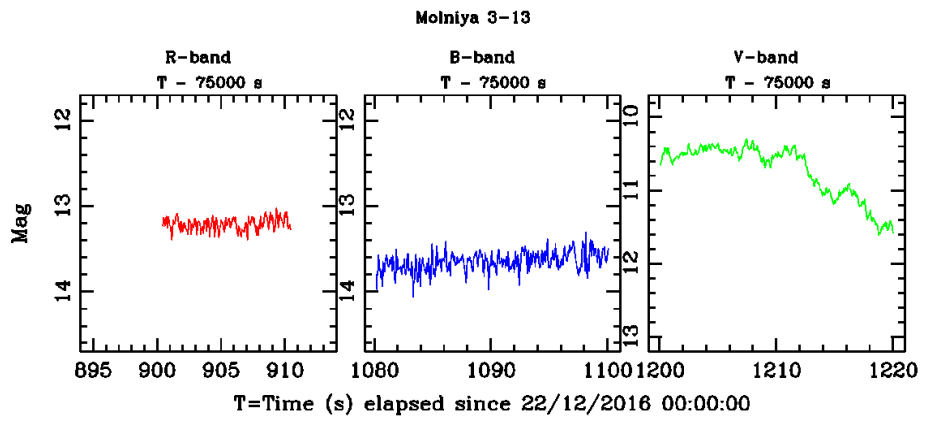


Figure A.155: Molniya 3-13 light curves

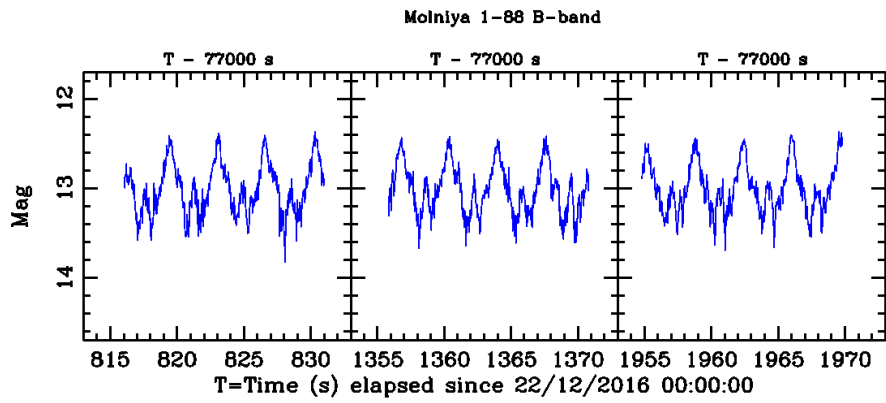


Figure A.156: Molniya 1-88 filter B light curves

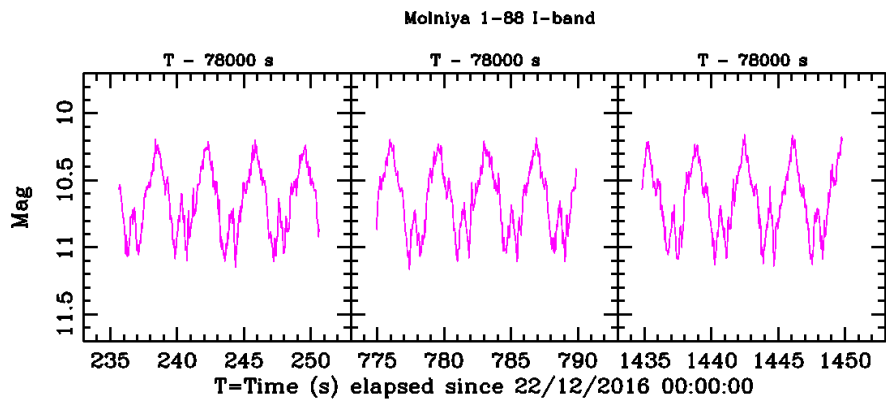


Figure A.157: Molniya 1-88 filter I light curves

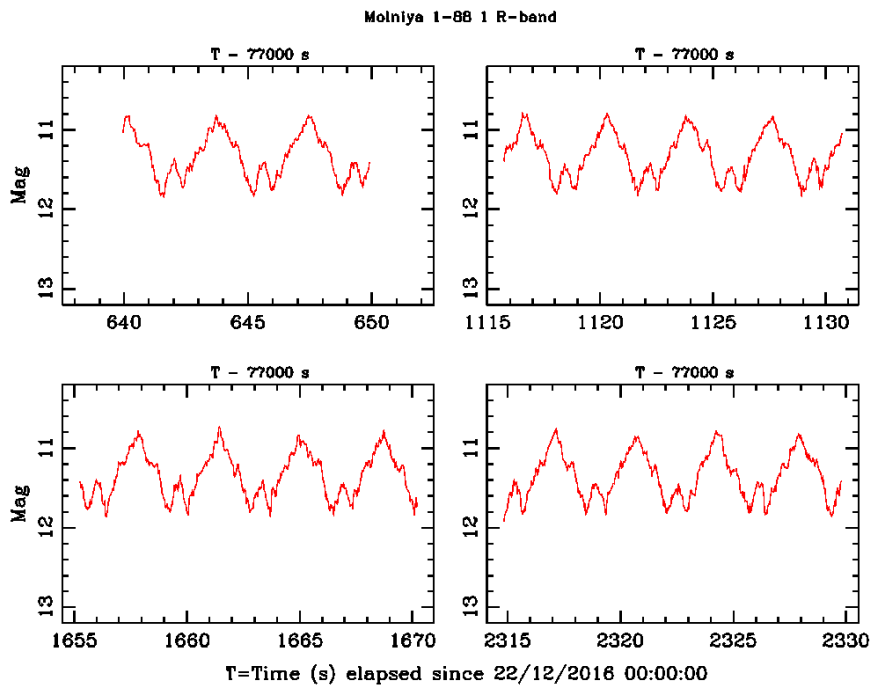


Figure A.158: Molniya 1-88 filter R light curves

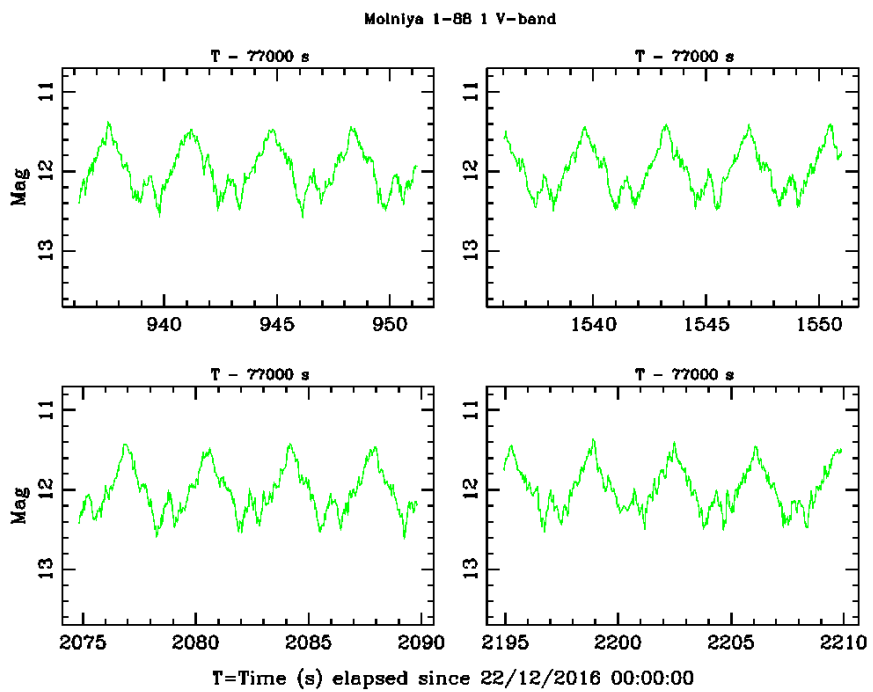


Figure A.159: Molniya 1-88 filter V light curves

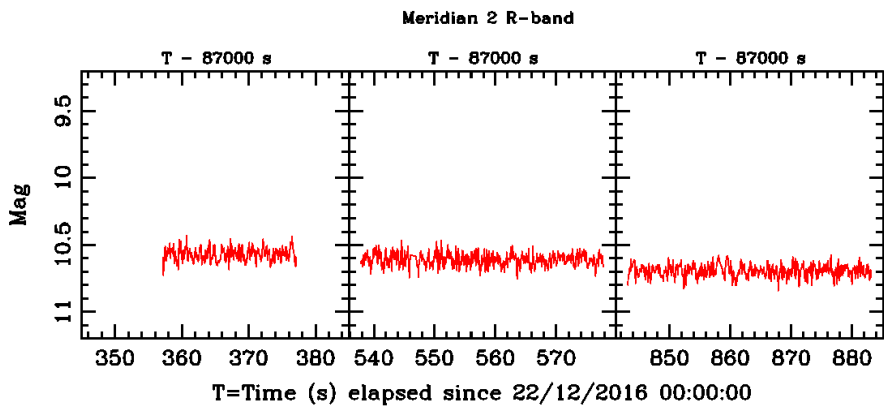


Figure A.160: Meridian 2 filter R light curves
che si discostavano di più di due

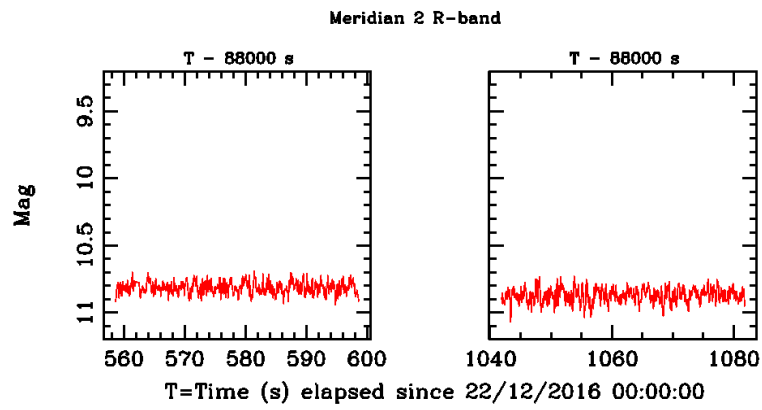


Figure A.161: Meridian 2 filter R light curves

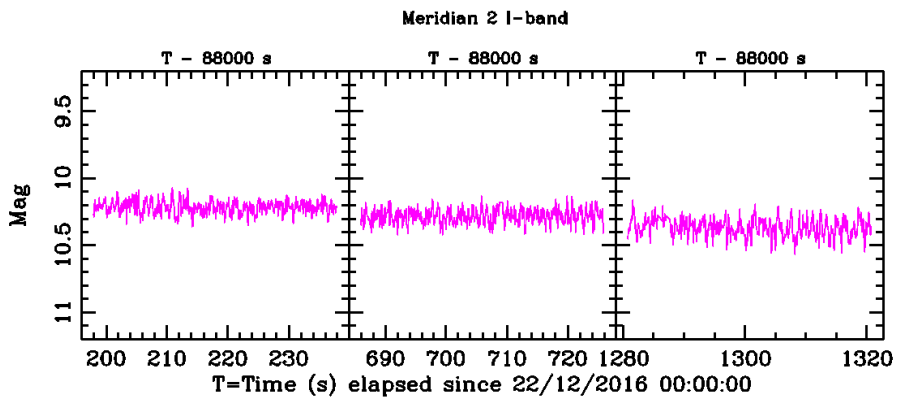


Figure A.162: Meridian 2 filter I light curves

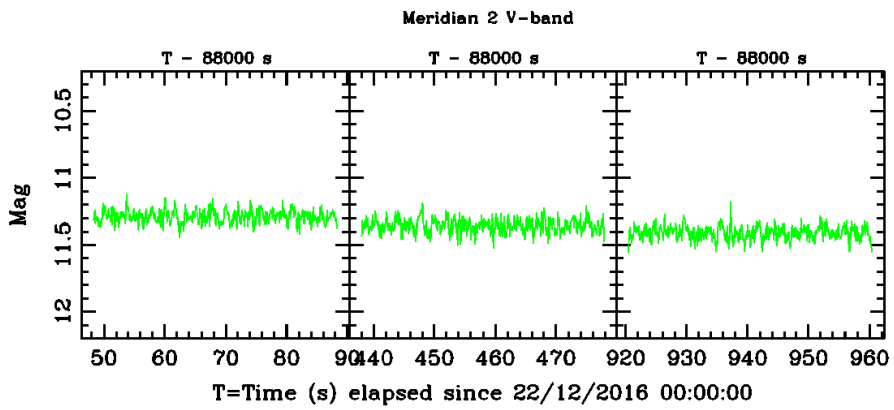


Figure A.163: Meridian 2 filter V light curves

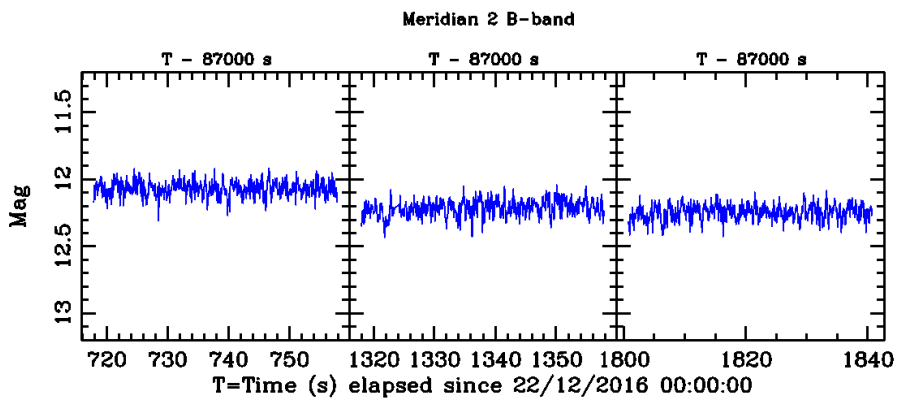


Figure A.164: Meridian 2 filter B light curves

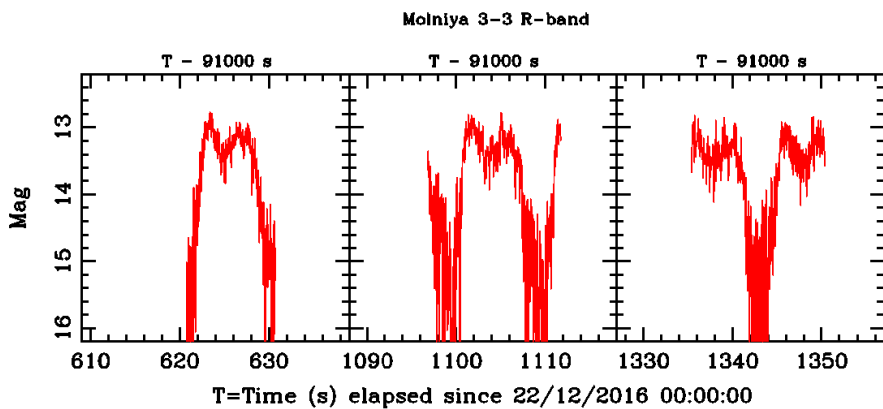


Figure A.165: Molniya 3-3 filter R light curves

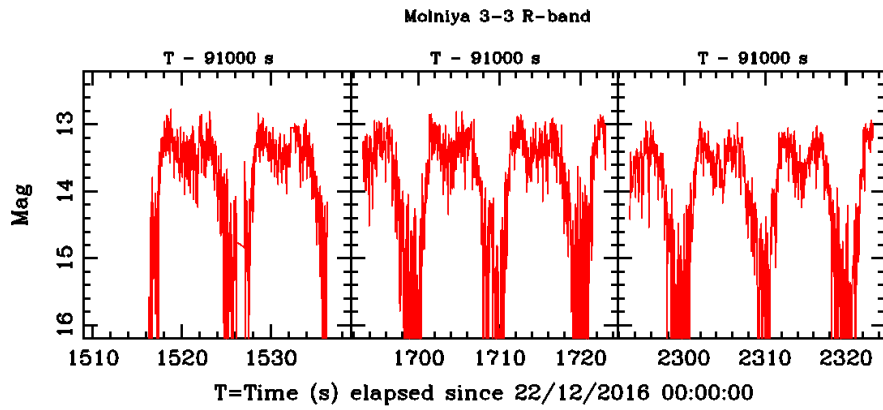


Figure A.166: Molniya 3-3 filter R light curves
che si discostavano di più di due

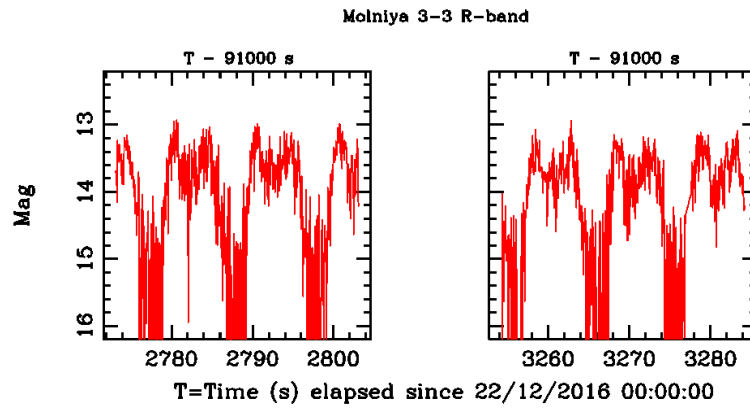


Figure A.167: Molniya 3-3 filter R light curves

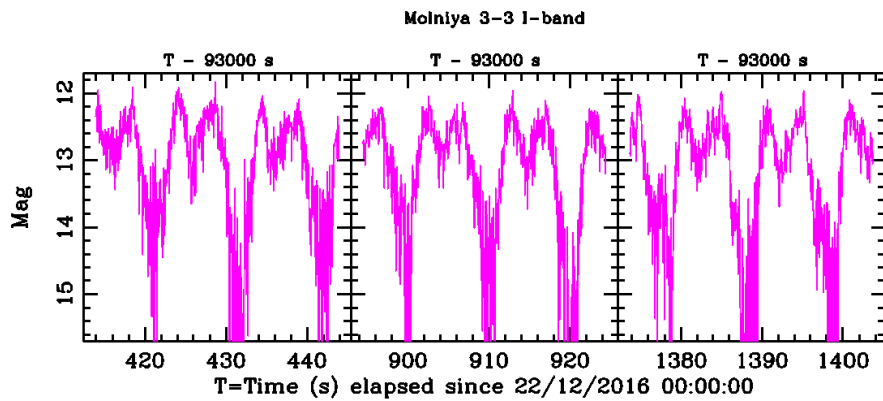


Figure A.168: Molniya 3-3 filter I light curves

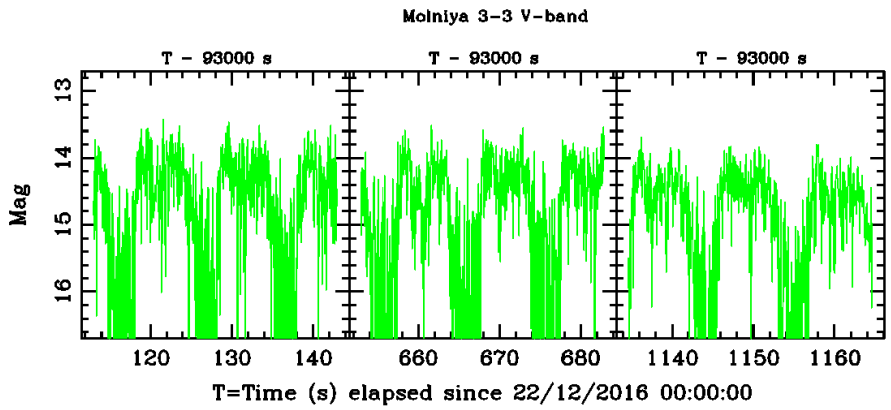


Figure A.169: Molniya 3-3 filter V light curves

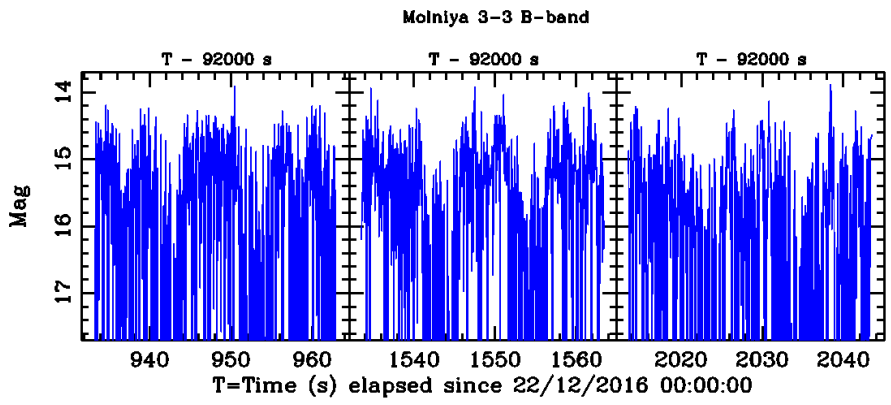


Figure A.170: Molniya 3-3 filter B light curves

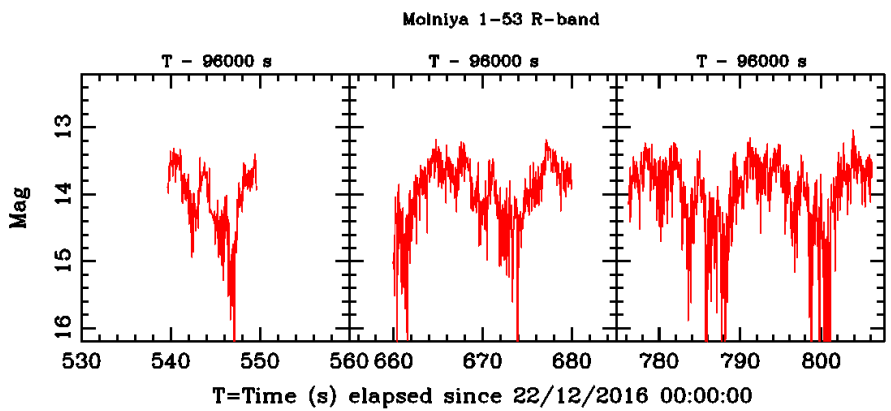


Figure A.171: Molniya 1-53 filter R light curves

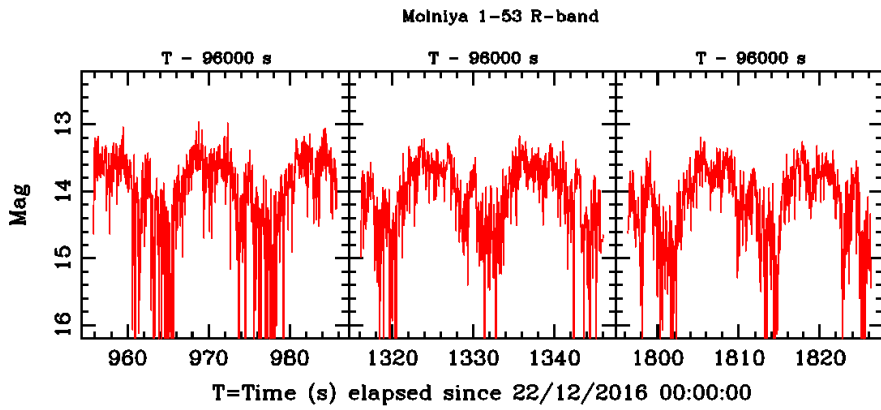


Figure A.172: Molniya 1-53 filter R light curves

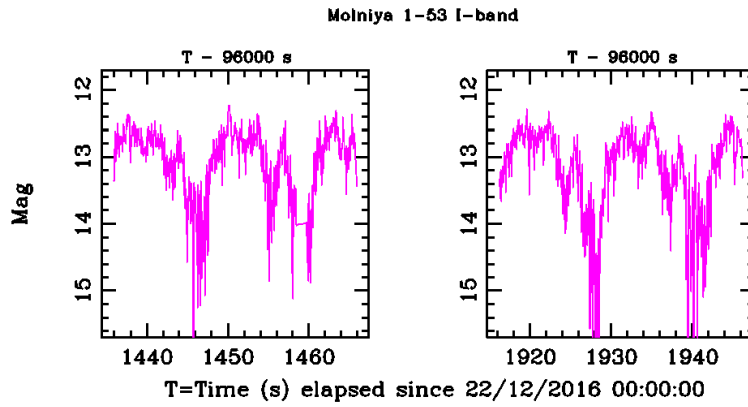


Figure A.173: Molniya 1-53 filter I light curves

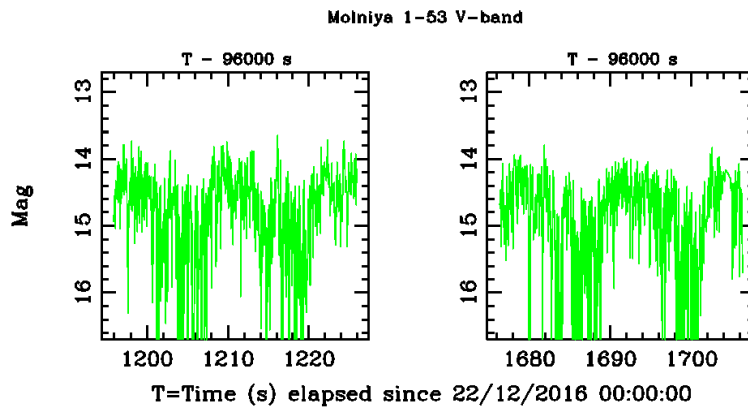


Figure A.174: Molniya 1-53 filter V light curves

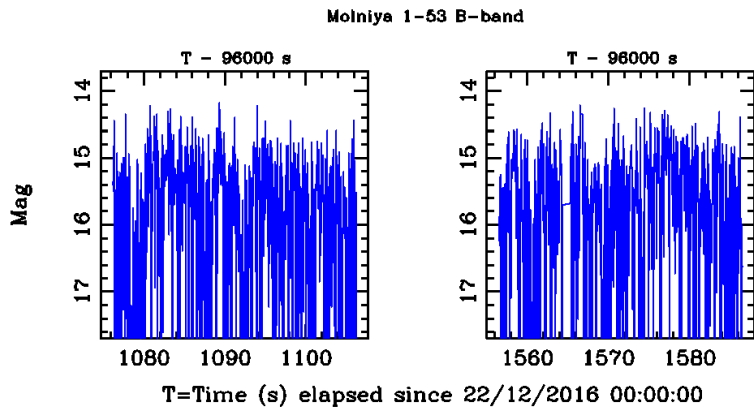


Figure A.175: Molniya 1-53 filter B light curves

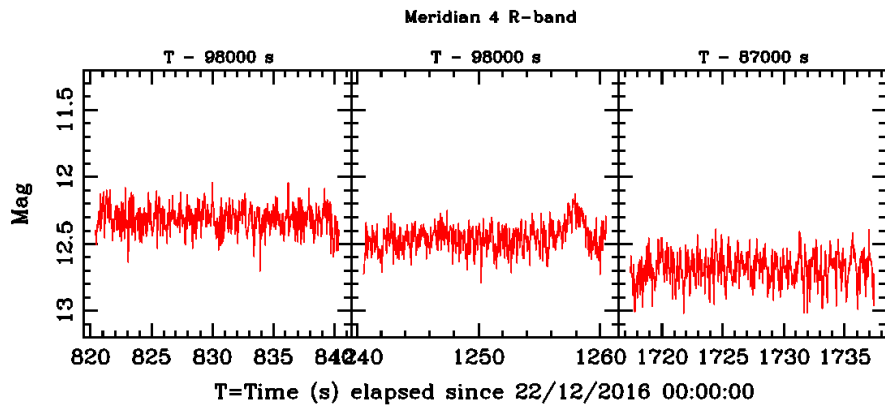


Figure A.176: Meridian 4 filter R light curves

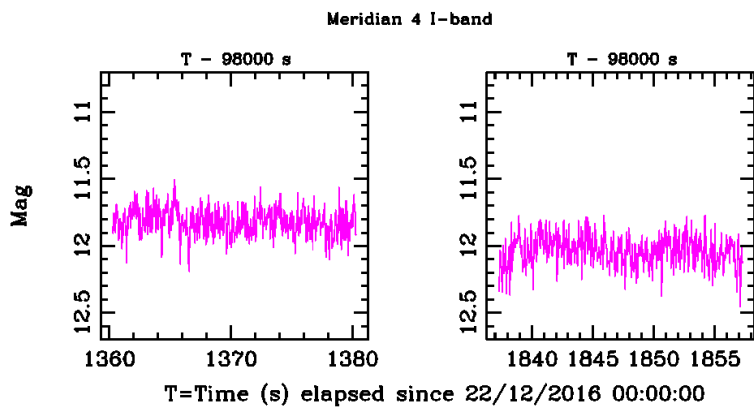


Figure A.177: Meridian 4 filter I light curves

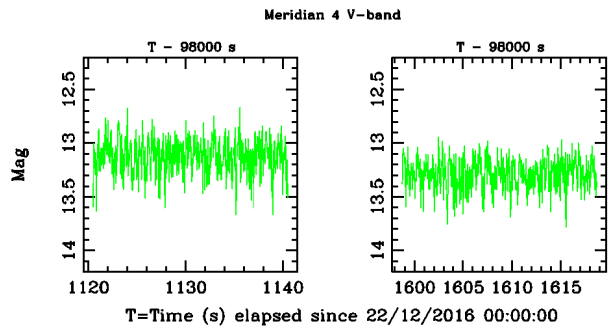


Figure A.178: Meridian 4 filter V light curves

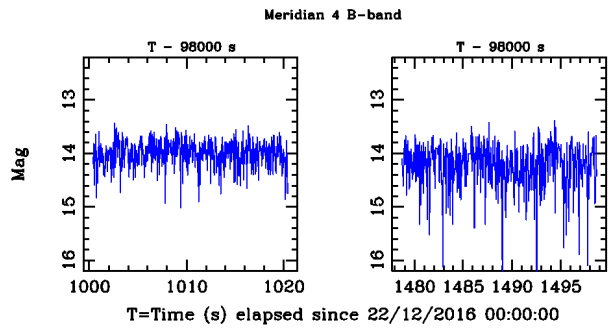


Figure A.179: Meridian 4 filter B light curves

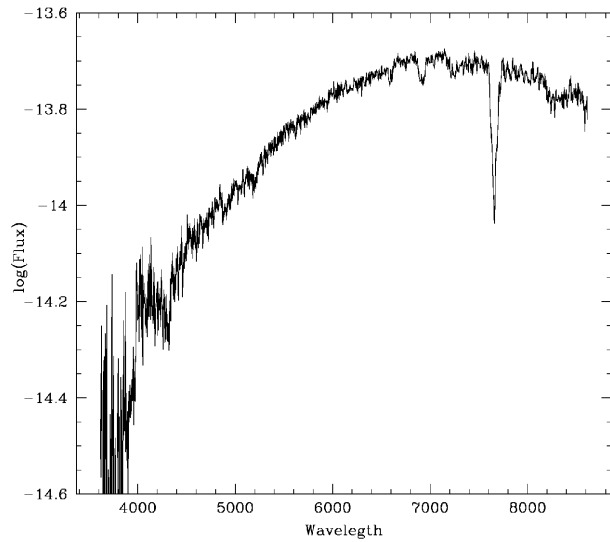


Figure A.180: Molniya 1-87 Spectra

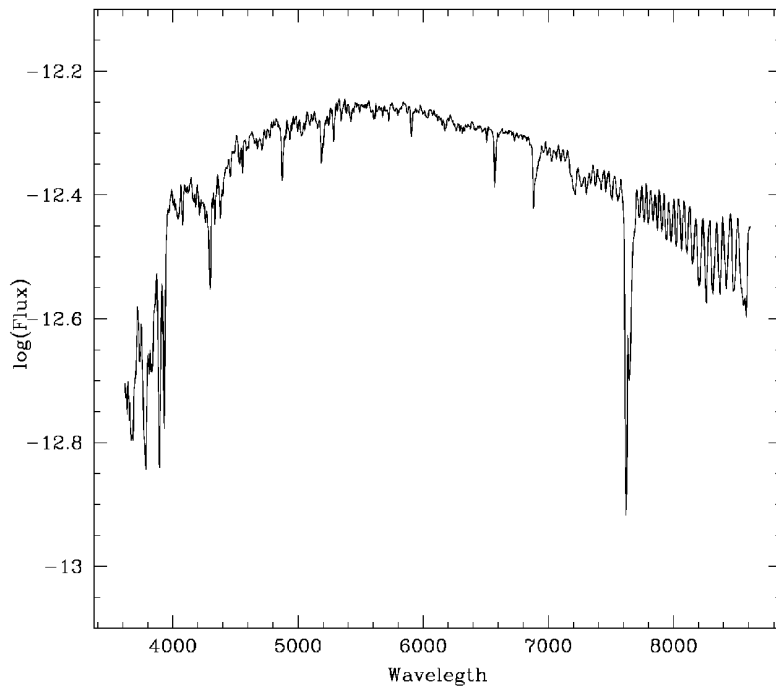
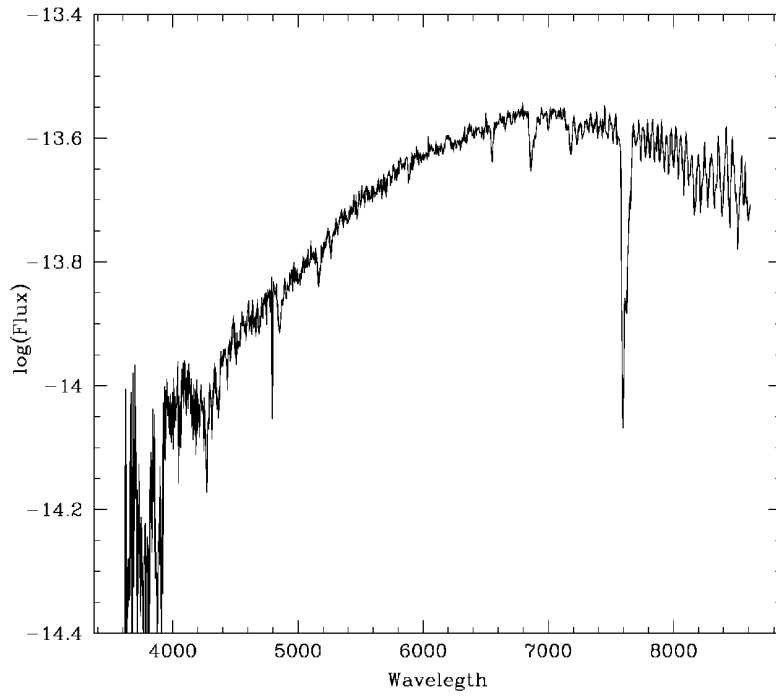


Figure A.181: Molniya 1-87 Spectra

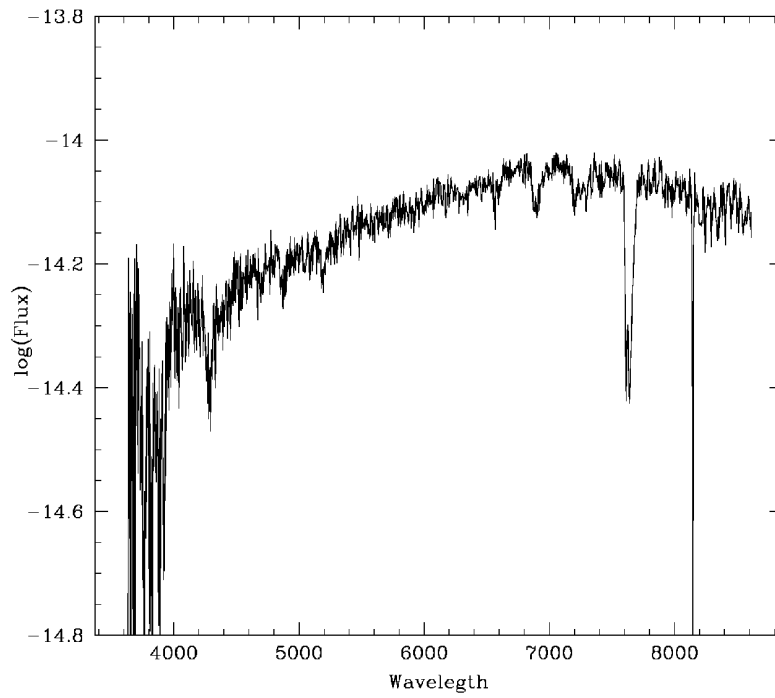
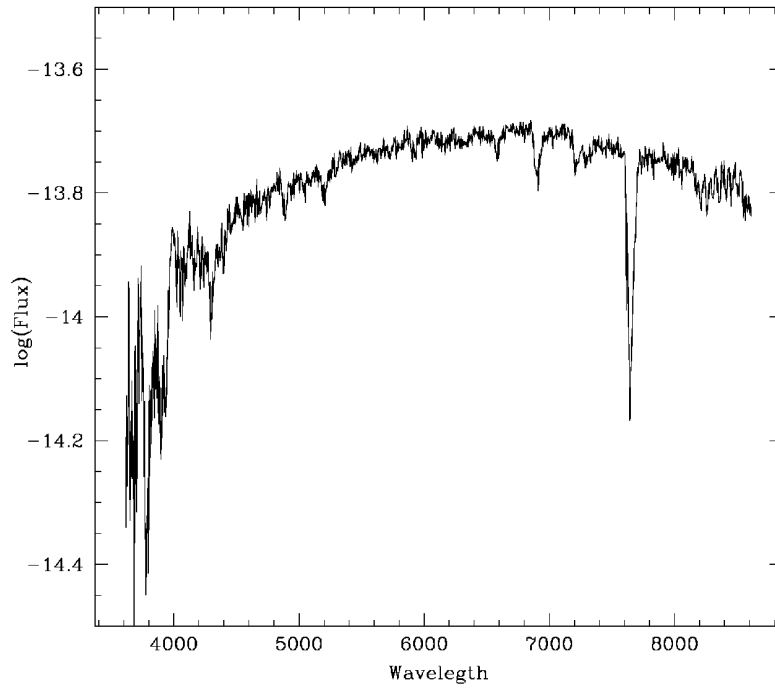


Figure A.182: Molniya 3-13 Spectra

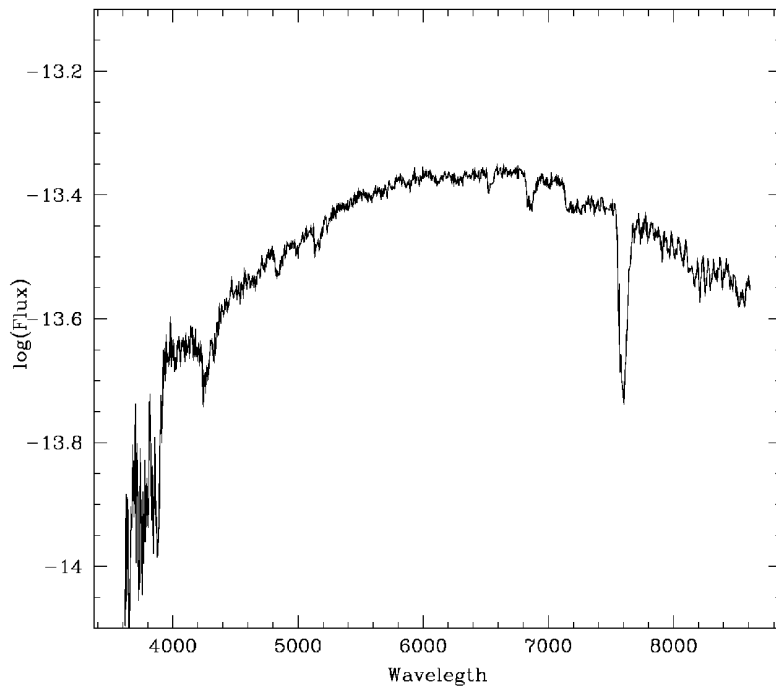
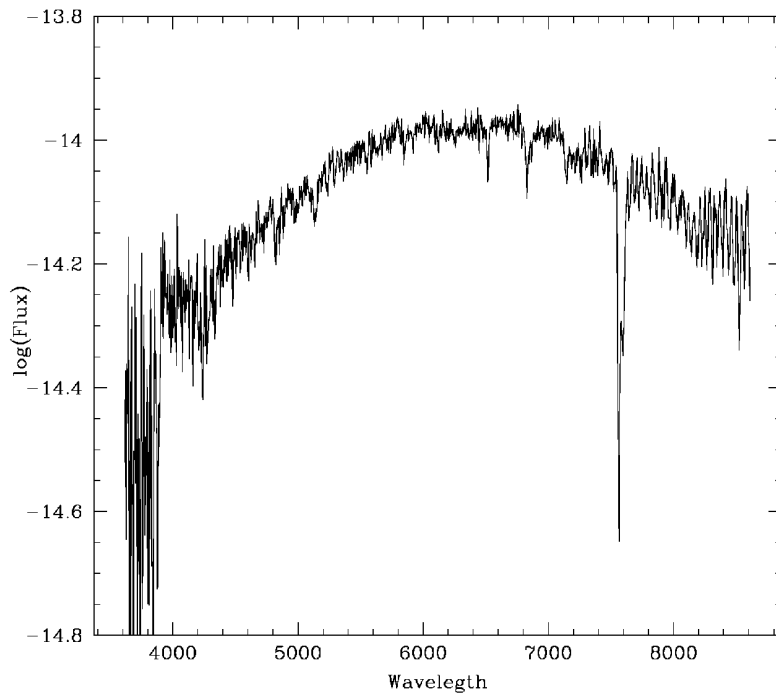


Figure A.183: Molniya 1-88 Spectra

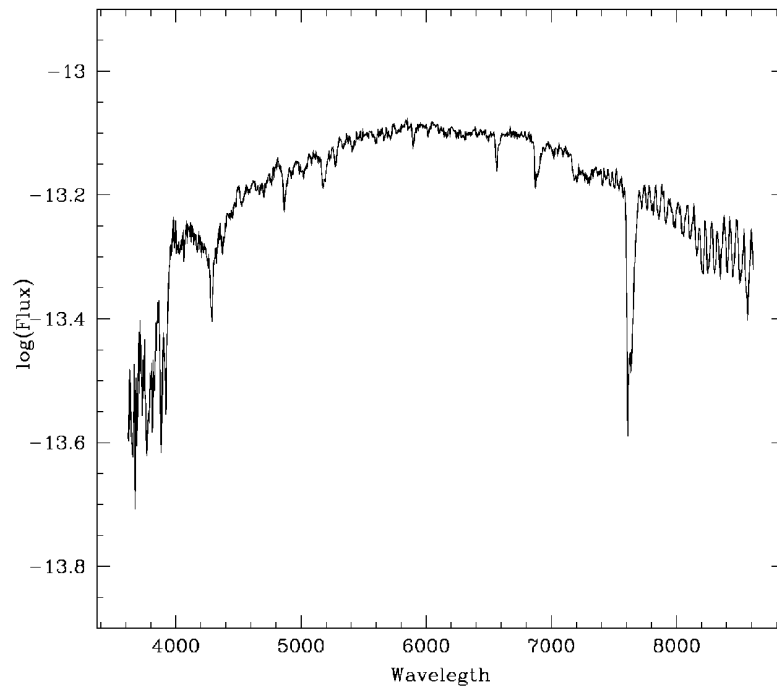
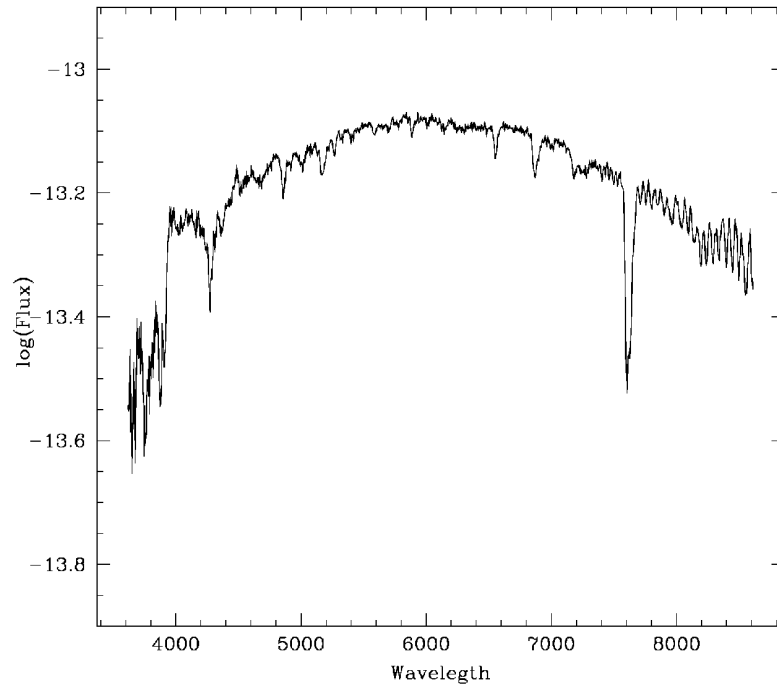


Figure A.184: Meridian 2 Spectra

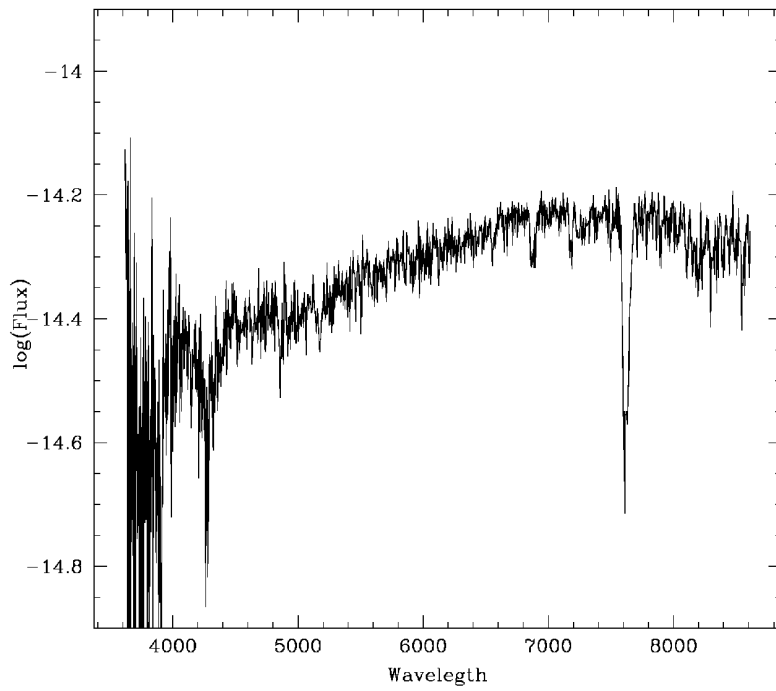
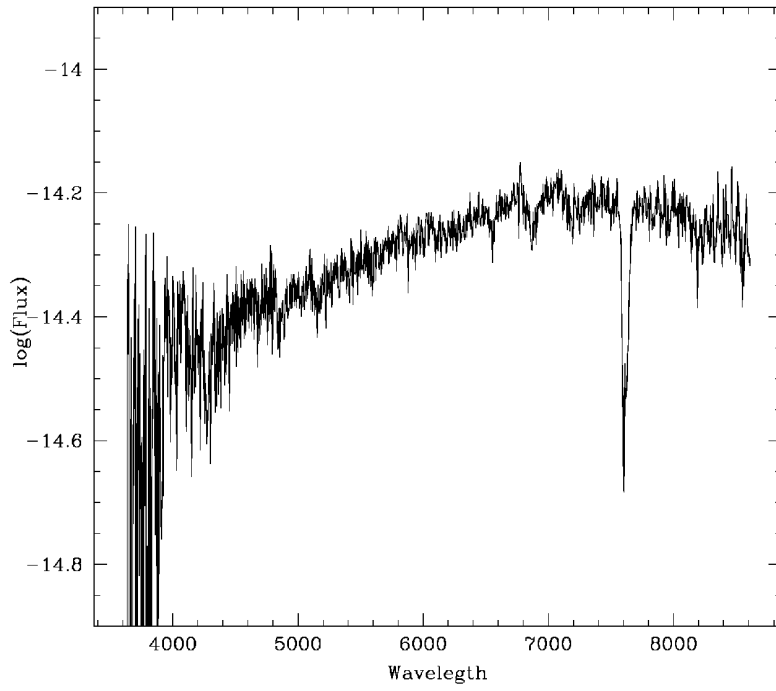


Figure A.185: Molniya 1-53 Spectra

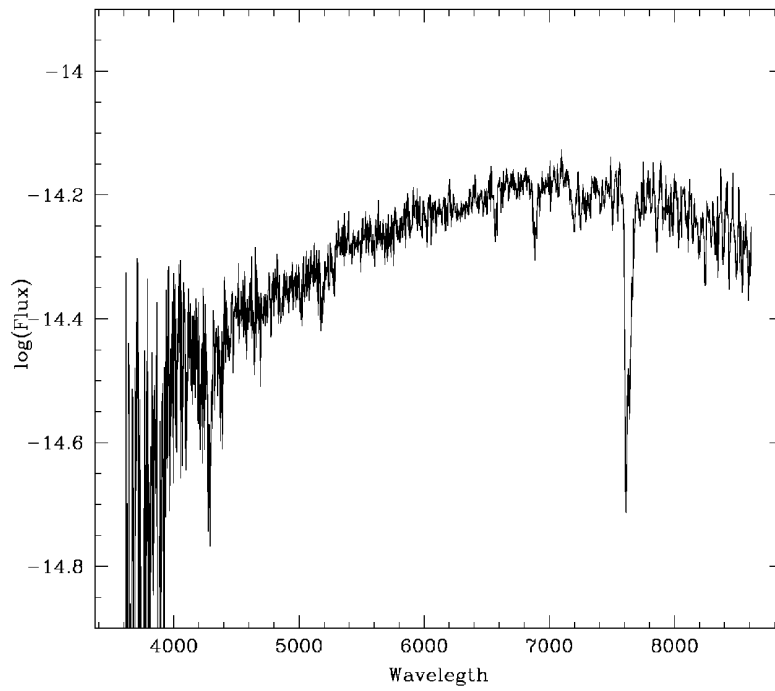
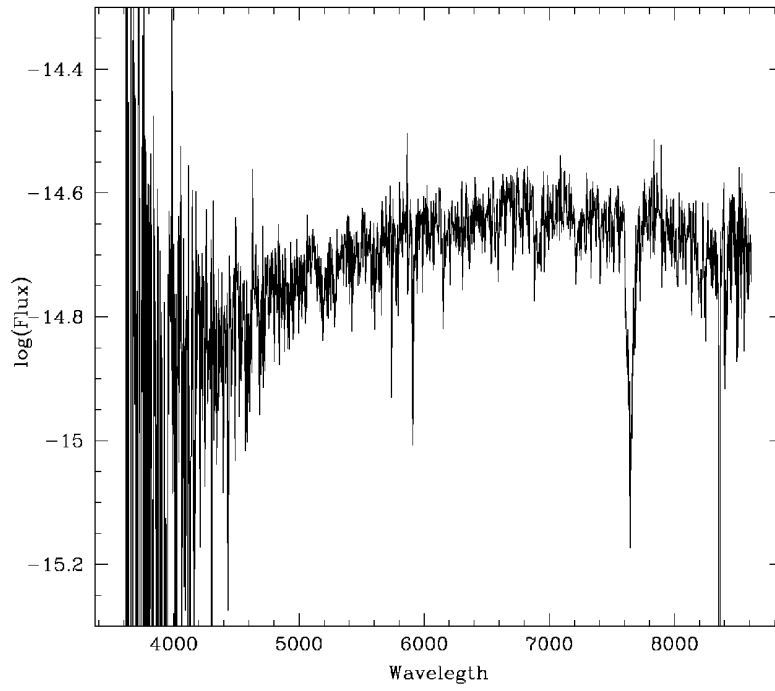


Figure A.186: Molniya 3-3 Spectra

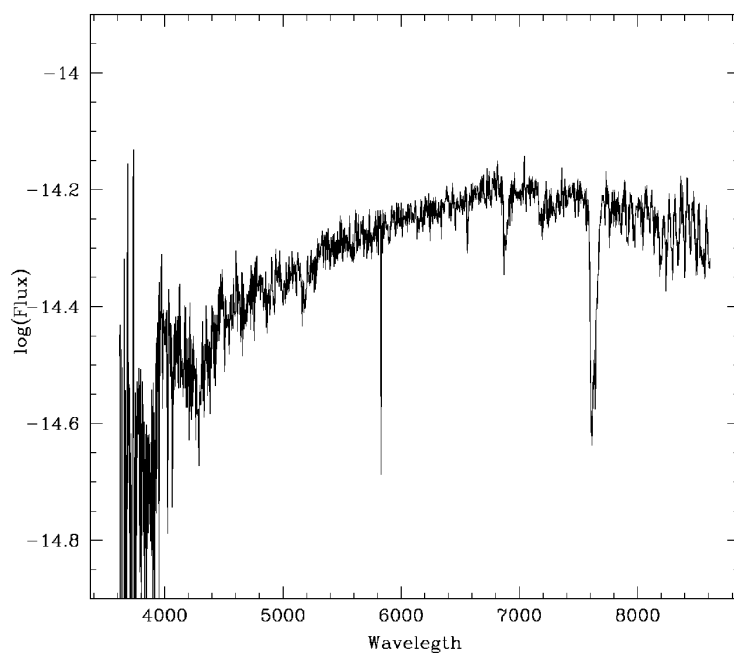


Figure A.187: Molniya 3-3 Spectra

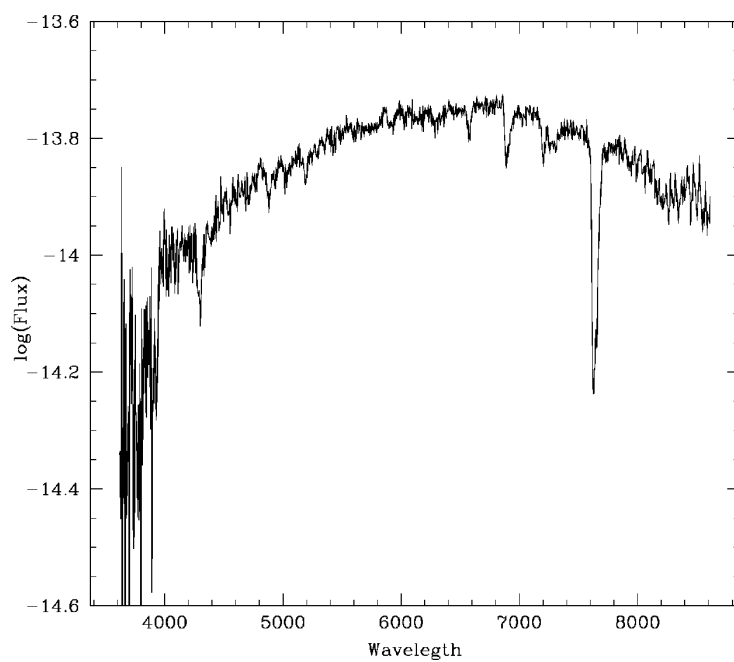


Figure A.188: Meridian 4 Spectra

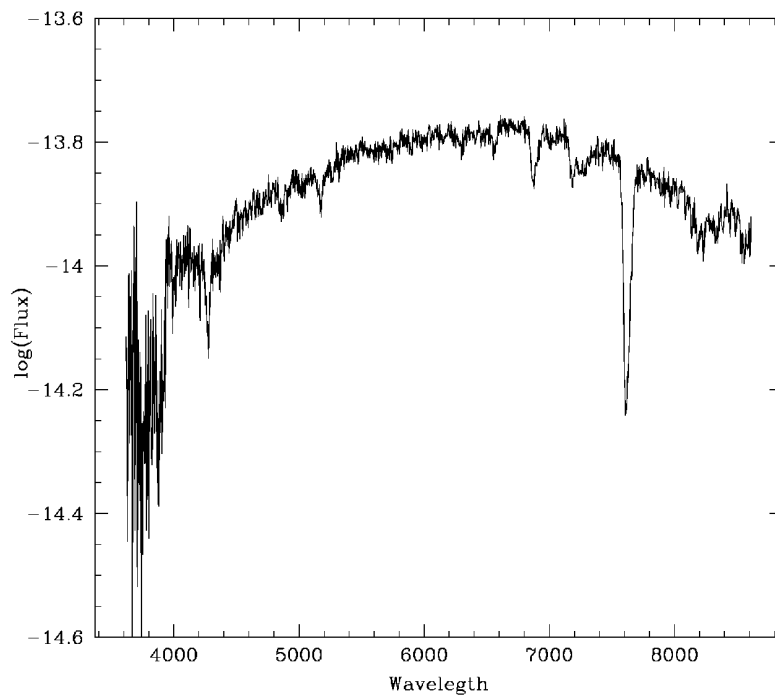
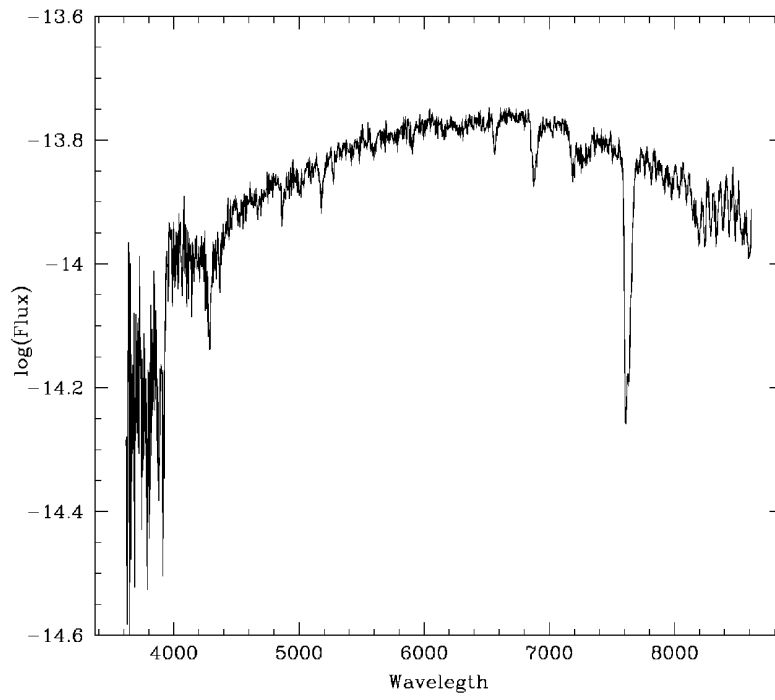


Figure A.189: Meridian 4 Spectra

A.7 Night 2016/12/23-24

- Seeing 1.3"
- Clear photometric sky
- Operator: Roberto Gualandi
- JD:2457745.5

UT(start)	Object	Airmass	Exptime(s)	Filter/Grism	Mag	Phase Angle
18:31:54	Molniya 3-8	20	1.54	R	11.90	17.55
18:37:54	Molniya 3-8	20	1.58	B	13.39	15.44
22:40:44	Molnja 171	60	1.51	GR4		
22:44:20	Molnja 171	60	1.52	GR4		
22:54:59	Molniya 1-90	120	1.13	GR4		48.24
23:07:53	Molniya 1-90	10	1.11	R	10.85	45.63
23:10:44	Molniya 1-90	30	1.11	R	11.04	45.05
23:14:39	Molniya 1-90	30	1.10	R	11.69	44.28
23:17:43	Molniya 1-90	30	1.10	R	11.45	43.72
23:20:39	Molniya 1-90	30	1.09	R	11.06	43.16
23:23:39	Molniya 1-90	30	1.09	B	12.28	42.61
23:26:40	Molniya 1-90	30	1.09	V	12.08	42.06
23:30:39	Molniya 1-90	30	1.08	R	11.56	41.34
23:33:40	Molniya 1-90	30	1.08	I	10.62	40.8
23:36:40	Molniya 1-90	30	1.08	B	11.75	40.27
23:40:40	Molniya 1-90	30	1.07	V	12.96	39.57
23:43:39	Molniya 1-90	30	1.07	R	11.93	39.04
23:46:40	Molniya 1-90	30	1.07	I	10.62	38.53
03:15:47	Molniya 1-63	20	1.82	R	11.31	41.34
03:18:24	Molniya 1-63	30	1.81	R	11.18	41.23
03:21:24	Molniya 1-63	30	1.81	R	11.14	41.06
03:24:23	Molniya 1-63	30	1.80	B	12.38	40.9
03:26:24	Molniya 1-63	30	1.79	V	11.60	40.8
03:28:24	Molniya 1-63	30	1.79	R	11.17	40.7
03:30:24	Molniya 1-63	30	1.78	I	10.37	40.61
03:43:24	Molniya 1-63	60	1.76	GR4		40.04
03:52:43	Molniya 1-63	60	1.74	GR4		39.67
03:55:16	Molniya 1-63	60	1.73	GR4		39.6

Table A.21: Logbook 2016/12/23-24

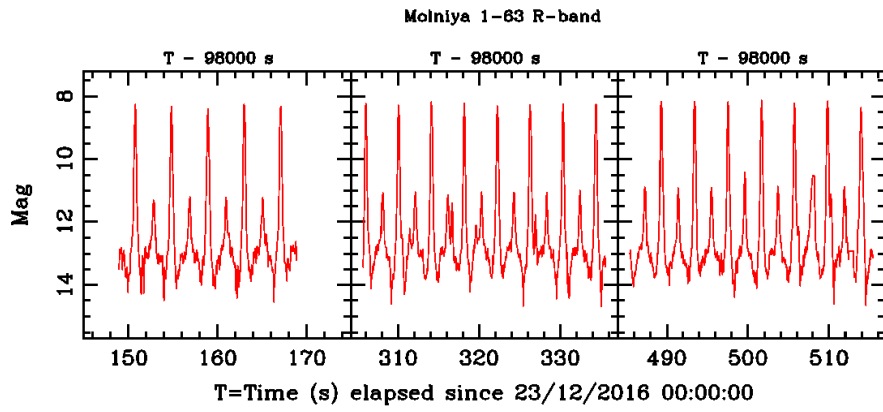


Figure A.190: Molniya 1-63 filter R light curves

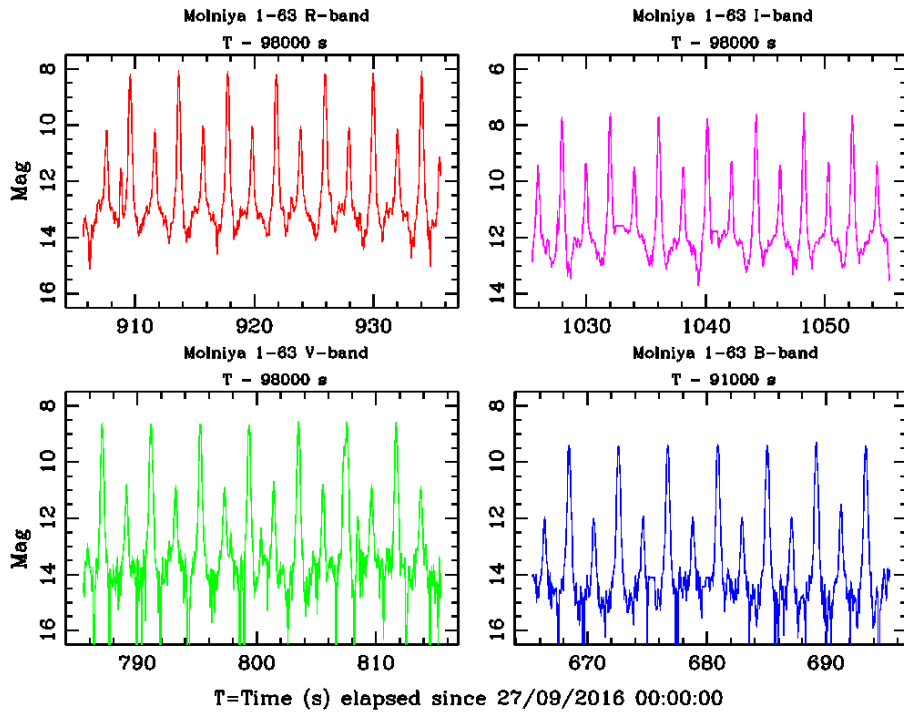


Figure A.191: Molniya 1-63 light curves

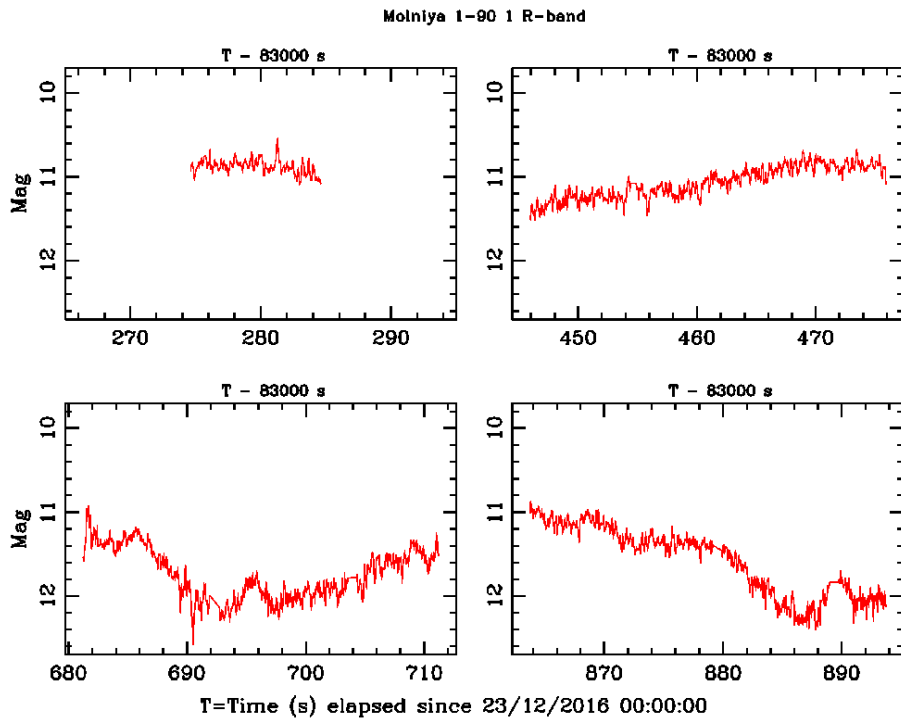


Figure A.192: Molniya 1-90 filter R light curves

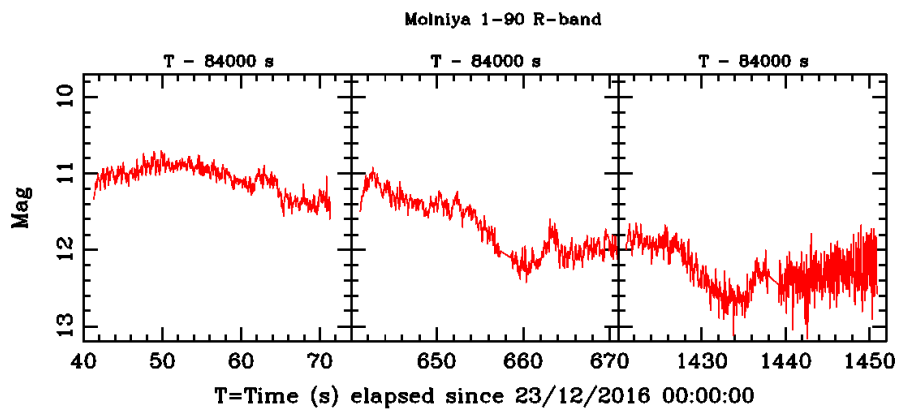


Figure A.193: Molniya 1-90 filter R light curves

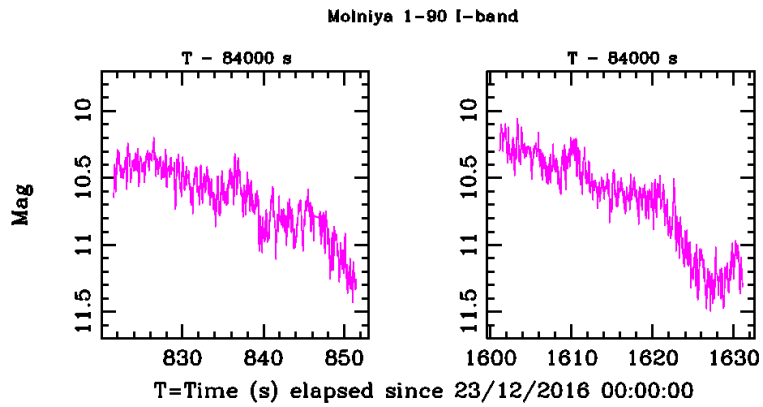


Figure A.194: Molniya 1-90 filter I light curves

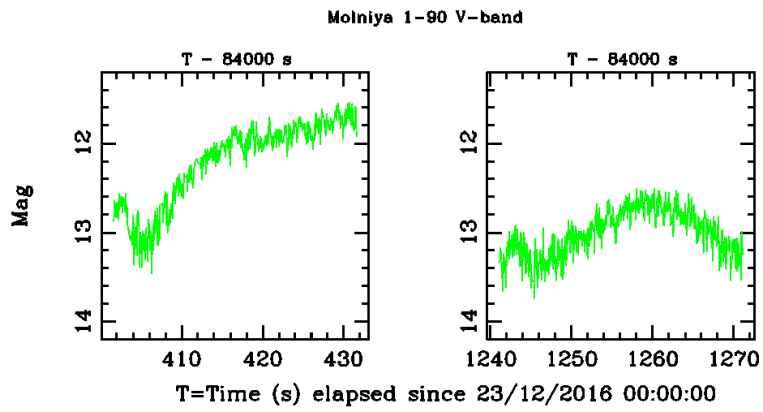


Figure A.195: Molniya 1-90 filter V light curves

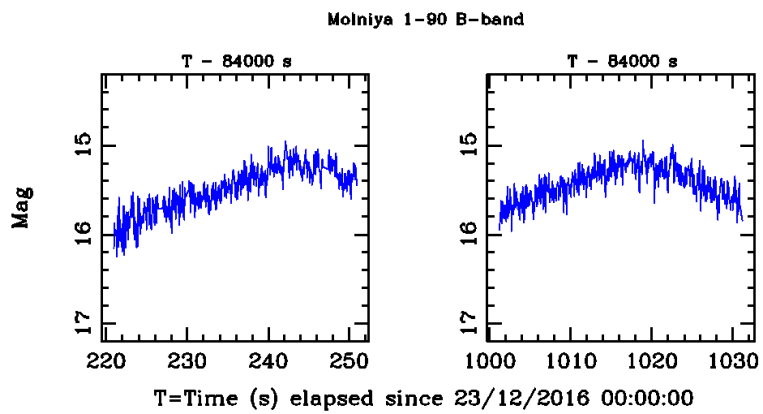


Figure A.196: Molniya 1-90 filter B light curves

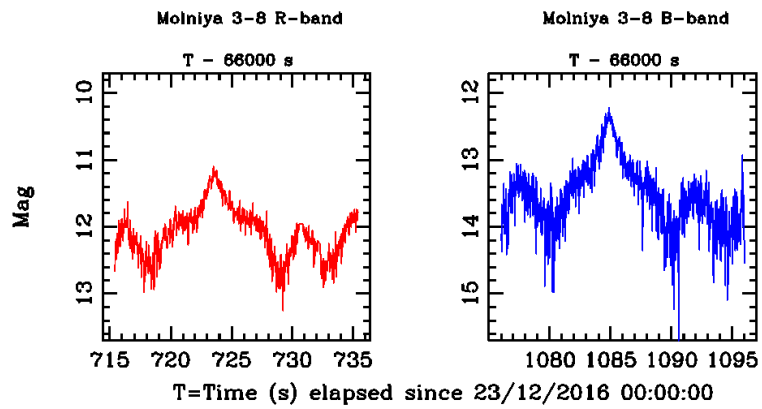


Figure A.197: Molniya 3-8 light curves

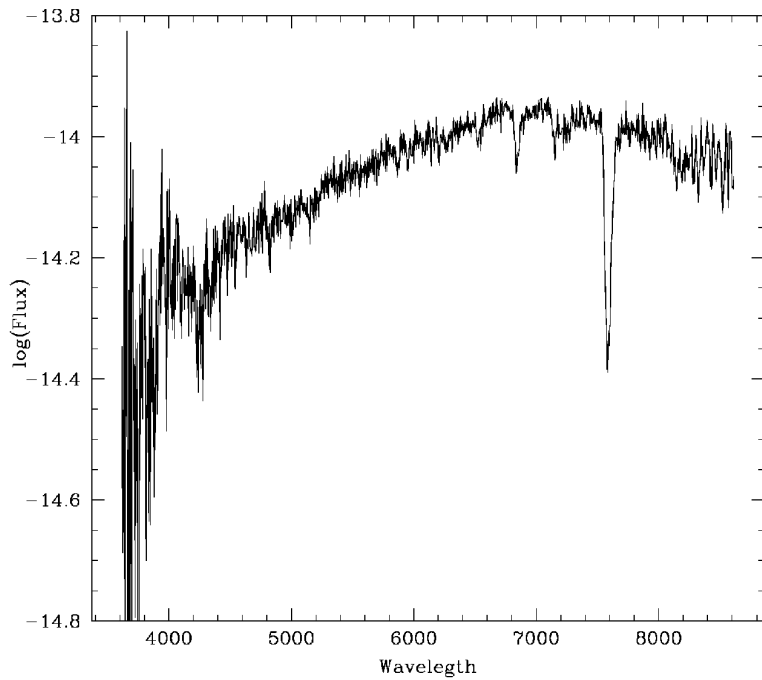


Figure A.198: Molniya 1-71 Spectra

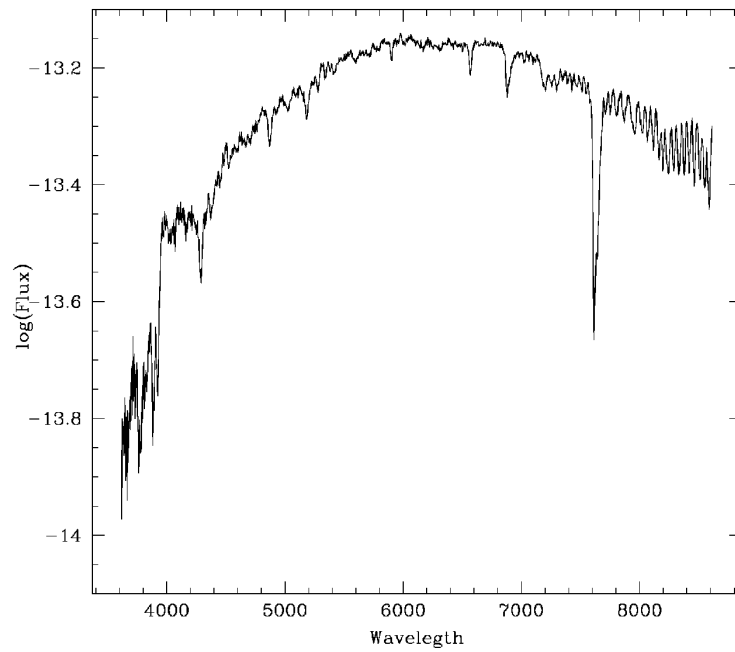


Figure A.199: Molniya 1-90 Spectra

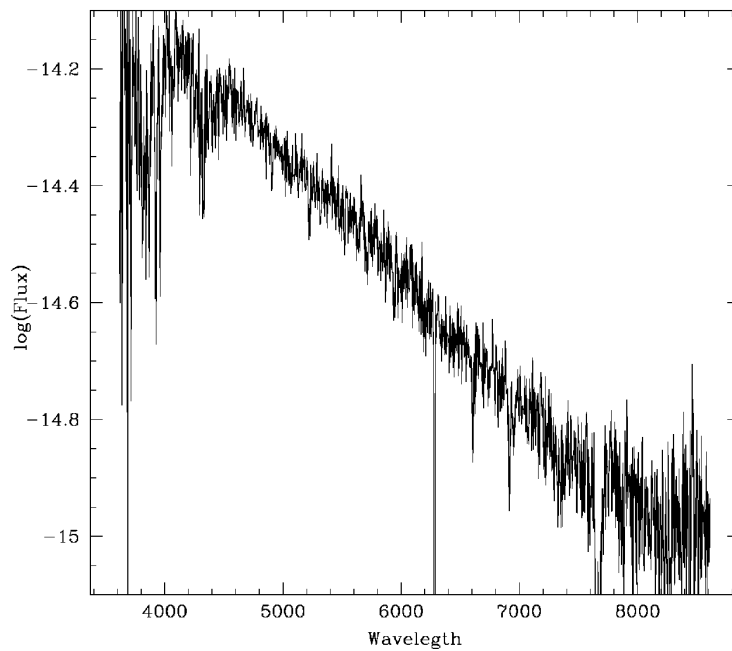


Figure A.200: Molniya 1-63 Spectra

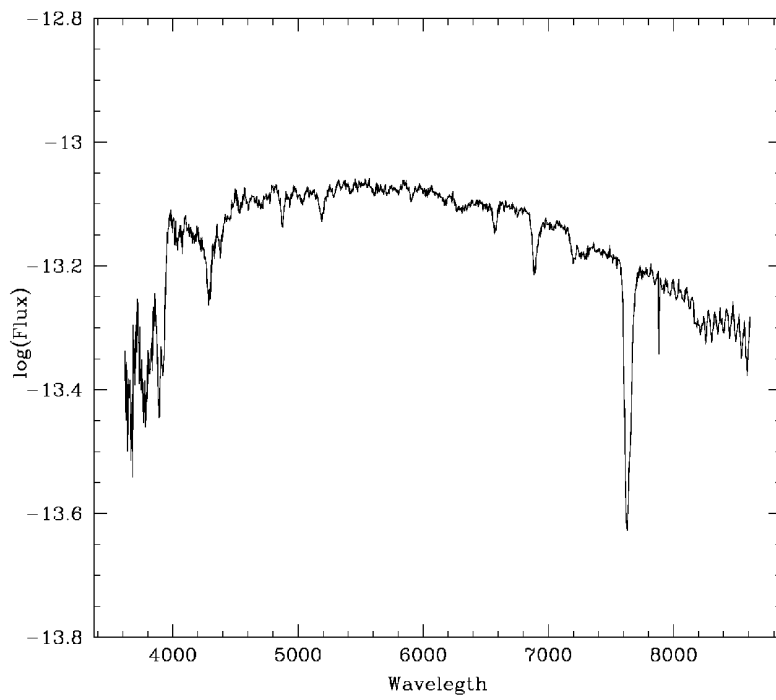
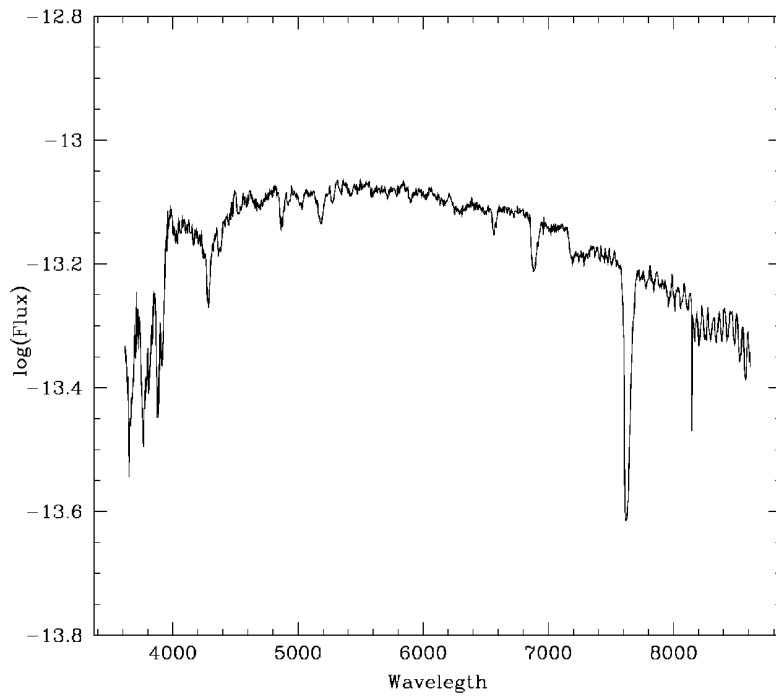


Figure A.201: Molniya 1-63 Spectra

Appendix B

Codes

B.1 Cubic spline c++ code

This program has one input file containing satellite ephemeris (α and δ) vs time, with step time one minute, and an output file containing satellite ephemeris with step time ten seconds.

```
#include<iostream>
#include<vector>
#include<algorithm>
#include<cmath>
#include <cstdio>
#include <cstdlib>
#include <vector>
#include <fstream>
#include <iomanip>
using namespace std;
typedef vector<double> vec;
struct SplineSet{
    double a;
    double b;
    double c;
    double d;
    double x;
};
vector<SplineSet> spline(vec &x, vec &y)
//here the spline is built
{
    int n = x.size()-1;
    vec a;
    a.insert(a.begin(), y.begin(), y.end());
    vec b(n);
    vec d(n);
    vec h;
    for(int i = 0; i < n; ++i)
        h.push_back(x[i+1]-x[i]);
```

```

vec alpha;
for(int i = 1; i <= n-1; ++i)
    alpha.push_back( 3*(a[i+1]-a[i])/h[i] - 3*(a[i]-a[i-1])/h[i-1] );
vec c(n+1);
vec l(n+1);
vec mu(n+1);
vec z(n+1);
l[0] = 1.;
mu[0] = 0;
z[0] = 0;
for(int i = 1; i < n-2; ++i)
{
    l[i] = 2 *(x[i+1]-x[i-1])-h[i-1]*mu[i-1];
    mu[i] = h[i]/l[i];
    z[i] = (alpha[i]-h[i-1]*z[i-1])/l[i];
}
l[n] = 1;
z[n] = 0;
c[n] = 0;
for(int j = n-3; j >= 0; --j)
{
    c[j] = z [j] - mu[j] * c[j+1];
    b[j] = (a[j+1]-a[j])/h[j]-h[j]*(c[j+1]+2*c[j])/3;
    d[j] = (c[j+1]-c[j])/3/h[j];
}
vector<SplineSet> output_set(n);
for(int i = 0; i < n-2; ++i)
{
    output_set[i].a = a[i];
    output_set[i].b = b[i];
    output_set[i].c = c[i];
    output_set[i].d = d[i];
    output_set[i].x = x[i];
}
return output_set;
}
using namespace std;
int main(int argc, char** argv) {
int number_of_lines = 0;
int i = 0;
ofstream plot("Satellite.txt");
string line;
ifstream myfile("effemeridi.txt");
//the file is uploaded with the heavensat ephemeris
if(myfile.is_open()){
while(!myfile.eof()){
    getline(myfile,line);
    number_of_lines++;
}
}
}

```

```

std::vector<double> x(number_of_lines),y(number_of_lines);
double a,b,c,d,f;
std::vector<double> z(number_of_lines),h(number_of_lines);
std::vector<double> m(number_of_lines),s(number_of_lines);
std::vector<double> RA(number_of_lines),dec(number_of_lines);
ifstream infile;
infile.open("effemeridi.txt");
if(myfile.is_open()){
int corrUT;
corrUT=1;
for(i=0;i<number_of_lines;i++)
//the ephemeris file is read (hours are correct to bring them back to universal time)
{
        infile>>a>>b>>c>>d>>f;
        h[i]=a-corrUT;
        m[i]=b;
        s[i]=c;
        y[i]=d*3600;
        z[i]=f*3600;
cout<< setprecision (15);
    }
}

int JDI;

double steptime=(m[4]-m[3])/60+(s[4]-s[3])/3600;
//cout<<steptime<<endl;
JDI=2457746;
for(i=0;i<number_of_lines;i++){
// Julian day is calculated
if(h[i]>12){
x[i]=JDI+(h[i]-12)/24+m[i]/1440+(s[i])/86400;
}
else{
x[i]=JDI+1+(h[i]-12)/24+m[i]/1440+(s[i])/86400;
}
}

    vector<SplineSet> cs = spline(x, y);
//spline is applied
int nint=6;
int e;
double Dt= (1./24)/(60*nint);
\ssteptime is defined
double JD[nint];
double Va[nint];
double jd;
for (i=0;i<cs.size()-2;i++){
jd=x[i];
    for (e=0;e<=nint-1;e++)
//the right ascension velocity is calculated

```

```

    {
        JD[e]=jd+e*Dt;
        Va[e]= ((3*cs[i].d*pow(JD[e]-JD[0],2)+2*cs[i].c
        *pow(JD[e]-JD[0],1)+cs[i].b)/24);
    }
    e=0;
vector<SplineSet> cd = spline(x, z);
int o;
double Vd[nint];
    for (o=0;o<=nint-1;o++)
//the declination velocity is calculated
    {
        JD[o]=jd+o*Dt;
        Vd[o]= ((3*cd[i].d*pow(JD[o]-JD[0],2)+2*cd[i].c
        *pow(JD[o]-JD[0],1)+cd[i].b)/24);
    }
    for (o=0;o<=nint-1;o++)
\\the new ephemeris file is written
    {
plot<<setprecision(13)<<JD[o]<<","<<int(Va[o])<<","<<int(Vd[o])<<endl;
        cout<<setprecision(13)<<JD[o]<<","<<int(Va[o])<<","<<int(Vd[o])<<endl;
    }
}
    myfile.close();
return 0;
}

```

B.2 Phase angle c++ calculation code

This program has two input files containing Sun and Satellite ephemeris (α and δ) vs time provided by Heavensat, and an output two columns file containing time and phase angle.

```

#include<iostream>
#include<vector>
#include<algorithm>
#include<cmath>
#include <cstdio>
#include <cstdlib>
#include <vector>
#include <fstream>
#include <iomanip>
using namespace std;

int main(int argc, char** argv) {
int number_of_lines = 0;
int i = 0;
ofstream plot("Phase.txt");
\\output file is defined
    ifstream myfile("Mol.txt");\loadind satellite coordinates file

```



```

\\input file is defined, with the ephemeris of the satellite
string line;
if(myfile.is_open()){
    while(!myfile.eof()){
        getline(myfile,line);
        number_of_lines++;
    }
}
double a,b,c,d,f;
std::vector<double> h(number_of_lines),m(number_of_lines);
std::vector<double> s(number_of_lines),RAmol(number_of_lines);
std::vector<double> decmol(number_of_lines),x(number_of_lines);
ifstream infile;
infile.open("Mol.txt");\\reading satellite coordiantes
if(myfile.is_open()){
for(i=0;i<number_of_lines;i++)
{
    infile>>a>>b>>c>>d>>f;
    if(a>=1){
h[i]=a-1;
    }
    else {
    h[i]=a-1+24;
}
m[i]=b;
    s[i]=c;
    RAMol[i]=d;
    decmol[i]=f;
}
}
int JDI=2457602;
for(i=0;i<number_of_lines;i++){
if(h[i]>12){
x[i]=JDI+(h[i]-12)/24+m[i]/1440+(s[i])/86400;
}
else{
x[i]=JDI+1+(h[i]-12)/24+m[i]/1440+(s[i])/86400;
}
}
int number_of_liness = 0;
ifstream myfilee("Sun.txt");\\loading of Sun coordinates file
\\file containing Sun ephemeris is loaded and read
if(myfilee.is_open()){
    while(!myfilee.eof()){
        getline(myfilee,line);
        number_of_liness++;
    }
    cout<<number_of_liness<<endl;
}
double g,k,j;

```

```

    int e = 0;
    std::vector<double> JD(number_of_lines),RASun(number_of_lines);
    std::vector<double> decsun(number_of_lines),cosph(number_of_lines);
    std::vector<double> ph(number_of_lines);
    ifstream onfile;
    onfile.open("Sun.txt"); \\reading Sun coordiantes
    if(myfilee.is_open()){
        //getline(myfile,line);
    for(e=0;e<number_of_lines;e++)
    {
        onfile>>g>>k>>j;
        JD[e]=g;
        RASun[e]=k;
        decsun[e]=j;
    }
}
for(i=0;i<number_of_lines;i++){
//phase angle is calculated
for(e=0;e<number_of_lines;e++)
{
if(JD[e]=x[i]){
cosph[i] = sin(-decsun[e]/57.2957795)*sin(decmol[i]/57.2957795)
+cos(-decsun[e]/57.2957795)*cos(decmol[i]/57.2957795)
*cos((RASun[e]-RAmol[i]+180)/57.2957795);
ph[i]=acos(cosph[i])*57.2957795;
}
}
cout<< setprecision (6);
//output file is written
plot<<h[i]<<" "<< m[i]<<" "<<s[i]<<" "<<ph[i]<<endl;
cout<<h[i]<<" "<< m[i]<<" "<<s[i]<<" "<<ph[i]<<endl;
}
return 0;
}

```

B.3 Periodogram supermongo macro

The input files are all the light curves of a satellite in a given filter, represented by a one column file with instrumental magnitude.

```

Per
#ligt curves reading and calibration
erase
data LightCurve1.dat #light curve loading
lines pix1 pix2 #light curve reading
read {F 1}
define ntot1 (dimen(F))
define texp (exposition time value)
define T (time at start of exposure)
do i=0,(dimen(F)-1){

```

```

if ( F[$i] > 1){
set F[$i]= F[$i]}
if ( F[$i] <= 1) {set F[$i]= 1}}
#do loop to bring the negative flux due to sky subtraction to 1
set y= lg(F)
set dt= ($texp/$ntot1)
define ddt ($texp/$ntot1)
set Airm= airmass value
set mag1= -2.5*y +2.5*lg($ddt)+22.15-0.2*(Airm)
-2.5*lg(npix)-5.*lg(Distance/30000.)
#light curve magnitude calibration
#npix = n of pixel on which the light curve has been averaged
set t1= ($T+($ntot1*dt)),$T+dt,(-dt)
#time axis assignment
#or set t1= $T+dt,($T+($ntot1*dt)),dt depending on satellite direction

data LightCurve2.dat
lines pix1 pix2
read {F 1}
define ntot1 (dimen(F))
define texp (exposition time value)
define T (time at start of exposure)
do i=0,(dimen(F)-1){
if ( F[$i] > 1){
set F[$i]= F[$i]}
if ( F[$i] <= 1) {set F[$i]= 1}}
set y= lg(F)
set dt= ($texp/$ntot2)
define ddt ($texp/$ntot2)
set Airm= airmass value
set mag2= -2.5*y +2.5*lg($ddt)+22.15-0.2*(Airm)
-2.5*lg(14.)-5.*lg(Distance/30000.)
set t2= ($T+($ntot2*dt)),$T+dt,(-dt)

#connection of the different light curves
set tplot = t1 concat t2
set mag = mag1 concat mag2
define stept ((texp1+texp2)/($ntot1+$ntot2))

location 5000 26000 20000 32000 #graphic instructions
ctype 0 lweight 3 expand 1.2
limits tplot 14 12
box
xlabel GPS time [sec]
ylabel Mag
lweight 1 expand 0.8
ltype 2 relocate 0 0 draw 100000 0 ltype 0
ptype 10 3 points tplot mag #plot magnitude vs time
limits 0 1 0 1 expand 0.8
define stround (int($stept*1000.+1.)/1000.)

```

```

#periodogram maximum and minimum period assignment
define pmin (minimum period)
define pmax (maximum period)

location 5000 26000 5000 17000 #graphic instructions
ctype 0 lweight 3 expand 1.2
limits $pmin $pmax 0. 4
box
xlabel Period
ylabel S/N

lweight 1 expand 0.8 ptype 10 3

#periodogram application
define err (10000)
do p=$pmin,$pmax,0.1 {
set fase1 = tplot/$p
set fase2 = int(fase1)
set fase = fase1-fase2
set mags = mag

sort {fase mags}

set d = fase-fase
do i=1,dimen(fase)-1 {
set d[$i] = (mags[$i]-mags[$i-1])**2
}
stats d md sd kd
define merit (sqrt($md))

smooth mags mag2 15
vecminmax mag2 mlow mup
define amp ($mup-$mlow)

#periodogram signal-to-noise ratio calculation
define ratio ($amp/$merit)
ctype 3
draw $p $ratio
relocate $p $ratio

#magnitude error estimator
if ($merit < $err) {
define err ($merit)
define perr ($p)}
}

#light curves phasing
Graf
erase

```

```

location 5000 25000 19000 31500 #graphic instructions
ctype 0 lweight 3 expand 1.2
limits 0 1.5 14 12
box
xlabel Phase
ylabel Mag

define p (periodogram resultant period)

set fase1 = tplot/$p #light curve phasing
set fase2 = int(fase1)
set fase = fase1-fase2
set mags = mag
sort {fase mags}

set fase_fold = fase+1.
set fase_ext = fase concat fase_fold
set mag_ext = mags concat mags

lweight 1 ptype 10 3 expand 0.9
connect fase_ext mag_ext #instruction to plot phased light curves
smooth mag_ext mag2 15 #smoothing function
lweight 3 ctype 3 connect fase_ext mag2
vecminmax mag2 mlow mup
define amp ($mup-$mlow)

```

B.4 Phase angle magnitude model supermongo macro

The input file is a two columns file containing phase angle and magnitude of each exposition in a give filter.

```

Phase
#reading of the phase angle magnitude file
erase
DATA Mag.txt
LINES 0 0
      READ {Ph 1 Mag 2}

#graphic instructions
ctype 0 lweight 2 expand 1.2
location 3000 27000 3000 18000
LIMITS 0 150 16.5 9.5
lweight 2
ctype 0
BOX
lweight 2
xlabel Phase Angle (deg)
lweight 2

```

```

ylabel Magnitude

#plotting of magnitude phase angle points
PTYPE 10 3 ctype 4
POINTS Ph Mag

#creation of fitting phase function
print fileint_V1.dat '' { }
define min (0.1/57.29578)
define max (150/57.29578)
do e = $min,$max,(0.1/57.29578) {
set alf = $e*57.29578
set fra = (sin($e)+((3.1415926-$e)*cos($e))/(3.1415926))
#fra = phase function depending on the model we are assuming
print + fileint_V1.dat '%d %d\n' { alf fra }
}

#least square test for best fit Aeff estimation
define R (30000000.)
#satellite magnitude calibrated with distance as they were at 30000 km
define Aeffmax (20)
define N (dimen(MagR))
define Aeffmin (0.01)
define step (0.01)
define BF (10000)
define num (dimen(PhR))

define NN ($Aeffmax/$step)
define N ($NN-1)
set dimen (check1) = $N
set dimen (check2) = $N
define Pi (3.14159)
define Rad (57.29578)
do Aeff = $Aeffmin,$Aeffmax-$step,0.01{
set Phasefunc = (sin(PhR/$Rad)+(($Pi-PhR/$Rad)*cos(PhR/$Rad)))/($Pi)
set Fluxexp = (1/(4*3.14))*$Aeff*Phasefunc/((R)**2)
set MagRexp = -26.764 - 2.5*lg(Fluxexp)
define CQ (0)
do i=0,dimn(MagR)-1,1{
define Chi ((MagR[$i]-MagRexp[$i])**2)
define CQ ($CQ + $Chi)
define Rap (sqrt($CQ/($num-1)))}
define inde ($Aeff-0.01)
define index ($nu*100)
set check1[$index] = $Aeff
set check2[$index] = $Rap
if ($BF>$CQ) {define BF ($CQ)}
}
define Rap (sqrt($BF/($num-1)))

```

```

#estimation of best fit Aeff minimising RMS value
vecminmax check2 checkmin checkmax
do Aeff = $Aeffmin,$Aeffmax-0.01,0.01{
define inde ($Aeff-0.01)
define index ($nu*100)
if (check2[$index] == $mlow){
define Aeffbf (check1[$index])}}

#fitting with best fit Aeff
DATA fileint_V1.dat
LINES 0 0
      READ {Phs1 1 Fph1 2}
define Aeff2 ($Aeffbf)
define R (30000000.)

set Fdiff1 = (1/(4*3.14))*$Aeff2*Fph1/$R**2
set mv1 = -26.764 - 2.5*lg(Fdiff1)

#creation of the final plot
ctype 0 lweight 2 expand 1.2
LIMITS 0 150 16.5 9.5
lweight 2
ctype 0
BOX
ctype 5
lweight 2
connect Phs1 mv1

```

B.5 Tumbling period slowdown model supermongo macro

```

Satellite
#this set of commands must be executed for each satellite
erase
location 3000 27000 3000 Sat00 #graphic instruction
ctype 0 lweight 2 expand 1.2
LIMITS -20 1000 3 4
lweight 2
ctype 0
BOX
lweight 2
xlabel Time (days)
lweight 2
ylabel Period (s)

define PiSat (initial period)

```

```

define PfSat (final period)
define tiSat (initial time (days))
define dtSat (final time (days))
set PSat = {initial_period final_period}
set tSat = {initial_time(days) final_time(days)}
set SigSat = {initial_period_error final_period_error}
define dPSat ($PfSat-$PiSat)

set dimen (t)= $dtSat
do i=1,$dtSat-1,1 {
set t[$i] = $i*86400} #setting time in seconds
set dimen (P) = dimen(t)

#determination of best fit exponential argument
do a=0.0000000001,0.000000002,0.000000000001{
set P = $PiSat*exp($a*t)
set d = t/86400
define bf (P[$dtSat-1]-$PfSat)
if (abs($bf)<0.0001){
define abestSat ($a)}
}

#creation and of fitting function
set dimen (tmod)=1000
do i=0,999,1{
set tmod[$i] = $i*86400}
set dimen (Pmod)=1000
set Pmod = $PiSat*exp($abestSat*tmod)
set d = tmod/86400
connect d Pmod

#data plotting instruction
ptype 4 3 ctype 4
points tSat PSat
ptype 4 0 ctype 0
points tSat PSat
ctype 0
errorbar tSat PSat SigSat 2
errorbar tSat PSat SigSat 4
limits 0 1 0 1 expand 1.0
ctype 0
relocate 0.02 0.15 putlabel 6 P = P0 exp(at) (s)
relocate 0.02 0.105 putlabel 6 a = $abestSat 1/s
relocate 0.02 0.06 putlabel 6 P0 = $PiSat s
ctype 3
relocate 0.8 0.06 putlabel 6 Molniya 1-88

#dp/dt plot creation
Dpdt
erase

```



```

define dPinSat ($abestSat*$PiSat*exp($abestSat*$tiSat*86400))
define dPfinSat ($abestSat*$PiSat*exp($abestSat*$dtSat*86400))
set dimen (dPpSat) = 2
set dPpSat[0]=$dPinSat
set dPpSat[1]=$dPfinSat
#the previous five commands must be executed for each satellite

set Sigma = SigSat1 concat SigSat2
set DdP = dPpSat1 concat dPpSat2
set Pp = PSat1 concat PSat2

location 3000 27000 3000 Sat00
ctype 0 lweight 2 expand 1.2
LIMITS 0 0.00000002 0 20
lweight 2
ctype 0
BOX
lweight 2
xlabel dP/dt
lweight 2
ylabel Period (s)
ptype 4 3 ctype 4
points DdP Pp
ptype 4 0 ctype 0
points DdP Pp
ctype 0
errorbar DdP Pp Sigma 2
errorbar DdP Pp Sigma 4

#linear regression
set Sx = 0.
set Sy = 0.
set Sxx = 0.
set Sxy = 0.
set S = 0.
define N dimen(DdP)
do i=1,$N-1,1 {
set Sx = Sx + DdP[$i]/(Sigma[$i])**2
set Sy = Sy + Pp[$i]/(Sigma[$i])**2
set Sxx = Sxx + (DdP[$i])**2/(Sigma[$i])**2
set Sxy = Sxy + DdP[$i]*Pp[$i]/(Sigma[$i])**2
set S = S + (1/Sigma[$i])**2}

define A (((Sxx*Sy)-(Sx*Sxy))/((S*Sxx)-(Sx*Sx)))
define B (((S*Sxy)-(Sx*Sy))/((S*Sxx)-(Sx*Sx)))
define x (2e-8)
define y ($B*$x + $A)
define x1 (0.)
define y1 ($B*$x1 + $A)
ctype 0

```

```

lweight 2
relocate $x $y
draw $x1 $y1
define Atot (1/$B)

limits 0 1 0 1 expand 1.0
ctype 0
relocate 0.02 0.96 putlabel 6 Linear regression:
relocate 0.02 0.915 putlabel 6  $P = B \frac{dP}{dt} + A$ 
relocate 0.02 0.87 putlabel 6  $B=\$B \text{ s and } A=\$A \text{ s}$ 

#Now we put together the data of all satellites
Sum
erase
location 3000 27000 3000 Sat00
ctype 0 lweight 2 expand 1.2
LIMITS 0 40000 0 20
lweight 2
ctype 0
BOX
lweight 2
xlabel Time (days)
lweight 2
ylabel Period (s)

#creation of common fitting function
set dimen (t) = dimen(Pp)
set dimen (ts) = dimen(Pp)
set ts = $B*ln(Pp/$A)
set t = ts/86400
set dimen (Pmod) = 40000
set dimen (tmod) = 40000
do i=1,39999,1{
set tmod[$i] = $i*86400
set Pmod[$i] = $A*exp(tmod[$i]/$B)}
set tmodday = tmod/86400
connect tmodday Pmod
define Atot (1/$B)

#plotting period vs time
ptype 4 3 ctype 4
points t Pp
ptype 4 0 ctype 0
points t Pp
ctype 0
errorbar t Pp Sigma 2
errorbar t Pp Sigma 4
limits 0 1 0 1 expand 1.0
ctype 0
relocate 0.02 0.96 putlabel 6  $P = P_0 \exp(at)$ 

```

```
relocate 0.02 0.915 putlabel 6 a = 1/Blinreg = $Atot
relocate 0.02 0.87 putlabel 6 P0 = Alinreg = $A
```

B.6 Spectral analysis macro

```
Spec
erase
data WFCal_Mol188_1.dat
lines 80 1300
read {x1 1 F1 2}

data WFCal_Mol188_2.dat
lines 80 1300
read {x2 1 F2 2}

define dr (30000)
define d1 (distance of satellite at first exposition)
define d2 (distance of satellite at second exposition)
define texp1 (time of the first exposition)
define texpw (time of the second exposition)
set j= lg(((texp1*F1*$d1**2/$dr**2)+(texp2*F2*$d2**2/$dr**2))/(texp1+texp2))

#here starts the smoothing of the spectra to a resolution of 10 Angstrom
set fase1 = x1/10
set fase2 = int(fase1)
set y = 10**j
do i=2,dimen(y)-1,1{
if (fase2[$i]==fase2[$i-1] and fase2[$i]==fase2[$i-2]){
set y[$i]=(y[$i]+y[$i-1]+y[$i-2])/3
set y[$i-1] = y[$i]
set y[$i-2] = y[$i]}}

do i=1,dimen(y)-1,1{
if (fase2[$i]==fase2[$i-1]){
set y[$i]=(y[$i]+y[$i-1])/2
set y[$i-1] = y[$i]}}

set lamb = fase2 *10

#solar spectrum reading
data Sun.txt
lines 0 0
read {lam 1 in 2}

#conversion of solar spectrum units in satellite spectrum units
set ipp = in*10000*10000000
#solar spectrum smoothing
set fase1 = lam
```

```

set fase2 = int(fase1)
set l = fase2*10
do i=1,dimen(in)-1,1{
if (l[$i]==l[$i-1]){
set ipp[$i]=(ipp[$i]+ipp[$i-1])/2
set ipp[$i-1] = ipp[$i]}}

#here the flux and wavelength vectors are rewritten
to prepare them for the division of the two spectra
define p (861-370)
set dimen (sunl) = $p
set dimen (satl) = $p
set dimen (sunf) = $p
set dimen (satf) = $p

do i=0,$p-1,1{
set sunl[$i] = 3700+$i*10
set satl[$i] = 3700+$i*10}

do i=0,$p-1,1{
do e=0,dimen(lamb)-1,1{
if (satl[$i] == lamb[$e]){
set satf[$i] = y[$e]}}}

do i=0,$p-1,1{
do e=0,dimen(l)-1,1{
if (sunl[$i] == l[$e]){
set sunf[$i] = ipp[$e]}}}
#the satellite spectra is finally divided by solar spectra
set rap = satf/sunf
#the result of the division is normalized to 7000 Angstrom
do i=0,dimen(rap)-1,1{
if (sunl[$i] == 7000){
define B (rap[$i])}}

set rapfin = rap/$B

#the result is written in a file
print Mol_rap.txt '%d %d\n' {sunl rapfin}

#the command since here must be executed for every satellite
#the resultant files are then read and plotted
erase
data Mol_rap1.txt
lines 0 0
read {lam1 1 rap1 2}

data Mol_rap2.txt
lines 0 0
read {lam2 1 rap2 2}

```

```

data Mol_rap3.txt
lines 0 0
read {lam3 1 rap3 2}

data Mol_rap4.txt
lines 0 0
read {lam4 1 rap4 2}

define TeX_strings 1
location 7000 27000 7000 25000
limits lam1 -0.3 1.5
expand 1.1
ctype 0
box
expand 1.3
xlabel Wavelnegth (\AA)
ylabel Ratio
expand 1.0
expand 1.5
ctype 3
connect lam1 rap1
ctype 4
connect lam2 rap2
ctype 7
connect lam3 rap3
ctype 5
connect lam4 rap4

```


Bibliography

- Abercromby, K., Hamada, K., Okada, J., Guyote, M., and Barker, E. (2006). Comparisons of Ground Truth and Remote Spectral Measurements of the FORMOSAT and ANDE Spacecraft. In *The Advanced Maui Optical and Space Surveillance Technologies Conference*, page E79.
- Baluev, R. V. (2008). Assessing the statistical significance of periodogram peaks. *Monthly Notices of the RAS*, 385:1279–1285.
- Bennett, B., Racey, T., Scott, R., and Wallace, B. (2006). Canadian surveillance of space concept demonstrator: Photometric variability of molniya-class objects.
- Boehnhardt, H., Koehnke, H., and Seidel, A. (1989). The acceleration and the deceleration of the tumbling period of Rocket Intercosmos 11 during the first two years after launch. , 162:297–313.
- Buratti, B. J., Hicks, M. D., Nettles, J., Staid, M., Pieters, C. M., Sunshine, J., Boardman, J., and Stone, T. C. (2011). A wavelength-dependent visible and infrared spectrophotometric function for the Moon based on ROLO data. *Journal of Geophysical Research (Planets)*, 116:E00G03.
- Buzzoni, A. (2005). Broad-band colours and overall photometric properties of template galaxy models from stellar population synthesis. *Monthly Notices of the RAS*, 361:725–742.
- Cognion, R. (2013). Observations and Modeling of GEO Satellites at Large Phase Angles. In *Advanced Maui Optical and Space Surveillance Technologies Conference*, page E64.
- Colombo, C. and Gkolias, I. (2017). Analysis of orbit stability in the geosynchronous region for end-of-life disposal. In *Proceedings of the 7th European Conference on Space Debris, April 18–21, 2017, Darmstadt (Germany)*.
- Cowardin, H., Seitzer, P., Abercromby, K., Barker, E., and Schildknecht, T. (2010). Characterization of Orbital Debris Photometric Properties Derived from Laboratory-Based Measurements. In *Advanced Maui Optical and Space Surveillance Technologies Conference*, page E47.
- F. Kolyuka, Y., M. Ivanov, N., I. Afanasieva, T., and A. Gridchina, T. (2017). Examination of the lifetime, evolution and re-entry features for the "molniya" type orbits.

- Gómez, N. O. and Walker, S. J. I. (2015). Earth’s gravity gradient and eddy currents effects on the rotational dynamics of space debris objects: Envisat case study. *Advances in Space Research*, 56:494–508.
- Gutierrez-Moreno, A., Moreno, H., Cortes, G., and Wenderoth, E. (1988). Spectrophotometry of stars of intermediate brightness. , 100:973–985.
- Hejduk, M. (2010). Catalogue-Wide Satellite Photometric Behavior Paradigms. In *Advanced Maui Optical and Space Surveillance Technologies Conference*, page E8.
- Hejduk, M. (2011). Specular and Diffuse Components in Spherical Satellite Photometric Modeling. In *Advanced Maui Optical and Space Surveillance Technologies Conference*, page E15.
- Hejduk, M., Cowardin, H., and Stansbery, E. (2012). Satellite Material Type and Phase Function Determination in Support of Orbital Debris Size Estimation. In *Advanced Maui Optical and Space Surveillance Technologies Conference*, page 14.
- Jin, H., Song, Y., Lee, Y., Kim, K., Lee, C., Choi, Y. E., Moon, H., and Yoon Lee J, D. (2011). The light curves of a geostationary satellite and its model.
- Kessler, D. J. (1991). Collisional cascading: The limits of population growth in low earth orbit. *Advances in Space Research*, 11(12):63 – 66.
- Kolyuka, Y. F., Afanasieva, T. I., and Gridchina, T. A. (2009). Orbit Evolution and Uncontrolled Re-Entry of the “Molniya” Type Satellites. In *Fifth European Conference on Space Debris*, volume 672 of *ESA Special Publication*, page 89.
- Landolt, A. U. (1992). UBVRI photometric standard stars in the magnitude range 11.5-16.0 around the celestial equator. *Astronomical Journal*, 104:340–371.
- Li, J.-Y., Helfenstein, P., Buratti, B., Takir, D., and Clark, B. E. (2015a). *Asteroid Photometry*, pages 129–150.
- Li, J.-Y., Helfenstein, P., Buratti, B., Takir, D., and Clark, B. E. (2015b). *Asteroid Photometry*, pages 129–150.
- Mulrooney, M., Matney, M., Hejduk, M., and Barker, E. (2008). An Investigation of Global Albedo Values. In *Advanced Maui Optical and Space Surveillance Technologies Conference*, page E65.
- O. Fulcoly, D., I. Kalamaroff, K., and K. Chun, F. (2012). Determining basic satellite shape from photometric light curves. 49:76–82.
- Seitzer, P., Abercromby, K. J., Barker, E. S., Cardona, T., Lederer, S. M., and Cowardin, H. (2012). Visible Light Spectroscopy of GEO Debris. In *Advanced Maui Optical and Space Surveillance Technologies Conference*, page 9.
- Veis, G. (1963). Optical Tracking of Artificial Satellites. , 2:250–296.